

539799

3172544

TR diss 2011

2 TR diss  
2011

**THE RADON TRANSFORM AND ITS APPLICATION TO THE  
INTERPRETATION OF SEISMIC DATA**

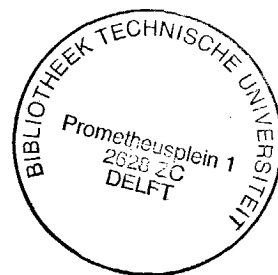
**THE RADON TRANSFORM AND ITS APPLICATION TO THE  
INTERPRETATION OF SEISMIC DATA**

**Proefschrift**

ter verkrijging van de graad van doctor aan de Technische Universiteit Delft,  
op gezag van de Rector Magnificus, prof. drs. P.A. Schenck, in het openbaar te  
verdedigen ten overstaan van een commissie aangewezen door het College van  
Dekanen op dinsdag 7 januari 1992 te 14.00 uur

door

**Marianne Vissinga  
geologe  
geboren te Rijswijk**



Dit proefschrift is goedgekeurd door de promotor  
Prof.A.M. Ziolkowski M.A., Ph.D., M.Sc. (Econ.)  
en door de toegevoegd promotor Dr. ir. J.T. Fokkema

*Aan mijn ouders*

*The research reported in this thesis has been performed at the Delft University of Technology, Department of Mining and Petroleum Engineering, Section Applied Geophysics. Part of this research has been financially supported by the European Community.*

---

**CONTENTS**

<b>NOTATIONS AND CONVENTIONS</b>	<b>1</b>
 <b>1 INTRODUCTION</b>	
1.1 The application of the Radon transform to the interpretation of seismic data: the motivation for this thesis	3
1.2 Historical overview of the Radon transform	9
1.3 Numerical aspects of the Radon transform	11
- The finite range of the integrations	11
- The interpolation	12
- Evaluation of the Bessel function	13
1.4 Outline of the thesis	14
 <b>2 MATHEMATICAL FRAMEWORK</b>	
2.1 Introduction	17
2.2 The mathematical introduction to the Radon transform	18
 <b>3 THE INVERSE RADON TRANSFORM APPLIED TO SYNTHETIC SEISMOGRAMS OVER PLANE HORIZONTAL LAYERS</b>	
3.1 Introduction	31
3.2 Development of the numerical implementation of the Hankel transform	32
3.3 The inverse Radon transform for the point source configuration	33
3.4 The computational procedure of the inverse Radon transform for the point source configuration	35
3.5 The inverse Radon transform for the line source configuration	38
3.6 Problems caused by the numerical implementation	39
- The singularity of the square-root in the Green's function	39
- Aliasing in the $f$ - $p$ domain	40

3.7	Interpolation	41
3.8	Numerical results:	49
	- modelled with the inverse Radon transform	49
	- modelled with the exact Cagniard-De Hoop technique	53
3.9	Artifacts due to the numerical implementation of the transform	54
4	<b>THE FORWARD &amp; INVERSE RADON TRANSFORMS APPLIED TO T-X DATA: A SHOT GATHER OR A CMP GATHER</b>	
4.1	Introduction	57
4.2	The Radon transform for the point source configuration	58
4.3	The Radon transform for the line source configuration	60
4.4	Problems caused by the numerical implementation	61
	- Aliasing in the $f$ - $p$ domain	61
	- Spatially finite aperture, including the lack of near-offset measurements	62
	- Suitable tapers for the transform	63
4.5	Main differences from the algorithm of Chapter 2	64
4.6	Synthetic data examples (2D & 3D)	65
5	<b>CLASSIFICATION OF EVENTS IN THE CONVENTIONAL T-P DOMAIN</b>	
5.1	Introduction	73
5.2	A hyperbolic event	74
5.3	A linear event	84
5.4	A diffractor	92
5.5	Edge effects	97
	- Summary	99
5.6	Field data examples	99
6	<b>THE FORWARD RADON TRANSFORM APPLIED TO T-X DATA: A SEISMIC LINE</b>	
6.1	Introduction	117
6.2	The formulation of the problem	118
6.3	Application: a pre-stack migration procedure	127
6.4	Problems and limitations due to the method and due to the data	130
	- Dip slowness curves	130

6.5	The computational procedure and the presentation of the data	133
-	Computational procedure	133
-	Presentation of the data	134
6.6	Data examples	136
-	Four point scatterers, all at the same spatial position	136
-	Four point scatterers, each at different spatial positions	141
-	A constantly dipping interface	143
-	A pyramid-shape interface	146
-	A pyramid-shape interface sandwiched between two horizontal interfaces	149
-	A land data set	152
 7	 CONCLUSIONS	 163
 A	 APPENDIX	
A.1	Calculation of the Green's function for the acoustic case	167
A.2	The method of stationary phase	172
A.3	Complex frequency	176
A.4	Interpolation as part of the Radon transform	179
 REFERENCES		 183
 SUMMARY		 189
 SAMENVATTING (DUTCH)		 191
 ACKNOWLEDGEMENTS		 193
 CURRICULUM VITAE		 194



---

NOTATIONS AND CONVENTIONS

---

In this thesis, vectors are typed bold-faced. To locate a point in space, the orthogonal Cartesian coordinates  $x_1$ ,  $x_2$  and  $x_3$  and the unit vectors  $i_1$ ,  $i_2$  and  $i_3$  are employed in a right-handed system with  $i_3$  pointing downwards. Temporal and spatial Fourier transforms are used, where quantities in the frequency ( $f$ ) domain are denoted by a circumflex (^) on top and in the wavenumber ( $k$ ), or slowness ( $p$ ) domain by a tilde (~) and in the double slowness domain by a double tilde (=) on top.

### Symbols

$i_1, i_2, i_3$	Cartesian unit vectors
$x_1, x_2, x_3$	Cartesian coordinates (m)
$x$	cylindrical coordinate (m)
$k_1, k_2$	wavenumber parameters ( $\text{m}^{-1}$ )
$p_1, p_2$	horizontal slowness parameters ( $\text{sm}^{-1}$ )
$q$	vertical slowness parameter ( $\text{sm}^{-1}$ )
$t$	time coordinate (s)
$f$	frequency ( $\text{s}^{-1}$ )
$s$	Laplace transform parameter ( $\text{s}^{-1}$ )
$\widehat{S}(f)$	source spectrum ( $\text{kgs}^{-1}$ )
$v$	compressional wave velocity ( $\text{ms}^{-1}$ )
$i$	complex number
$P$	pressure ( $\text{kgm}^{-1}\text{s}^{-2}$ )
$J_0$	Bessel function of the first kind and zero order
$R_n$	global reflection coefficient of the $n$ -th layer
$r_n$	local reflection coefficient of the $n$ -th layer
$\delta(t)$	temporal delta function ( $\text{s}^{-1}$ )
$\delta(x)$	spatial delta function ( $\text{m}^{-1}$ )

$\tau$	intercept time (s)
$\omega$	angular frequency (rads <sup>-1</sup> )
$\lambda$	wavenumber parameter (m <sup>-1</sup> )
$\varepsilon$	imaginary part of complex frequency (rads <sup>-1</sup> )
$\rho$	volume density of mass (kgm <sup>-3</sup> )

## Abbreviations

2D	2-dimensional
2 <sup>1</sup> / <sub>2</sub> D	2 <sup>1</sup> / <sub>2</sub> -dimensional
3D	3-dimensional
CMP	Common midpoint
DMO	Dip move out
DRT	Discrete Radon Transform
FFT	Fast Fourier Transform
GRT	Generalized Radon Transform
PWD	Plane Wave Decomposition
RT	Radon Transform
VSP	Vertical Seismic Profile

---

## INTRODUCTION

### *1.1 The application of the Radon transform to the interpretation of seismic data: the motivation for this thesis.*

The Radon transform has conventionally been applied to seismic data to decompose the data into plane wave components. This decomposition allows waves which travel with different slownesses to be separated. In land seismic reflection data for example, the Radon transform can be applied to separate compressional waves, shear waves and surface waves (Tatham et al., 1982). In vertical seismic profiling (VSP) data the Radon transform may be applied to separate the upgoing waves from the downgoing waves, and to separate different converted modes (Moon, 1986).

In the calculation of synthetic seismograms from well-logs the theory of wave propagation in plane horizontal layers is very often handled in the frequency-slowness domain using the reflectivity method (Fuchs and Müller, 1971; Kennett, 1983), especially when there is a large number of layers in the model, or when some of the layers are thin. In order to compare the synthetic seismograms with field data in the time-space domain, the synthetic data have to be transformed to the time-space domain with the inverse Radon transform.

Thus the forward Radon transform is required for plane wave decomposition and allows further data processing to proceed on each wave component separately. The inverse Radon transform is required either to get the data back to the time-space domain after processing in the plane wave domain, or to transform synthetic data to the time-space domain for comparison with field data.

An example of the application of the forward transform is shown in Fig.1.1.1. Fig.1.1.1a shows a shot gather from the northern part of the North Sea in which there is a big problem with reverberation of the source energy trapped between the sea floor and the sea surface.

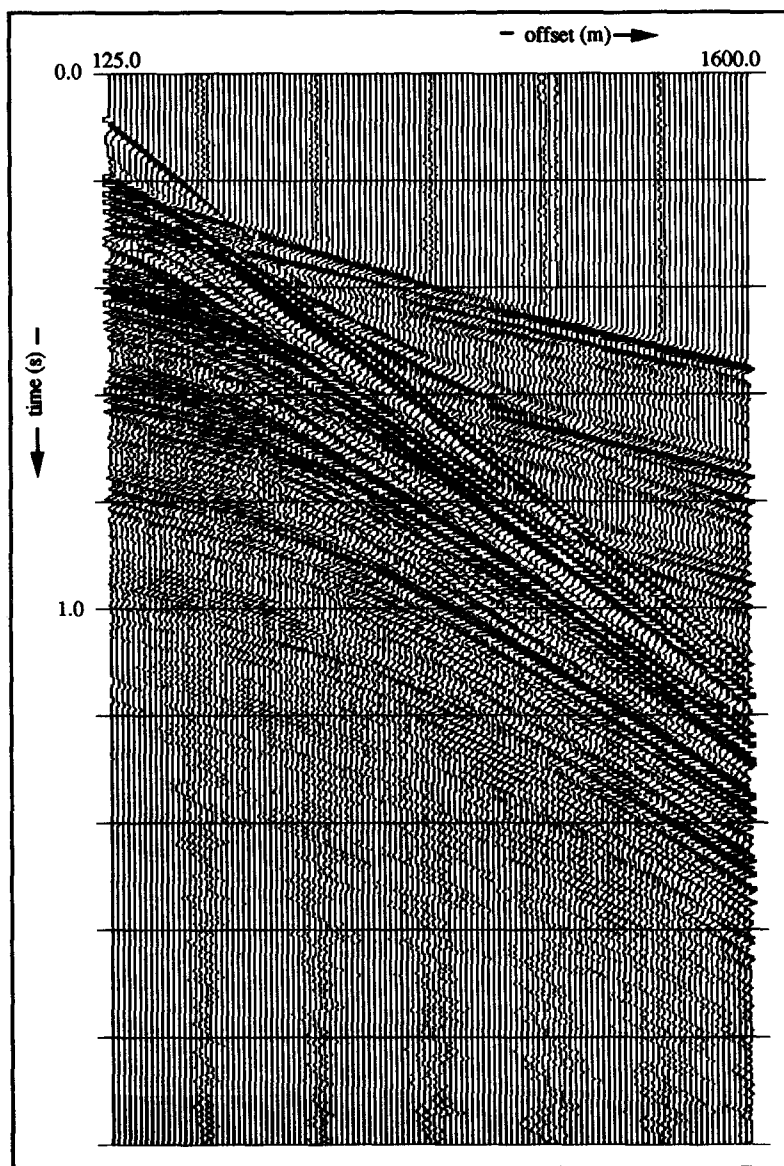


Fig.1.1.1a: The North Sea data set; first offset = 125 m,  $\Delta x = 12.5$  m.

Fig.1.1.1b shows the Radon transform of this shot record: the multiples, which are not periodic in the time-space domain (Fig.1.1.1a), become periodic in the intercept time-slowness domain, the period decreasing with increasing slowness.

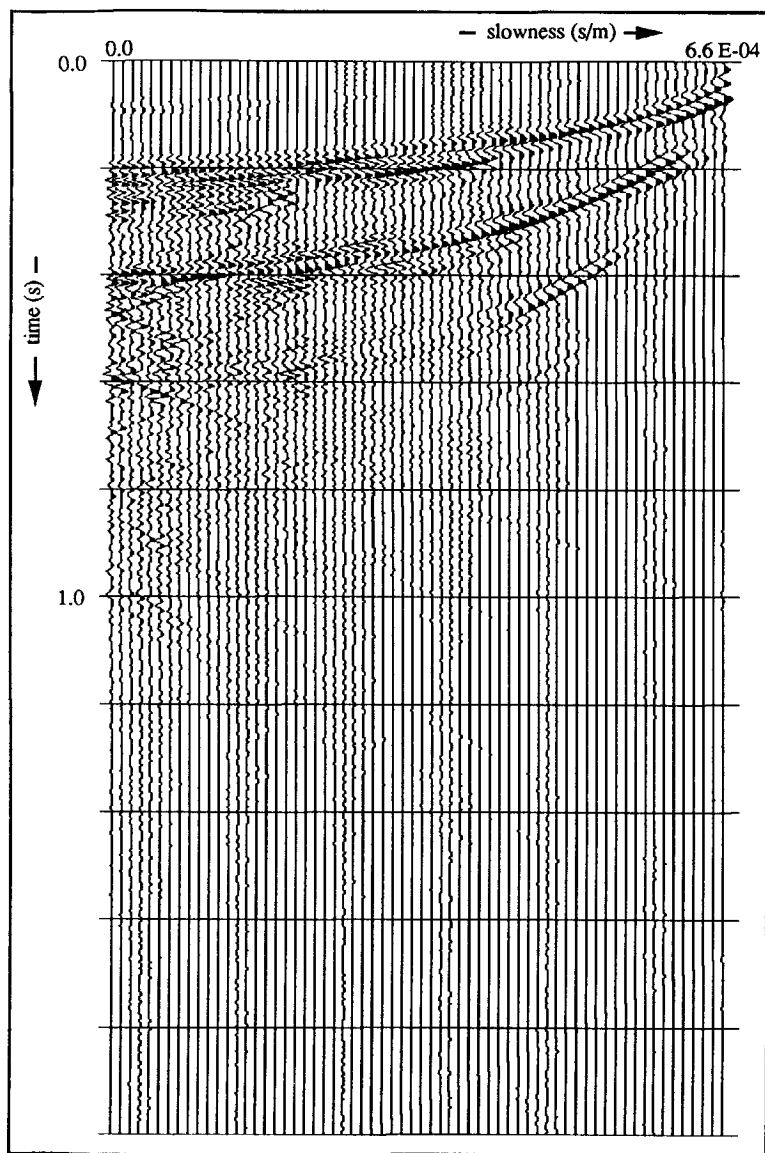


Fig.1.1.1b: The intercept time-slowness response of the North Sea data set;  $\Delta p = 5.28$  ms/km.

An example of the application of the inverse Radon transform is shown in Figs.1.1.2 - 1.1.5. Fig.1.1.2 shows the configuration of an airgun array and a 100-channel streamer in the water overlying a 326-layer acoustic earth model with the acoustic impedance profile shown in Fig.1.1.3.

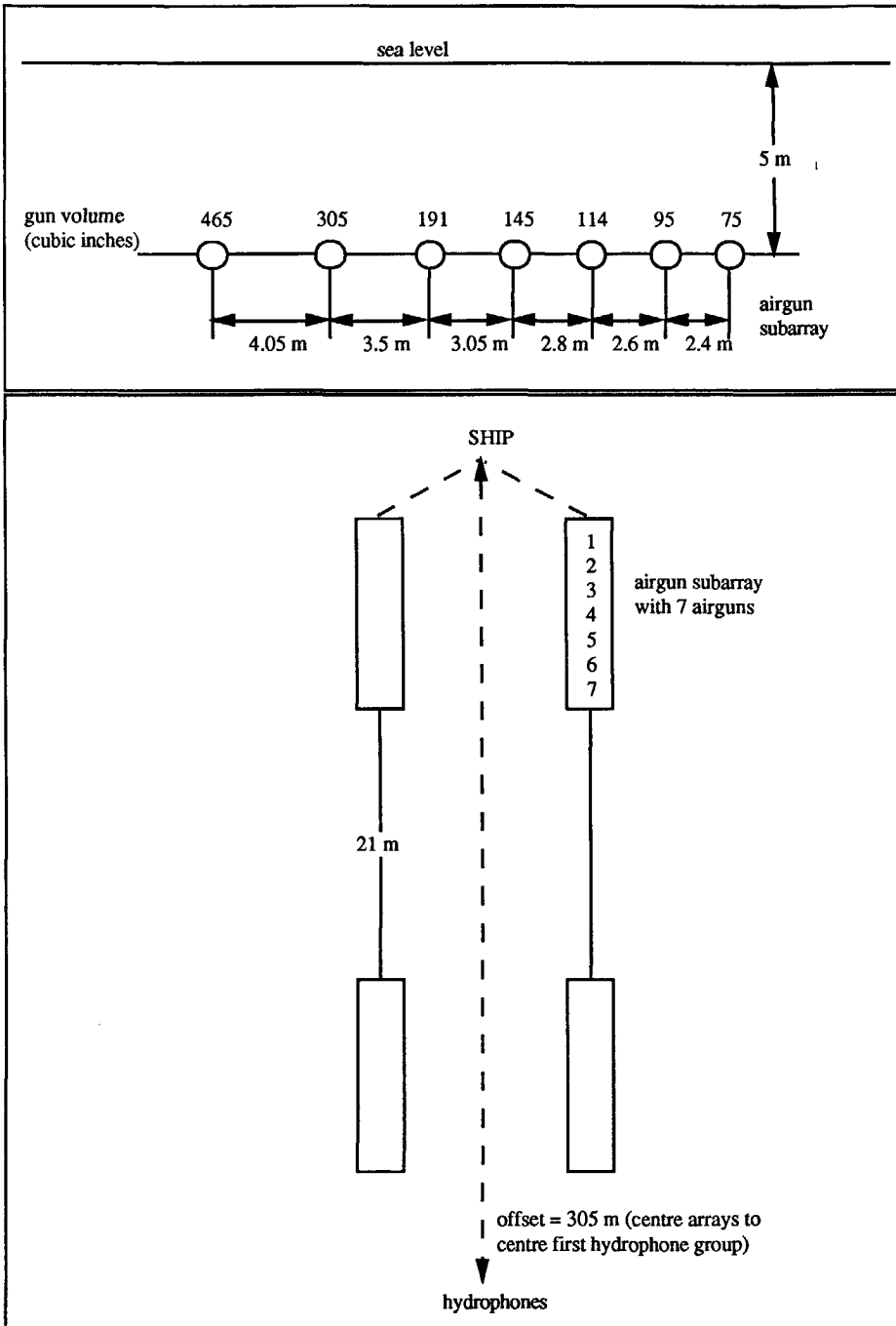


Fig.1.1.2: The configuration of an airgun array of the Delft Airgun experiment.

Fig.1.1.4 shows the corresponding synthetic seismogram in the time-space domain. This was calculated by Tijdens (1990) in the following way: the point source response was first calculated in the frequency-slowness domain (Appendix A); the result was transformed to the time-space domain with the appropriate offset for each airgun position, using the inverse Radon transform, and then convolved with the appropriate notional source signature for that airgun, as shown in Fig.1.1.5 (Ziolkowski et al., 1982, Parkes et al., 1984, Ziolkowski, 1987); the resulting synthetic seismograms for the full array of airguns were then superposed.

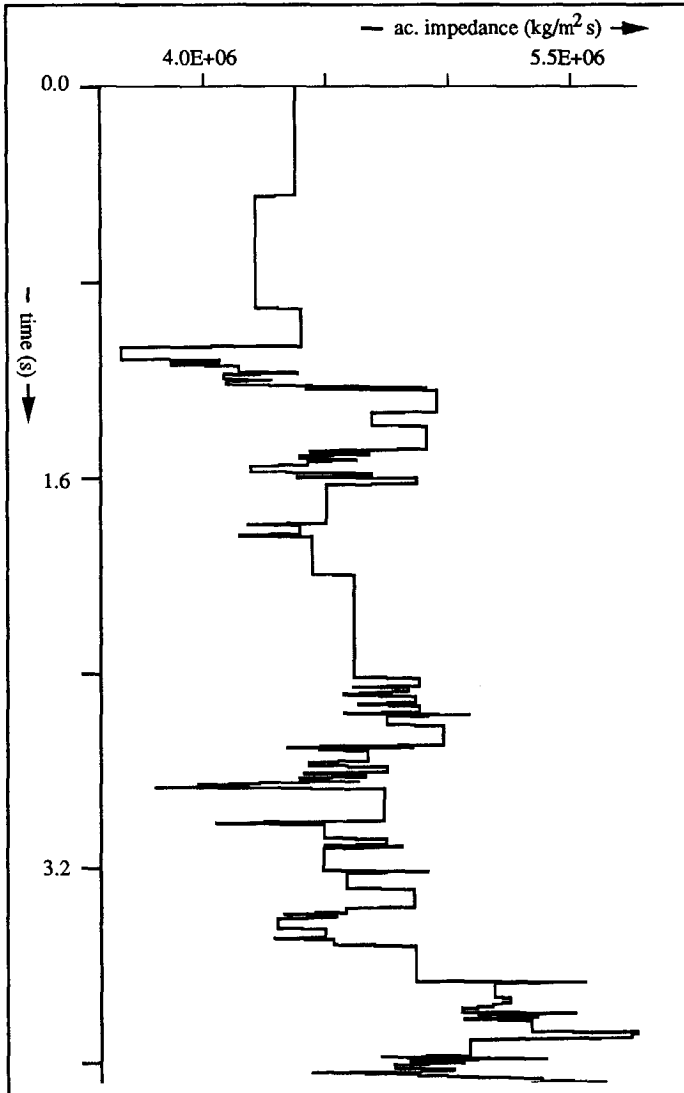


Fig.1.1.3: The acoustic impedance profile of the well log from the Delft Airgun experiment.

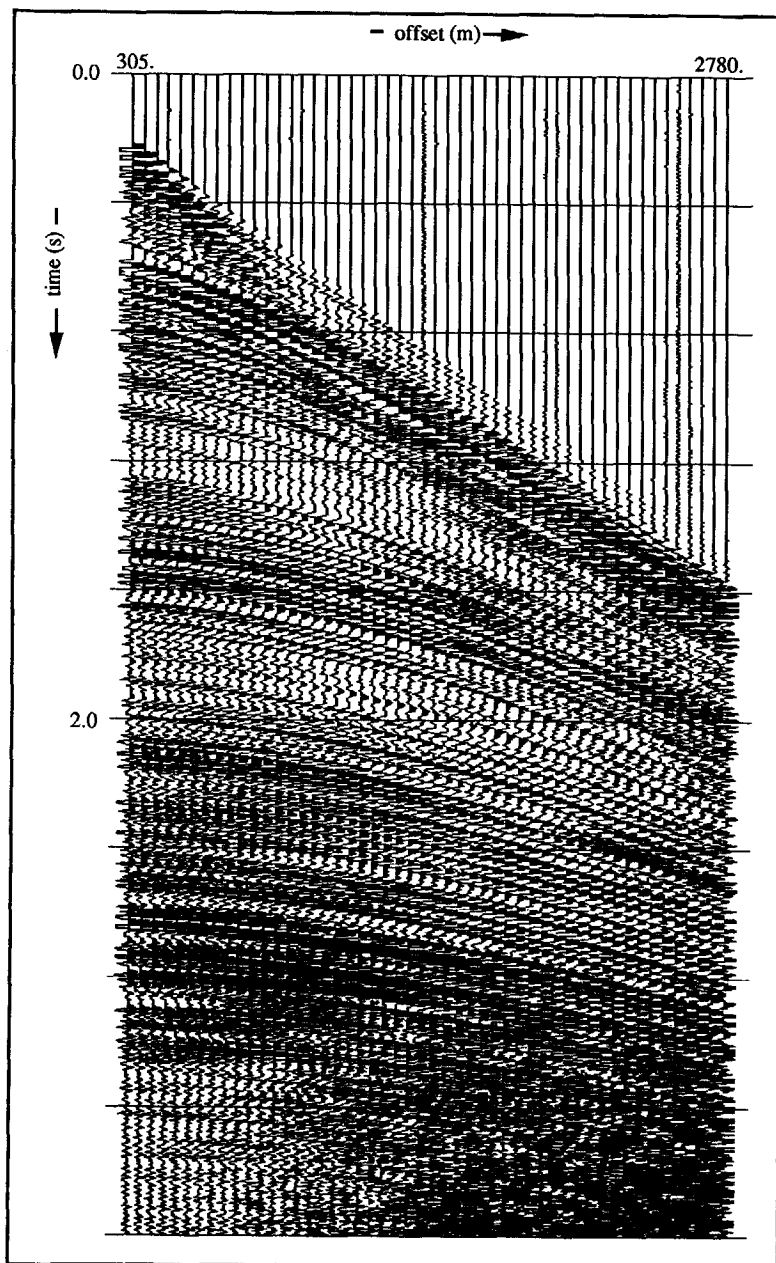


Fig.1.1.4: The time-space response of 326-layer earth model.



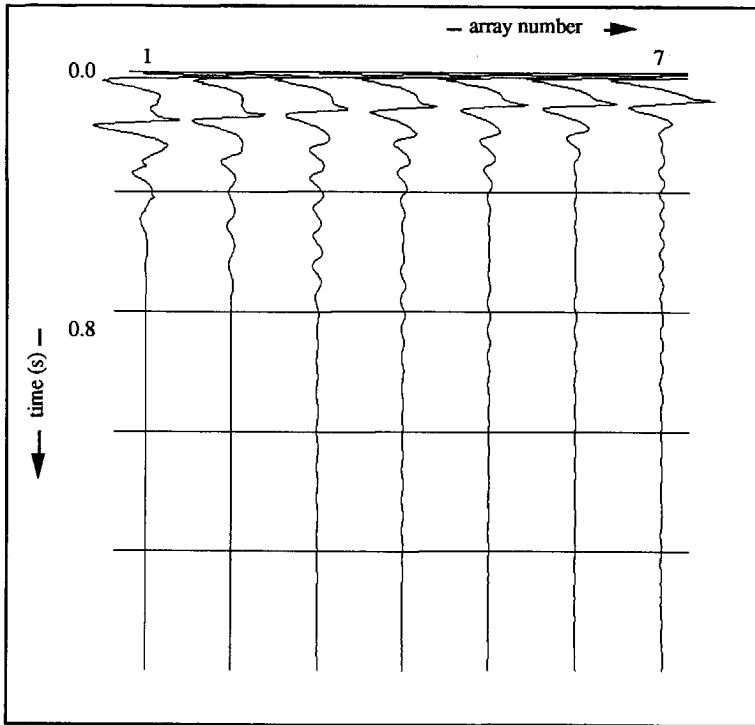


Fig.1.1.5: The calculated notional sources of the airgun subarray, shown in Fig.1.1.2.

The requirement for forward and inverse Radon transformations is clear. The reason that the Radon transform is not used very extensively in seismic data processing is because of a number of difficulties in its numerical implementation. One difficulty is that the forward and inverse discrete Radon transforms are not exactly reversible, unlike, for example, the forward and inverse discrete Fourier transforms. Something is always lost when the discrete Radon transform is applied to field data. However, this price may be worth paying in order to decompose the data into the plane wave components. Another difficulty is that the transform can be very costly to perform accurately.

It is the aim of this thesis to examine the theory of the Radon transform, and to develop and apply a theory for its efficient and accurate numerical implementation. The theory is worked out first for the case of plane horizontal layers, or a one-dimensional earth, and is then extended to two- and three-dimensional earth models.

## 1.2 Historical overview of the Radon transform

A good agreement between a synthetic seismic record and the raw seismic data implies a good understanding of the seismic source, the earth structure and the theory of wave

propagation relevant to the frequency content of the data. The Radon transform lends itself to the purpose of transformations as well as to the analysis of seismograms. While the ray aspects of the  $\tau$ - $p$  (intercept time-slowness) interpretation were being developed and implemented over many years, the corresponding wave aspects were almost ignored. Schultz and Claerbout (1978) first recognized the connection between slant stacking and the synthesis of plane-wave equivalents from the data. As Treitel et al. (1982) pointed out, the idea of representing harmonic spherical waves as a superposition of plane-wave components (homogeneous as well as inhomogeneous) is hardly new. It goes at least back to Whittaker (1902), Sommerfeld (1909) and Weyl (1919). But Treitel et al. (1982) observed that the reflectivity method of wave analysis had been developed independently some time earlier, and closely related results on the synthesis of plane waves had appeared (Fuchs and Müller, 1971) without noting the connection. They covered wave propagation in a uniform medium and emphasized the importance of the point-source wave treatment for an optimum deconvolution.

The most thorough wave theory of the  $\tau$ - $p$  method was given by Chapman (1978, 1979, 1981). Chapman included explicit recognition of its proper application for point sources as well as for other source geometries. His technique of evaluating the frequency integral first and keeping the slowness integral real was new, and enabled each seismogram to be interpreted as an integrated cross section of a "density" function at a given angle. Chapman also acknowledged the affinity to the much older mathematical formulation of the Radon transform. Phinney et al. (1981), Henry et al. (1980) and Harding (1985) concentrated on details of the numerical computations and related asymptotic evaluations. McMechan and Ottolini (1980) made extensive use of the observation that slant stacking is capable of unfolding triplications present in refraction data. Later on, in 1986, Brysk and McCowan rewrote the Radon transform for a 3D geometry such that the original integral is replaced by a conventional slant-stack procedure followed by a square-root filter.

A different algorithm was submitted by Benoliel et al. (1987). They proposed a  $f$ - $k$  (frequency-wavenumber) approach to the Radon transform which is a 2D FFT followed by an interpolation and then by an inverse-time FFT. To reduce edge effects, a mute due to the Nyquist wavenumber is incorporated. However the use of their algorithm is restricted because they use the asymptotic approximation of the Bessel function. Zero-offset cannot be calculated and near-offset amplitudes are unreliable. In the same year, Beylkin (1987) presented the discrete Radon transform (DRT) as a matrix-vector multiplication which has a block-circulant<sup>1</sup> structure and hence allows construction of fast direct and inverse transforms. His definition of the DRT gives an exactly invertible and efficient back transform. Moreover, Beylkin (1987) extended his DRT into the generalized Radon transform (GRT), in which the integrals over more general curves (hypersurfaces) instead of over hyperplanes are evaluated.

Kappus et al. (1990) compare existing Radon transform methods. They discuss five methods: the conventional slant stack (2D), the slant stack for the point source configuration

---

<sup>1</sup> a mathematical determinant in which each row is derived from the preceding by cyclic permutation, each constituent being pushed into the next column and the last into the first so that constituents of the principal diagonal are all the same.

(3D), the cylindrical slant stack according to Brysk and McCowan (1986, 3D), the point source configuration with the asymptotic approximation of the Bessel function (2D+), and the linear inverse approach to construct the entire wavefield in  $\tau$ - $p$  (3D). They conclude that if accurate amplitudes are required, a full 3D Radon transform should be used. If only correct arrival times are needed, an asymptotic approximate method will do. The techniques and uses of the Radon transform in a more general context (medical applications in particular) were detailed by Deans (1983), including a translation of Radon's paper in 1917.

### *1.3 Numerical aspects of the Radon transform*

There are three numerical problems that must be tackled in order to implement the Radon transform on discrete, sampled data. First, because the data are collected over a finite aperture, the range of integrations is finite. Second, because the data are sampled in space at discrete points, an interpolation is required in the transformation to the slowness domain. Third, for cylindrical symmetry, a Bessel function of the first kind has to be evaluated.

#### *The finite range of the integrations*

The analytic expression for the classical Radon transform requires the projection of the data as a continuous function, infinitely differentiable, of two variables: space and time. In practice this continuous function is never available, as only a finite number of data can be collected. Therefore the analytic expression must be approximated by a form suitable for the finite, discrete data set. Such approximations are extremely common in data processing. Once the function has been sampled at a finite number of discrete points, the integral must be approximated, normally by the finite series.

The performance of the integrations over a finite range is the first main problem of the numerical implementation, because the lack of a spatially infinite aperture causes so-called edge effects. The edge effects or truncation effects, which can be severe, introduce coherent noise and have been noticed by several geophysicists. Durrani (1984) amongst others noticed that, because of the spatially finite integration, a linear event in the  $t$ - $x$  (time-space) domain does not map into a point in the  $\tau$ - $p$  domain, according to the conventional view (Phinney, 1981), but maps into an hour-glass structure in  $\tau$ - $p$ . Several techniques to reduce these effects have been developed, which are outlined below.

The application of an appropriate spatial window function reduces the truncation effects according to Schultz and Claerbout (1978), Brysk and McCowan (1986) and Singh (1989). The same sort of solution was given by Stoffa et al. (1981) who introduced a window function based on semblance, which can be considered as the ratio of output to input energy along a proposed trajectory. Another approach was submitted by VerWest et al. (1984), Harding (1985), Dobbs et al. (1990) and Dietrich (1988, 1990). These authors all made use of the asymptotic approximation of the Bessel function which consists of two exponential factors, one

with a positive argument and the other with a negative argument. Then, they use only the part that represents the downgoing waves, the positive argument. The upgoing waves, associated with the negative argument introduce only numerical artifacts and cause the negative-dip events in the  $\tau$ - $p$  domain, according to Harding (1985).

Dobbs et al. (1990) grouped the aliased energy caused by the finite aperture into two types. The first type is due to a lack of energy recorded by the finite aperture array, and the second type is due to the finite integration and appears as linear artifacts. They derived a linear  $p$ -dependent filter and demonstrated that these artifacts could be predicted by their filter. While Milkereit (1987) focused his attention on the localized slant stack which has to deal even more with a finite aperture of the data set, he noticed that his bow-tie effects (truncation effects) were also predictable and could therefore be minimized by a decorrelation process used for image restoration in optics following Bagnuolo (1985).

Another kind of problem, also related to the finite range of the integrations, is the maximum available  $p$ -range present in a  $t$ - $x$  data set. Usually the restriction on the  $p$ -range in the transformed  $t$ - $x$  data is not taken into consideration and this results in numerical noise. One way to avoid this is to apply a velocity filter (Noponen and Keeney, 1982; Kelamis and Mitchell, 1989 and Mitchell and Kelamis, 1990). This filter puts a restriction on the range of possible velocities related to the traveltimes. The larger the traveltimes, the higher the velocities are allowed to be. The improvement achieved by this filter is worthwhile. The near-offset and far-offset information gets lost, but this was never really available in the first place. The problem of the edge effects and the restrictions on the available  $p$ -range present in a  $t$ - $x$  data set, are extensively discussed in Chapter 4.

### ***The interpolation***

Interpolation is the second main problem of the transform (Fig.1.3.1). For example, a linear event with a certain slope in  $t$ - $x$  maps into a point in  $\tau$ - $p$  in the ideal case, and this point in  $\tau$ - $p$  describes the linear event completely in  $t$ - $x$  without loss of information. But the linear event in  $t$ - $x$  is known only at regular grid points and not necessarily known at points intersecting with the dipping linear event. Therefore some kind of interpolation is needed.

The first question is the order of the interpolation procedure. The higher the order, the more accurate the results, but the more expensive the algorithm. Then the next question is: Where and how should the interpolation step be introduced in the algorithm? Brysk and McCowan (1986) implement the interpolation in the time domain, performing their cylindrical slant stack as a double integral over time-shifted traces. But the entire operation can also be carried out in the frequency domain (Beylkin, 1987; Benoliel et al., 1987; Vissinga et al., 1989). This results in an incorporation of the interpolation in the frequency dependence of the filter coefficients. Less numerical noise is generated by this minor but essential change. This problem is explained in more detail in the Chapters 3 and 4.

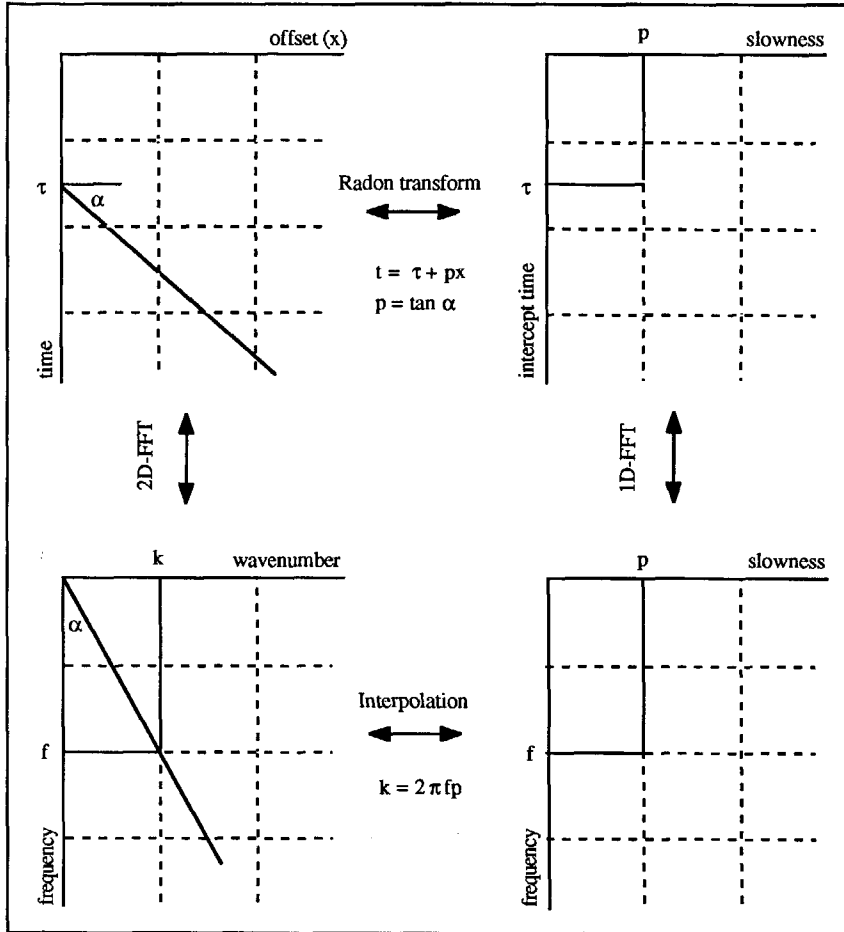


Fig.1.3.1: The non-uniqueness problem of the Radon transform.

### Evaluation of the Bessel function

For the point source solution of the Radon transform the Bessel function of the first kind and zero order is involved and has to be evaluated. Because direct numerical evaluation of the Bessel function is rather inefficient and difficult to control due to its oscillatory behaviour, it is usually reformulated. A possibility is to replace the Bessel function by its asymptotic approximation. The only restriction for this option is that when the argument of the Bessel function becomes smaller than a certain number, the approximation fails (Mithal and Vera, 1987). Another option is to make use of symmetry properties of the Bessel function and rewrite it as a square-root filter combined with a slant stack operator (Brysk and McCowan, 1986, amongst others).

## 1.4 Outline of the thesis

The mathematical framework of the Radon transform is given in Chapter 2. The algorithm developed for implementation of the transform on discrete data developed in this thesis is a combination of those derived by Brysk and McCowan (1986) and by Benoliel et al. (1987). Instead of rewriting the algorithm as the conventional slant stack operator followed by a square-root filter, it is reformulated as a spatial Fourier transform with the same square-root filter except that these filter coefficients are frequency dependent instead of time dependent. This minor but essential change of integration variable improves the results significantly. Moreover, a  $\text{sinc}^2$ -operator (the Fourier transform of the linear interpolator) is introduced to make a better performance of the interpolator. This is discussed in Chapter 3. Then according to the aliasing criterion in the frequency-slowness domain, only the unaliased part of the data is used for the transform (Benoliel, 1987). Chapters 3 and 4 cover this. Chapter 3 focuses on the numerical implementation of the inverse transform given a synthetic data set in the  $f$ - $p$  domain, and Chapter 4 covers the numerical implementation and limitations of the forward and inverse Radon transform given a data set in the  $t$ - $x$  domain, either recorded or synthetic. The point source as well as the line source solution of the algorithm are derived and special attention is paid to the interpolation procedure. Furthermore, in Chapter 4 the consequences of the common problems of spatially limited aperture and the lack of near-offset measurements are reviewed. Chapters 3 and 4 both conclude with some data examples.

Chapter 5 deals with the classification of the events in the  $\tau$ - $p$  domain. In order to be able to do this, the method of stationary phase is employed. The theory developed is supported by a number of data examples such as the hyperbolic event, the linear event, a noise pulse and the diffraction hyperbola. Further, there is another limitation which is also discussed by Benoliel et al. (1987) on the  $\tau$ - $p$  data besides the "anti-aliasing" restriction. Given the minimum and maximum offset and the velocity-depth model of the input data set, one can calculate which values of slowness  $p$  for certain values of intercept time  $\tau$  are reliable. Outside this range, only noise due to the end effects, is present. Knowledge of the reliability of the  $p$ -values is indispensable when, for instance, the  $\tau$ - $p$  data are used for inversion purposes. After the synthetic data examples, two marine data sets are displayed and the main events in their  $\tau$ - $p$  responses are discussed.

Chapter 6 gives a numerical procedure to process a seismic line or 3D survey by means of the double Radon transform. When the seismic survey is considered as a coherent set of information, its spatial complexity shows a well-defined topological subdivision in the double Radon transformed domain. The main advantage of the algorithm is that the restriction of a planar velocity distribution is withdrawn. Therefore it offers a number of applications with respect to the allowed laterally varying velocity distribution. The application we discuss is a migration procedure, comparable with the well-known DMO (Dip move out) technique. The theory developed in this chapter is supported by some synthetic data sets and to conclude the chapter, a split-spread land seismic data set is transformed and discussed.

Chapter 7 gives the overall conclusions, summarizing the main limitations of the Radon transform and secondly, the limitations due to the input data.

---

## MATHEMATICAL FRAMEWORK

### 2.1 Introduction

The problem of reconstruction from projections is an old one and can be found in many fields such as astronomy, medical science, molecular biology, optics and geophysics. An appropriate unifying mathematical framework for this is given by the Radon transform (Radon, 1917). However, major developments in these areas did not come as a result of Radon's work. In fact, all of these fields were highly developed before connections with the Radon transform were recognized. Today its relevance is apparent in several different fields.

The Radon transform of an arbitrary function  $f$  defined on an  $n$ -dimensional Euclidean space  $R^n$ , is determined by the integration of  $f$  over all hyperplanes of dimension  $n-1$ . A hyperplane/hypersurface is a figure corresponding to a plane/surface in hyperspace, where a hyperspace is a space of more than three dimensions. Thus, if  $f$  is defined on the plane  $R^2$ , then its Radon transform is determined by the line integrals of  $f$ , and if  $f$  is defined on the plane  $R^3$ , its Radon transform is determined by the surface integrals of  $f$  over 2D planes (Deans, 1983). Conforming this general definition with current usage in geophysics for a 2D configuration gives basically a reformulation of the way a line is parameterized. Instead of characterizing a line in normal form, the line is expressed in a slope-intercept form, where  $p$  is the slope and  $\tau$  the intercept. Then the Radon transform is performed by sweeping over the wavefield (the function) with lines, each given by its  $p$ - and  $\tau$ -value, adding (integrating) all the values on each line and finally associating the sum (integral) with its slope  $p$  and intercept  $\tau$ . Now for a 3D configuration, the connection of the Radon transform with the plane-wave decomposition (PWD, Treitel et al., 1982) is easily conceived. A point-source data set can be decomposed into a set of plane-wave components for arbitrary angles of incidence in which each plane-wave component is defined by its angle of incidence and the slowness, being the parameter  $p$ .



## 2.2 The mathematical introduction to the Radon transform

To relate the algorithm of the Radon transform, developed in this thesis, to the published literature, and to clarify the cohesion between the existing methods an outline is given of the most important derivations. In order to do that the basic tools, which are the temporal and spatial Fourier transform and the definition of the Radon transform by Radon (1917) are given.

The temporal Fourier transform pair for causal time functions is defined by

$$\hat{u}(x, f) = \int_0^{+\infty} e^{i2\pi ft} u(x, t) dt, \quad (2.2.1)$$

and

$$u(x, t) = \int_{-\infty}^{+\infty} e^{-i2\pi ft} \hat{u}(x, f) df, \quad (2.2.2)$$

where the integral of the inverse transform (eq.(2.2.2)) is performed for negative and positive frequencies. Since we need a unique relation between the wavenumber  $k$  which may be positive or negative and the horizontal slowness  $p$  ( $k = 2\pi p$ ) which may also be positive or negative, we need to know the inverse transform for positive frequencies only.

Therefore the Heaviside step function  $\hat{h}(f)$  (Fig.2.2.1) is introduced as

$$\hat{h}(f) = \begin{cases} 1 & f > 0 \\ 1/2 & f = 0 \\ 0 & f < 0 \end{cases}. \quad (2.2.3)$$

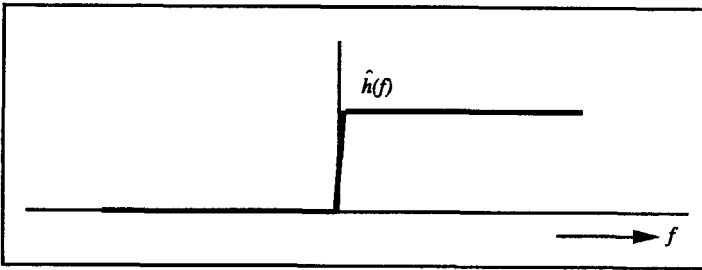


Fig.2.2.1: The Heaviside step function.

The next step is to introduce the analytic function as

$$\hat{u}^{\wedge}(x, t) = \int_{-\infty}^{+\infty} e^{-i2\pi ft} \hat{h}(f) \hat{u}(x, f) df, \quad (2.2.4)$$

where the inverse Fourier transform of the step function,  $\hat{h}(f)$  is, according to Bracewell (1978), given by

$$\begin{aligned} h(t) &= \int_{-\infty}^{+\infty} e^{-i2\pi ft} \hat{h}(f) df = \int_0^{\infty} e^{-i2\pi ft} df \\ &= \frac{1}{2} \delta(t) - \frac{i}{2\pi t} . \end{aligned} \quad (2.2.5)$$

Then, eq.(2.2.4) is rewritten as a convolution

$$\begin{aligned} u^A(x, t) &= \int_0^{+\infty} h(t-\tau) u(x, \tau) d\tau \\ &= \frac{1}{2} [u(x, t) - i\mathcal{H}[u(x, t)]] , \end{aligned} \quad (2.2.6)$$

where  $\mathcal{H}$  denotes the Hilbert transform and is, in accordance with Bracewell (1978, p. 267), defined as

$$\mathcal{H}[u(x, t)] = \frac{1}{\pi} \oint_{-\infty}^{+\infty} \frac{u(x, \tau)}{t-\tau} d\tau , \quad (2.2.7)$$

where the right-hand side of eq.(2.2.7) is to be understood as a Cauchy principal value integral. The last part of eq.(2.2.6) is also known as the analytic signal. Note that  $u(x, t) = 2\text{Re}[u^A(x, t)]$ . Therefore the temporal Fourier transform pair for causal time functions (eqs.(2.2.1) and (2.2.2)) is now obtained, by combining eq.(2.2.4) and using the fact that  $u(x, t) = 2\text{Re}[u^A(x, t)]$ , as

$$\hat{u}(x, f) = \int_0^{\infty} e^{i2\pi ft} u(x, t) dt , \quad (2.2.8)$$

and

$$u(x, t) = 2\text{Re} \left[ \int_0^{\infty} e^{-i2\pi ft} \hat{u}(x, f) df \right] , \quad (2.2.9)$$

where  $\text{Re} [\dots]$  denotes the real part, and eq.(2.2.9) is clearly evaluated for positive frequencies only, as required.



When line integrals or integrals over hyperplanes have to be evaluated, the classical Radon transform is used. Extending now the classical Radon transform to a more general form, the generalized Radon transform (GRT) is introduced (Beylkin, 1983)

$$\tilde{u}(p, \xi) = \int_{R^n} u(x) a(x, \xi) \delta(p - \xi \cdot x) dx, \quad (2.2.14)$$

where  $a(x, \xi)$  defines some weighting function. In this case, the integral over more general curves or hypersurfaces has to be evaluated.

An example of the classical Radon transform for a 2D geometry is shown below in Fig.2.2.3 where the line  $L$  is defined by the normal  $p$ :

$$p = x_1 \cos \phi + x_2 \sin \phi. \quad (2.2.15)$$

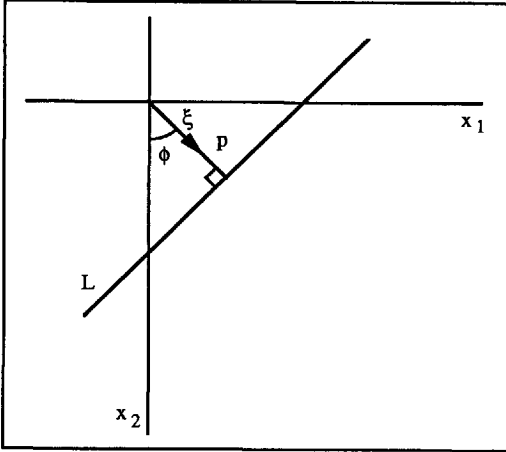


Fig.2.2.3: The line integral depending on  $p$  and  $\phi$ .

The reformulation for use in seismology is based on the different way a line (in the case of a 2D geometry) is parameterized. Instead of writing the equation in normal form, the equation is expressed in slope-intercept form as

$$t = \tau + px_1, \quad (2.2.16)$$

where  $p$  now represents the slope of the line  $L$  in the  $t$ - $x$  plane and  $\tau$  denotes the intercept of  $L$  with the  $t$ -axis. The origin of the reference is chosen such that negative  $\tau$ -values violate the causality constraint, hence  $\tau \geq 0$ . This is shown in Fig.2.2.4.

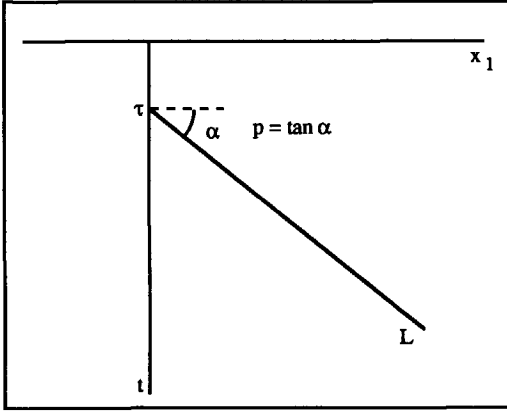


Fig.2.2.4: The line integral depending on  $p$  and  $\tau$ .

The adjusted formulation due to eq.(2.2.16) then redefines the classical Radon transform in two-dimensions as

$$\tilde{u}(p, \tau) = \int_{-\infty}^{+\infty} \int_0^{+\infty} u(x_1, t) \delta(t - \tau - px_1) dt dx_1, \quad (2.2.17)$$

or as

$$\begin{aligned} \tilde{u}(p, \tau) &= \int_{-\infty}^{+\infty} u(x_1, \tau + px_1) dx_1, \quad \text{for } \tau + px_1 > 0 \\ &= 0, \quad \text{for } \tau + px_1 \leq 0, \end{aligned} \quad (2.2.18)$$

where the causality condition of  $u(x, t)$  is used. The latter formulation is mostly found in the literature for the forward 2D Radon transform. To obtain the frequency equivalent of eq.(2.2.18), we apply a forward temporal FFT (eq.(2.2.8)), resulting in

$$\hat{\tilde{u}}(p, f) = \int_0^{\infty} e^{i2\pi f\tau} \tilde{u}(p, \tau) d\tau. \quad (2.2.19)$$

Then, substituting eq.(2.2.17) and using the expression for the line in slope-intercept form (eq.(2.2.16)) gives

$$\begin{aligned}
\widehat{u}(p, f) &= \int_{-\infty}^{+\infty} dx_1 \int_0^{\infty} u(x_1, t) dt \int_0^{\infty} e^{i2\pi f\tau} \delta(t-\tau-px_1) d\tau \\
&= \int_{-\infty}^{+\infty} e^{-i2\pi fpx_1} dx_1 \int_0^{\infty} e^{i2\pi ft} u(x_1, t) dt
\end{aligned} \tag{2.2.20}$$

where the last part is rewritten as

$$\widehat{u}(p, f) = \int_{-\infty}^{+\infty} e^{-i2\pi fpx_1} \widehat{u}(x_1, f) dx_1. \tag{2.2.21}$$

The inverse transform for a 2D geometry is obtained by using the Fourier inversion form of eq.(2.2.21) as

$$\widehat{u}(x_1, f) = \int_{-\infty}^{+\infty} e^{i2\pi fpx_1} \widehat{u}(p, f) f dp. \tag{2.2.22}$$

The eqs.(2.2.21) and (2.2.22) are part of the projection-slice theorem (Mersereau and Oppenheim, 1974) which provides a connection with the spatial Fourier transform pair (eqs.(2.2.10) and (2.2.11); Bracewell, 1956). According to this, the following relation is used

$$\widehat{U}(k, f) = \widehat{u}(2\pi fp, f), \tag{2.2.23}$$

which clearly shows the implicit interpolation. To obtain the inverse classical Radon transform, eq.(2.2.9) is applied on eq.(2.2.22) and results in

$$u(x_1, t) = 2\text{Re} \left[ \int_0^{\infty} e^{-i2\pi ft} df \int_{-\infty}^{+\infty} e^{i2\pi fpx_1} \widehat{u}(p, f) f dp \right]. \tag{2.2.24}$$

Then, changing the order of integration and transforming  $f$  to  $\frac{i}{2\pi} \frac{\partial}{\partial t}$ , this becomes

$$u(x_1, t) = 2\text{Re} \left[ \int_{-\infty}^{+\infty} dp \frac{i}{2\pi} \frac{\partial}{\partial t} \int_0^{\infty} e^{-i2\pi f(t-px_1)} \widehat{u}(p, f) df \right]. \tag{2.2.25}$$

Using eqs.(2.2.5) and (2.2.6) we obtain

$$u(x_1, t) = 2\text{Re} \left[ \int_{-\infty}^{+\infty} d\phi \frac{i}{2\pi} \frac{\partial}{\partial t} \frac{1}{2} \left[ \tilde{u}(p, t - px_1) - i\mathcal{H} \tilde{u}(p, t - px_1) \right] \right], \quad (2.2.26)$$

and finally

$$u(x_1, t) = \frac{1}{2\pi} \frac{\partial}{\partial t} \int_{-\infty}^{+\infty} \mathcal{H} \left[ \tilde{u}(p, t - px_1) \right] d\phi, \quad (2.2.27)$$

where  $\mathcal{H}$  denotes the well-known Hilbert transform. The inverse Radon transform derived by Chapman (1978) differs by the minus sign due to his different definition of the Hilbert transform. The formulation of the classical Radon transform for a 2D geometry (eqs.(2.2.18) and (2.2.26)) is also mentioned as slant stacking. When the slant stack operator is employed, the calculation is performed in the time domain. Therefore the frequency domain version of the classical Radon transform, given by the eqs.(2.2.21) and (2.2.22), must no longer be called slant stack.

The classical Radon transform or slant stack for a 2D geometry is

$$\begin{aligned} \tilde{u}(p, \tau) &= \int_{-\infty}^{+\infty} u(x_1, \tau + px_1) dx_1 \\ u(x_1, t) &= \frac{1}{2\pi} \frac{\partial}{\partial t} \int_{-\infty}^{+\infty} \mathcal{H} \left[ \tilde{u}(p, t - px_1) \right] d\phi \end{aligned} \quad (2.2.28)$$

and its frequency domain equivalent is

$$\begin{aligned} \hat{\tilde{u}}(p, f) &= \int_{-\infty}^{+\infty} e^{-i2\pi f p x_1} \hat{u}(x_1, f) dx_1 \\ \hat{u}(x_1, f) &= f \int_{-\infty}^{+\infty} e^{i2\pi f p x_1} \hat{\tilde{u}}(p, f) d\phi \end{aligned} \quad (2.2.29)$$

Formulating now the classical Radon transform or slant stack operator for a 3D geometry (Fig.2.2.2) in Cartesian coordinates (Brysk and McCowan, 1986), eq.(2.2.18) is extended to

$$\tilde{u}(p_1, p_2, \tau) = \int_{-\infty}^{+\infty} \int_{-\infty}^{+\infty} u(x_1, x_2, \tau + p_1 x_1 + p_2 x_2) dx_1 dx_2, \quad (2.2.30)$$

and this formulation is also referred to as plane-wave decomposition (PWD), by Treitel et al. (1982). Its equivalent in the frequency domain is obtained by applying eq.(2.2.8) on eq.(2.2.30)

$$\widehat{u}(p_1, p_2, f) = \int_0^\infty e^{i2\pi f\tau} \widetilde{u}(p_1, p_2, \tau) d\tau. \quad (2.2.31)$$

Then substituting eq.(2.2.17) into eq.(2.2.31) and using eq.(2.2.16) gives

$$\begin{aligned} \widehat{u}(p_1, p_2, f) &= \int_{-\infty}^{+\infty} \int_{-\infty}^{+\infty} dx_1 dx_2 \int_0^\infty u(x_1, x_2, t) dt \int_0^\infty e^{i2\pi f\tau} \delta(t-\tau-p_1x_1-p_2x_2) d\tau \\ &= \int_{-\infty}^{+\infty} \int_{-\infty}^{+\infty} e^{-i2\pi f(p_1x_1+p_2x_2)} dx_1 dx_2 \int_0^\infty e^{i2\pi ft} u(x_1, x_2, t) dt, \end{aligned} \quad (2.2.32)$$

where the last part is rewritten as

$$\widehat{u}(p_1, p_2, f) = \int_{-\infty}^{+\infty} \int_{-\infty}^{+\infty} e^{-i2\pi f(p_1x_1+p_2x_2)} \widehat{u}(x_1, x_2, f) dx_1 dx_2. \quad (2.2.33)$$

Eqs.(2.2.32) and (2.2.33) for the 3D case are exactly analogous to eqs.(2.2.20) and (2.2.22) for the 2D case. To derive the inverse slant stack operator of eq.(2.2.30), eq.(2.2.22) is extended to

$$\widehat{u}(x_1, x_2, f) = f^2 \int_{-\infty}^{+\infty} \int_{-\infty}^{+\infty} e^{i2\pi f(p_1x_1+p_2x_2)} \widehat{u}(p_1, p_2, f) dp_1 dp_2. \quad (2.2.34)$$

Then applying again eq.(2.2.9)

$$u(x_1, x_2, t) = 2\text{Re} \left[ \int_0^{+\infty} e^{-i2\pi ft} f^2 df \int_{-\infty}^{+\infty} \int_{-\infty}^{+\infty} e^{i2\pi f(p_1x_1+p_2x_2)} \widehat{u}(p_1, p_2, f) dp_1 dp_2 \right], \quad (2.2.35)$$

and, changing the order of integration and transforming  $f^2$  to  $-\frac{1}{4\pi^2} \frac{\partial^2}{\partial t^2}$



$$u(x_1, x_2, t) = 2\text{Re} \left[ \int_{-\infty}^{+\infty} \int_{-\infty}^{+\infty} \phi_1 \phi_2 \right. \\ \left. \frac{-1}{4\pi^2} \frac{\partial^2}{\partial t^2} \int_0^{+\infty} e^{-i2\pi f(t-p_1x_1-p_2x_2)} \hat{u}(p_1, p_2, f) df \right]. \quad (2.2.36)$$

After transforming to the time domain in the same way as we did before, we obtain

$$u(x_1, x_2, t) = -\frac{1}{4\pi^2} \frac{\partial^2}{\partial t^2} \int_{-\infty}^{+\infty} \int_{-\infty}^{+\infty} \tilde{u}(p_1, p_2, t - p_1x_1 - p_2x_2) \phi_1 \phi_2. \quad (2.2.37)$$

The Radon transform or slant stack for a 3D geometry is thus given by

$$\tilde{u}(p_1, p_2, \tau) = \int_{-\infty}^{+\infty} \int_{-\infty}^{+\infty} u(x_1, x_2, \tau + p_1x_1 + p_2x_2) dx_1 dx_2 \quad (2.2.38)$$

$$u(x_1, x_2, t) = -\frac{1}{4\pi^2} \frac{\partial^2}{\partial t^2} \int_{-\infty}^{+\infty} \int_{-\infty}^{+\infty} \tilde{u}(p_1, p_2, t - p_1x_1 - p_2x_2) \phi_1 \phi_2$$

and its frequency domain equivalent is

$$\hat{u}(p_1, p_2, f) = \int_{-\infty}^{+\infty} \int_{-\infty}^{+\infty} e^{-i2\pi f(p_1x_1 + p_2x_2)} \hat{u}(x_1, x_2, f) dx_1 dx_2 \quad (2.2.39)$$

$$\hat{u}(x_1, x_2, f) = f^2 \int_{-\infty}^{+\infty} \int_{-\infty}^{+\infty} e^{i2\pi f(p_1x_1 + p_2x_2)} \hat{u}(p_1, p_2, f) \phi_1 \phi_2$$

Exploiting the cylindrical or radial symmetry of the medium in the configuration, the configurational parameters are written in a radial and angular parameter (Fig.2.2.2), as

$$\begin{aligned} p_1 &= p \cos \chi' & x_1 &= x \cos \theta' \\ p_2 &= p \sin \chi' & x_2 &= x \sin \theta' \end{aligned}, \quad (2.2.40)$$

and eqs.(2.2.39) become

$$\hat{u}(p, f) = \int_0^\infty \int_0^{2\pi} e^{-i2\pi f p x \cos \theta} \hat{u}(x, f) d\theta x dx, \quad (2.2.41)$$

$$\widehat{u}(x, f) = f^2 \int_0^\infty \int_0^{2\pi} e^{i2\pi f p x \cos \chi} \widehat{u}(p, f) d\chi p dp, \quad (2.2.42)$$

where  $\theta = \theta' - \chi'$  and  $\chi = \chi' - \theta'$ . Because axisymmetry is demanded for the source as well as for the medium, the functions in the latter two equations are independent of the angles  $\chi$  and  $\theta$ . However, the angular integrations cannot be eliminated because they involve the relative orientation of the position vector (eq.(2.2.41)) and of the direction of propagation (eq.(2.2.42)). Therefore the latter two equations can also be written as a Hankel transform or a Fourier-Bessel transform (Abramowitz and Stegun, 1965) as

$$\widehat{u}(p, f) = 2\pi \int_0^{+\infty} \widehat{u}(x, f) J_0(2\pi f p x) x dx, \quad (2.2.43)$$

$$\widehat{u}(x, f) = 2\pi f^2 \int_0^{+\infty} \widehat{u}(p, f) J_0(2\pi f p x) p dp, \quad (2.2.44)$$

where  $J_0$  is the Bessel function of the first kind and zero order. So in the case of cylindrical symmetry the Hankel transform comes out of the solution. A direct numerical evaluation of the Hankel transform is relatively inefficient. Therefore the second integral in eq.(2.2.41) is considered again and rewritten as

$$\int_0^{2\pi} e^{-i2\pi f p x \cos \theta} d\theta = 2 \int_0^{\pi/2} \left( e^{-i2\pi f p x \cos \theta} - e^{i2\pi f p x \cos \theta} \right) d\theta. \quad (2.2.45)$$

Since  $\widehat{u}(p, f) = \widehat{u}(-p, f)$  and  $\widehat{u}(x, f) = \widehat{u}(-x, f)$ , that is, they are even, the eqs.(2.2.41) and (2.2.42) after substitution of eq.(2.2.45) and extension of the definition of  $p$  and  $x$  to the range of  $-\infty < p < \infty$  and  $-\infty < x < \infty$  result in

$$\widehat{u}(p, f) = 2 \int_{-\infty}^{+\infty} \widehat{u}(|x|, f) |x| dx \int_0^{\pi/2} e^{-i2\pi f p x \cos \theta} d\theta, \quad (2.2.46)$$

$$\widehat{u}(x, f) = 2 f^2 \int_{-\infty}^{+\infty} \widehat{u}(|p|, f) |p| dp \int_0^{\pi/2} e^{i2\pi f p x \cos \chi} d\chi. \quad (2.2.47)$$

Then the same procedure can be applied to the 3D slant stack operator and eq.(2.2.38) is rewritten as

$$\tilde{u}(p, \tau) = 2 \int_0^{+\infty} x dx \int_0^{\pi/2} [u(x, \tau + px \cos \theta) + u(x, \tau - px \cos \theta)] d\theta, \quad (2.2.48)$$

$$u(x, t) = -\frac{1}{2\pi^2} \frac{\partial^2}{\partial t^2} \int_0^{+\infty} p dp \int_0^{\pi/2} [\tilde{u}(p, t - px \cos \chi) + \tilde{u}(p, t + px \cos \chi)] d\chi. \quad (2.2.49)$$

The Radon transform or slant stack for a 3D geometry with the assumption of axisymmetry is

$$\begin{aligned} \tilde{u}(p, \tau) &= 2 \int_0^{+\infty} x dx \int_0^{\pi/2} [u(x, \tau + px \cos \theta) + u(x, \tau - px \cos \theta)] d\theta \\ u(x, t) &= -\frac{1}{2\pi^2} \frac{\partial^2}{\partial t^2} \int_0^{+\infty} p dp \int_0^{\pi/2} [\tilde{u}(p, t - px \cos \chi) + \tilde{u}(p, t + px \cos \chi)] d\chi \end{aligned} \quad (2.2.50)$$

and its frequency domain equivalent is

$$\begin{aligned} \hat{\tilde{u}}(p, f) &= 2 \int_{-\infty}^{+\infty} \hat{u}(|x|, f) |x| dx \int_0^{\pi/2} e^{-i2\pi f p x \cos \theta} d\theta \\ \hat{u}(x, f) &= 2f^2 \int_{-\infty}^{+\infty} \hat{u}(|p|, f) |p| dp \int_0^{\pi/2} e^{i2\pi f p x \cos \chi} d\chi \end{aligned} \quad (2.2.51)$$

Introducing a new variable of integration,  $p' = p \cos \theta$  and  $x' = x \cos \chi$ , and changing the order of integration, turns eqs.(2.2.50) into

$$\tilde{u}(p, \tau) = 2 \int_0^p \frac{dp'}{\sqrt{p^2 - p'^2}} \int_0^{+\infty} [u(x, \tau + p'x) + u(x, \tau - p'x)] x dx, \quad (2.2.52)$$

$$u(x, t) = -\frac{1}{2\pi^2} \frac{\partial^2}{\partial t^2} \int_0^x \frac{dx'}{\sqrt{x^2 - x'^2}} \int_0^{+\infty} [\tilde{u}(p, t - px') + \tilde{u}(p, t + px')] p dp. \quad (2.2.53)$$

These two expressions were also derived by Brysk and McCowan (1986).

Instead of defining the Radon transform as a function of the horizontal slowness  $p$  and the intercept time  $\tau$ , it can also be formulated as a function of the direction of the propagation angle  $\gamma$  of the plane-wave component and the frequency (Treitel et al., 1982). Then, defining a new function,

$$\widehat{U}(k,f) = \widehat{u}(2\pi f p, f) \equiv \widehat{u}_a(\gamma, f) \text{ where } p = \frac{\sin \gamma}{v_0}, \quad (2.2.54)$$

and where  $v_0$  denotes the velocity in the first layer (Fig.2.2.5), eq.(2.2.46) is rewritten as

$$\widehat{u}_a(\gamma, f) = 2 \int_{-\infty}^{+\infty} \widehat{u}(|x|, f) |x| dx \int_0^{\pi/2} e^{-i2\pi f \frac{\sin \gamma}{v_0} x \cos \theta} d\theta. \quad (2.2.55)$$

Note that  $\gamma$  is restricted to the range of  $-\pi < \gamma < \pi$  because only the propagating part of the wavefield is taken into consideration. Then introducing a new variable of integration,  $t_h = t_0 \cos \theta$ , which denotes the horizontal travel time, and where  $t_0 = x \sin \gamma / v_0$ , and changing the order of integration in eq.(2.2.55), yields

$$\widehat{u}_a(\gamma, t) = 2 \int_0^{\infty} x dx \int_0^{t_0} \frac{dt_h}{\sqrt{t_0^2 - t_h^2}} e^{-i2\pi f t_h} \widehat{u}(x, f). \quad (2.2.56)$$

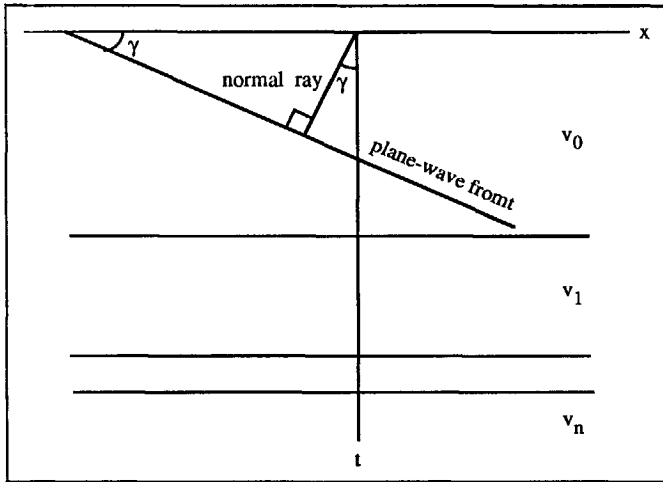


Fig.2.2.5: The plane-wave front in relation with the propagation angle  $\gamma$ .

Although the last equation is hardly used, it shows clearly the connection between the PWD, the slant stack operator and the other related Radon transforms.

The inverse operator following eq.(2.2.47) results in

$$\widehat{u}(x, f) = \frac{2f^2}{v_0^2} \int_{-\pi}^{+\pi} \widehat{u}_a(\gamma, f) \sin \gamma \cos \gamma d\gamma \int_0^{\pi/2} e^{i2\pi f \frac{\sin \gamma}{v_0} x \cos \chi} d\chi, \quad (2.2.57)$$

where the lower and upper limit of the angular integral is restricted from  $-\pi$  to  $+\pi$ . Then again introducing the same variable of integration,  $t_h = t_0 \cos \chi$ , where  $t_0 = x \sin \gamma / v_0$ , and changing the order of integration, turns eq.(2.2.57) into

$$\widehat{u}(x,t) = \frac{2f^2}{x^2} \int_{-x/v_0}^{+x/v_0} t_0 dt_0 \int_0^{t_0} \frac{dt_h}{\sqrt{t_0^2 - t_h^2}} e^{i2\pi f t_h} \widehat{u}_a(\gamma, f). \quad (2.2.58)$$

The transform pair for the PWD is thus

$$\begin{aligned} \widehat{u}_a(\gamma, t) &= 2 \int_0^\infty x dx \int_0^{t_0} \frac{dt_h}{\sqrt{t_0^2 - t_h^2}} e^{-i2\pi f t_h} \widehat{u}(x, f) \\ \widehat{u}(x, t) &= \frac{2f^2}{x^2} \int_{-x/v_0}^{+x/v_0} t_0 dt_0 \int_0^{t_0} \frac{dt_h}{\sqrt{t_0^2 - t_h^2}} e^{i2\pi f t_h} \widehat{u}_a(\gamma, f) \end{aligned} \quad (2.2.59)$$

---

## THE INVERSE RADON TRANSFORM APPLIED TO SYNTHETIC SEISMOGRAMS OVER PLANE HORIZONTAL LAYERS

---

### 3.1 Introduction

The aim of this chapter is to generate a synthetic seismogram in the  $t$ - $x$  domain. When the elastic/acoustic parameters of the model vary only with depth in a plane, cylindrical or spherical geometry, the computation of synthetic seismograms reduces to the solution of an ordinary differential equation (first part) plus the evaluation of the inverse transform (second part). Several methods exist to solve the first part, that is the differential equation but in this thesis it is based on the reflectivity method (Fuchs and Müller, 1971) and the critical reflection theorem (Fokkema and Ziolkowski, 1987). The solution of the differential equation gives a Green's function which is extensively described by Koster (1991) for the marine case in which the hydrophones measure the pressure, and by Baeten (1989) for the land situation in which the geophones record the particle velocity. The free surface is included in both cases. Internal multiples and free surface multiples are treated as part of the forward modelling scheme. The model configuration is shown in Fig.3.1.1 and a summary of the algorithm to generate a Green's function is given in the appendix (A.1).

The second part concerns the inverse Radon transform which is the goal of this chapter. Because cylindrical symmetry is assumed the inverse Radon transform according to eq.(2.2.39) – (2.2.44) can be written as a Hankel transform. The method is illustrated for the simple case of scalar wave motion but can be easily extended to more complicated problems as, for example, full elastic-wave propagation problems.

In section 3.2 an overview is given of the literature published on the numerical computation of Hankel transforms. After that the transform itself is discussed for the 3D-case in sections 3.3 (analytic expression) and 3.4 (discrete expression) and for the 2D-case in section 3.5. Then section 3.6 goes into detail on the main problems caused by the numerical implementation of the

transform and the solutions for them. The interpolation used in the transform is discussed in section 3.7. Further, two synthetic data sets are shown, one of them compared with the

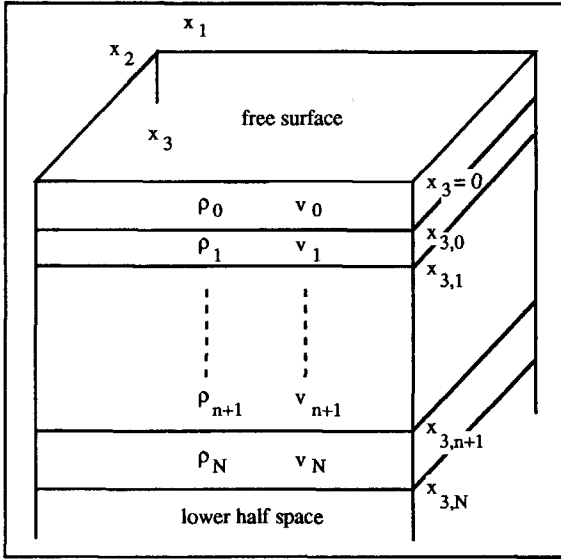


Fig.3.1.1: The earth model, bounded by a free surface on top and a homogeneous half space at the bottom with  $N$  plane, isotropic and homogeneous layers in between.

Cagniard-De Hoop technique (section 3.8) which calculates the response exactly. Finally the artifacts due to the numerical implementation of the transform are briefly discussed in section 3.9.

### 3.2 Development of the numerical implementation of the Hankel transform

The Hankel or Fourier-Bessel transform plays an important role in optics, acoustics and geophysics. The linear filter method, based upon the theory of Fourier analysis and the theory of convolution was introduced by Ghosh (1971) and provided an algorithm to avoid Bessel function evaluations. In 1977 Siegman presented a nonlinear change of variables used to convert the one-sided Hankel transform integral into a two-sided cross integral. This correlation integral is then evaluated on a discrete sampled basis using a FFT. The latter inspired Johansen and Sørensen (1979) among others to develop a more general theory for numerical evaluation of integrals of the Hankel type. They replaced the Hankel transform by a Fourier integral and evaluated it as a contour integral in the complex plane. The necessary interpolation was performed by the *sinc*-function. Further improvements were obtained by properly adjusting the sampling interval as well as the abscissa shift according to Guptasarma (1982). Hence the digital linear convolution or the linear filter method can be speeded up according to Anderson (1982) by

using both related and lagged convolution concepts. The Hankel transform can also be computed as a combination of an Abel transform which maps an axisymmetric 2D function into a line integral projection and a 1D Fourier transform (Hansen, 1985; Wilson, 1986). His line integral, the Abel transform, is interpreted as a shift-variant recursive filter in which he exploits the "zero-order hold" approximation. He tested his implementation with known transform pairs. All applications mentioned above are related to resistivity, electromagnetic and optical problems.

The algorithm introduced here is based on a frequency-wavenumber approach and exhibits a 2D FFT (temporal and spatial FFT) followed by an interpolation and an inverse temporal FFT (Vissinga et al., 1989). What is new about this algorithm is the introduction of the  $\text{sinc}^2$  function. The  $\text{sinc}^2$  function is the Fourier transform of the triangle function and is implemented before the spatial FFT to improve the subsequent linear interpolation of the triangle function. When a higher than linear order interpolation is used, the  $\text{sinc}^2$  function is replaced by the Fourier transform of its interpolator. Furthermore the algorithm exploits causality and the interpolator, first presented by Chapman (1981) and later reformulated by Brysk and McCowan (1986), is performed in the frequency domain instead of the time domain. In this way higher accuracy is accomplished, which is necessary because it appears that the slant stack procedure in  $\tau$ - $p$  is too coarse to show the details needed for the modelling. For numerical reasons, complex frequency is introduced (see Appendix A.3).

### 3.3 The inverse Radon transform for the point source configuration

In the configuration shown in Fig.3.1.1 the Cartesian coordinates  $x_1$ ,  $x_2$  and  $x_3$  locate a point in a horizontally stratified medium. The impulsive wave motion  $u(x_1, x_2, x_3, t)$ , is generated by a point source that starts to act at  $t = 0$ . The model parameters depend only on  $x_3$ . But the wave motion  $u(x_1, x_2, x_3, t)$  is a function of all three space coordinates and the time coordinate  $t$ . Since we are interested in the behaviour of the wave motion in a time-invariant configuration and since the source starts to act at  $t = 0$ , the Fourier transform pair of the causal wave motion is, following the eqs.(A.3.10) and (A.3.11), given by

$$\hat{u}(x_1, x_2, x_3, f' + i\epsilon) = \int_0^\infty e^{i2\pi f't} u(x_1, x_2, x_3, t) dt, \quad (3.3.1)$$

and

$$u(x_1, x_2, x_3, z, t) = 2e^{2\pi\epsilon t} \text{Re} \left[ \int_0^\infty e^{-i2\pi f't} \hat{u}(x_1, x_2, x_3, f' + i\epsilon) df' \right], \quad (3.3.2)$$



where  $\varepsilon$  is positive (Fig.A.3.1). As soon as  $\hat{u}(x_1, x_2, x_3, f' + i\varepsilon)$  has been calculated, the integral on the right hand side can be computed efficiently using a FFT-routine, provided a proper positive value of  $\varepsilon$  is chosen. The function  $e^{2\pi i t}$  is the so-called inverse taper.

In view of the shift invariance in space of the configuration in horizontal directions, the 2D Fourier transform of the wave motion, the spectral quantity in eq.(2.2.10) is extended to

$$\hat{\hat{U}}(k_1, k_2, x_3, f' + i\varepsilon) = \int_{-\infty}^{+\infty} \int_{-\infty}^{+\infty} e^{-ik_1 x_1 - ik_2 x_2} \hat{u}(x_1, x_2, x_3, f' + i\varepsilon) dx_1 dx_2, \quad (3.3.3)$$

in which  $k_1$  and  $k_2$  denote the wavenumber parameters. As soon as the spectral quantity  $\hat{\hat{U}}(k_1, k_2, x_3, f' + i\varepsilon)$  has been calculated, the wave motion  $\hat{u}(x_1, x_2, x_3, f' + i\varepsilon)$  is obtained from the inverse Fourier transform, shown as

$$\hat{u}(x_1, x_2, x_3, f' + i\varepsilon) = \frac{1}{4\pi^2} \int_{-\infty}^{+\infty} \int_{-\infty}^{+\infty} e^{ik_1 x_1 + ik_2 x_2} \hat{\hat{U}}(k_1, k_2, x_3, f' + i\varepsilon) dk_1 dk_2. \quad (3.3.4)$$

The next step is to take advantage of the rotational symmetry in the horizontal directions (Fig.2.2.2). The Cartesian coordinates  $x_1$  and  $x_2$  reduce to one parameter,  $x$ ; the same applies to the wavenumber parameters,  $k_1$  and  $k_2$ . They reduce to  $\lambda$  and this is pointed out as

$$\begin{aligned} x_1 &= x \cos \theta', & k_1 &= 2\pi \lambda \cos(\chi + \theta') \\ x_2 &= x \sin \theta', & k_2 &= 2\pi \lambda \sin(\chi + \theta'), \end{aligned} \quad (3.3.5)$$

$$\begin{aligned} \hat{u}(x, x_3, f' + i\varepsilon) &= \hat{u}(x_1, x_2, x_3, f' + i\varepsilon) \\ \hat{\hat{U}}(\lambda, x_3, f' + i\varepsilon) &= \hat{\hat{U}}(k_1, k_2, x_3, f' + i\varepsilon), \end{aligned} \quad (3.3.6)$$

where  $0 \leq x < \infty$ ,  $0 \leq \lambda < \infty$ , the angles  $0 \leq \theta' < 2\pi$  and  $0 \leq \chi < 2\pi$ . Further, using the property that the spectral quantity  $\hat{\hat{U}}(k_1, k_2, x_3, f' + i\varepsilon)$  is an even function of  $k$  and following

eqs.(2.2.41) - (2.2.47), the latter is then with the substitution of  $\lambda = p \sqrt{(f'^2 + \varepsilon^2)}$  given by

$$\hat{u}(x, x_3, f' + i\varepsilon) = 2(f'^2 + \varepsilon^2) \int_{-\infty}^{+\infty} \hat{\hat{u}}(|p|, x_3, f' + i\varepsilon) |p| dp \int_0^{\pi/2} e^{i \sqrt{f'^2 + \varepsilon^2} p x \cos \chi} d\chi. \quad (3.3.7)$$

Introducing now a new variable of integration  $y = w \cos \chi$  where  $w = x \sqrt{(f'^2 + \varepsilon^2)}$  and changing the order of integrations, we arrive at

$$\widehat{u}(x, x_3, z, f' + i\varepsilon) = \int_0^w \frac{\widehat{v}(y, x_3, f' + i\varepsilon) dy}{\sqrt{w^2 - y^2}}, \quad w > 0, \quad (3.3.8)$$

where  $\widehat{v}(y, x_3, f' + i\varepsilon)$  is obtained from the Fourier transform with  $y$  as transform parameter: viz.

$$\widehat{v}(y, x_3, f' + i\varepsilon) = \int_{-\infty}^{+\infty} e^{i2\pi p y} \widetilde{v}(p, x_3, f' + i\varepsilon) dp, \quad (3.3.9)$$

in which

$$\widetilde{v}(p, x_3, f' + i\varepsilon) = 2(f'^2 + \varepsilon^2)^{-1/2} |p| \widetilde{u}(|p|, x_3, f' + i\varepsilon). \quad (3.3.10)$$

The inverse Fourier transform of eq.(3.3.9) is

$$\widetilde{v}(p, x_3, f' + i\varepsilon) = \int_{-\infty}^{+\infty} e^{-i2\pi p y} \widehat{v}(y, x_3, f' + i\varepsilon) dy. \quad (3.3.11)$$

The main difference with Brysk and McCowan (1986) is the addition of the frequency as part of the new integration variable  $y$ . Note that in the special case  $x = 0$ , eq.(3.3.7) reduces to

$$\widehat{u}(0, x_3, f' + i\varepsilon) = \frac{\pi}{2} \widehat{v}(0, x_3, f' + i\varepsilon), \quad x = 0. \quad (3.3.12)$$

### 3.4 The computational procedure of the inverse Radon transform for the point source configuration

For the various values of  $y$ , a discretized version of the Fourier transform of eq.(3.3.9) can be computed efficiently using a FFT. In order to calculate the integral of the right hand side of eq.(3.3.8), we need the values of  $\widehat{v}(y, x_3, f' + i\varepsilon)$  for all  $y$  in the range of the integration  $0 < y < w$ . The discretization of the FFT, applied to eq.(3.3.9), yields these values at discrete  $y$ -points only. A direct numerical approximation of eq.(3.3.8) leads to inaccuracies. Therefore in this section, a proper interpolation technique is discussed.

Since the data are calculated at a number of discrete points  $p_n = n\Delta p$ , where  $n \in \{-N+1, \dots, N\}$  and  $\Delta p$  is the sampling interval, we also define the discrete Fourier transform pair in eq.(3.4.1) and eq.(3.4.2), where  $y_m = m\Delta y$  with  $m \in \{-N+1, \dots, N\}$  and  $\Delta y$  is the sampling interval in the  $y$ -domain. The transform pair is given by

$$\hat{v}_m = \Delta p \sum_{n=-N+1}^N \tilde{v}_n e^{i\pi \frac{nm}{N}}, \quad (3.4.1)$$

$$\tilde{v}_n = \Delta y \sum_{m=-N+1}^N \hat{v}_m e^{-i\pi \frac{nm}{N}}, \quad (3.4.2)$$

in which  $\Delta y$  and  $\Delta p$  are defined by

$$\Delta y \Delta p = \frac{1}{2N}. \quad (3.4.3)$$

However, a continuous representation for  $\hat{v}(y, x_3 f' + i\varepsilon)$  in the analytical integration of eq.(3.3.8) is needed and therefore an interpolation function  $\phi$  is introduced

$$\hat{v}(y, x_3 f' + i\varepsilon) = \sum_{m=-N+1}^N \hat{v}(y_m, x_3 f' + i\varepsilon) \phi(y - y_m), \quad y_{-N+1} \leq y < y_N. \quad (3.4.4)$$

Then eq.(3.3.8) can be rewritten as

$$\hat{u}(x, x_3 f' + i\varepsilon) = \sum_{m=-N+1}^N \hat{v}(y_m, x_3 f' + i\varepsilon) \int_0^w \frac{\phi(y - y_m) dy}{\sqrt{w^2 - y_m^2}}, \quad 0 < w < y_N, \quad (3.4.5)$$

The interpolation function  $\phi$  is chosen such that the integral of eq.(3.4.5) can be calculated analytically. The aim is to match the representation of eq.(3.4.4) to the known discrete values  $\hat{v}(p, x_3 f' + i\varepsilon)$  in the  $p$ -domain. To determine the coefficients of  $\hat{v}(y_m, x_3 f' + i\varepsilon)$ , eq.(3.4.4) has to be transformed to the  $p$ -domain using eq.(3.3.11). Then

$$\tilde{v}(p, x_3 f' + i\varepsilon) = \tilde{\phi}(p) \sum_{m=-N+1}^N \hat{v}(y_m, x_3 f' + i\varepsilon) e^{-i2\pi p y_m}, \quad (3.4.6)$$

where

$$\tilde{\phi}(p) = \int_{-\infty}^{+\infty} e^{-i2\pi p y} \phi(y) dy. \quad (3.4.7)$$

Further,  $\phi(y)$  is chosen such that  $\phi(p)$  can be calculated analytically via the Fourier transform (eq.(3.4.7)). Subsequently, the coefficients of  $\hat{v}(y_m, x_3 f' + i\varepsilon)$  are determined by requiring that eq.(3.4.6) holds in the discrete points  $p = p_n$ . This implies that

$$\tilde{v}(p_n, x_3 f' + i\varepsilon) = \tilde{\phi}(p_n) \sum_{m=-N+1}^N \hat{v}(y_m, x_3 f' + i\varepsilon) e^{-i\pi \frac{nm}{N}}. \quad (3.4.8)$$

Using the definitions of the discrete Fourier transform pair of eqs.(3.4.1) and (3.4.2), we conclude that the coefficients of  $\hat{v}(y_m, x_3 f' + i\varepsilon)$  are given by

$$\hat{v}(y_m, x_3 f' + i\varepsilon) = \frac{1}{2N} \sum_{n=-N+1}^N \frac{\tilde{v}(p_n, x_3 f' + i\varepsilon)}{\tilde{\phi}(p_n)} e^{i\pi \frac{nm}{N}}. \quad (3.4.9)$$

Note that the discrete Fourier transform of eq.(3.4.9) can be carried out by a FFT routine as soon as we have identified the data  $\tilde{v}(p_n, x_3 f' + i\varepsilon)$  and the analytical values of  $\tilde{\phi}(p_n)$ .

A suitable choice of the interpolation function is the triangle function (Harrington, 1968, p. 12). The triangle function and its Fourier transform are given as

$$\phi(y) = \begin{cases} 1 - \frac{|y|}{\Delta y}, & |y| \leq \Delta y \\ 0, & |y| > \Delta y \end{cases} \quad \text{FFT} \quad \Leftrightarrow \quad \tilde{\phi}(p) = \frac{\sin^2(\frac{\pi p \Delta y}{2})}{(\pi p)^2 \Delta y}. \quad (3.4.10)$$

Nevertheless, higher-order interpolation functions such as the cubic cardinal spline (Ahlberg et al., 1967) can be used as well and are discussed in section 3.7. In eq.(3.4.9) the values of eq.(3.4.10) for the discrete points  $p = p_n = n\Delta p$  are required. Then using eq.(3.4.3) the second expression in eq.(3.4.10) becomes

$$\tilde{\phi}(p_n) = \frac{\sin^2(\frac{\pi n}{2N})}{(\frac{\pi n}{2N})^2} \frac{1}{2N\Delta p}. \quad (3.4.11)$$

Using the interpolation function of eq.(3.4.11) in the integral of eq.(3.4.5), these integrals can be computed analytically and the values of  $\hat{u}(y, x_3 f' + i\varepsilon)$  can be calculated from eq.(3.4.5). However, the particular choice of eq.(3.4.10) together with eq.(3.4.4) results in a simplification of the integral of eq.(3.3.8). Using the triangle function as interpolator, we note that eq.(3.4.4) represents a linear interpolation of  $\hat{v}(y, x_3 f' + i\varepsilon)$  in the interval  $y_{n-1} < y < y_n$ . The  $\hat{v}(y_{n-1}, x_3 f' + i\varepsilon) = A_{n-1}$  and  $\hat{v}(y_n, x_3 f' + i\varepsilon) = A_n$  are consecutive function values at the end points of each interval. The linear interpolation used in eq.(3.3.8) leads to

$$\hat{u}(x, x_3, f' + i\varepsilon) = \sum_{n=1}^k \int_{y_{n-1}}^{y_n} \frac{\hat{v}(y, x_3, f' + i\varepsilon) dy}{\sqrt{w^2 - y^2}} + \int_{y_k}^w \frac{\hat{v}(y, x_3, f' + i\varepsilon) dy}{\sqrt{w^2 - y^2}}, \quad k = \text{int}\left(\frac{w}{\Delta y}\right), \quad (3.4.12)$$

where

$$\hat{v}(y, x_3, f' + i\varepsilon) = \frac{y_n A_{n-1} - y_{n-1} A_n}{\Delta y} + \frac{A_n - A_{n-1}}{\Delta y} y, \quad (3.4.13)$$

in which  $y_n/\Delta y$  and  $y_{n-1}/\Delta y$  represent the weighting factors for the function values  $A_n$  and  $A_{n-1}$  according to the linear interpolation. Then carrying out the integrations in eq.(3.4.12), the final result is obtained as

$$\begin{aligned} \hat{u}(x, x_3, f' + i\varepsilon) = & \sum_{n=1}^k \left[ (n A_{n-1} - (n-1) A_n) \arcsin \left( \frac{n \gamma_{n-1} - (n-1) \gamma_n}{(rn)^2} \right) + \right. \\ & \left. (A_{n-1} - A_n) (\gamma_{n-1} - \gamma_n) \right] + (A_{k+1} - A_k) \arcsin \left( \frac{\gamma_k}{rn} \right) + \\ & (A_{k+1} - A_k) \gamma_k, \quad \gamma_n = \sqrt{(rn)^2 - \left( \frac{y_n}{\Delta y} \right)^2} \quad \text{and} \quad rn = \frac{w}{\Delta y}. \quad (3.4.14) \end{aligned}$$

Finally, a simple FFT-routine and the inverse taper in eq.(3.3.2) transform the complete point source response to the time domain.

### 3.5 The inverse Radon transform for the line source configuration

In this configuration the coordinates  $x$  and  $x_3$  locate a point in a horizontally stratified medium. The impulsive wave motion  $u(x, x_3, t)$ , is generated by a line source that starts to act at  $t = 0$ . The model parameters depend only on  $x_3$ . But the wave motion  $u(x, x_3, t)$  is a function of both space coordinates and the time coordinate  $t$ . Since the source starts to act at  $t = 0$ , one can take advantage of this situation mathematically, by carrying out a one-sided Laplace transform with respect to time. Then following eq.(3.3.1) - (3.3.4) and substituting  $k = 2\pi f p$ , and using the property that the spectral quantity  $\hat{\hat{U}}(k, x_3, f' + i\varepsilon)$  is an even function of  $k$ , the wave motion  $\hat{u}(x, x_3, f' + i\varepsilon)$  is obtained as

$$\hat{u}(x, x_3, f' + i\varepsilon) = \sqrt{f'^2 + \varepsilon^2} \int_{-\infty}^{+\infty} e^{i\sqrt{f'^2 + \varepsilon^2} p x} \tilde{u}(|p|, x_3, f' + i\varepsilon) dp. \quad (3.5.1)$$

Then, following the same procedure as for the point source configuration, the final result is obtained as

$$\begin{aligned} \hat{u}(x, x_3, f' + i\varepsilon) = \frac{(rn)^2}{2} & \left( \hat{v}(y_{n-1}, x_3, f' + i\varepsilon) - 2\hat{v}(y_n, x_3, f' + i\varepsilon) + \hat{v}(y_{n+1}, x_3, f' + i\varepsilon) \right) + \\ & \frac{rn}{2} \left( \hat{v}(y_{n+1}, x_3, f' + i\varepsilon) - \hat{v}(y_{n-1}, x_3, f' + i\varepsilon) \right), \quad rn = \frac{\sqrt{f'^2 + \varepsilon^2} x}{\Delta y}, \end{aligned} \quad (3.5.2)$$

where

$$\hat{v}(y, x_3, f' + i\varepsilon) = \int_{-\infty}^{+\infty} e^{i2\pi p y} \tilde{v}(p, x_3, f' + i\varepsilon) dp, \quad (3.5.3)$$

and

$$\tilde{v}(p, x_3, f' + i\varepsilon) = \sqrt{f'^2 + \varepsilon^2} \tilde{u}(|p|, x_3, f' + i\varepsilon). \quad (3.5.4)$$

Again, a simple FFT-routine and the inverse taper in eq.(3.3.2) transform the line source response into the time domain.

### 3.6 Problems caused by the numerical implementation

#### The singularity of the square-root in the Green's function

The evaluation of the recursion algorithm based on the reflectivity method is unstable. This instability is caused by the singularities of the square-root when  $|p| = 1/v_n$ . The square-root, being a part of eq.(A.1.5) is given by

$$q_n = \sqrt{\frac{1}{v_n^2} - p^2}, \quad (3.6.1)$$

where  $q_n$  represents the vertical slowness,  $p$  the horizontal slowness and  $v_n$  the velocity of the  $n$ -th layer. Usually  $q_n$  is calculated for a fixed number of  $p$ -values in which the  $p$ -increment is held constant. As  $p$  approaches  $1/v_n$  the vertical slowness  $q_n$  rapidly decays to zero. This rapid decay causes a region of rapid oscillations in the frequency domain. Therefore the evaluation of this region leads to inaccuracies. Two options are used to damp these rapid oscillations. The first

option is to introduce the complex frequency which is discussed in Appendix A.3 and, the second option is to improve the sampling by changing the  $p$ -increment per frequency component.

The introduction of the complex frequency is shown in eq.(3.3.3) and compensation for it is easily obtained by the multiplication of the inverse taper  $e^{2\pi\epsilon t}$  when the impulse response of the model is in the complex frequency-space domain (shown in eq.(3.4.14)). Including the complex frequency, changes eqs.(3.6.1) and (A.1.13), respectively, as follows

$$q_n = \sqrt{\frac{e^{i2 \arctan(\epsilon/f)}}{v_n^2} - p^2}, \quad (3.6.2)$$

$$\hat{\bar{R}}_n(p f' + i\epsilon) = \frac{r_n + \hat{\bar{R}}_{n+1}(p f' + i\epsilon) e^{\left[4\pi i \sqrt{f'^2 + \epsilon^2} q_n x_{3,n+1}\right]}}{1 + r_n \hat{\bar{R}}_{n+1}(p f' + i\epsilon) e^{\left[4\pi i \sqrt{f'^2 + \epsilon^2} q_n x_{3,n+1}\right]}}, \quad (3.6.3)$$

where  $f$  denotes the frequency,  $r_n$  the local reflection coefficient and  $R_n$  the global reflection coefficient of the  $n$ -th layer. A proper value of  $\epsilon$  ( $s^{-1}$ ) is dependent upon the numerical precision of the computer, the temporal sampling interval and the number of temporal samples of the data set. When, for example  $e^{2\pi\epsilon t} = 10$  is acceptable as the maximum value of the inverse taper,  $\epsilon$  should be something like  $0.4 s^{-1}$  with a recording time of the data set of 1 s. When the recording time of the data set is 2 s,  $\epsilon$  should be something like  $0.2 s^{-1}$ . And the chosen maximum value of the inverse taper is acceptable when the noise does not outweigh the signal of the data set after applying the inverse taper.

Another side-effect of the complex frequency is the suppression of wrap-around noise. This noise is an anti-causal effect and is generated by a too large  $p$ -increment compared with the steepness of the last part of the elliptic and quasi-elliptic events, when  $p$  approaches  $1/v_n$ .

### ***Aliasing in the $f$ - $p$ domain***

The second option introduces a frequency-dependent  $p$ -increment according to

$$\Delta p = \frac{1}{2Nf\Delta x} \text{ in which } \Delta x = \frac{v_0}{2f_{nyq}}, \quad (3.6.6)$$

in which  $N$  denotes the number of  $p$ -samples,  $f_{nyq}$  the Nyquist frequency,  $\Delta x$  the spatial sampling according to the aliasing criterion and  $v_0$  presents the velocity in the upper layer. In this way the  $p$ -increment is chosen such that the unaliased part of the data in the  $f$ - $p$  domain (Fig.3.6.2) are sampled with a constant number  $N$ , meaning the same number of  $p$ -traces is calculated for each frequency. Thus the number  $N$ ,  $v_0$  and the  $f_{nyq}$  are chosen and they fix  $\Delta x$  and  $\Delta p$ . But this  $\Delta x$  is not necessarily the desired receiver-spacing in the ultimate result. And

because the  $p$ -increment changes per frequency, the generated data set in the  $f$ - $p$  domain cannot be shown without interpolation in, for example, the  $\tau$ - $p$  domain.

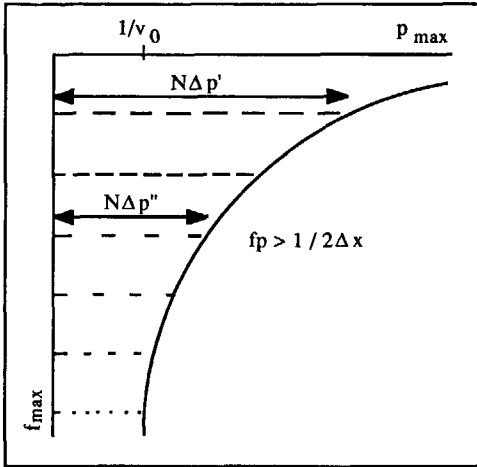


Fig.3.6.2: The  $p$ -dependence on the frequency.

Owing to this restriction put upon the modelled data in the  $f$ - $p$  domain, the wrap-around noise is reduced as well. Still the modelled elliptic and quasi-elliptic events have to map into hyperbolic and quasi-hyperbolic events with finite aperture, so the sampling interval and the number of samples of the slowness as well as of the frequency have to be accurate; that is, a small increment and a large number of increments are required. Any carelessness in choosing the parameters can still result in wrap-around noise. Another point worth considering is the complexity of the model. The more complex the model, that is the greater the number of layers, the larger the number of samples that is required in order to get a satisfactory result.

### 3.7 Interpolation

In the inverse Radon transform linear interpolation is preferred to cubic spline interpolation because of the relatively short calculation time. But in general, an interpolation procedure of higher than linear order should improve the results (Brysk and McCowan, 1986). In order to support or to reject this statement, the cardinal cubic spline (Appendix A.4) is taken to test this assumption and thereby compare with the above discussed linear interpolation procedure. The number of points of support ( $M$ , eqs.(A.4.1) and (A.4.2)) determines the accuracy of the interpolation. The larger  $M$  is, the more accurate the result will be, but the more calculation time is required. In order to determine an appropriate value for  $M$  a simple cosine function is taken for testing. The function  $f(n)$  is given by



$$f(n) = \cos^2 \left[ \frac{2\pi n \Delta t}{50} \right], \quad n = 0, 49, \quad (3.7.1)$$

and is shown in the upper half of Fig.3.7.1. In the lower part, the relative error is plotted for the linear interpolator compared with the spline interpolator for  $M = 4$  and 6. Because of the large improvement of the spline interpolator already for  $M = 4$ , it was decided to continue with this spline for further comparison. The largest relative errors correspond to the change of sign of the first derivative of the cosine function.

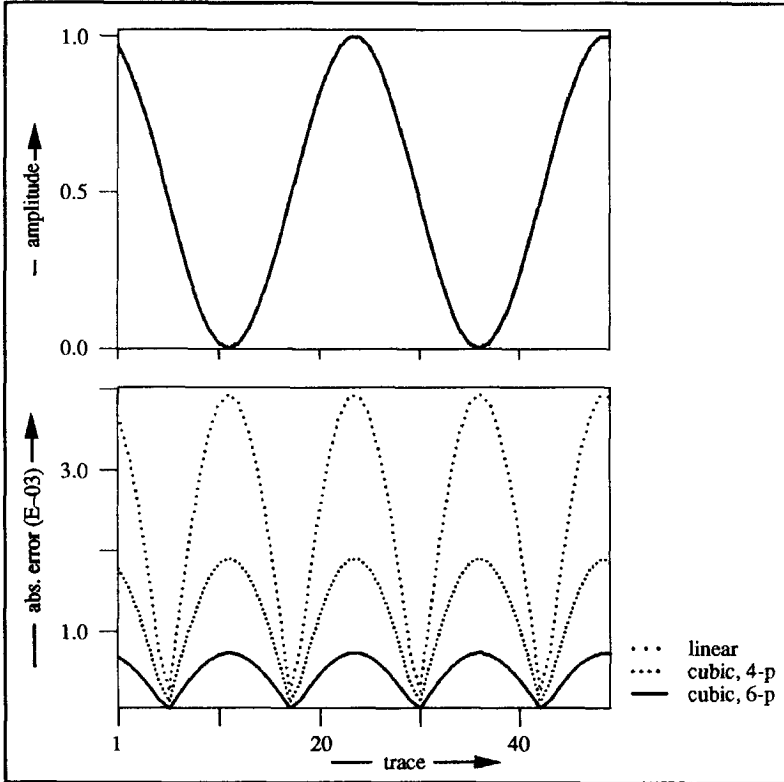


Fig.3.7.1: (a) The cosine function to interpolate and (b) the relative error of the linear interpolator compared with the spline interpolator with 4 and 6-points of support.

Fig.3.7.2 shows the 4-point spline and the triangle function (eq.(3.4.10)) with their Fourier transforms respectively.

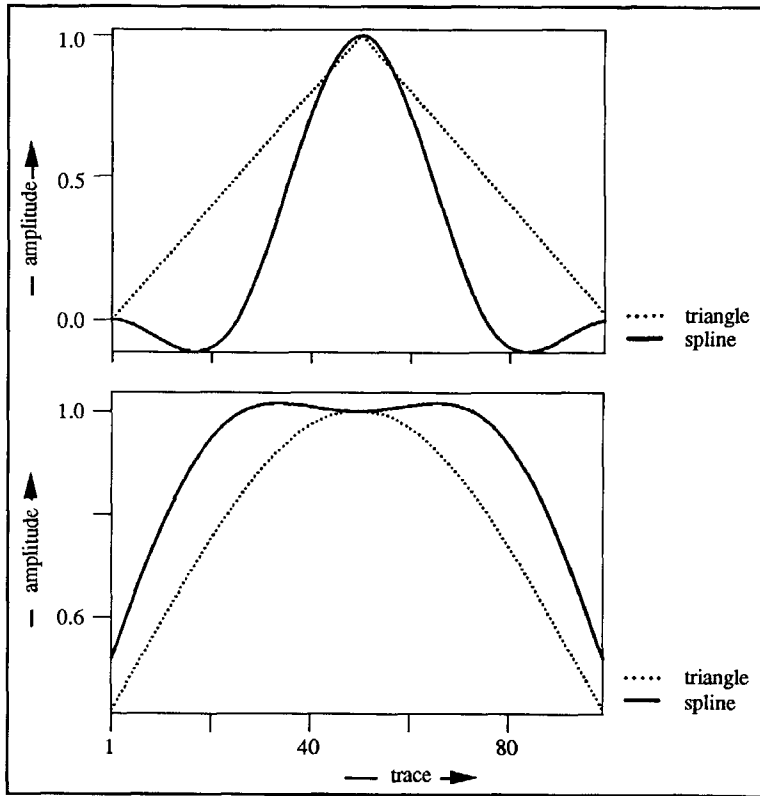


Fig.3.7.2: (a) The 4-point spline compared with the triangle function and (b) their Fourier transforms.

The next step is to substitute a cosine function in the Fourier-Bessel transform because it has a known analytic solution and is given by

$$J_0(wt) = 4 \int_0^w \frac{\cos(2\pi ft) df}{\sqrt{w^2 - (2\pi f)^2}}. \quad (3.7.2)$$

Figs.3.7.3 and 3.7.4 show the result of the integration (eq.(3.7.2)) for the linear and the spline interpolator (eq.(A.4.5)). When the sampling interval is twice as small, the relative error for both interpolators becomes less, but the spline interpolator is far more accurate than the linear interpolator. Again it is clear that the local maxima and minima of the Bessel function, that is the change of sign of the first derivative, cause problems for both interpolators.

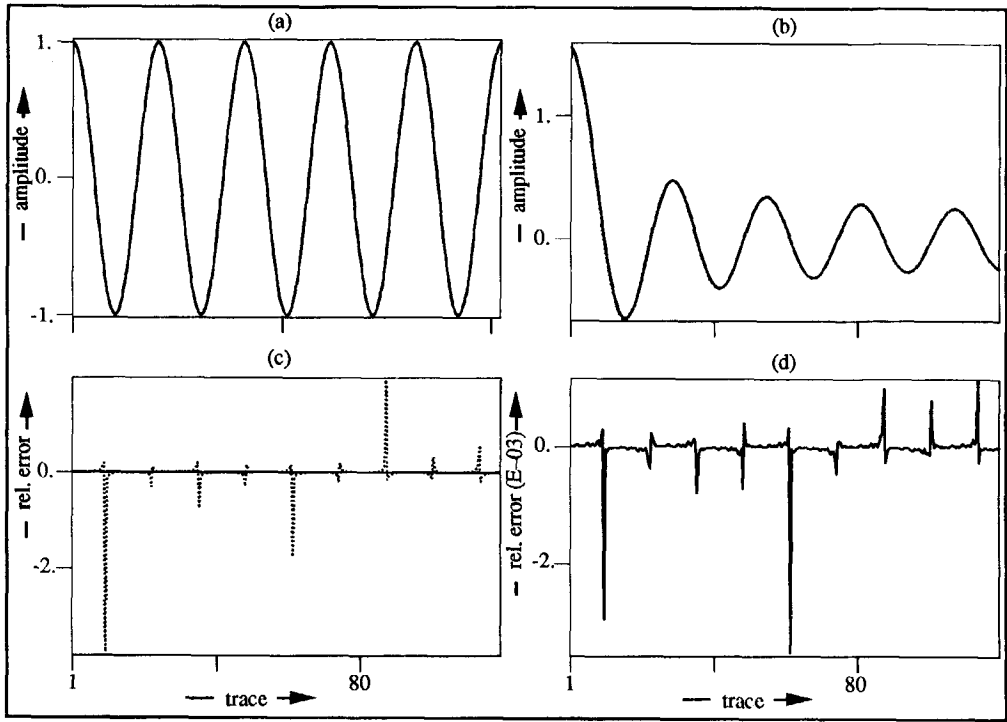


Fig.3.7.3: The cosine function substituted in the Sommerfeld Weyl integral; (a) denotes the cosine itself, (b) is the result of the integration for the linear and spline interpolator (they coincide), (c) represents the relative error for both (dotted line: linear, solid line: spline) and (d) is the enlargement of (c) for the latter.

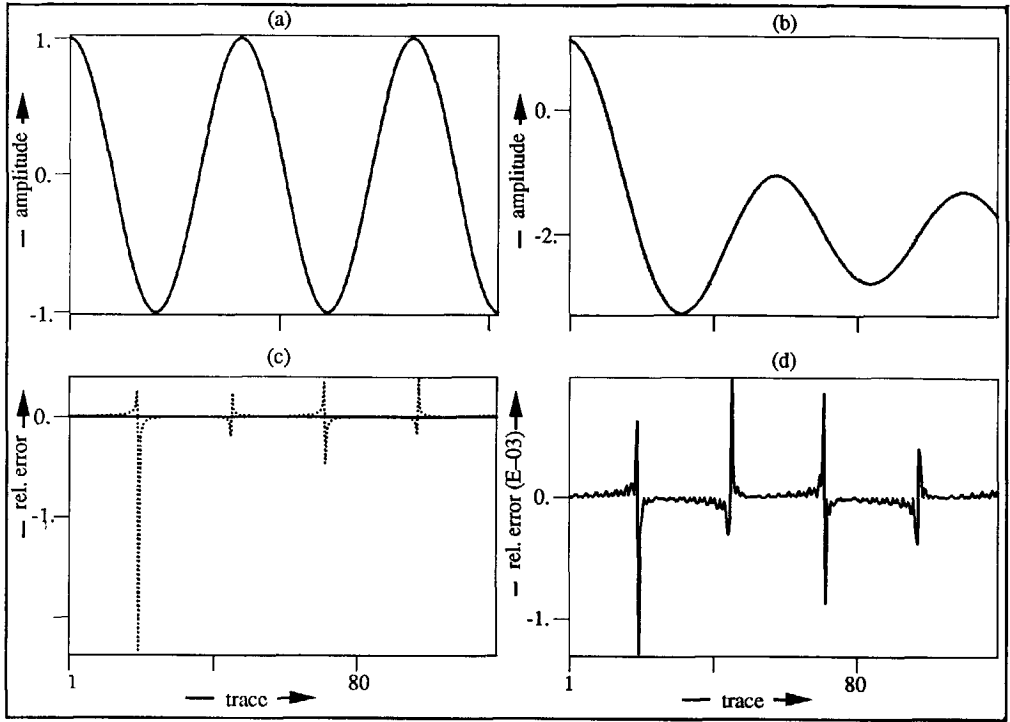


Fig.3.7.4: The cosine function substituted in the Sommerfeld Weyl integral; (a) denotes the cosine itself, (b) is the result of the integration for the linear and spline interpolator (they coincide), (c) represents the relative error for both (dotted line: linear, solid line: spline) and (d) is the enlargement of (c) for the latter.

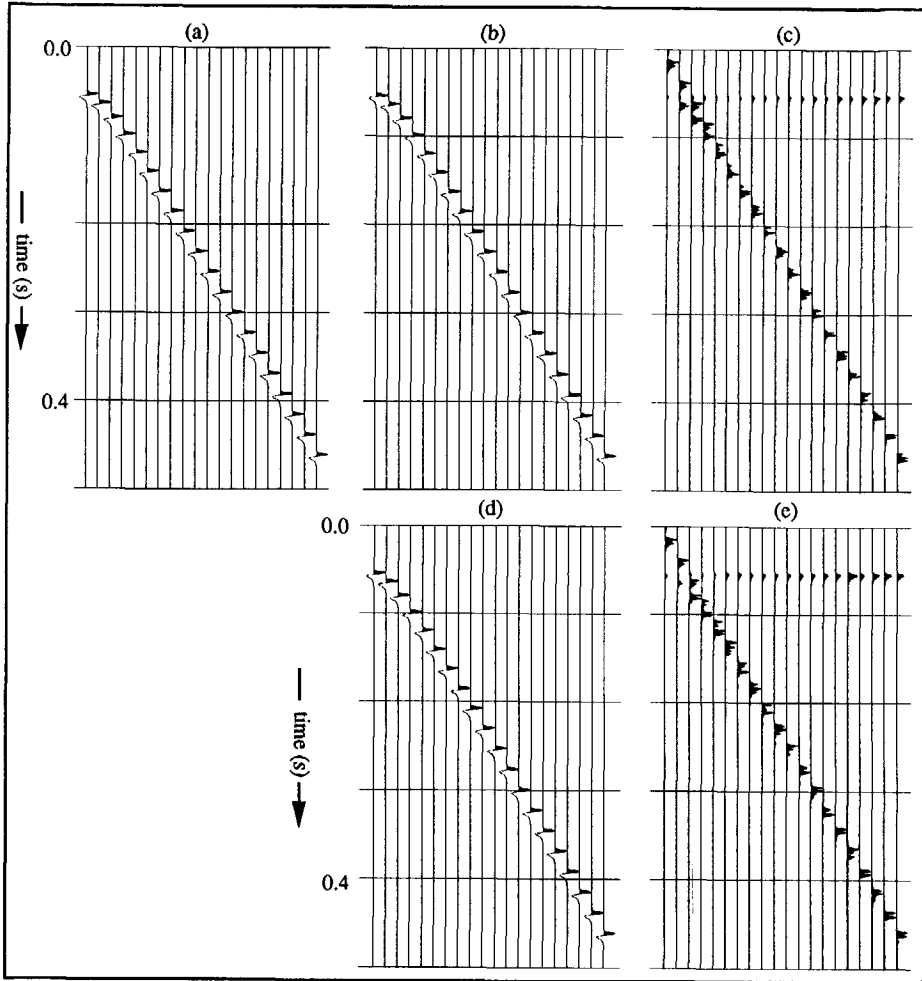


Fig.3.7.5: (a) The analytic solution, (b) the model calculated for the linear procedure and (d) the model calculated for the 4-point spline procedure; (c) denotes the difference between the analytic solution and the linear procedure and (e) denotes the difference between the analytic solution and the spline procedure;  $\Delta x = 10$  m,  $\Delta t = 0.002$  s and  $v_0 = 855$  m/s.

The last step is to implement both interpolators in the algorithm and the results are shown in Fig.3.7.5. The analytic solution is represented by (a), the model for the linear procedure by (b) and the model for the spline procedure by (d). No difference is visible with the naked eye. Taking the absolute difference between the analytic solution and (a) the linear and (d) the spline procedure respectively gives (c) and (e). Fig.3.7.6 compares the relative difference of the linear with the spline interpolator in more detail for the 7-th trace in the time domain as well as in the frequency domain.

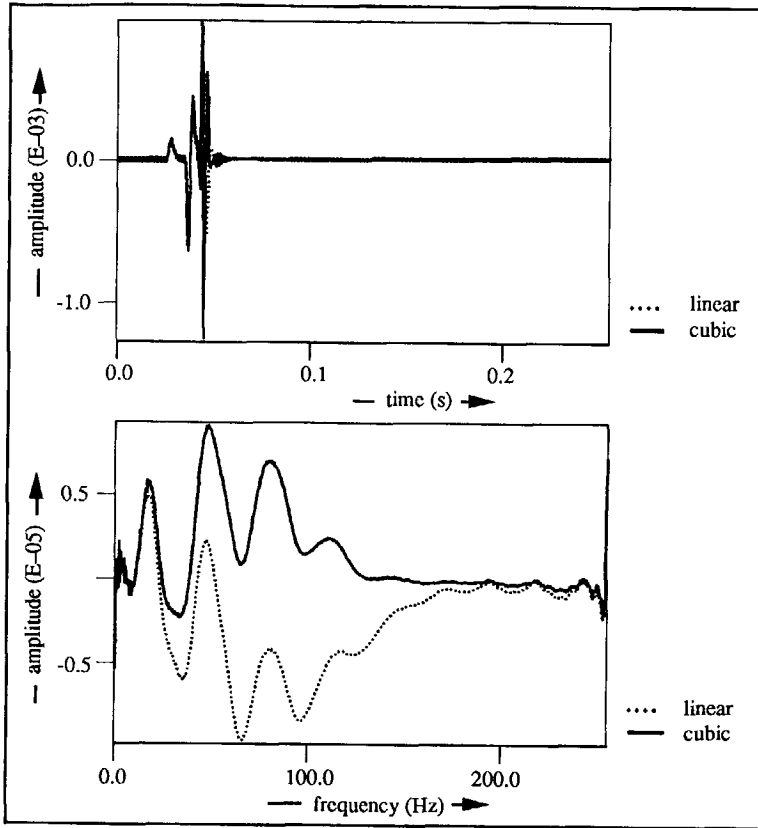


Fig.3.7.6: The relative difference in more detail in the time domain (max. error = 1.5 %) and the relative difference of the amplitude of the 7-th trace (max. error = 0.3 %).

From Fig.3.7.6, it is not quite clear which interpolator does a better job. Applying it to the other traces of Fig.3.7.5, the outcome is more or less the same. Therefore, another measure for the error is introduced, that is the cumulative error energy,  $E_{\text{cum}}$

$$E_{\text{cum}} = \frac{\sum_{k=1}^N \{ \text{tr}_{\text{an}} - \text{tr}_{\text{int}} \}^2(k)}{\sum_{k=1}^N \text{tr}_{\text{an}}^2(k)}, \quad (3.7.3)$$

where  $\text{tr}_{\text{an}}$  denotes the analytic result and  $\text{tr}_{\text{int}}$  the interpolated result.

In the next figure (3.7.7) four different situations are considered. Part (a) and (b) yield the results when  $w = y_k$  and part (c) and (d) show the results when  $w \neq y_k$ . Further, for part (a) and

(c) the division by the Fourier transform of the interpolator respectively is carried out and for part (b) and (d) the division by the Fourier transform of the interpolator respectively is omitted. The accuracy of the interpolation procedure in the algorithm is determined by the division of its Fourier transform (eqs.(3.4.8) and (3.4.10)) as well as by the difference between  $w$  and  $y_k$  according to eq.(3.4.4) and may be dependent on the offset.

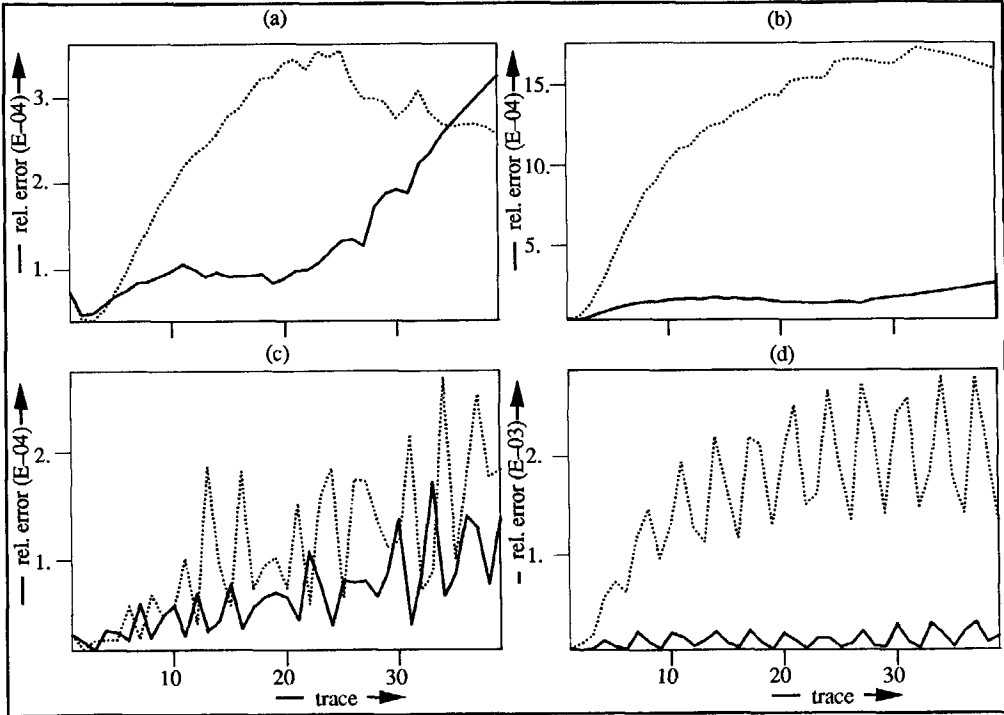


Fig.3.7.7: The cumulative error energy (dotted line: linear, solid line: spline) in the calculation when  $w = y_k$  where (a) represents the energy when divided by the Fourier transform of the interpolator respectively and (b) when the division by the Fourier transform is omitted; the cumulative error energy in the calculation when  $w \neq y_k$  where (c) represents the energy when divided by the Fourier transform of the interpolator respectively and (d) when not divided by the Fourier transform.

Considering all the results in this section, the conclusion can be drawn that the spline procedure is more accurate than the linear procedure when the division by the Fourier transform of the interpolator is omitted. The major difference in accuracy is obtained when the spline is used as interpolator alone (Figs.3.7.3 and 3.7.4). However the difference in accuracy when implemented in the algorithm is far less pronounced. Since the division by the Fourier transform of the interpolator is part of the mathematical solution, the results are improved when it is done (Fig.3.7.7) and are worse when it is not done as far as the linear interpolator is concerned. Thus, the linear interpolator is more benefitted by the division of its Fourier transform than the

spline interpolator is. Furthermore, there is hardly any difference in accuracy between  $w = y_k$  and  $w \neq y_k$ . And finally, the offset slightly influences the accuracy when the division of the Fourier transform is carried out, and substantially affects it when the division is omitted.

What explanation can be given for the unexpectedly good resemblance in accuracy between the interpolators? When the division by the Fourier transform of the interpolator is carried out, the performance of the two interpolators is more or less equal. This means that the division by the Fourier transform of the interpolator preconditions the data such that a linear interpolation is as good as the spline interpolator (more expensive) when the data is not aliased. Thus, any higher order interpolation is only time consuming and does not improve the results significantly. This is also confirmed by Benoliel et al. (1987).

### 3.8 Numerical results

#### *Modelled with the inverse Radon transform*

Two synthetic data sets are shown, a 9-layer model containing small density/velocity contrasts shown in Fig.3.8.2, and a complicated 326-layer model extracted from a well log (Fig.3.8.3) and shown in Fig.3.8.5. The well log is originated from the Delft Air Gun experiment, shot over well 2/1-2 of B.P. Both data sets are modelled for the marine situation with a free surface. Internal multiples as well as free surface multiples, are included. The temporal sampling interval is 2 ms and 4 ms respectively, the spatial sampling interval is 12.5 m and the nearest offset is 0 m. Elastic effects are neglected. For the 9-layer model, the Blackman-Harris function is taken as the source wavelet (Fig.3.8.1)

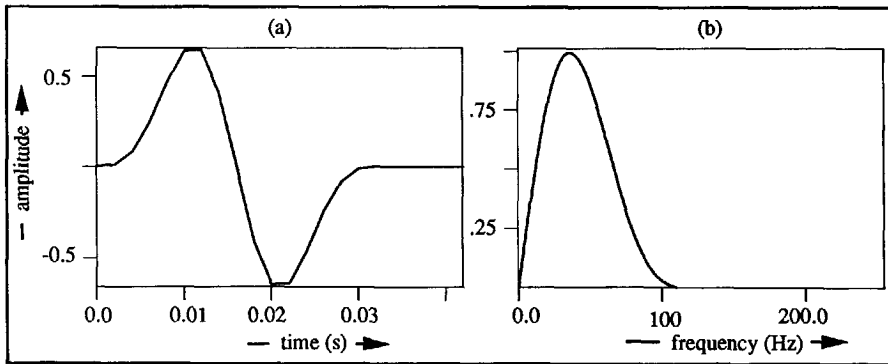


Fig.3.8.1: (a) The Blackman-Harris function and (b) its spectrum

and calculated according to

$$w(i) = .48829 \sin\left(\frac{2\pi i \Delta t}{N \Delta t}\right) + .28256 \sin\left(\frac{4\pi i \Delta t}{N \Delta t}\right) + .02561 \sin\left(\frac{6\pi i \Delta t}{N \Delta t}\right), \quad i = 0, N, \quad (3.8.1)$$



where  $\Delta t$  denotes the temporal sampling interval,  $i$  the sampling number and  $N$  the total number of samples of the wavelet.

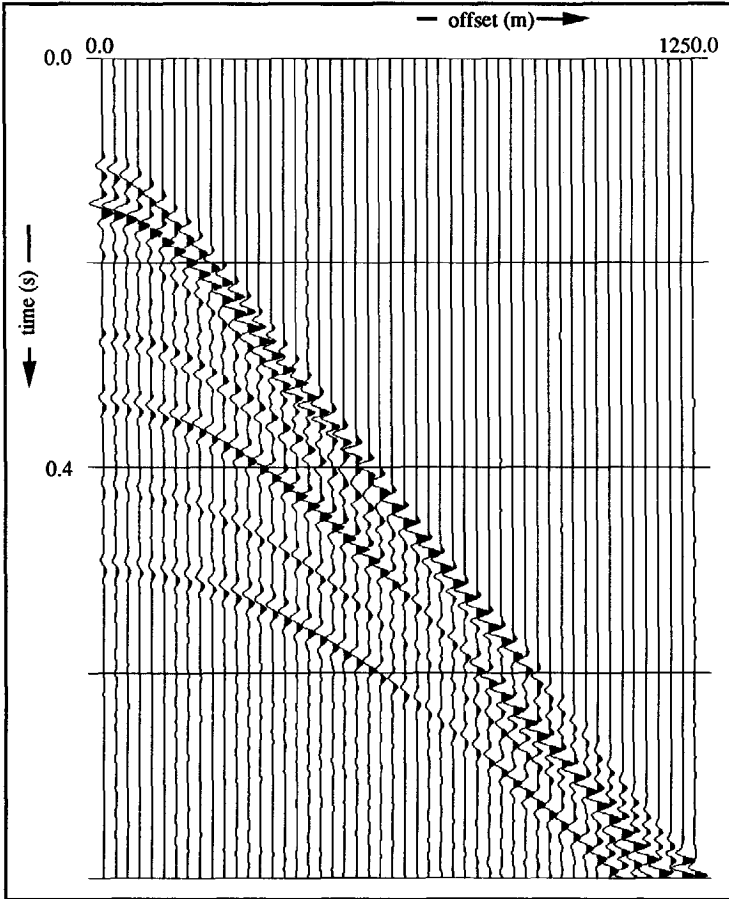


Fig.3.8.2: The simple 9-layer model calculated with the inverse Radon transform

For the 326-layer model, the notional sources are used as source signatures (Fig.3.8.4). These are derived from the near-field hydrophone measurements that were recorded during the experiment (Ziolkowski et al., 1982).

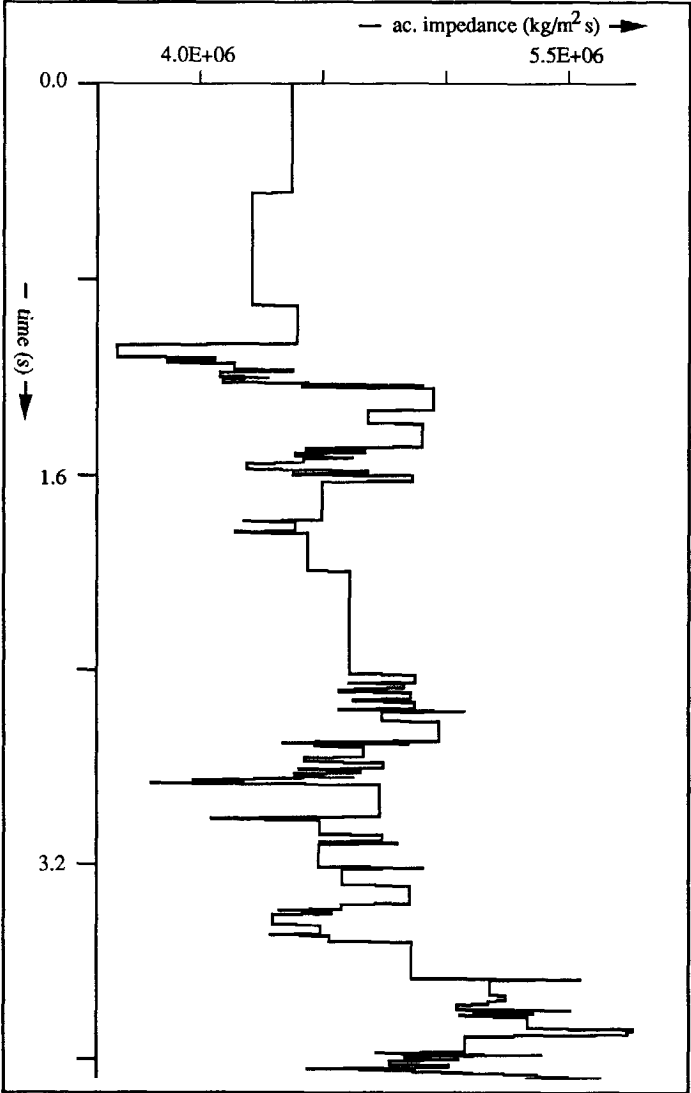


Fig.3.8.3: The acoustic impedance profile of the well log from the Delft Airgun experiment.

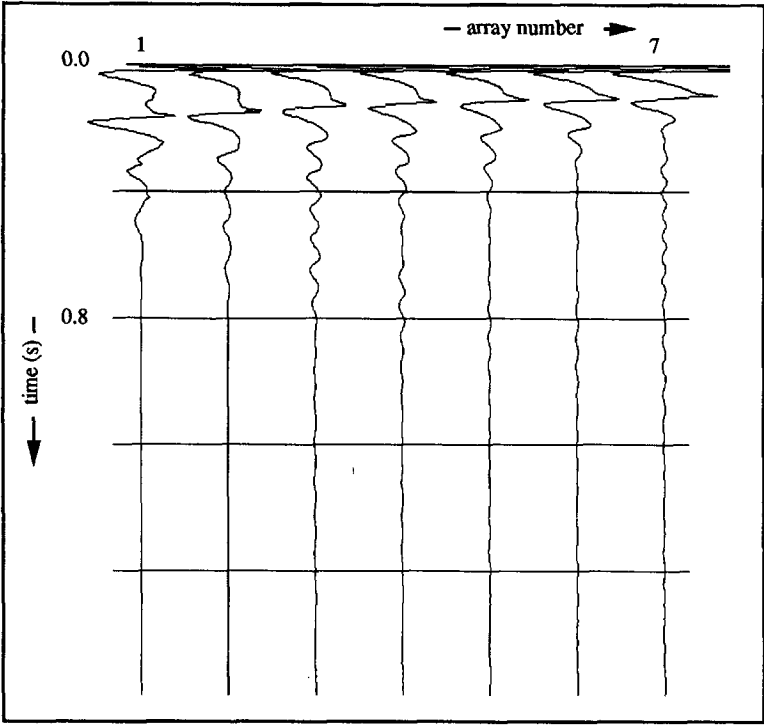


Fig.3.8.4: The calculated notional sources of the airgun array of the Delft Airgun experiment.

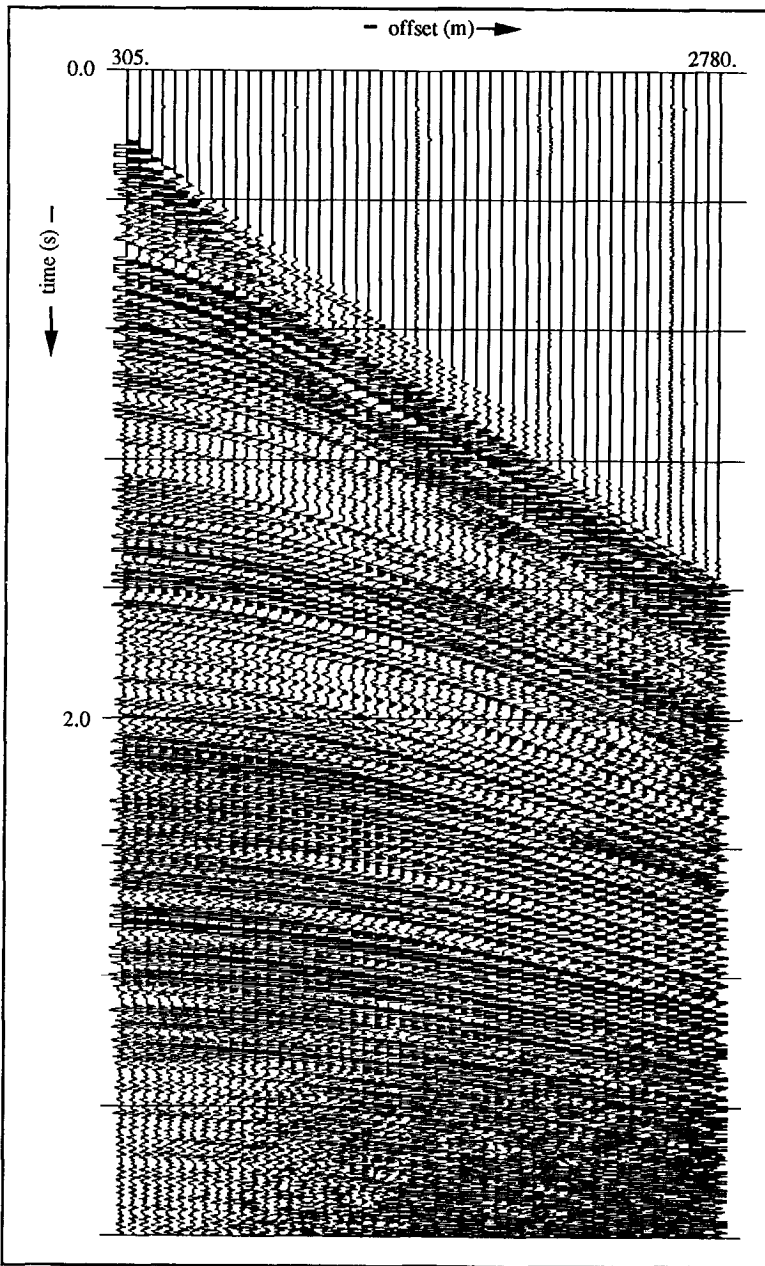


Fig.3.8.5: The complicated 326-layer model calculated with the inverse Radon transform

#### *Modelled with the exact Cagniard-De Hoop technique*

In Fig.3.8.6 a comparison of the calculation with the reflectivity method for the 9-layer model is made with the exact Cagniard-De Hoop technique (Drijkoningen and Fokkema, 1987) for the

same configuration as shown above including the use of the Blackman-Harris function, except that only primary reflections are computed. The first offset is 50 m instead of 0 m. No noticeable difference can be observed. However with a small increase of computation time, all internal multiples can be included in the reflectivity method. This is in contrast with the Cagniard-De Hoop technique where the inclusion of an extra generalized ray leads to extra computational effort. Because of the large amount of calculation time the 326-layer model was not calculated with the exact Cagniard-De Hoop technique.

For this model, our method needed 5 minutes CPU time, where the exact Cagniard-De Hoop technique used 3 hours CPU time. Including the internal multiples (only 1-st order) would double the calculation time for the exact Cagniard-De Hoop technique and increase the calculation time for our method with 1 %.

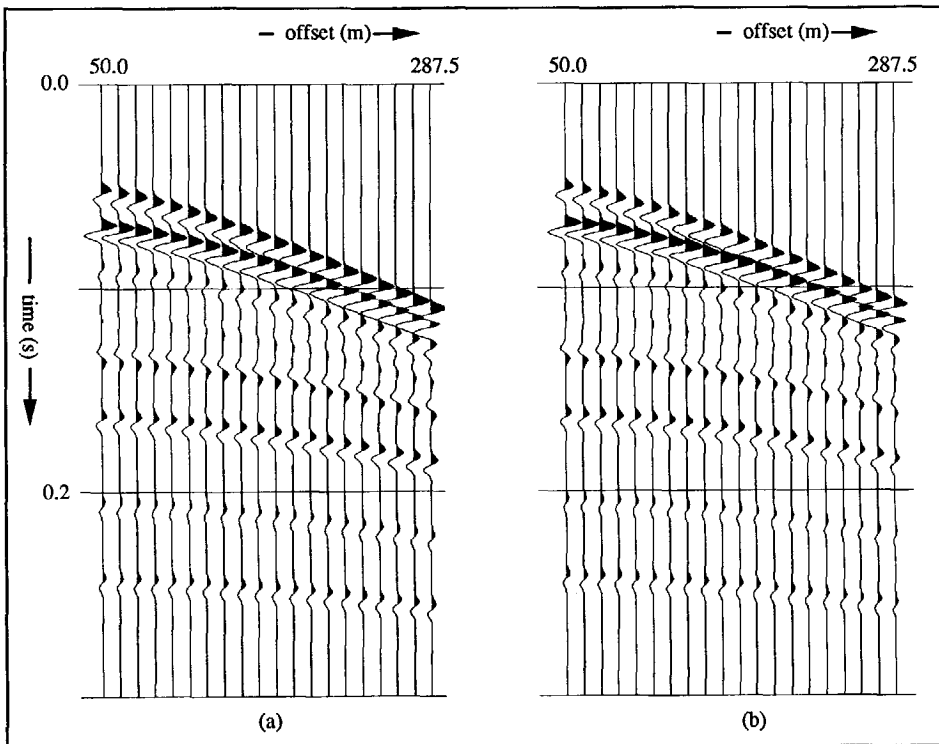


Fig.3.8.6: The simple 9-layer model; (a), the inverse Radon transform; (b), the exact Cagniard-De Hoop technique.

### 3.9 Artifacts due to the numerical implementation of the transform

The synthetic seismogram of the 326-layer model (Fig.3.8.5) contains a considerable amount of noise in the lower right hand part, that is at large offset and at relatively late times. Here no

primary reflections occur, only internal multiples are present. Because the internal multiples are very weak at these times, they are smaller than the numerical noise. When the inverse taper is applied (eq.(3.3.2)), it blows up the noise for large time-values, because it increases exponentially with time. The noise level is constant along the trace and the amplitude of the reflectors decays with increasing depth of the reflectors.

This kind of noise is lacking in the simple 9-layer model. Here the chosen parameters are accurate enough because the Green's function in this model is much simpler than the Green's function of the 326-layer model. To improve the latter, a larger number of samples and a smaller increment in slowness as well as in time has to be used for the calculation.

---

## THE FORWARD & INVERSE RADON TRANSFORMS APPLIED TO T-X DATA: A SHOT GATHER OR A CMP GATHER

---

### 4.1 Introduction

The aim of this chapter is to derive a numerical procedure for a 3D configuration as well as for a 2D configuration that maps  $t$ - $x$  seismic data into  $\tau$ - $p$  and vice versa. In the introduction two main problems (section 1.3) inherent to the Radon transform are mentioned. These are (1) the interpolation necessary for stacking of the slant lines and (2) the limited aperture (in space) of the data set. The latter problem does not exist in the previous chapter because the synthetic data are generated in the  $f$ - $p$  domain. The numerical implementation of the Radon transform changes for field data. Although Brysk and McCowan (1986) managed to improve the numerical procedure of the Radon transform for the point source configuration, their procedure still suffers from severe edge effects. These edge effects play an increasingly important role as the aperture of the data set decreases.

Another point worth improvement is the operation of the square-root filter of Brysk and McCowan (1986) in the time domain. According to Beylkin (1987) and Vissinga et al. (1990) more accurate results are obtained when the filter coefficients of the square-root filter are frequency dependent.

In section 4.2 the modification of the Brysk and McCowan algorithm (1986) is derived for the Radon transform (forward and inverse) for the point source, and in section 4.3 for the line source configuration, following the same procedure as in the previous chapter and again assuming rotational symmetry and plane horizontal layers. In section (4.4) the problems due to the numerical implementation are discussed. The main differences with the inverse Radon transform in Chapter 3 are the omitted complex frequency, the absence of the  $\text{sinc}^2$  operator (eq.3.4.9) and the constant  $p$ -increment. Section 4.5 outlines these differences. At last section

4.6 shows some synthetic data examples of a hyperbolic event (2D & 3D) with their inseparable frequency reduction due to aliasing criterion in the  $f$ - $p$  domain.

#### 4.2 The Radon transform for the point source configuration

Starting with the frequency equivalent of the 3D slant stack operator and assuming cylindrical symmetry

$$\begin{aligned}\hat{u}(p, f) &= 2 \int_{-\infty}^{+\infty} \hat{u}(|x|, f) |x| dx \int_0^{\pi/2} e^{-i2\pi f p x \cos \theta} d\theta \\ \hat{u}(x, f) &= 2 f^2 \int_{-\infty}^{+\infty} \hat{u}(|p|, f) |p| dp \int_0^{\pi/2} e^{i2\pi f p x \cos \chi} d\chi ,\end{aligned}\tag{4.2.1}$$

new variables of integration are introduced. Instead of introducing  $p' = p \cos \theta$  and  $x' = x \cos \chi$  according to Brysk and McCowan (1986), the variables  $q = f p \cos \theta$  and  $b = f x \cos \chi$  are proposed by us. Then, changing the order of the integrations, we arrive at

$$\hat{u}(p, f) = \int_0^{fp} \frac{\hat{v}(q, f) dq}{\sqrt{(fp)^2 - q^2}} , \quad fp > 0 ,\tag{4.2.2}$$

where

$$\hat{v}(q, f) = \int_{-\infty}^{+\infty} e^{-i2\pi q x} \hat{v}(x, f) dx ,\tag{4.2.3}$$

and

$$\hat{v}(x, f) = 2 |x| \hat{u}(|x|, f) .\tag{4.2.4}$$

For the inverse operator we arrive at

$$\hat{u}(x, f) = \int_0^{fx} \frac{\hat{w}(b, f) db}{\sqrt{(fx)^2 - b^2}} , \quad fx > 0 ,\tag{4.2.5}$$

where



$$\widehat{w}(b, f) = \frac{1}{2\pi} \int_{-\infty}^{+\infty} e^{i2\pi b p} \widehat{w}(p, f) dp, \quad (4.2.6)$$

and

$$\widehat{\widehat{w}}(p, f) = 4\pi f^2 |p| \widehat{u}(|p|, f). \quad (4.2.7)$$

Note that in the special case for  $fp = 0$  or  $fx = 0$ , eqs.(4.2.2) and (4.2.5) respectively reduce to

$$\begin{aligned} \widehat{u}(0, f) &= \frac{\pi}{2} \widehat{v}(0, f), & p &= 0 \\ \widehat{u}(p, 0) &= \frac{\pi}{2} \widehat{v}(p, 0), & f &= 0, \end{aligned} \quad (4.2.8)$$

and

$$\begin{aligned} \widehat{u}(0, f) &= \frac{\pi}{2} \widehat{w}(0, f), & x &= 0 \\ \widehat{u}(x, 0) &= \frac{\pi}{2} \widehat{w}(x, 0), & f &= 0. \end{aligned} \quad (4.2.9)$$

The values of  $\widehat{v}(q, f)$  and  $\widehat{w}(b, f)$  are available only in a discrete number of points  $q_n = n\Delta q$ , where  $\Delta q$  is the sampling interval and  $b_n = n\Delta b$ , where  $\Delta b$  is the sampling interval and  $n \in \{-N+1, \dots, N\}$  respectively. In order to calculate the integral of the right hand side of eqs.(4.2.2) and (4.2.5), we need the values of  $\widehat{v}(q, f)$  and  $\widehat{w}(b, f)$  for all  $q$  or for all  $b$  in the range of the integration  $0 < q < fp$  and  $0 < b < fx$  respectively. Since the interpolation procedure is the same for the eqs.(4.2.2) and (4.2.5), they are replaced by

$$\widehat{h}(a, f) = \int_0^{fa} \frac{\widehat{g}(y, f) dy}{\sqrt{(fa)^2 - y^2}}, \quad (4.2.10)$$

where the function  $\widehat{g}(y, f)$  is interpolated linearly on each subinterval. This linear interpolation leads to

$$\widehat{h}(a, f) = \sum_{n=1}^k \int_{y_{n-1}}^{y_n} \frac{\widehat{g}(y, f) dy}{\sqrt{(fa)^2 - y^2}} + \int_{y_k}^{fa} \frac{\widehat{g}(y, f) dy}{\sqrt{(fa)^2 - y^2}}, \quad k = \text{int} \left( \frac{fa}{\Delta y} \right), \quad (4.2.11)$$

with

$$\hat{g}(yf) = \frac{y_n A_{n-1} - y_{n-1} A_n}{\Delta y} + \frac{A_n - A_{n-1}}{\Delta y} y, \quad (4.2.12)$$

and where the  $\hat{g}(y_{n-1}f) = A_{n-1}$  and  $\hat{g}(y_n f) = A_n$  are consecutive function values at the end points of each interval. The weighting factors for the function values  $A_n$  and  $A_{n-1}$  according to the linear interpolation are represented by  $y_n/\Delta y$  and  $y_{n-1}/\Delta y$ . Higher-order interpolation functions such as cardinal cubic spline (Ahlberg et al., 1967) can be used as well and are explained in the section 3.7. Then, carrying out the integrations in eq.(4.2.11), the final result is obtained as

$$\begin{aligned} \hat{h}(af) = & \sum_{n=1}^k \left[ (n A_{n-1} - (n-1)A_n) \arcsin \left( \frac{n \gamma_{n-1} - (n-1) \gamma_n}{(rn)^2} \right) + \right. \\ & \left. (A_{n-1} - A_n) (\gamma_{n-1} - \gamma_n) \right] + (k+1) A_k - k A_{k+1} \arcsin \left( \frac{\gamma_k}{rn} \right) + \\ & (A_{k+1} - A_k) \gamma_k, \quad \gamma_n = \sqrt{(rn)^2 - \left( \frac{y_n}{\Delta y} \right)^2} \text{ and } rn = \frac{fa}{\Delta y}. \end{aligned} \quad (4.2.13)$$

Finally, a simple FFT-routine transforms the complete point source response to the time domain.

### 4.3 The Radon transform for the line source configuration

Now the seismic data are considered to be due to a line source that starts to act at  $t = 0$ . Then, starting from the frequency equivalent of the 2D slant stack operator

$$\begin{aligned} \hat{u}(pf) &= \int_{-\infty}^{+\infty} e^{-i2\pi f p x_1} \hat{u}(x_1, f) dx_1 \\ \hat{u}(x_1, f) &= f \int_{-\infty}^{+\infty} e^{i2\pi f p x_1} \hat{u}(p, f) dp, \end{aligned} \quad (4.3.1)$$

the forward transform, following eq.(4.2.13) is written as

$$\hat{u}(pf) = \frac{(rn)^2}{2} (A_{n-1} - 2A_n + A_{n+1}) + \frac{rn}{2} (A_{n+1} - A_{n-1}), \quad rn = \frac{fp}{\Delta y}, \quad (4.3.2)$$

where  $y = fp$ ,  $\hat{g}(y_{n-l}, f) = A_{n-l}$ ,  $\hat{g}(y_n, f) = A_n$  and  $\hat{g}(y_{n+l}, f) = A_{n+l}$  are the consecutive function values and given as

$$\hat{g}(y, f) = \int_{-\infty}^{+\infty} e^{-i2\pi x, y} \hat{u}(x, f) dx. \quad (4.3.3)$$

The inverse transform is immediately deduced as

$$\hat{u}(x, f) = \frac{(rn)^2}{2} (A_{n-l} - 2A_n + A_{n+l}) + \frac{rn}{2} (A_{n+l} - A_{n-l}), \quad rn = \frac{fx}{\Delta y}, \quad (4.3.4)$$

where  $y = fx$ ,  $\hat{g}(y_{n-l}, f) = A_{n-l}$ ,  $\hat{g}(y_n, f) = A_n$  and  $\hat{g}(y_{n+l}, f) = A_{n+l}$  are the consecutive function values and given as

$$\hat{g}(y, f) = f \int_{-\infty}^{+\infty} e^{i2\pi p y} \hat{u}(p, f) dp. \quad (4.3.5)$$

Again, a simple FFT-routine transforms the line source response to the time domain.

#### 4.4 Problems caused by the numerical implementation

##### Aliasing in the $f$ - $p$ domain

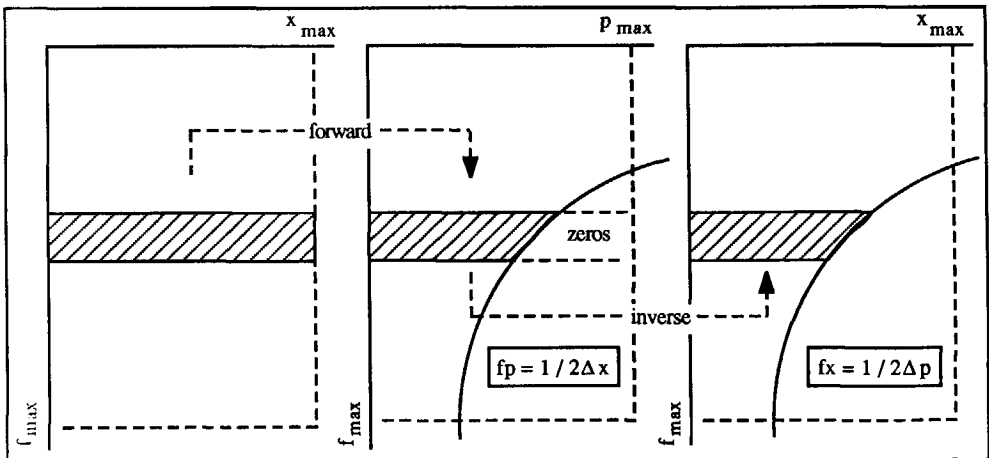


Fig.4.4.1: The restriction on the Radon transform.

Aliasing in the  $f$ - $p$  domain versus the  $f$ - $x$  domain has been well described by Turner (1990) and by Benoliel et al. (1987). The data are not aliased if

$$fp \leq \frac{1}{2\Delta x} \quad \text{and} \quad fx \leq \frac{1}{2\Delta p}. \quad (4.4.1)$$

According to eq.(4.4.1) part of the input data has to be muted in the  $f$ - $x$  domain and replaced by zeros before the actual Radon transform is applied. The muting accounts for both transforms, i.e. the forward and the inverse Radon transforms and is shown in Fig.4.4.1. Unless the orthogonal hyperbola (eq.(4.4.1)) falls outside the range of the data, the data after application of a forward and an inverse Radon transform are never the same. This is not true of forward and inverse Fourier transforms applied to the same data, whether aliased or not.

#### *Spatially finite aperture, including the lack of near-offset measurements*

Aliasing of the data in the  $f$ - $p$  domain is one reason for padding with zeros. Another reason to pad zeros is the frequent absence of near-offset measurements. In order to get the correct curvature of the elliptic and quasi-elliptic events, some values have to be added. Since it is unknown which values are missing, zeros are filled in because incorrect values are even worse. And since the number of input traces must be a power of two because of the use of the FFT-routine, usually some zero traces must be appended at the end of the data set.

Abrupt changes in the data set generate the well known Gibb's phenomenon after an exposure of the data to a FFT-routine. In order to protect the transformed data set from these artifacts, proper windowing is required in the space direction to both ends of the data set and in the time direction to the end of the data set (Fig.4.4.2). Thus, padding zeros and windowing both

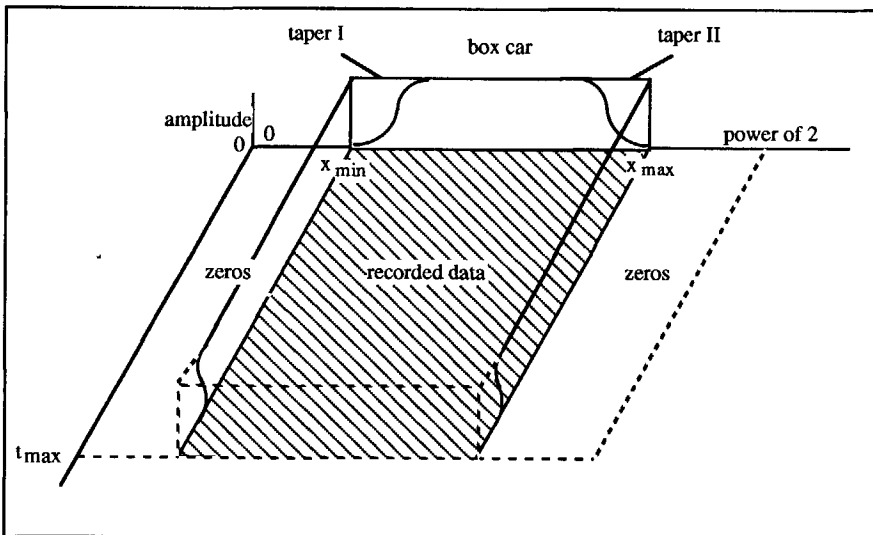


Fig.4.4.2: The average recorded data set.

decrease the quality of the transformed data set.

### Suitable tapers for the transform

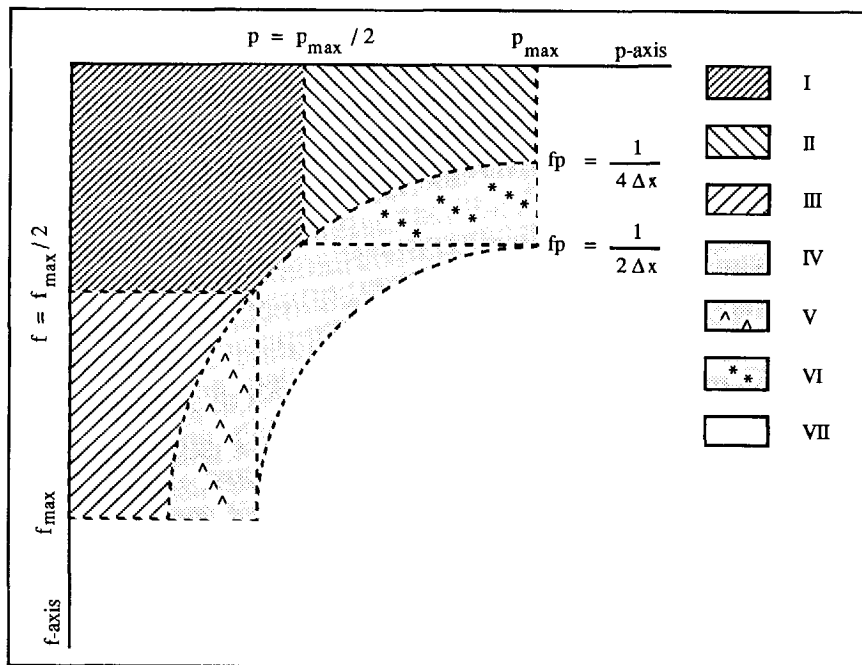


Fig.4.4.3: The subdivision in several areas for a 2D-taper.

$$\text{-I-} \quad p < \frac{p_{\max}}{2} \quad \wedge \quad fp < \frac{1}{4\Delta x} \quad \wedge \quad f < \frac{f_{\max}}{2}$$

$$\text{-II-} \quad p > \frac{p_{\max}}{2} \quad \wedge \quad fp < \frac{1}{4\Delta x}$$

$$\text{-III-} \quad f > \frac{f_{\max}}{2} \quad \wedge \quad fp < \frac{1}{4\Delta x}$$

$$\text{-IV-} \quad f < \frac{1}{2\Delta x p_{\max}} \quad \wedge \quad p < \frac{1}{2\Delta x f_{\max}} \quad \wedge \quad \frac{1}{4\Delta x} < fp < \frac{1}{2\Delta x}$$

$$\text{-V-} \quad f > \frac{f_{\max}}{2} \quad \wedge \quad fp > \frac{1}{4\Delta x} \quad \wedge \quad p < \frac{1}{2\Delta x f_{\max}}$$

$$\text{-VI-} \quad p > \frac{p_{\max}}{2} \quad \wedge \quad fp > \frac{1}{4\Delta x} \quad \wedge \quad f < \frac{1}{2\Delta x p_{\max}}$$

$$\text{-VII-} \quad fp > \frac{1}{2\Delta x}$$

Several kind of tapers are available and there are also some possibilities how to apply the chosen taper. Following Oppenheim and Schafer (1975) three tapers are tested, the Gaussian taper

$$w(n) = e^{-\alpha n^2}, \quad (4.4.2)$$

the Hanning taper

$$\begin{aligned} w(p, f) &= \frac{1}{2} [1 - \cos \frac{(fp - \beta)}{\alpha}] , \quad \alpha = \frac{1}{2\Delta x} \quad \text{and} \quad \beta = 2\pi\alpha = \frac{\pi}{\Delta x} \\ &= \frac{1}{2} [1 - \cos (2fp\Delta x)] . \end{aligned} \quad (4.4.3)$$

and the Hamming taper

$$w(p, f) = 0.54 - 0.46 \cos (2fp\Delta x) . \quad (4.4.4)$$

The taper coefficients can be dependent on one parameter (1D) being slowness or offset, or on two parameters (2D) being frequency and slowness or offset. Both methods give good results. As far as the kind of taper is concerned, the best result, having the least muting and the smallest artifacts is obtained by the Hanning taper. An example of a 2D-taper is shown in Fig.4.4.3.

#### 4.5 Main differences from the algorithm of Chapter 3

The interpolation in the square-root filter is linear, just as in Chapter 3. The  $\text{sinc}^2$  operator to improve the above mentioned interpolation is omitted. No noticeable difference can be seen when the operator is applied or is not applied because the noise level present in field data usually outweighs the improvement. For the introduction of a cubic spline interpolation, the same arguments can be used as before (section 3.7). Another but essential difference between the above algorithm and the numerical procedure in Chapter 3 is the non-varying  $p$ -increment per frequency component. Since the receiver increment is a field parameter and therefore constant, the possibility to vary it is lost according to eq.(3.6.6).

The next problem is closely related to a variable versus a constant  $p$ -increment. The measure of inaccuracy of the linear interpolation in the square-root filter is amongst others dependent upon the difference between  $fa$  and  $y_k$  following eq.(4.3.13). Since this difference is constant per frequency component, but gradually changes per frequency depending on the desired receiver interval in the ultimate result, its response in the time domain turns into linear events (down-dip) showing up in the lower right hand part of the  $\tau$ - $p$  response, for example Fig.4.6.2d. The oscillating precision is illustrated in the test function,  $f(x) = x^2$  in Fig.4.5.1.

The first part is the function itself and the second part denotes the absolute and the relative error. This problem disappears when the  $p$ -increment decreases per increasing frequency component according to eq.(3.6.6).

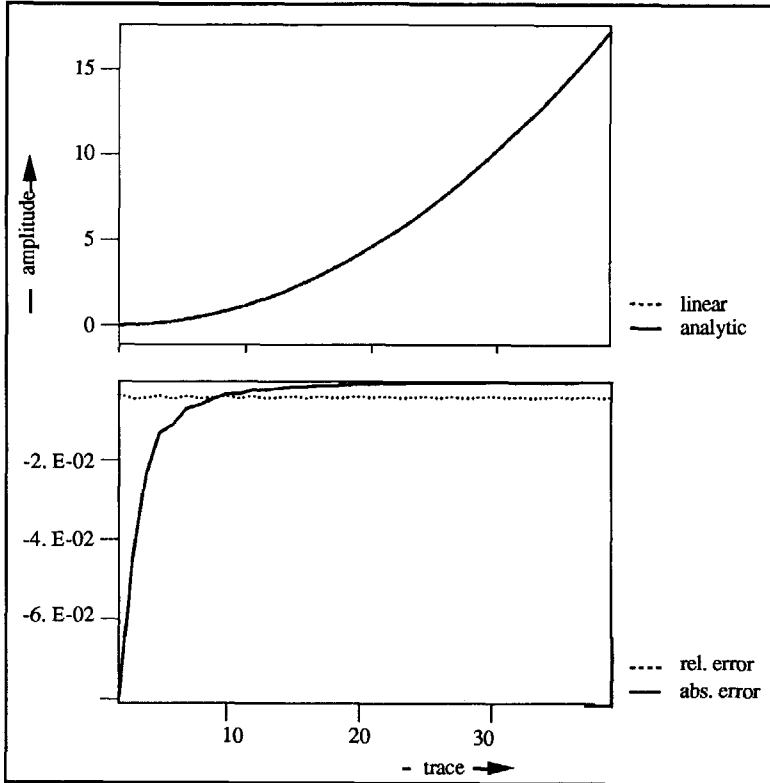


Fig.4.5.1: The oscillating behaviour of the linear interpolation procedure; (a) denotes the test function,  $f(x) = x^2$  and (b) presents the absolute and relative error;  $\Delta x_{\text{input}} = 0.2$  and  $\Delta x_{\text{output}} = 0.12$ .

Further, the complex frequency is also taken out of the transform because there is no need for it. That part of the  $t$ - $x$  data set which should map into the end of the elliptic and quasi-elliptic events and can cause errors is absent in field data. Therefore the elliptic and the quasi-elliptic events only approximate the ideal case where the events reach the refraction points.

#### 4.6 Synthetic data examples

To show the accuracy of the forward and inverse Radon transforms two synthetic data sets are presented. Of both examples the input data in  $t$ - $x$ , its  $\tau$ - $p$  response and the response after the forward and inverse Radon transform and the amplitude spectra in  $f$ - $x$  and in  $f$ - $p$  are depicted.

The results are shown for a line source configuration (2D) as well as for a point source configuration (3D). The main differences between the 2D and 3D situation is the decay of the amplitude related to increasing offset and the way the edge effects are treated, but this is extensively discussed in Chapter 5. The model parameters for the first example are  $\Delta x = 10$  m,  $\Delta t = 0.002$  s,  $\Delta p = 1.3$  ms/km and  $v_0 = 3000$  m/s. The number of spatial samples is chosen to be 256 and the number of temporal samples is 512. The wavelet used for the calculation is shown in Fig.4.6.1. In the chosen set-up of the model parameters, there is at least 150 Hz available in the  $\tau$ - $p$  response when  $\Delta x = 10$  m; it becomes a quarter of this (37 Hz.) when  $\Delta x = 40$  m.

Furthermore, the  $\tau$ - $p$  response of a data set is multiplied with  $-i\omega q$  ( $\omega$  denotes the angular frequency,  $q$  the vertical slowness and  $i$  the imaginary number) because the data set is integrated. This is inherent to a forward Radon transform (eq.(4.2.1)). From an interpretational point of view, it is convenient that the bandwidth of the data set in both domains remains the same as much as possible, which is established by this differentiation factor. When the  $\tau$ - $p$  response is transformed back to  $t$ - $x$ , the data set is divided by this factor in order to recover the original data set, as far as possible after the forward and inverse Radon transform. And this factor comes from the reflectivity method as part of the solution for the Green's function (eq.(A.1.10)).

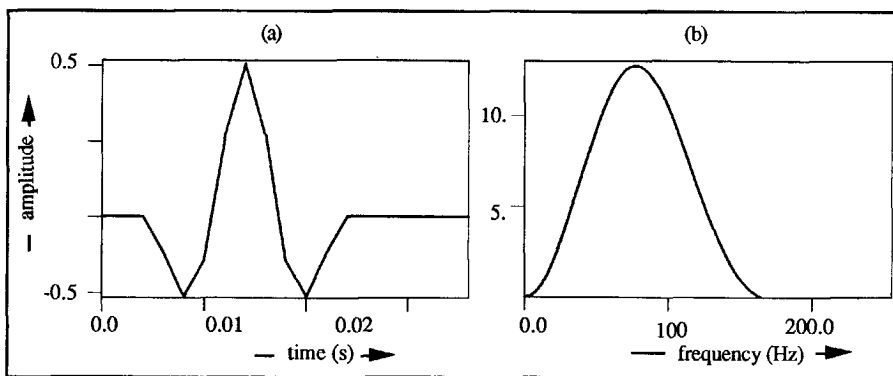


Fig.4.6.1: The wavelet: (a) its time response and (b) its amplitude spectrum.

Then in Fig.4.6.2 a seismogram of a hyperbolic event in  $t$ - $x$ , starting at zero offset (a) and its amplitude spectrum in  $f$ - $x$  (right hand side) are shown. The amplitude spectrum is represented by "iso-amplitude" contour lines. Figs.4.6.2b & 4.6.2c give the  $\tau$ - $p$  responses for the 3D and 2D configuration with their amplitude spectra respectively, and the elliptic events do not reach the critical point where  $p = 1 / v_0$ . This is explained in Chapter 5. At the amplitude spectra the changing frequency reduction per  $p$ -value following the orthogonal hyperbola is not visible, only the reduction due to the tapering in the spatial direction. Because the 2D Radon transform does not treat the  $t$ - $x$  data set correctly, due to a point source configuration, the edge effects are more severe. This holds in particular for the zero-offset trace, causing the edge effect to be horizontal (Fig.4.6.2c).



The responses after the forward and inverse Radon transform of the hyperbolic event (Figs.4.6.2d and 4.6.2e) show some decrease in resolution due to the frequency reduction (eq.(4.4.1)) and the tapering (eq.(4.4.3)). Again it is clear that a 2D Radon transform, applied to a  $t$ - $x$  data set, due to a point source gives worse results than a 3D Radon transform does.

The next data set (Fig.4.6.3) is composed of a quarter of the number of input traces of the data set shown in Fig.4.6.2, thus the receiver spacing is four times as large and a  $\Delta p = 5.2$  ms/km. Then the inevitable frequency reduction following the orthogonal hyperbola, depicted clearly in Figs.4.6.3a and 4.6.3b is more severe and lowers the resolution of Figs.4.6.3c & 4.6.3d (transformed back to  $t$ - $x$ ). Again the 2D transformed data set suffers more from the incorrect treatment of the source than the 3D transformed data set.

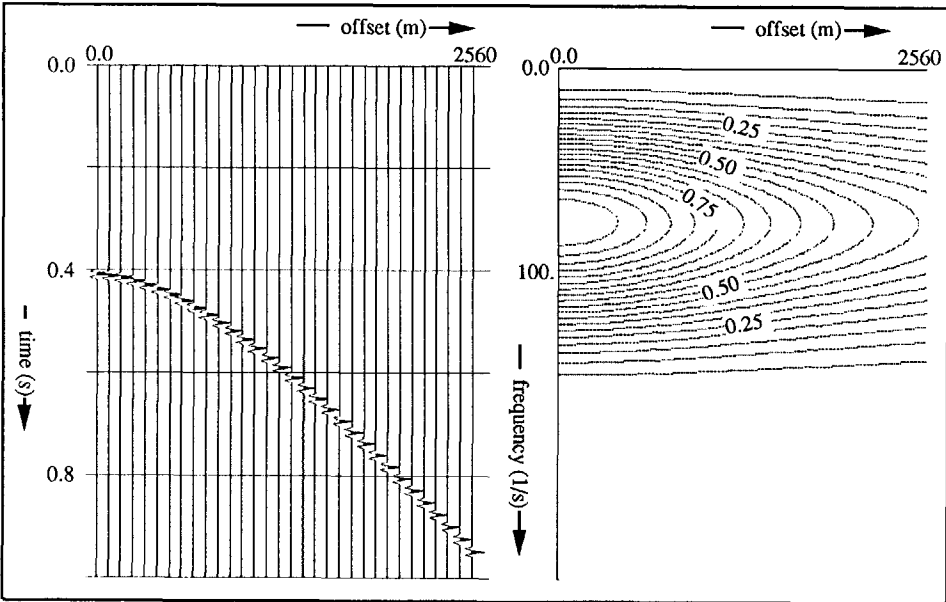


Fig.4.6.2a: A hyperbolic event, starting at zero-offset in  $t$ - $x$ ;  $\Delta x = 10$  m (256 input traces).

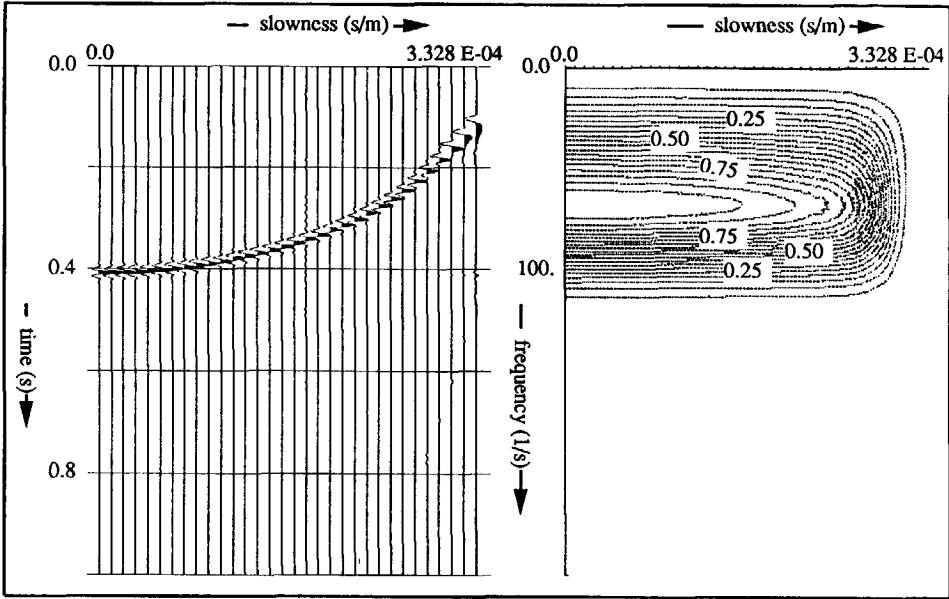


Fig.4.6.2b: The  $\tau$ - $p$  response (3D) of the hyperbolic event;  $\Delta p = 1.3$  ms/km (256 input traces).

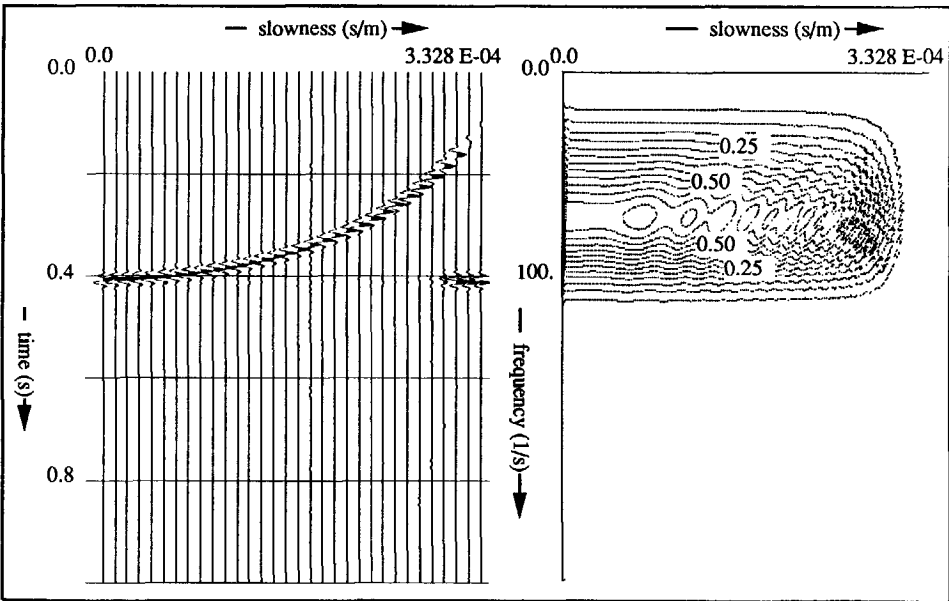


Fig.4.6.2c: The  $\tau$ - $p$  response (2D) of the hyperbolic event;  $\Delta p = 1.3$  ms/km (256 input traces).

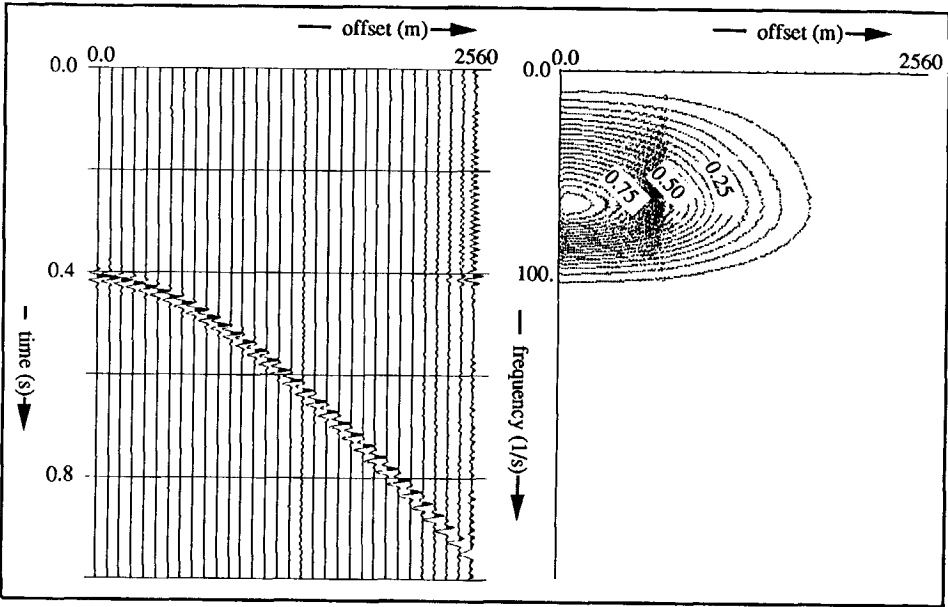


Fig.4.6.2d: The  $t$ - $x$  response (3D) of (b);  $\Delta x = 10$  m (256 input traces).

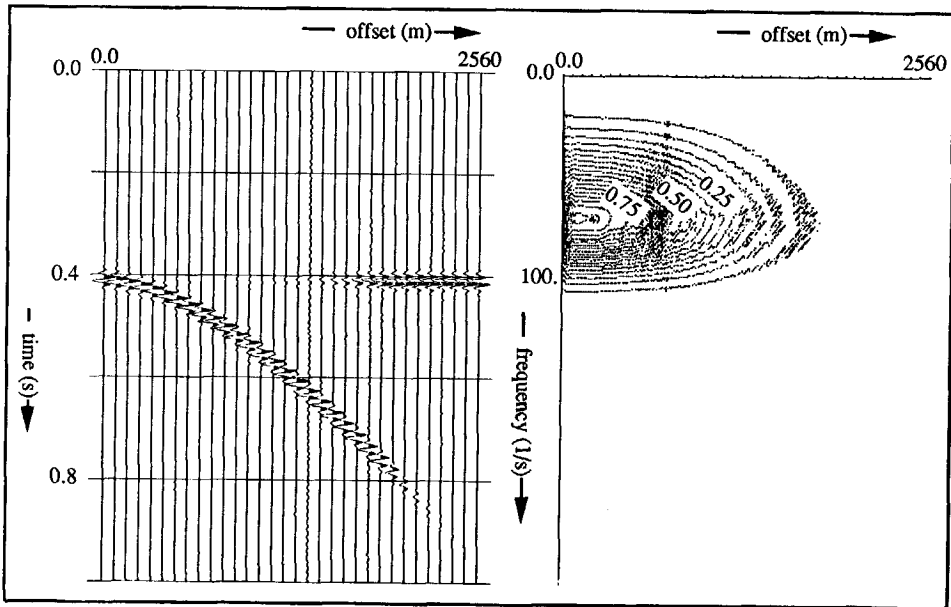


Fig.4.6.2e: The  $t$ - $x$  response (2D) of (c);  $\Delta x = 10$  m (256 input traces).

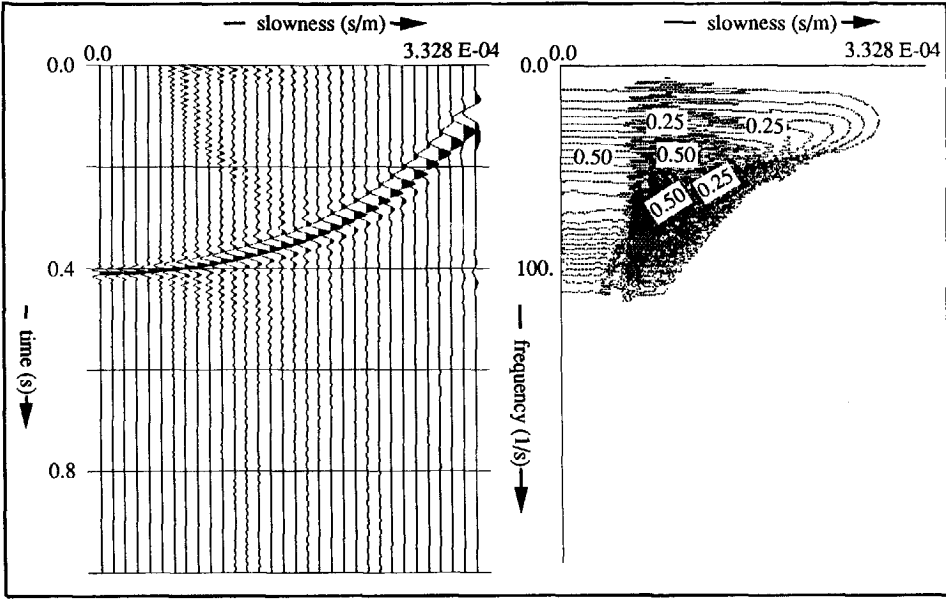


Fig.4.6.3a: The  $\tau$ - $p$  response (3D) of the hyperbolic event;  $\Delta p = 5.2$  ms/km ( $\Delta x = 40$  m, i.e. each 4-th trace of the  $t$ - $x$  section of Fig.4.6.2).

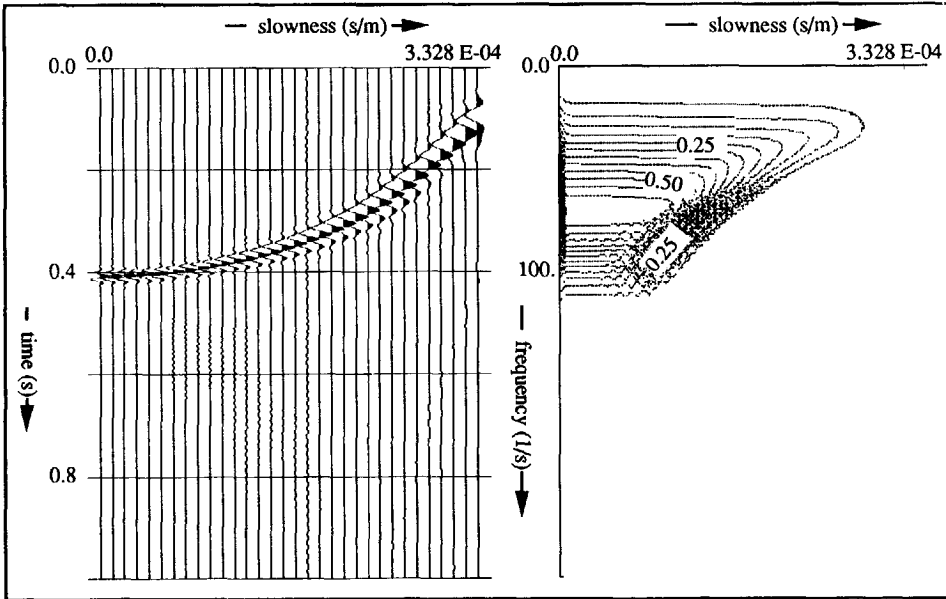


Fig.4.6.3b: The  $\tau$ - $p$  response (2D) of the hyperbolic event;  $\Delta p = 5.2$  ms/km ( $\Delta x = 40$  m, i.e. each 4-th trace of the  $t$ - $x$  section of Fig.4.6.2).

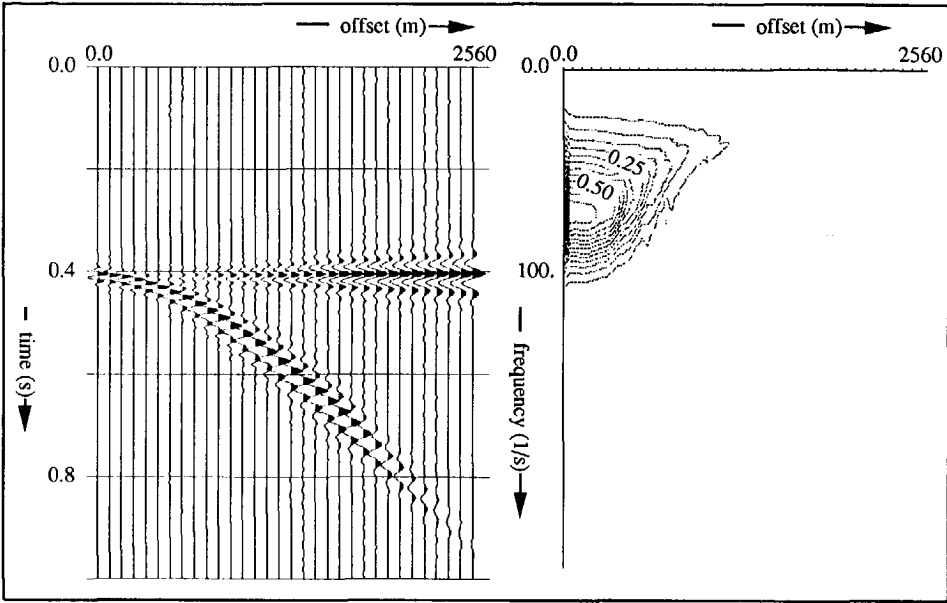


Fig.4.6.3c: The  $t$ - $x$  response (3D) of (a);  $\Delta x = 40$  m.

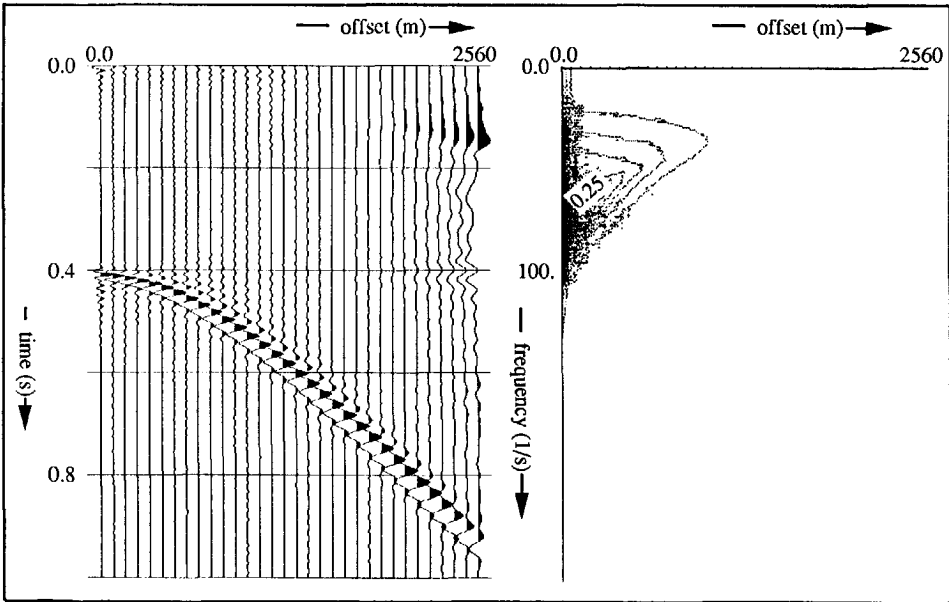


Fig.4.6.3d: The  $t$ - $x$  response (2D) of (b);  $\Delta x = 40$  m.

---

## CLASSIFICATION OF EVENTS IN THE $\tau$ - $p$ DOMAIN

---

### 5.1 Introduction

Now the events in the  $\tau$ - $p$  domain can be classified. If the arrival times only are considered, a seismic record in time and space may be regarded as a coherent set of events: hyperbolic, quasi-hyperbolic (primary and multiple reflections) and linear events (headwaves) are distinguished. After a proper plane-wave decomposition (eq.(4.2.12) or eq.(4.3.3)) the  $t$ - $x$  data are transformed into the  $\tau$ - $p$  domain. By applying an asymptotic expansion using the method of stationary phase (Båth, 1968, Felsen and Marcuvitz, 1973, Stokes and Kelvin, 1887; Erdélyi, 1956, Fuchs, 1971) it is shown that the hyperbolic and quasi-hyperbolic events map into the well-known elliptic and quasi-elliptic events (Vissinga et al., 1990).

However the linear events do not map into points as is suggested by the conventional point of view of the  $\tau$ - $p$  representation (Phinney, 1981, amongst others) because there are no stationary points in the transform integral. The major contribution to the value of the integral according to Stokes and Kelvin (1887) arises from the immediate vicinity of the endpoints of the integral. Consequently, a linear event in  $t$ - $x$  maps into two linear events in  $\tau$ - $p$  with a positive dip (up-dip) and a negative slope (down-dip) starting at the  $\tau$ -axis. The intercept time on the  $\tau$ -axis relates to the time value in the  $t$ - $x$  domain where the linear event starts, while the slope in  $\tau$ - $p$  represents the corresponding offset  $x$ . In the case of headwaves, the up-dip linear event is tangent to the ellipse at the focus point in the conventional view.

Furthermore, it will be shown that the positive and negative dip events for the point source configuration have a different temporal behaviour that is predicted by the theory. This knowledge allows us to interpret the linear events corresponding to headwaves in more detail. Specifically, the negative-dip events can be isolated either by  $f$ - $k$  filtering of the  $\tau$ - $p$  data or by taking only the negative offset of the transform integral into account. Since the data set is finite in space there are also edge effects. These discontinuities show the same behaviour as headwaves in the  $\tau$ - $p$  domain, so they also map into linear up-dip and down-dip events. These effects are

minimized by employing a suitable window in the  $t$ - $x$  domain. The linear events are often interpreted as artificial consequences of an imperfect plane-wave decomposition and therefore removed by filtering. However, after proper windowing in  $t$ - $x$ , the linear events that remain are headwaves and contain valuable information which should not be removed.

Section 5.2 starts with the equation for a hyperbolic event in  $f$ - $x$ , applies the forward Radon transform (for the 3D configuration, eq.(2.2.51)) to the event and employs an asymptotic expansion to arrive at the elliptic event. If the lower and upper limit of the spatial integral are replaced by more realistic numbers instead of the zero and infinite offset, one can calculate the range of reliable  $p$ -values in the  $\tau$ - $p$  response as well as the behaviour of the edge effects. The same procedure is also followed for a linear event (headwave) in section 5.3 and for a diffractor in section 5.4. Section 5.5 covers the edge effects. For the 2D configuration, the same events as for the 3D configuration are discussed and then the method of stationary phase is applied (only one integral has to be evaluated). Further, all equations representing the events in section 5.2–5.4 are given in the frequency domain since the phase function is as clear in the frequency domain representation as in the time domain representation. The amplitude factor is only an approximation and therefore not worth while transforming to the time domain. After that a summary is given of the main events in  $t$ - $x$  and their  $\tau$ - $p$  responses. The last section (5.6) discusses two marine data sets.

## 5.2 Hyperbolic event

Consider the model in Fig.5.2.1, where  $z$  denotes the thickness,  $v$  the rms velocity of the  $n$ -th layer and  $\theta$  the angle of incidence. Further, for the 3D configuration when cylindrical symmetry is assumed,  $x$  represents the horizontal component of the polar coordinate system. For the 2D configuration,  $x$  represents one of the horizontal components of the Cartesian coordinate system.

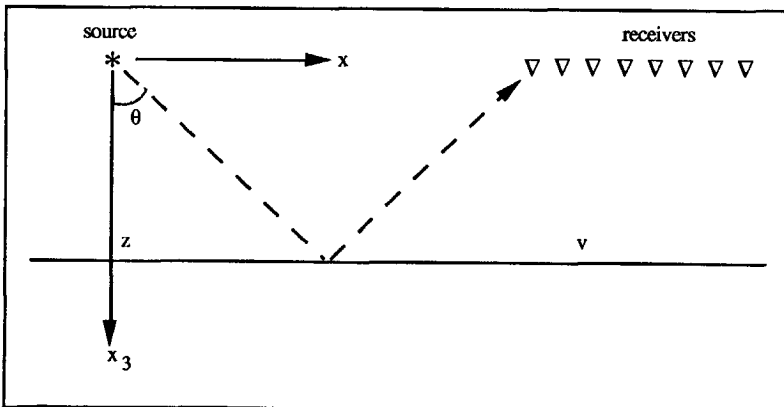


Fig.5.2.1: The  $x$ - $z$  model for the hyperbolic event.

This is valid for all the synthetic data examples.

A hyperbolic event in the  $f$ - $x$  domain is then formulated as

$$\hat{u}(x, f) = A(x) e^{i2\pi f \frac{\sqrt{4z^2 + x^2}}{v}}, \quad (5.2.1)$$

where  $A(x)$  represents some space dependent amplitude factor. The next step is to subject eq.(5.2.1) to the forward Radon transform following eq.(2.2.51) and this results in

$$\begin{aligned} \hat{u}(p, f) = 2 \left( \int_0^{+\infty} \int_0^{\pi/2} A(x) e^{i2\pi f \left\{ \frac{\sqrt{4z^2 + x^2}}{v} - px \cos \theta \right\}} d\theta x dx + \right. \\ \left. \int_0^{+\infty} \int_0^{\pi/2} A(x) e^{i2\pi f \left\{ \frac{\sqrt{4z^2 + x^2}}{v} + px \cos \theta \right\}} d\theta x dx \right), \end{aligned} \quad (5.2.2)$$

where the spatial integral is split into two parts. The method of stationary phase assumes that the major contribution to the integral comes from that region where the phase function is stationary on condition that the space dependent amplitude factor,  $A(x)$  is varying smoothly in that region. Since that condition is fulfilled and using eq.(A.2.11) and substituting the two stationary points, the phase function can be approximated by

$$h(p, x, \theta) = \frac{\sqrt{4z^2 + x^2}}{v} \pm px \cos \theta \approx 2zq + \frac{\theta^2}{2} \frac{2zp^2}{q} + \frac{(x-x_s)^2}{2} \frac{q^3 v^2}{2z}, \quad (5.2.3)$$

where  $x_s$  and  $\theta_s$ , given by

$$x_s = \frac{2zp}{q} \quad \text{and} \quad \theta_s = 0, \quad \text{with} \quad q = \sqrt{1/v^2 - p^2}, \quad (5.2.4)$$

are the stationary points where the first derivatives are zero. Note that the first-order terms are taken zero in eq.(5.2.3). Substituting now eq.(5.2.3) in the full integral (eq.(5.2.2)) results, according to Felsen and Marcuvitz (1973) and following eq.(A.2.14) finally in

$$\hat{u}(p, f) = A(x_s) \frac{i2z}{vfq^2} e^{i4\pi f z q}. \quad (5.2.5)$$

The spatial stationary point  $x_s$  is valid only for the first part of eq.(5.2.2), and not for the second part because the latter does not give a contribution. In the final result, eq.(5.2.5), the exponential term introduces the well-known elliptic move-out with the intercept time  $\tau = 2zq$ .



The result given in eq.(5.2.5) is based upon an infinite aperture. But what happens if the stationary point  $x_s$  falls outside the range of the integrals in eq.(5.2.2), i.e.  $x_{min} > x_s$ ? When, for example, the near-offset measurements are missing, the lower limit of the spatial integral in eq.(5.2.2) changes from 0 to  $x_{min}$

$$\hat{u}(p, f) = 2 \left( \int_{x_{min}}^{+\infty} \int_0^{\pi/2} A(x) e^{i2\pi f \left\{ \frac{\sqrt{4z^2 + x^2}}{v} - px \cos \theta \right\}} d\theta x dx + \int_{x_{min}}^{+\infty} \int_0^{\pi/2} A(x) e^{i2\pi f \left\{ \frac{\sqrt{4z^2 + x^2}}{v} + px \cos \theta \right\}} d\theta x dx \right). \quad (5.2.6)$$

Then, we take an expansion around the point where

$$\frac{\partial}{\partial \theta} h(p, x_{min}, \theta) \Big|_{\theta = \theta_s} = 0. \quad (5.2.7)$$

Now, we do not get a contribution of the spatial stationary point, only the end contributions. Then following eq.(A.2.11), the phase function is approximated by

$$h(p, x, \theta) \approx x_{min} \left( 1/v^2 p_{min} \pm p \right) + (x - x_{min}) (p_{min} \pm p) \pm \frac{\theta^2}{2} p x_{min}, \quad (5.2.8)$$

with

$$p_{min} = \frac{x_{min}}{v \sqrt{4z^2 + x_{min}^2}}. \quad (5.2.9)$$

Substituting the expansion of the phase function into eq.(5.2.6) and determining the amplitude factor using eqs.(A.2.12) - (A.2.14) then gives

$$\hat{u}(p, f) = A(x_{min}) \frac{1}{-i2\pi f} \sqrt{\frac{x_{min}}{-ifp}} \left[ \frac{e^{i2\pi f x_{min} (1/v^2 p_{min} - p)}}{p_{min} - p} + \frac{ie^{i2\pi f x_{min} (1/v^2 p_{min} + p)}}{p_{min} + p} \right], \quad 0 < p < p_{min}, \quad (5.2.10)$$

where the first exponential term has a contribution for negative  $p$ -values and the second exponential term for positive  $p$ -values. Note that the  $i$  in front of the second exponential term in eq.(5.2.10) is part of the contribution of the stationary point  $\theta_s$  to the principal value of the integral. Further, this approximation only holds for  $p \neq 0$  and, compared with eq.(5.2.5), the extra factor,  $\sqrt{1-iffp}$  results in a lower frequency contribution. In the exponential term, we recognise that the intercept time  $\tau = x_{min} (1/v^2 p_{min} \mp p)$ .

In eq.(5.2.8), we assumed that  $x_{min} > x_s$  but if  $x_{min}$  is very close to  $x_s$  neither the approximation shown in eq.(5.2.5) nor the approximation shown in eq.(5.2.10) applies. In order to determine the major contribution to the integral, we start again with eq.(5.2.6) but now the expansion of the phase function in eq.(5.2.3) is still valid instead of in eq.(5.2.8). Then, the evaluation of the spatial integral gives

$$\int_{x_{min}}^{+\infty} e^{i2\pi f \left\{ \frac{(x-x_s)^2}{2} \frac{q^3 v^2}{2z} \right\}} dx = e^{i\pi/4} \sqrt{\frac{2z}{fq^3 v^2}} \text{erfc}(x_{min}) . \quad (5.2.11)$$

where the error function,  $\text{erfc}(x_{min})$  is given in Abramowitz (1965, p. 297). The final result is obtained as

$$\widehat{u}(pf) = A(x_s) \frac{i2z}{vfq^2} e^{i4\pi f z q} \text{erfc}(x_{min}) , \quad (5.2.12)$$

only differing from eq.(5.2.5) by the error function. The same procedure can also be followed when the infinity sign of the upper limit is changed into  $x_{max}$  and then in eqs.(5.2.10) and (5.2.12)  $x_{min}$  are replaced by  $x_{max}$ .

Now, taking into account the influence of a limited aperture (eq.(5.2.10)), one can quantify the reliable  $p$ -values in the  $\tau$ - $p$  seismogram. Given the velocity distribution of the input data and the minimum and maximum offset  $x_{min}$  and  $x_{max}$ , the reliable  $p$ -values are, due to eq.(5.2.4), restricted to

$$\frac{x_{min}}{v \sqrt{4z^2 + x_{min}^2}} \leq p \leq \frac{x_{max}}{v \sqrt{4z^2 + x_{max}^2}} , \quad (5.2.13)$$

which, after substitution of

$$2z = \frac{\tau}{q} = \frac{\tau v}{\sqrt{1 - (pv)^2}} , \quad (5.2.14)$$

into eq.(5.2.4) may be rewritten as

$$\sqrt{\frac{1}{v^2} + \frac{\tau^2}{4x_{min}^2}} - \frac{\tau}{2x_{min}} \leq p \leq \sqrt{\frac{1}{v^2} + \frac{\tau^2}{4x_{max}^2}} - \frac{\tau}{2x_{max}}. \quad (5.2.15)$$

As soon as  $p$  falls outside the range of eq.(5.2.15) as a result of the limitation of the input data, eqs.(5.2.10) and (5.2.12) become valid and when  $x_{min} > x_s$  the elliptic event is no longer "elliptic" but turns into two linear events both starting at the  $\tau$ -axis. One is tangent to the elliptic event at the stationary point and the other has the same but opposite dip. The linear event being tangent to the elliptic event is proven as

$$\lim_{x_s \downarrow x_{min}} \frac{\partial \tau}{\partial p} \{2zq\} = \lim_{x \uparrow x_{min}} \frac{\partial \tau}{\partial p} \left\{ x_{min} \left( 1/v^2 p_{min} - p \right) \right\} = -x_{min}, \quad (5.2.16)$$

and

$$\lim_{x_s \downarrow x_{min}} 2zq = \lim_{x \uparrow x_{min}} x_{min} \left( 1/v^2 p_{min} - p \right). \quad (5.2.17)$$

Mitchell and Kelamis (1990) also quantify which  $p$ -values should be reliable with respect to the spatial aperture and to the estimated velocity model of the input data. Their result is almost the same as eq.(5.2.15) although their derivation runs along different lines. They start with the traveltine equation for a hyperbolic event

$$t^2 = \frac{\sqrt{4z^2 + x^2}}{v}. \quad (5.2.18)$$

Then they obtain the slowness  $p$  by differentiating with respect to the spatial coordinate

$$p = \frac{\partial t}{\partial x} = \frac{x}{tv^2}. \quad (5.2.19)$$

Next, they replace  $t = \tau + px$  into the expression for  $p$  (eq.(5.2.19)) and end up with

$$|p| \leq \sqrt{\frac{1}{v^2} + \frac{\tau^2}{4x^2}} - \frac{\tau}{2x}. \quad (5.2.20)$$

By associating a stacking velocity range ( $v_{min}, v_{max}$ ) with each  $(t, x)$  point, a limited range of  $p$ -values can be determined from eq.(5.2.19) by the inequalities

$$\frac{x}{tv_{min}} \leq p \leq \frac{x}{tv_{max}} \quad (5.2.21)$$

The velocity values,  $v_{min}$  and  $v_{max}$  associated with the point  $(t, x)$  are chosen such that all possible stacking velocities associated with that point are within the chosen range. Therefore the inequalities in eq.(5.2.20) change into

$$\sqrt{\frac{1}{v_{max}^2} + \frac{\tau^2}{4x^2}} - \frac{\tau}{2x} \leq p \leq \sqrt{\frac{1}{v_{min}^2} + \frac{\tau^2}{4x^2}} - \frac{\tau}{2x} \quad (5.2.22)$$

Then, by fixing the offset  $x$ , the inequalities of eq.(5.2.22) may be interpreted as a mute pattern in  $\tau$ - $p$ , which is convenient when a slant stack algorithm is performed.

Given a generated data set in the  $\tau$ - $p$  domain with a certain  $p_{min}$  and  $p_{max}$ , the same procedure can be followed to calculate the reliable  $x$ -values in the back transformed  $\tau$ - $p$  data set. Then starting from eq.(5.2.5) and applying the inverse Radon transform (eq.(2.2.51)), the first-order derivative of the phase function with respect to the slowness  $p$  is given by

$$\frac{\partial}{\partial p} h(p, x, \theta) = \frac{-2zp}{\sqrt{1/v^2 - p^2}} + x \cos \theta_s = 0 \quad \text{with } \theta_s = 0, \quad (5.2.23)$$

where after rewriting its stationary point defines the reliable offset range as

$$\frac{2zp_{min}}{\sqrt{1/v^2 - p_{min}^2}} \leq x \leq \frac{2zp_{max}}{\sqrt{1/v^2 - p_{max}^2}} \quad (5.2.24)$$

Then, substituting  $p_{min}$  and  $p_{max}$  due to eq.(5.2.13) into the inequalities of eq.(5.2.24), we notice that there is a unique relation between  $x_{min}$  and  $p_{min}$  and  $x_{max}$  and  $p_{max}$  respectively.

For the 2D configuration, the Bessel function is absent and eq.(5.2.2) becomes

$$\begin{aligned} \hat{u}(p, f) = \int_0^\infty A(x) e^{i2\pi f \frac{\sqrt{4z^2 + x^2}}{v} - i2\pi f p x} dx + \\ \int_0^\infty A(x) e^{i2\pi f \frac{\sqrt{4z^2 + x^2}}{v} + i2\pi f p x} dx \end{aligned} \quad (5.2.25)$$

Then applying the method of stationary phase (A.2.7), the final result yields

$$\hat{u}(p, f) = A(x_s) \sqrt{\frac{i2z}{f v^2 q^3}} e^{i4\pi f z q} \quad (5.2.26)$$

When the aperture is not infinite, the same procedure as for the point source configuration can be followed. Then eq.(5.2.10) changes into

$$\hat{u}(p, f) = A(x_{min}) \left[ e^{i2\pi f x_{min} (1/v^2 p_{min} - p)} + e^{i2\pi f x_{min} (1/v^2 p_{min} + p)} \right], \quad (5.2.27)$$

where  $p_{min}$  is given in eq.(5.2.9). The differences with eq.(5.2.10) are the absence of the  $i$  in front of the second exponential term, and a scaling factor.

In order to support the theory, some synthetic data sets are generated for both the 2D as well as the 3D configuration. The Radon transform used is given in Chapter 4. In all the synthetic examples the model parameters are the same:  $\Delta t$  is 2 ms,  $\Delta x$  is 10 m except for the diffractor event ( $\Delta x$  is 12.5 m), the depth of the interface is 600 m and the velocity is chosen to be 3000 m/s. For the transform there are 256 spatial and 512 temporal sample points taken into account. All pictures are plotted and scaled relative to the maximum value of each trace. The wavelet to generate the synthetic data is shown in Fig.5.2.2 as well as its Hilbert transform. Note that the latter becomes non-causal due to discretization.

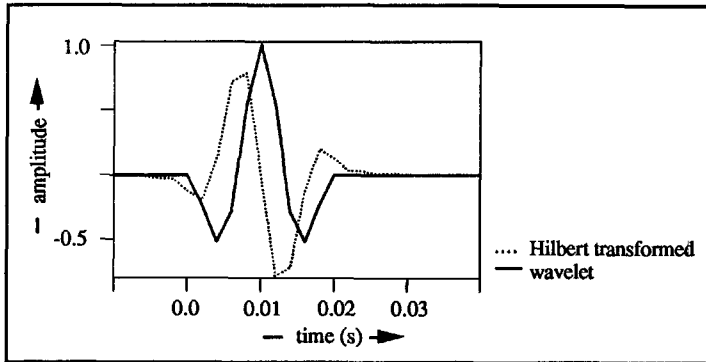


Fig.5.2.2: The time response of the wavelet (solid line) and its Hilbert transform (dashed line).

The first example, Fig.5.2.3a shows a reflection hyperbola with the first offset at 400 m. As expected, the reflection hyperbola turns into an ellipse (Figs.5.2.3b & 5.2.3c). However, because the offset of the data set is non-zero and finite, the curvature of the beginning of the ellipse is incorrect and the ellipse does not reach the critical point. The linear up-dip and down-dip events resulting from the lack of zero offset, are Hilbert transforms of each other according

to the theory. Then following eq.(5.2.13), the reliable  $p$ -range of the  $\tau$ - $p$  response is between the  $p$ -values  $1.04 \cdot 10^{-5}$  and  $3.02 \cdot 10^{-4}$  (Fig.5.2.3e). Further, the curvature of the ellipse at the  $p$ -value of  $3.02 \cdot 10^{-4}$  shades off into the up-dip linear event, which is tangent to the local curvature of the ellipse at that particular  $p$ -value (eq.(5.2.16)).

Fig.5.2.3d shows the result of the inverse transform applied to Fig.5.2.3c and Fig.5.2.3f displays the result of the inverse transform applied to Fig.5.2.3e. The edge effects in both back transformed seismograms differ. When eq.(5.2.13) is ignored the first 4 traces of the back transformed seismogram show only noise and no signal since it was never present in the first place. Further, the signal in the far offset is rather weak and has become smaller than the edge effect of the first  $p$ -trace. This edge effect is horizontal because its  $p_{min} = 0$ . Looking at the edge effects in Fig.5.2.3f, their amplitude in the first 4 traces is larger than the noise, present in Fig.5.2.3d and again there is an up-dip and down-dip linear event because in the latter case its  $p_{min} \neq 0$ . Despite the different edge effects, both the back transformed seismograms show the same decrease in resolution due the Radon transform.

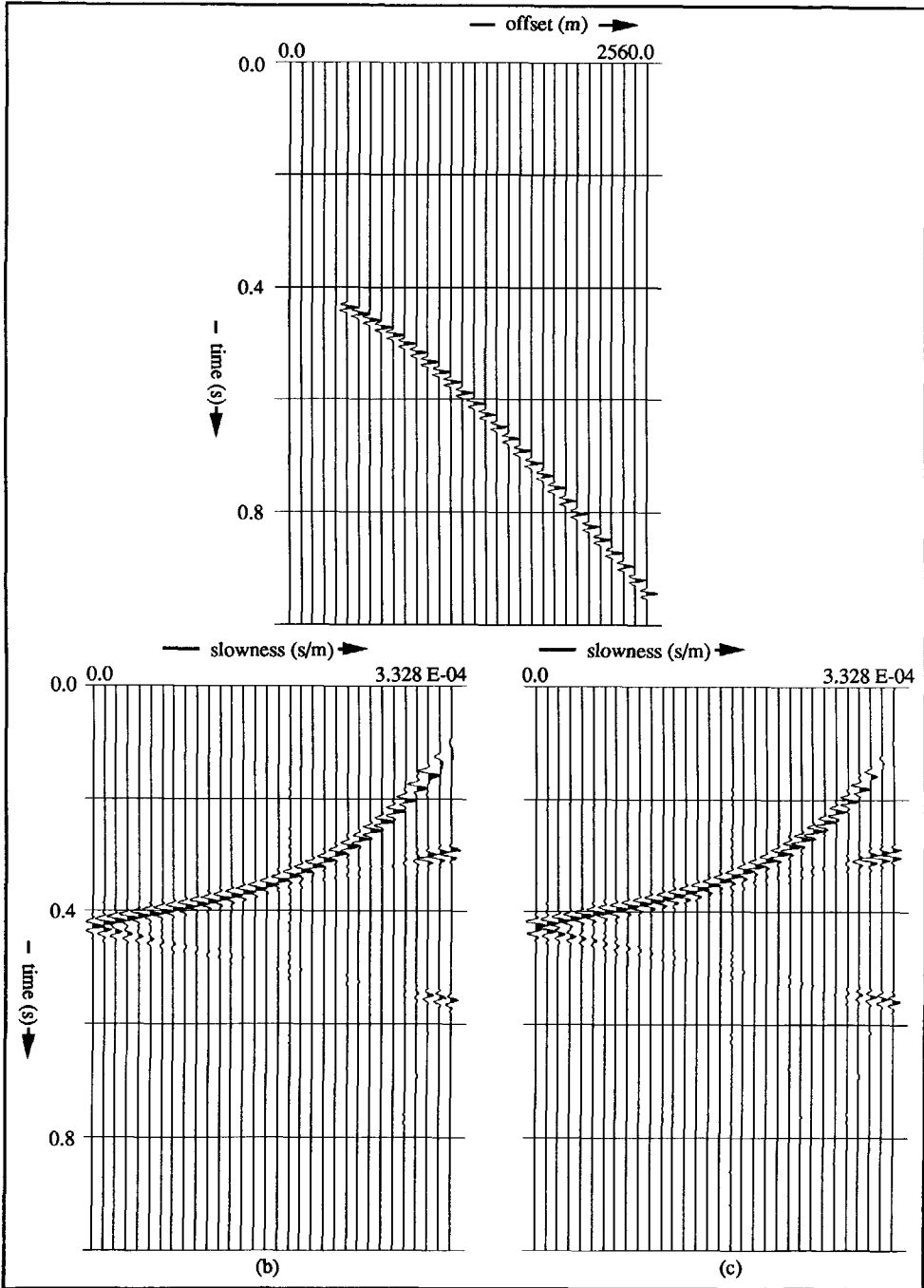


Fig.5.2.3: (a) A reflection hyperbola in  $t$ - $x$ , and its  $\tau$ - $p$  response; (b) the 3D response and (c) the 2D response;  $p_{max} = 1/3000$  s/m,  $\Delta x = 10$  m and first offset = 400 m.

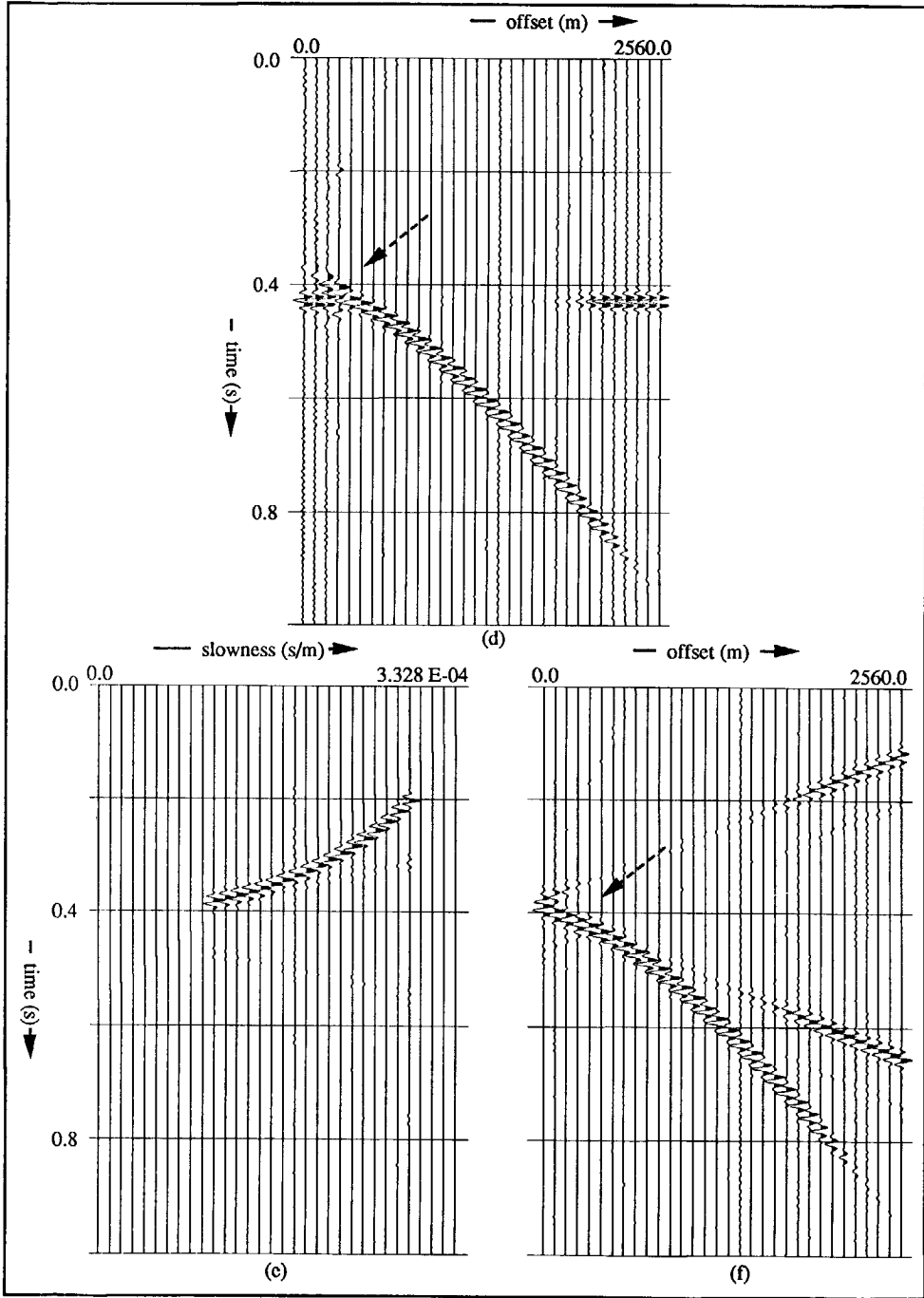


Fig.5.2.3: (d) The  $t$ - $x$  response of (c), 2D inverse transformed, (e) the reliable  $p$ -range of (c) and (f) the  $t$ - $x$  response of (e), 2D inverse transformed;  $p_{\max} = 1/3000 \text{ s/m}$ ,  $\Delta x = 10 \text{ m}$ .



### 5.3 Linear event

The next step is to derive the  $\tau$ - $p$  response of a linear event (for example, a headwave in  $t$ - $x$ ). The configuration is shown below.

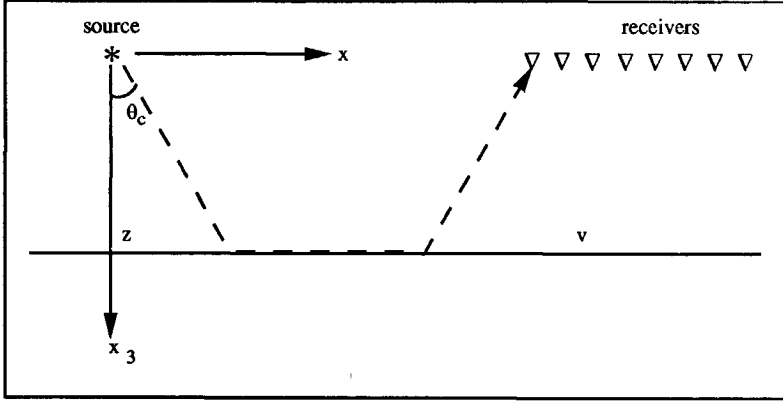


Fig.5.3.1: The  $x$ - $z$  model for the headwave.

Suppose the linear event, for example the headwave is presented in the  $f$ - $x$  domain as

$$\begin{aligned} \hat{u}(x, f) &= A(x) e^{i2\pi f \left( \tau_c + \frac{x}{v} \right)}, \quad \text{for } x > x_c \\ &= 0, \quad \text{for } x \leq x_c, \end{aligned} \quad (5.3.1)$$

and exists only for  $x$ -values larger than the critical distance  $x_c$ . Next, the forward Radon transform according to eq.(2.2.51) is applied and results in

$$\begin{aligned} \hat{\hat{u}}(p, f) &= 2 \left( \int_0^{\pi/2} d\theta \int_{x_c}^{\infty} A(x) e^{i2\pi f \left\{ x \left( \frac{1}{v} - p \cos \theta \right) + \tau_c \right\}} x dx + \right. \\ &\quad \left. \int_0^{\pi/2} d\theta \int_{x_c}^{\infty} A(x) e^{i2\pi f \left\{ x \left( \frac{1}{v} + p \cos \theta \right) + \tau_c \right\}} x dx \right). \end{aligned} \quad (5.3.2)$$

Note that the lower boundary of the integral is  $x_c$ , and only the angular stationary point is present. The spatial stationary point is absent, therefore we do not use the stationary phase method. The next step is to introduce a new variable of integration,  $\tau = x \left( 1/v \pm p \cos \theta \right) + \tau_c$ , leading to

$$\hat{u}(p, f) = 2 \left( \int_0^{\pi/2} \frac{d\theta}{\left(\frac{l}{v} - p \cos \theta\right)^2} \int_{x_c \left(\frac{l}{v} - p \cos \theta\right) + \tau_c}^{\infty} (\tau - \tau_c) \bar{A}^-(\tau, \theta) e^{i2\pi f \tau} d\tau + \right. \\ \left. \int_0^{\pi/2} \frac{d\theta}{\left(\frac{l}{v} + p \cos \theta\right)^2} \int_{x_c \left(\frac{l}{v} + p \cos \theta\right) + \tau_c}^{\infty} (\tau - \tau_c) \bar{A}^+(\tau, \theta) e^{i2\pi f \tau} d\tau \right), \quad (5.3.3)$$

where

$$\bar{A}^{\pm}(\tau, \theta) = A \left( \frac{\tau - \tau_c}{\left(\frac{l}{v} \pm p \cos \theta\right)} \right). \quad (5.3.4)$$

The minus sign of eq.(5.3.4) is used for the first part of eq.(5.3.3), derived from the first part of eq.(5.3.2) where the phase function in the spatial exponent is negative and the plus sign is used for the second part of eq.(5.3.3). Then, we split up the integration path into two parts and change the order of integration

$$\hat{u}(p, f) = 2 \left( \int_{x_c \left(\frac{l}{v} - p\right) + \tau_c}^{\frac{x_c}{v} + \tau_c} (\tau - \tau_c) e^{i2\pi f \tau} d\tau \int_0^{\theta_e(\tau)} \frac{\bar{A}^-(\tau, \theta) d\theta}{\left(\frac{l}{v} - p \cos \theta\right)^2} + \right. \\ \left. \int_{\frac{x_c}{v} + \tau_c}^{\infty} (\tau - \tau_c) e^{i2\pi f \tau} d\tau \int_0^{\pi/2} \frac{\bar{A}^-(\tau, \theta) d\theta}{\left(\frac{l}{v} - p \cos \theta\right)^2} + \right. \\ \left. \int_{x_c \left(\frac{l}{v} + p\right) + \tau_c}^{\frac{x_c}{v} + \tau_c} (\tau - \tau_c) e^{i2\pi f \tau} d\tau \int_0^{\theta_e(\tau)} \frac{\bar{A}^+(\tau, \theta) d\theta}{\left(\frac{l}{v} + p \cos \theta\right)^2} + \right. \\ \left. \int_{\frac{x_c}{v} + \tau_c}^{\infty} (\tau - \tau_c) e^{i2\pi f \tau} d\tau \int_0^{\pi/2} \frac{\bar{A}^+(\tau, \theta) d\theta}{\left(\frac{l}{v} + p \cos \theta\right)^2} \right). \quad (5.3.5)$$

where the angular integration limit  $\theta_e(\tau)$  is given by

$$\theta_e(\tau) = \arccos \left( \mp \frac{l}{p} \left( \frac{l}{v} + \frac{\tau_c - \tau}{x_c} \right) \right). \quad (5.3.6)$$

Since we are not interested at the amplitude factor but only at the timing of the event in  $\tau$ - $p$ , we rewrite eq.(5.3.5) as

$$\begin{aligned} \hat{u}(p, f) = & \int_{x_c \left( \frac{l}{v} - p \right) + \tau_c}^{\infty} E^-(\tau) e^{i2\pi f \tau} d\tau + \\ & \int_{x_c \left( \frac{l}{v} + p \right) + \tau_c}^{\infty} E^+(\tau) e^{i2\pi f \tau} d\tau, \end{aligned} \quad (5.3.7)$$

and recognize the representation of the Fourier transform. The arrival times of the linear events are given by the lower limit of the integrals and the overall amplitude function is captured by  $E^\pm(\tau)$ , representing the angular integral. Further, the first integral of eq.(5.3.7) represents the up-dip linear event and the second integral denotes the down-dip linear event. And, the factor  $px_c$ , shown at the lower limit of the integral gives the slope of the linear events which implies that they become steeper as  $x_c$  gets larger.

For the 2D configuration, eq.(5.3.2) changes into

$$\hat{u}(p, f) = \int_{x_c}^{\infty} A(x) e^{i2\pi f \left( \frac{x}{v} - px + \tau_c \right)} dx + \int_{x_c}^{\infty} A(x) e^{i2\pi f \left( \frac{x}{v} + px + \tau_c \right)} dx, \quad (5.3.8)$$

and introducing a new variable of integration,  $\tau = x(l/v \pm p) + \tau_c$  the final result is given by

$$\hat{u}(p, f) = \int_{x_c \left( \frac{l}{v} - p \right) + \tau_c}^{\infty} \frac{\bar{A}^-(\tau)}{\left( \frac{l}{v} - p \right)} e^{i2\pi f \tau} d\tau + \int_{x_c \left( \frac{l}{v} + p \right) + \tau_c}^{\infty} \frac{\bar{A}^+(\tau)}{\left( \frac{l}{v} + p \right)} e^{i2\pi f \tau} d\tau, \quad (5.3.9)$$

where

$$\bar{A}^\pm(\tau) = A \left( \frac{\tau - \tau_c}{\left( \frac{l}{v} \pm p \right)} \right). \quad (5.3.10)$$

The minus sign of eq.(5.3.10) is used for the first integral of eq.(5.3.9), and the plus sign is used for the second integral of eq.(5.3.10). When comparing eq.(5.3.9) with eq.(5.3.7), we notice that the arrival times of the linear events, given by the lower limit of the integral are the same, but the amplitude factor is different.

The next example, Fig.5.3.2 exhibits a linear event in  $t$ - $x$  and its  $\tau$ - $p$  response. The linear event in  $t$ - $x$  does not start at offset equals zero but at offset equals 400 m. Its  $\tau$ - $p$  response shows two linear events as predicted by our theory and the up-dip and down-dip have an equal but opposite slope. The  $\tau$ -value for  $p = 0$  is the same as the  $t$ -value at which the linear event in  $t$ - $x$  starts to exist and the dip of the linear events in  $\tau$ - $p$  corresponds to the offset of the linear event in  $t$ - $x$ . When a linear event in  $t$ - $x$  starts at zero offset, its  $\tau$ - $p$  response collapses into one horizontal linear event, which is shown in Fig.5.3.3.

Furthermore, the down-dip linear events in the previous examples can easily be omitted by, for example, changing eq.(5.3.2) into

$$\hat{u}(p, f) = 2 \int_0^{\pi/2} d\theta \int_{x_c}^{\infty} A(x) e^{i2\pi f \left\{ x \left( \frac{1}{v} - p \cos \theta \right) + \tau_c \right\}} x dx . \quad (5.3.11)$$

As a consequence, the second term in the final result of eq.(5.3.7) is lost. In the following example, Fig.5.3.4b shows the result of this omission. The same parameters are used as for Fig.5.3.2 and only the 3D configuration is calculated. The up-dip linear event can be dropped in the same way, but then the elliptic and quasi-elliptic events, if present, are dropped as well unfortunately. Fig.5.3.4c shows the down-dip linear event only.

In order to prove that a headwave in  $t$ - $x$  transforms into two linear events in  $\tau$ - $p$ , a point source response is calculated with the exact Cagniard-De Hoop technique (Drijkoningen and Fokkema, 1987). The same model parameters are used as for the hyperbolic event in Fig.5.2.1. Then, the  $t$ - $x$  response is shown at the upper part of Fig.5.3.5 and its  $\tau$ - $p$  response at the bottom. The trace at which the headwave starts is indicated by an arrow. This  $t_c$ -value indicates the intercept time on the  $\tau$ -axis which gives the starting time of the headwave and is clearly visible in Fig.5.3.5b.

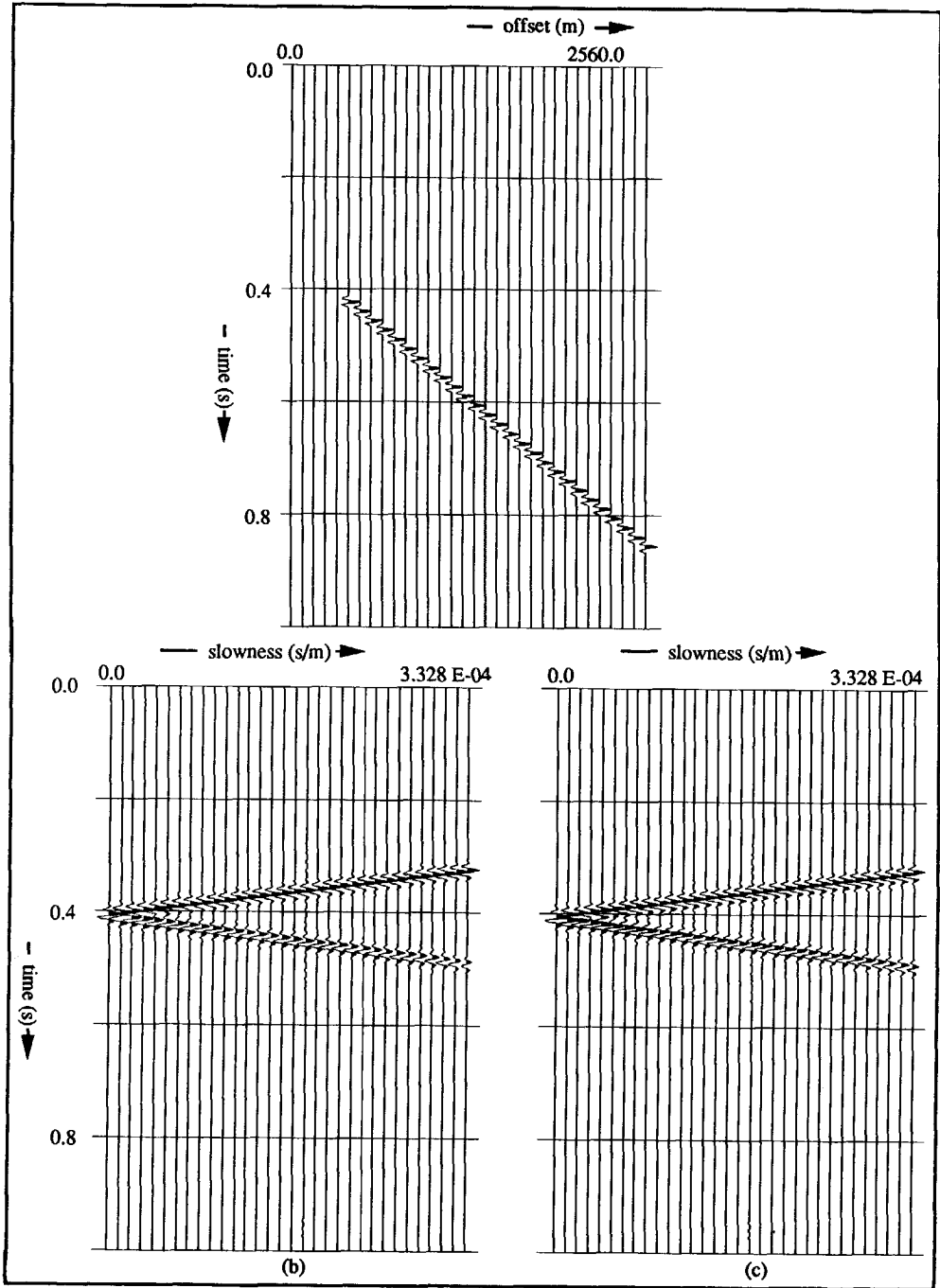


Fig.5.3.2: (a) A linear event in  $t$ - $x$  with offset = 400 m and its  $\tau$ - $p$  response: (b) the 3D response and (c) the 2D response;  $p_{max} = 1/3000 \text{ s/m}$ .

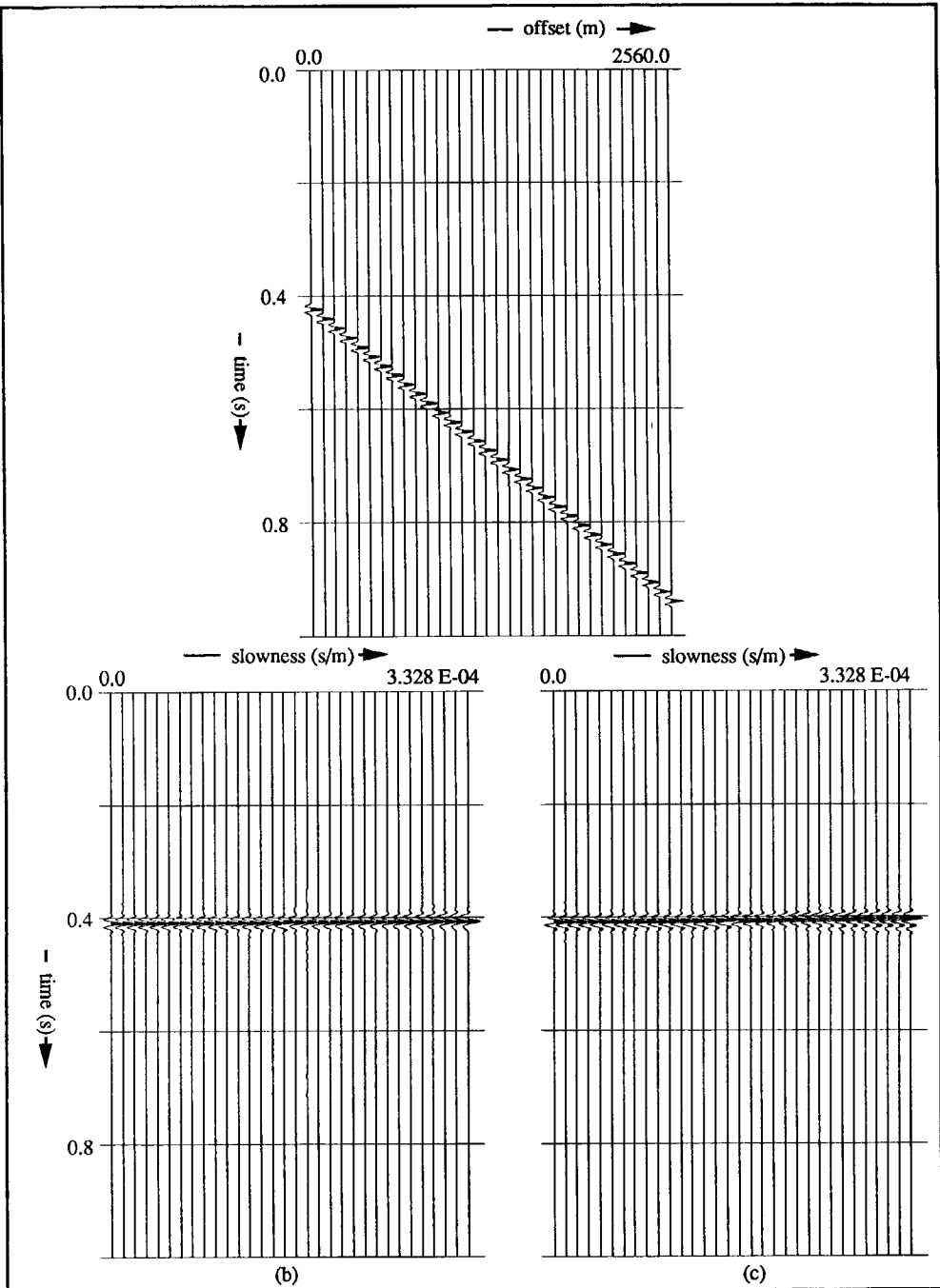


Fig.5.3.3: (a) A linear event in  $t$ - $x$  with zero offset and its  $\tau$ - $p$  response: (b) the 3D response and (c) the 2D response;  $p_{max} = 1/3000$  s/m.

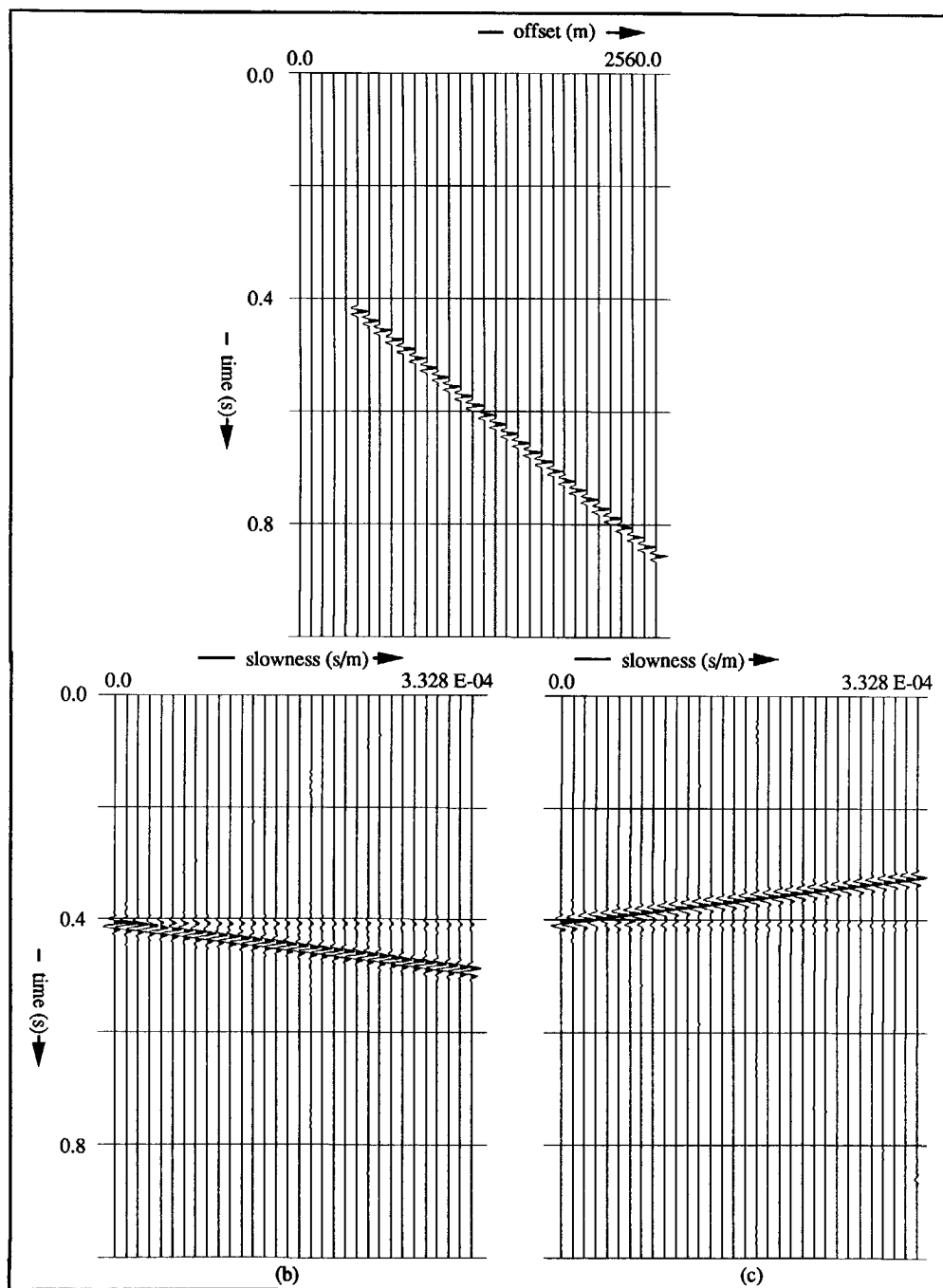


Fig.5.3.4: (a) A linear event in  $t$ - $x$  with offset = 400 m and its  $\tau$ - $p$  response: (b) the 3D response for positive offset only and (c) the 3D response for negative offset only;  $p_{\max} = 1/3000$  s/m.

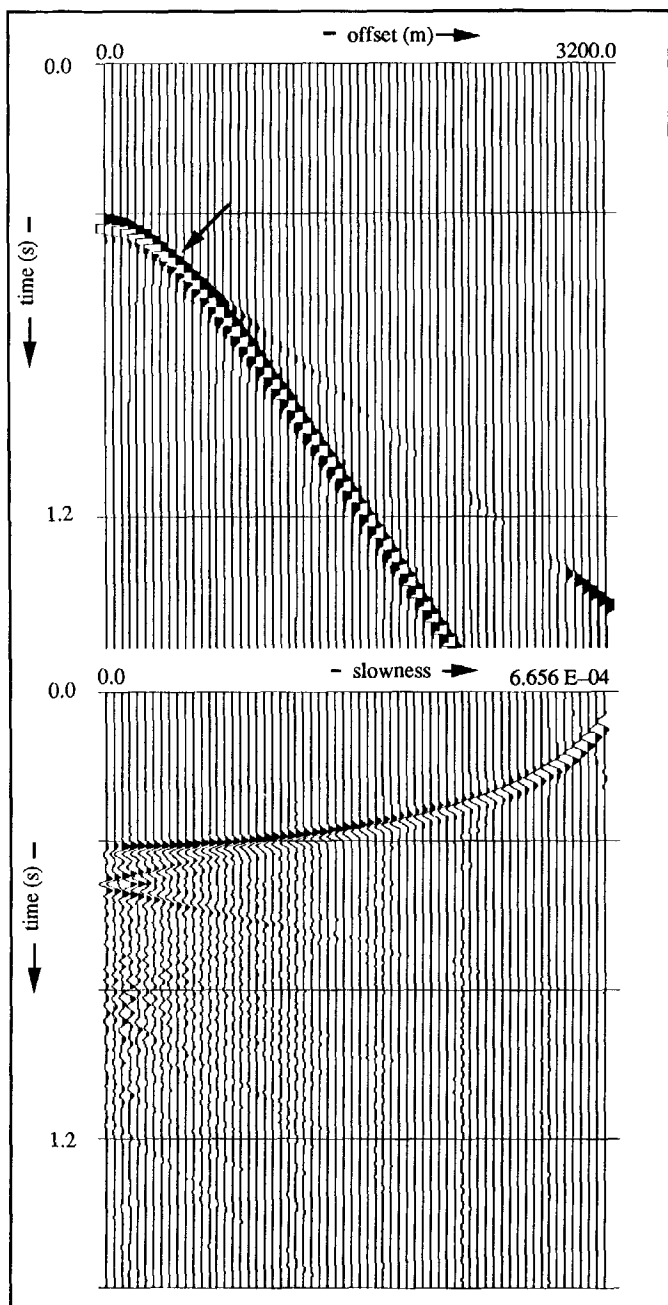


Fig.5.3.5: The point source response of a reflector: (a) the  $t$ - $x$  response and (b) its  $\tau$ - $p$  response.



### 5.4 Diffractor

Given the following configuration,

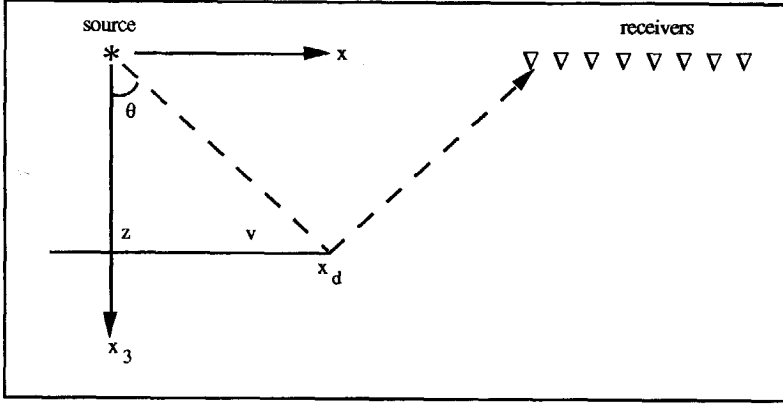


Fig.5.4.1: The  $x$ - $z$  model for the diffractor.

a diffractor in the  $f$ - $x$  domain may be formulated as

$$\hat{u}(x, f) = A(x) e^{i2\pi f \frac{\sqrt{4z^2 + (x-x_d)^2}}{v}}, \quad (5.4.1)$$

where  $x_d$  denotes the diffraction point. Note that if  $x_d = 0$ , eq.(5.4.1) becomes eq.(5.2.1). The next step is to apply the forward Radon transform following eq.(2.2.51) on eq.(5.4.1) and this results in

$$\begin{aligned} \hat{u}(p, f) = 2 \left( \int_0^\infty \int_0^{\pi/2} A(x) e^{i2\pi f \left\{ \frac{\sqrt{4z^2 + (x-x_d)^2}}{v} - px \cos \theta \right\}} d\theta x dx + \right. \\ \left. \int_0^\infty \int_0^{\pi/2} A(x) e^{i2\pi f \left\{ \frac{\sqrt{4z^2 + (x-x_d)^2}}{v} + px \cos \theta \right\}} d\theta x dx \right). \end{aligned} \quad (5.4.2)$$

Then following eq.(5.2.3), the expansion of the phase function gives

$$\begin{aligned} h(p, x, \theta) = \frac{\sqrt{4z^2 + (x-x_d)^2}}{v} \pm px \cos \theta \approx \{2zq \pm px_d\} + \\ \frac{\theta^2}{2} \left\{ \frac{2zp^2}{q} \pm px_d \right\} + \frac{(x-x_s)^2}{2} \frac{q^3 v^2}{2z}, \end{aligned} \quad (5.4.3)$$

substituting this in eq.(5.4.2) and employing the asymptotic expansion (eq.(A.2.14)), the following result is obtained

$$\widehat{u}(p, f) = \frac{i2z \sqrt{Q}}{vfq^2} A(x_s) \left[ e^{i2\pi f \{2zq - px_d\}} + e^{i2\pi f \{2zq + px_d\}} \right]. \quad (5.4.4)$$

The factor  $Q$  is given by

$$Q = 1 + \frac{qx_d}{2zp}$$

and, the three stationary points by

$$x_s = x_d \pm \frac{2zp}{q} \quad \text{and} \quad \theta_s = 0. \quad (5.4.5)$$

The plus sign of the spatial stationary points is valid for the first part (negative  $p$ -values) and the minus sign applies for the second part (positive  $p$ -values) of eq.(5.4.2). In the final result (eq.(5.4.4)), the exponential factor no longer exhibits the well-known ellipse but another curve with a shift according to the factor  $px_d$ . And there are two contributions as opposed to the hyperbolic event because both parts of eq.(5.4.2) give a contribution. The numerator of the scaling factor consists of two parts in which the first part represents the known scaling factor for the hyperbolic event in eq.(5.2.5) and the second part denotes the extra factor for the diffractor.

For the diffraction hyperbola for the 2D configuration, eq.(5.4.2) becomes

$$\begin{aligned} \widehat{u}(p, f) = & \int_0^\infty A(x) e^{i2\pi f \frac{\sqrt{4z^2 + (x-x_d)^2}}{v} - i2\pi f p x} dx + \\ & \int_0^\infty A(x) e^{i2\pi f \frac{\sqrt{4z^2 + (x-x_d)^2}}{v} + i2\pi f p x} dx, \end{aligned} \quad (5.4.6)$$

and as final result

$$\widehat{u}(p, f) = A(x_s) \sqrt{\frac{i2z}{fv^{\frac{2}{3}}q}} \left[ e^{i2\pi f \{2zq - px_d\}} + e^{i2\pi f \{2zq + px_d\}} \right]. \quad (5.4.7)$$

Again there are two contributions, but now the scaling factor is the same as for the hyperbolic event of the line source configuration.

In Fig.5.4.2 a diffraction hyperbola is shown and, according to the eqs.(5.4.4) and (5.4.7) its  $\tau$ - $p$  response is composed of two curves, one with a positive shift of  $px_d$  and the other with a negative shift. The  $\tau_d$ -value in the  $\tau$ - $p$  responses corresponds to the  $T_0$  of the diffraction hyperbola, being 0.4 s. The next example (Fig.5.4.3) also shows a diffractor which is present at each trace. Because of that, the edge effects are different from those in the previous example. In Fig.5.4.3, the edge effects are horizontal where in Fig.5.4.2, they have a certain dip. Note that the horizontal edge effects in the last example interfere with the down-dip curve for large  $p$ -values at 0.65 s.

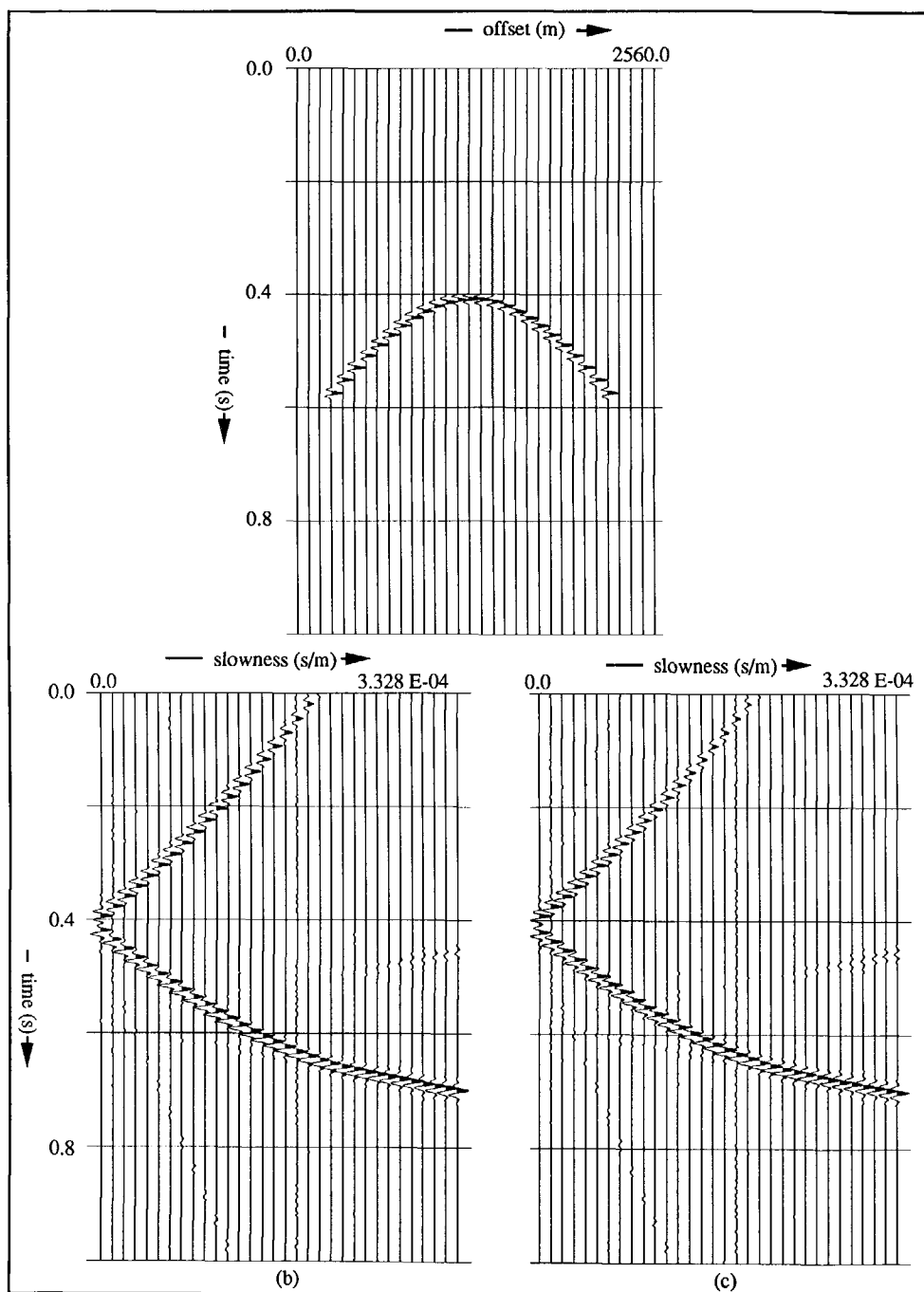


Fig.5.4.2: (a) A diffraction hyperbola in  $t$ - $x$  and its  $\tau$ - $p$  response; (b) the 3D response and (c) the 2D response;  
 $p_{max} = 1/3000$  s/m.

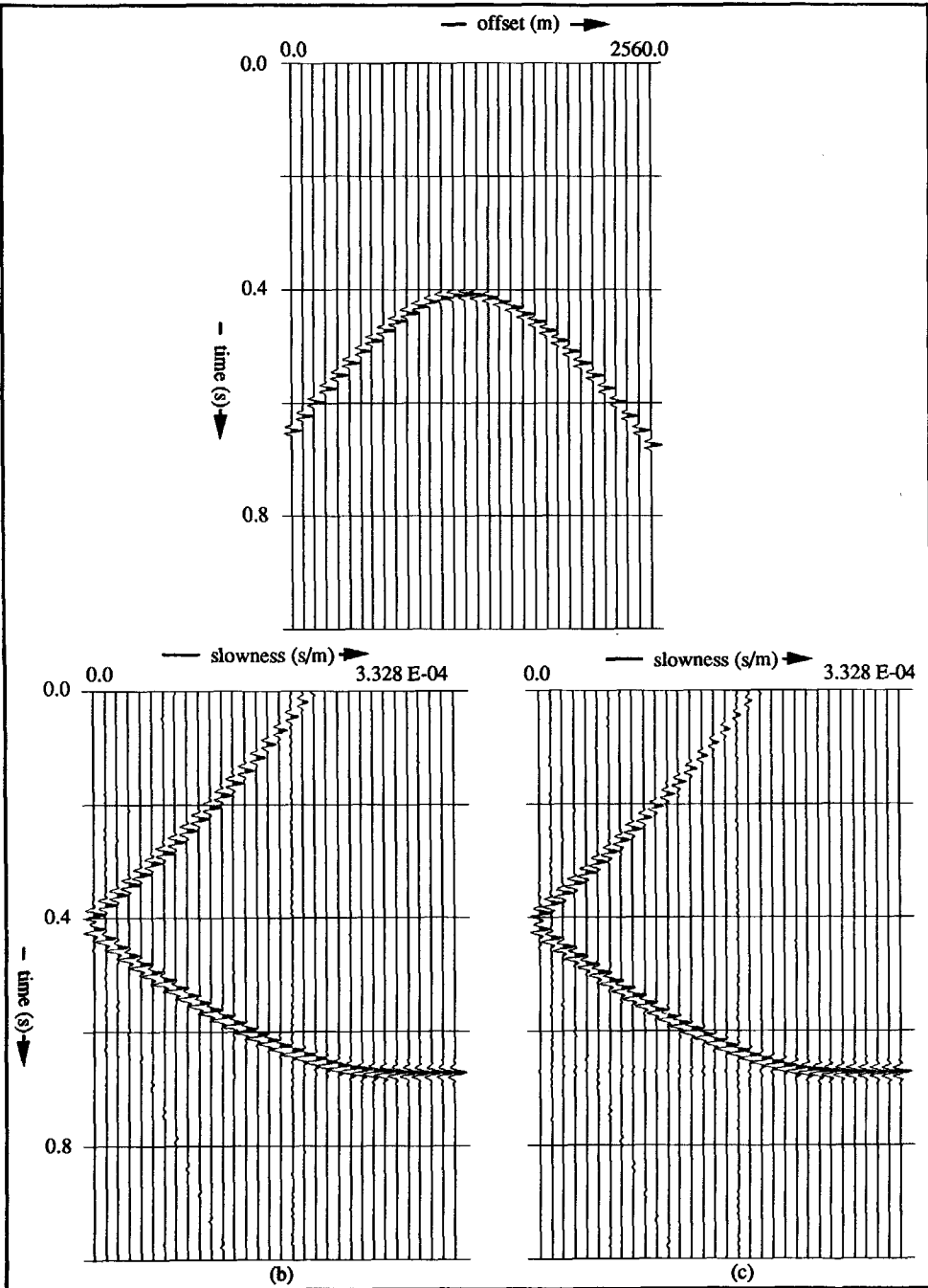


Fig.5.4.3: (a) A diffraction hyperbola in  $t$ - $x$  and its  $\tau$ - $p$  response: (b) the 3D response and (c) the 2D response;  
 $p_{max} = 1/3000$  s/m.

### 5.5 *Edge effects*

As mentioned before, edge effects are caused by the non-ideal values of the lower and upper limit of the spatial integral. Comparing the  $\tau$ - $p$  response of the headwaves and that of the edge effect the following is noticed. As the amplitude decreases with increasing offset, the amplitude of the headwaves is much larger than the amplitude at the end of the seismic section. And so, after suitable windowing, the edge effects as far as the upper limit of the integral is concerned are taken care of properly, but the headwaves cannot be. However, the amplitudes of the edge effect caused by the lower limit of the spatial integral are larger than those caused by the upper limit of the integral. But because of windowing (Fig.4.4.2), the amplitudes of the "lower limit" edge effects are far less strong than those belonging to headwaves. Moreover, by taking a careful look at the  $t$ - $x$  data set one can tell what linear events in the  $\tau$ - $p$  domain belong to headwaves and what linear events belong to the edge effects.

The last example of the synthetic data presents a noise pulse and its  $\tau$ - $p$  response (Fig.5.5.1). As is seen, the noise pulse shows the same behaviour in  $\tau$ - $p$  as the linear event does. However the dip of the two linear events in  $\tau$ - $p$  differ from the previous case, because the larger the offset, the steeper the event in  $\tau$ - $p$  becomes.

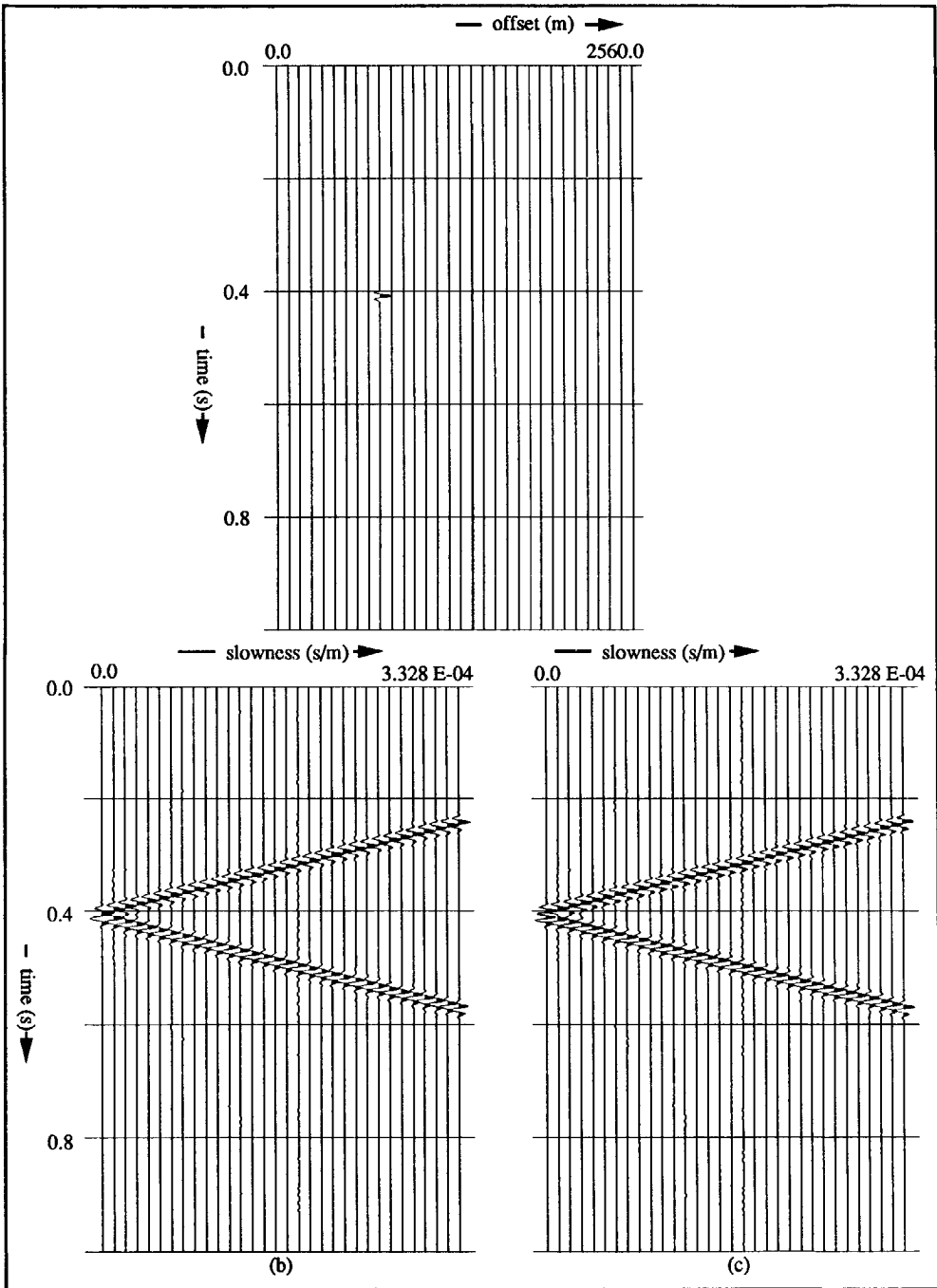


Fig.5.5.1: (a) A noise pulse in  $t$ - $x$  and its  $\tau$ - $p$  response; (b) the 3D response and (c) the 2D response;  
 $p_{\max} = 1/3000 \text{ s/m}$ .

### Summary

A summary is given of the main events, where we concentrate on the phase. The first example denotes the hyperbolic event, the second the linear event, the third the diffractor and the last shows the noise pulse. As far as the stationary points are concerned, only the spatial points are mentioned. The angular stationary point is the same for the three of them and is only present for the 3D configuration.

t-x	$\tau$ -p	stationary points
$t = \frac{\sqrt{4z^2 + x^2}}{v}$	$\tau = 2z \sqrt{1/v^2 - p^2}$	$x_s = \frac{2zp}{q}$
$t = \tau_c + \frac{x - x_c}{v}$	$\tau = \begin{cases} \tau_c - px_c \\ \tau_c + px_c \end{cases}$	none
$t = \frac{\sqrt{4z^2 + (x - x_d)^2}}{v}$	$\tau = \begin{cases} 2zq - px_d \\ 2zq + px_d \end{cases}$	$x_s = x_d \pm \frac{2zp}{q}$
$t = \delta(x_p)$	$\tau = \begin{cases} \tau_p - px_p \\ \tau_p + px_p \end{cases}$	none

### 5.6 Field data examples

Two field data sets (shot gathers) are shown. Both data sets are marine shot gathers and are collected in the northern part of the North Sea. Both gathers are transformed with the same  $\Delta p$  and because the receiver spacing is also the same, the frequency reduction due to eq.(4.4.1) is comparable in the two data sets.

#### Draugen data

In the first data set headwaves are showing up at about one and a half kilometre, that means that the velocity contrast between the water layer and the first solid layer is relatively small but the water is also quite deep. The first offset is 125 m and the receiver interval is 12.5 m (Fig.5.6.1a). Since the first offset is not zero, zero traces have to be padded at the beginning in



order to get the correct curvature of the elliptic events. For the first  $\tau$ - $p$  response only part of the data set, that is 119 traces, are taken for the transformation and this is shown in Fig.5.6.1b. According to eq.(5.2.15) the range of reliable  $p$ -values is calculated in which  $x_{min}$  is 125 m and  $x_{max}$  is 1600 m. Then, knowing the velocity model (picked from the conventional velocity contour plots) two curves can be estimated, one for the minimum and one for the maximum reliable  $p$ -values. This range is marked by two solid lines in Fig.5.6.1b. Outside this range, only edge effects as part of the noise, are present. The headwaves just mentioned are present in the data but hardly in the first 119 traces, therefore the typical linear up-dip and down-dip linear events are absent in this  $\tau$ - $p$  response.

For the Figs.5.6.1c and 5.6.1d, the same number of input traces are used as for Fig.5.6.1b, only the  $\Delta p$  is chosen smaller. Therefore, the frequency reduction due to eq.(4.4.1) becomes less and the resolution of the two seismograms increases.

The Fig.5.6.1f shows however a different picture. All 208 traces are taken as input (Fig.5.6.1e) and a clear up-dip at 1.2 s linear event is visible in the  $\tau$ - $p$  response. The down-dip linear event however is hardly visible. Here, also the reliable  $p$ -range is calculated and the curve for  $x_{min}$  is unchanged but the curve for  $x_{max}$  (= 2725 m) has shifted to the right. At 0.5 s for the higher  $p$ -values, down-dip edge effects become visible. When the latter including the unreliable parts is transformed back to  $t$ - $x$ , the result is shown in Fig.5.6.1g. The direct wave, present in the original  $t$ - $x$  data set has disappeared and the first ten traces consist only of noise because there was no signal in the first place. Furthermore, there is a slight frequency reduction due to the Radon transform, which is explained in section 4.4 and shown schematically in Fig.4.4.1.

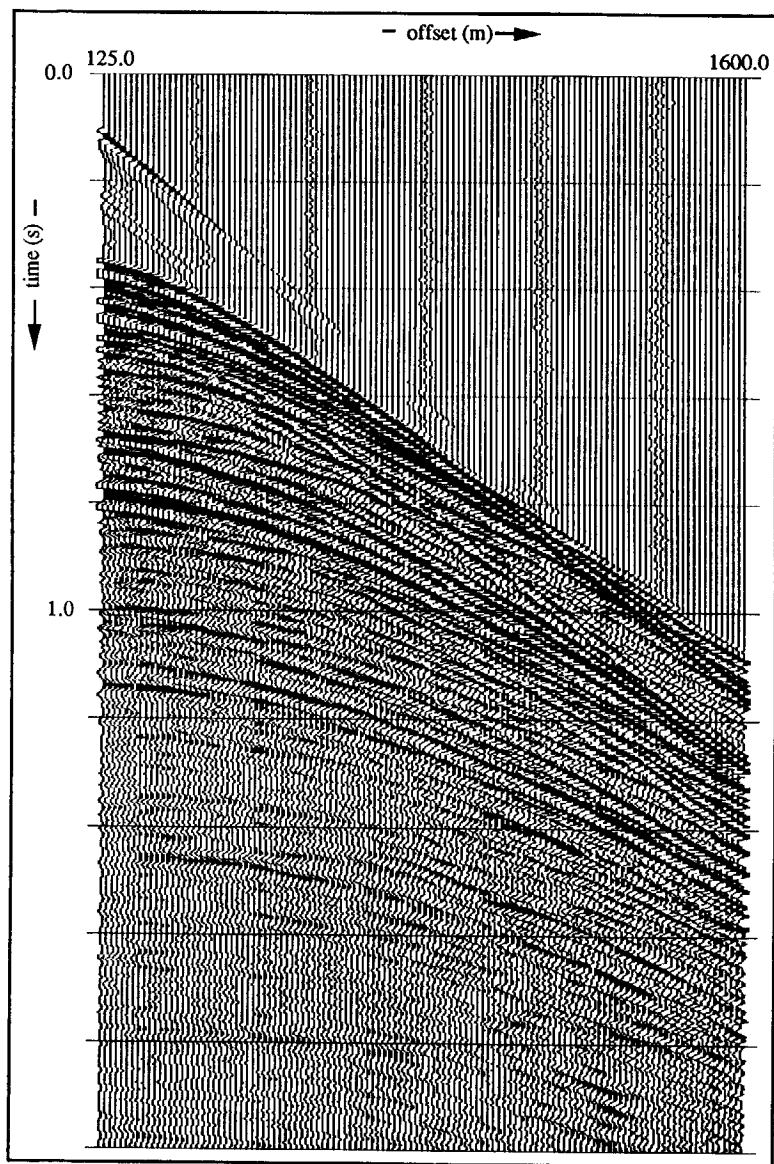


Fig.5.6.1a: The Draugen data set in  $t$ - $x$ ; first offset = 125 m,  $\Delta x = 12.5$  m and 119 input traces.

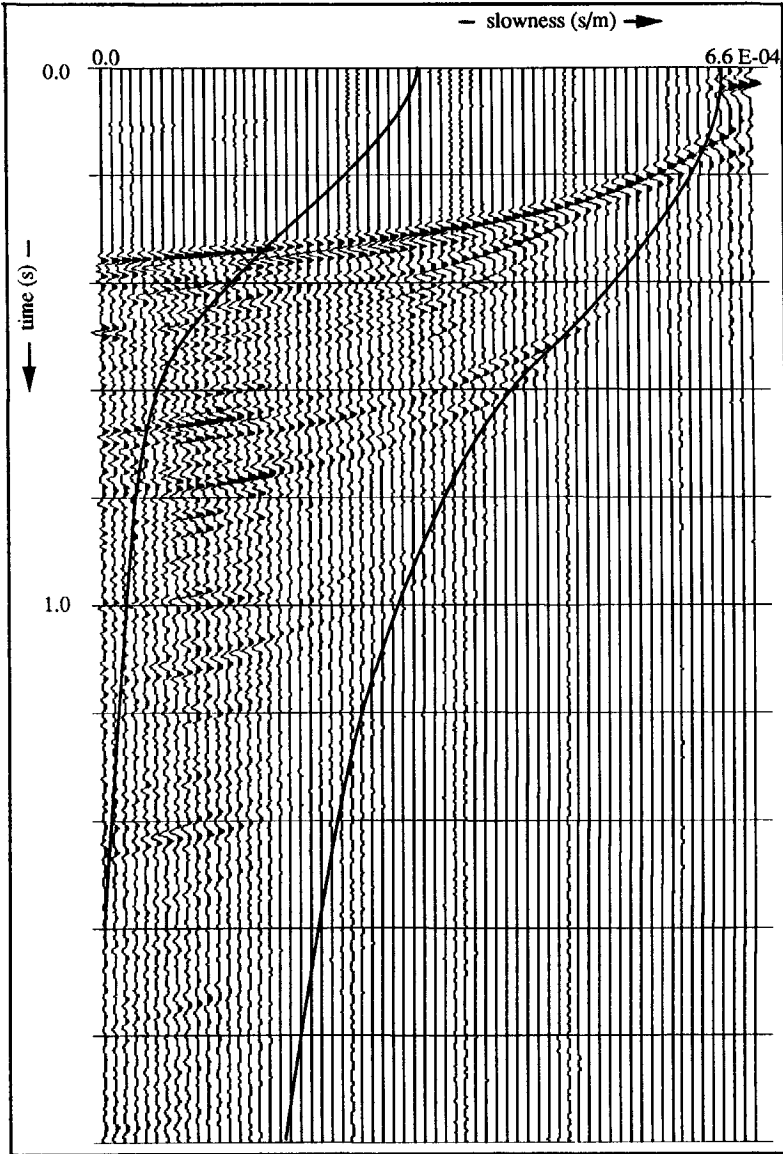


Fig.5.6.1b: The  $\tau$ - $p$  response of the Draugen data set;  $\Delta p = 5.2787$  ms/km and 119 input traces.

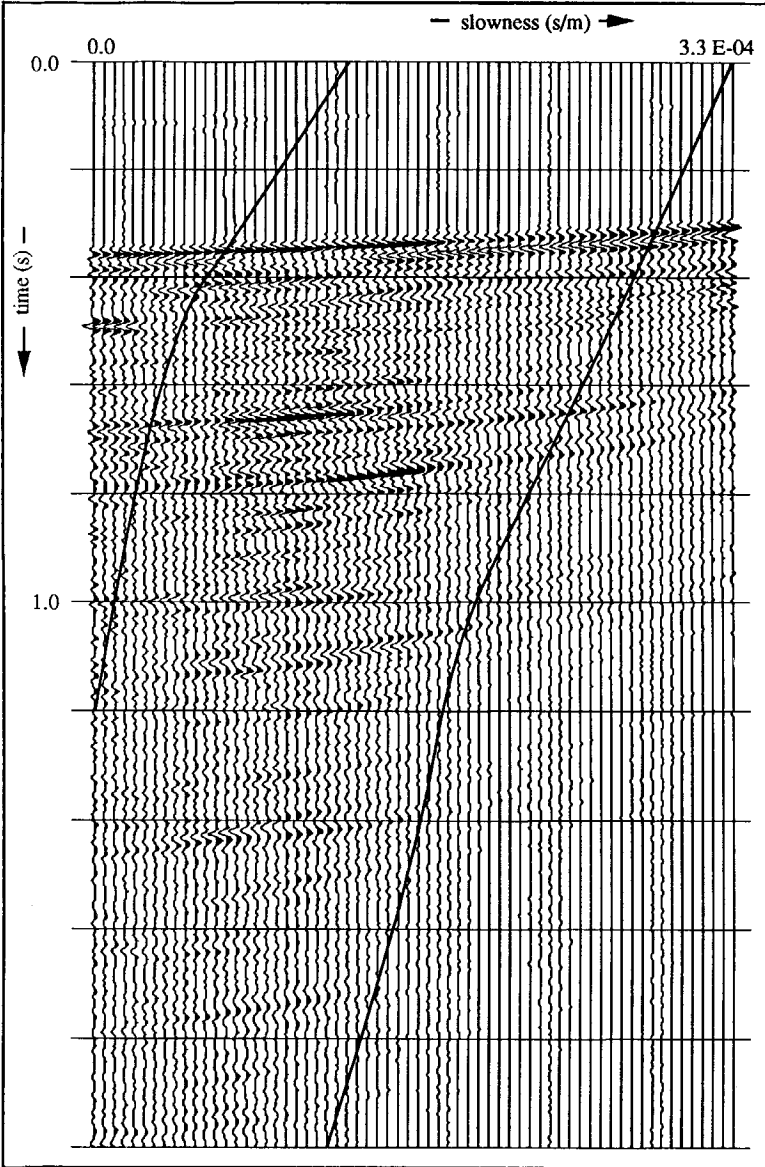


Fig.5.6.1c: The  $\tau$ - $p$  response of the Draugen data set;  $\Delta p = 2.6394$  ms/km and 119 input traces.

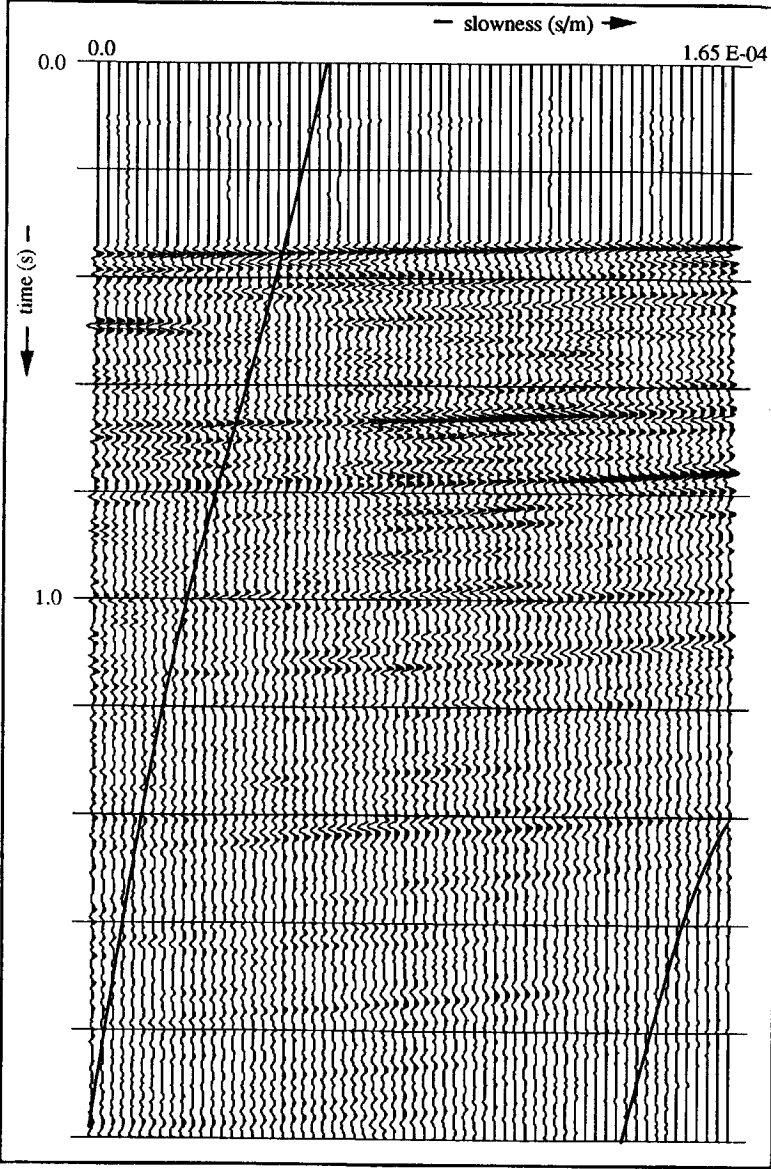


Fig.5.6.1d: The  $\tau$ - $p$  response of the Draugen data set;  $\Delta p = 1.3197$  ms/km and 119 input traces.

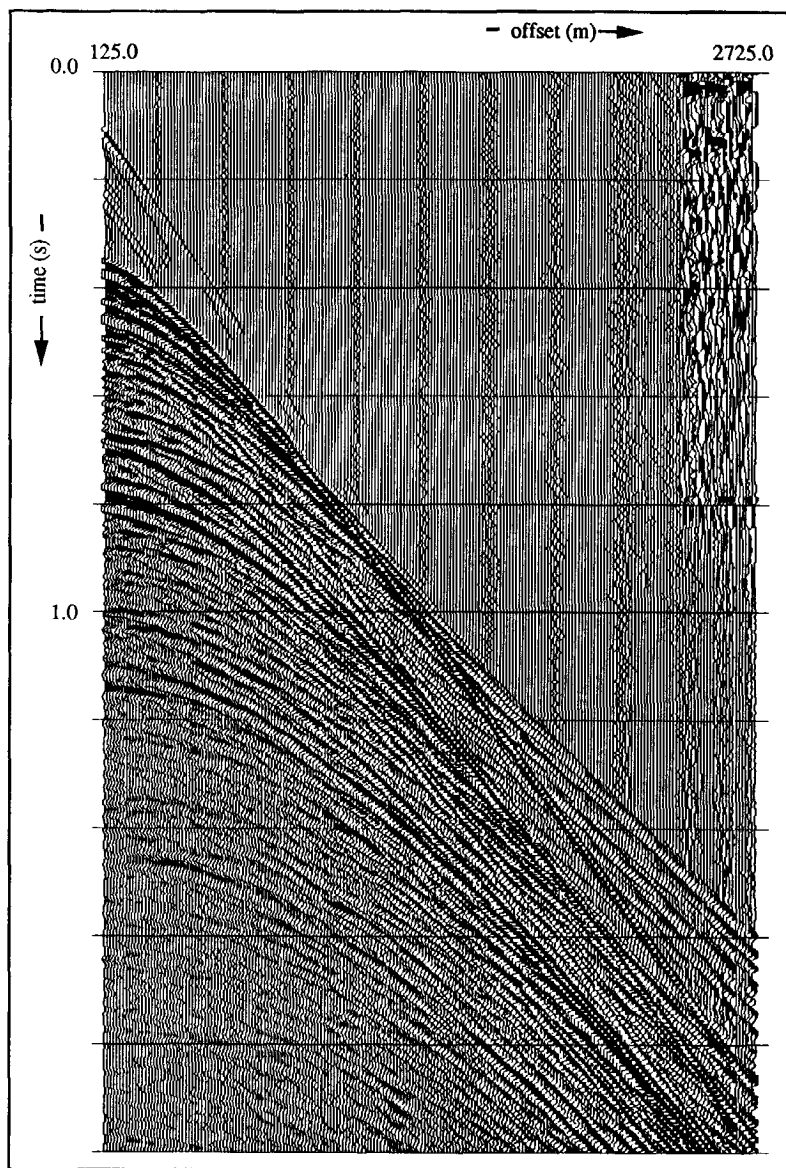


Fig.5.6.1e: The Draugen data set in  $t$ - $x$ ; first offset = 125 m,  $\Delta x = 12.5$  m and all 208 input traces.

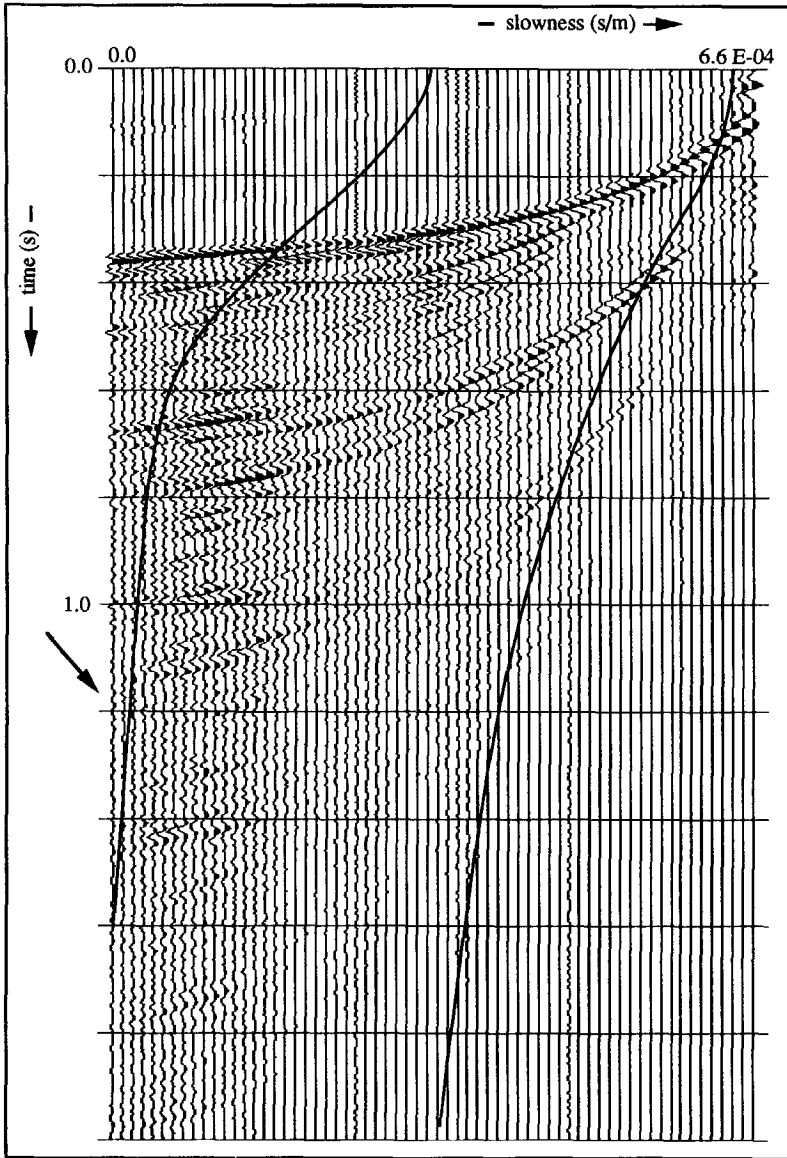


Fig. 5.6.1f: The  $\tau$ - $p$  response of the Draugen data set;  $\Delta p = 5.2787$  ms/km and 208 input traces.

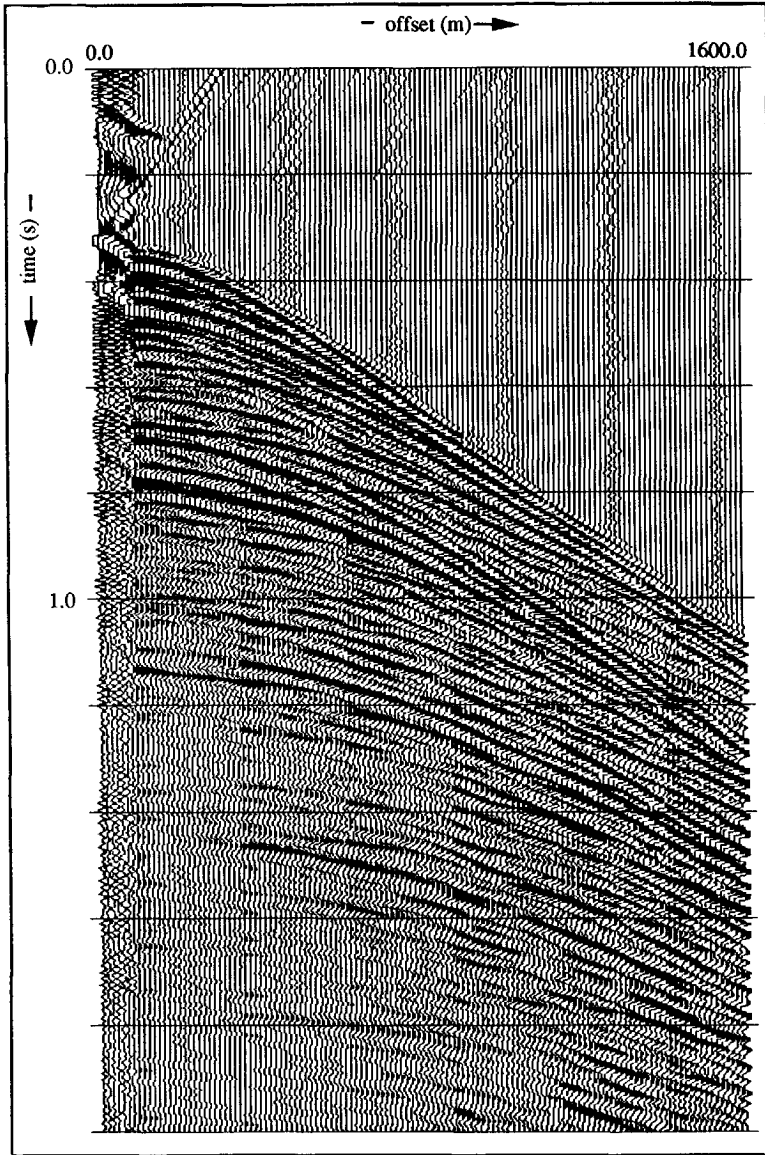


Fig.5.6.1g: The  $t$ - $x$  response of the Draugen data set after forward and inverse Radon transform; first offset = 125 m,  $\Delta x = 12.5$  m and 208 input traces.

#### *North Sea data*

The second data set suffers from severe free surface effects (Fig.5.6.2a). Because of the large impedance contrast in the data set between the water layer and the first solid layer strong headwaves, P headwaves as well as P-S converted headwaves, show up at a relatively small offset. The presence of severe free surface effects in the data set implies that a large amount of



the energy generated by the airguns is kept in the water layer, bouncing up and down and only a small amount of the energy travels into the underlying layers. Because the data set is spatially aliased, Fig.5.6.2a is conventionally  $f-k$  filtered which is shown in Fig.5.6.2b. Then, Fig.5.6.2c shows the  $\tau-p$  response of the data set of Fig.5.6.2a and Fig.5.6.2d depicts the  $\tau-p$  response of the  $f-k$  filtered data set. Because the headwaves show up at such a relatively short offset, the linear up-dip and down-dip events (only in Fig.5.6.2c) are much more evident here than in the previous case.

The dip of these linear up-dip events gives us the exact starting position of the headwaves. And it tells also something about the character of the source wavelet since the up-dip and down-dip linear events are Hilbert transforms of each other. When the  $t-x$  data are first filtered in the  $f-k$  domain to get rid of the spatially aliased part, the  $\tau-p$  response of the  $f-k$  filtered data set lacks the down-dip linear events (Fig.5.6.2d). Again according to eq.(5.2.15) the reliable  $p$ -values are between the two solid lines in the last two figures. In this case because of higher velocities at smaller times the unreliable part of the data has increased. In Fig.5.6.2d, the interpolation error, mentioned in section 3.5 is quite clear at 0.8 s (down-dip event).

Then, the Figs.5.6.2e and 5.6.2f reflect respectively the  $t-x$  responses of the previous two seismograms. Again the first ten traces only exhibit noise. The  $f-k$  filtered seismogram shows less noise than the unfiltered seismogram, and the discontinuities marked by an arrow indicate the starting positions of refractions. In the last few traces of the back transformed seismograms the noise outweighs the signal.

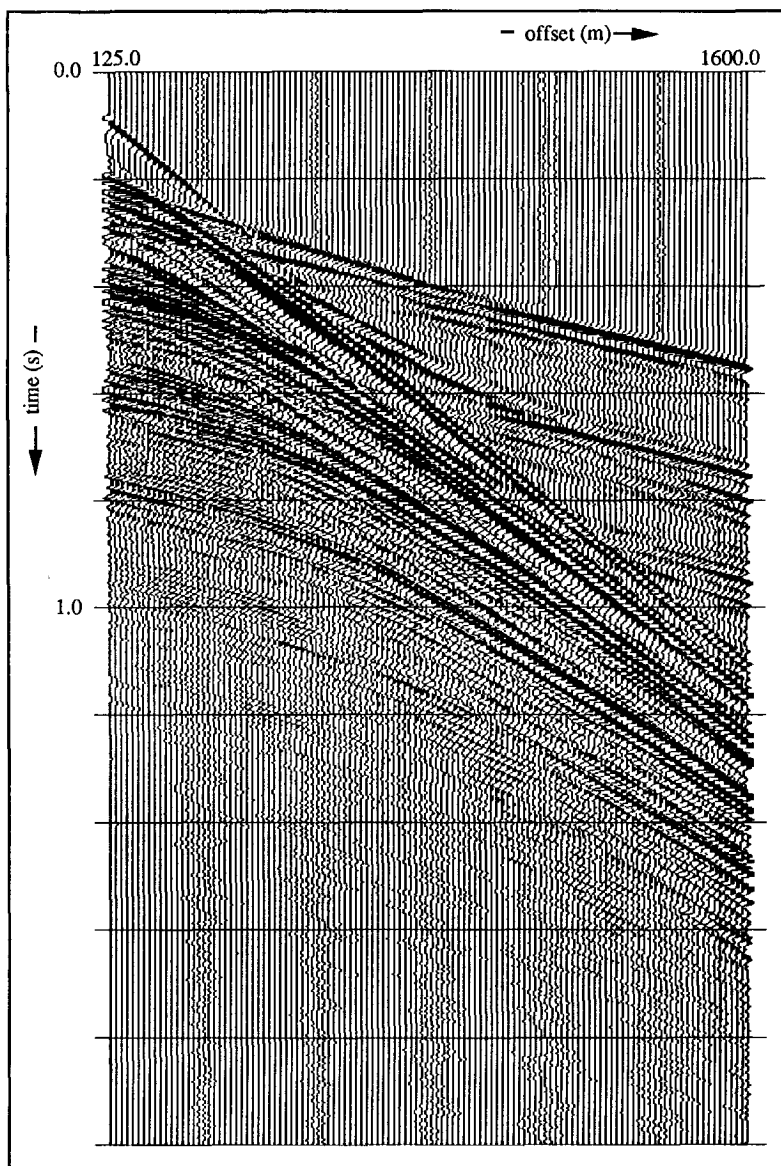


Fig.5.6.2a: The North Sea data set; first offset = 125 m,  $\Delta x = 12.5$  m and 128 input traces.

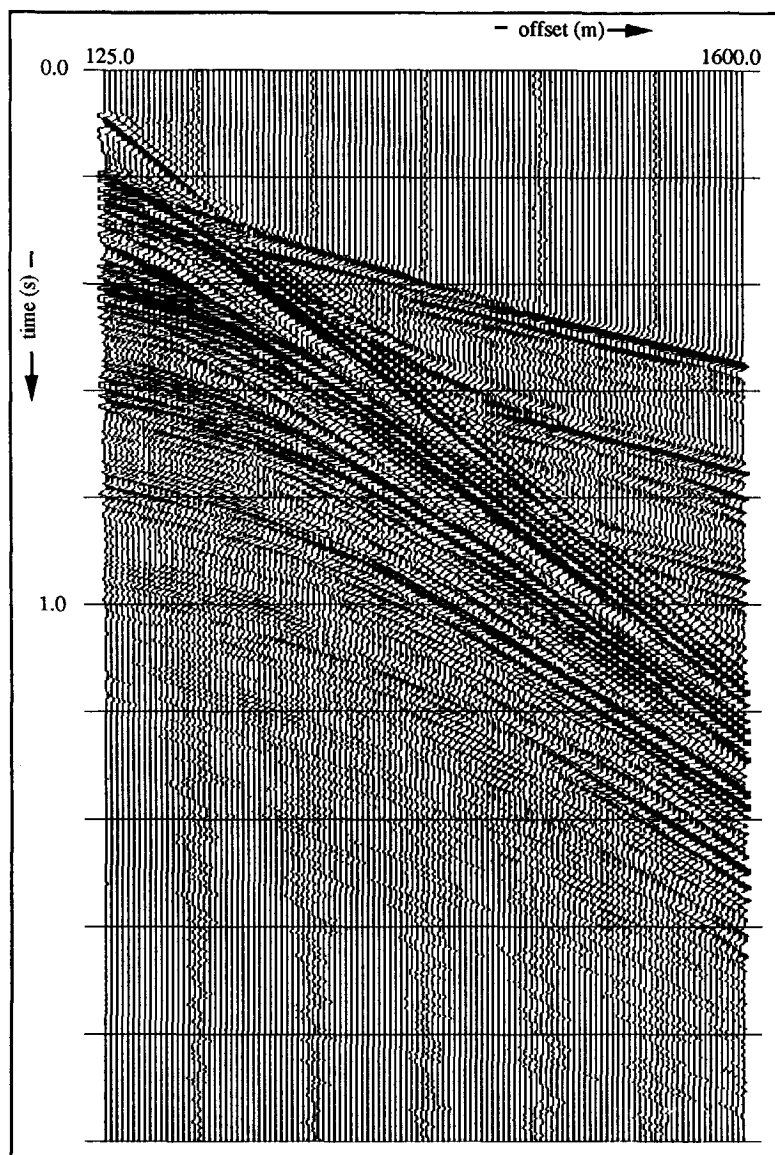


Fig.5.6.2b: The  $f$ - $k$  filtered North Sea data set; first offset = 125 m,  $\Delta x = 12.5$  m.

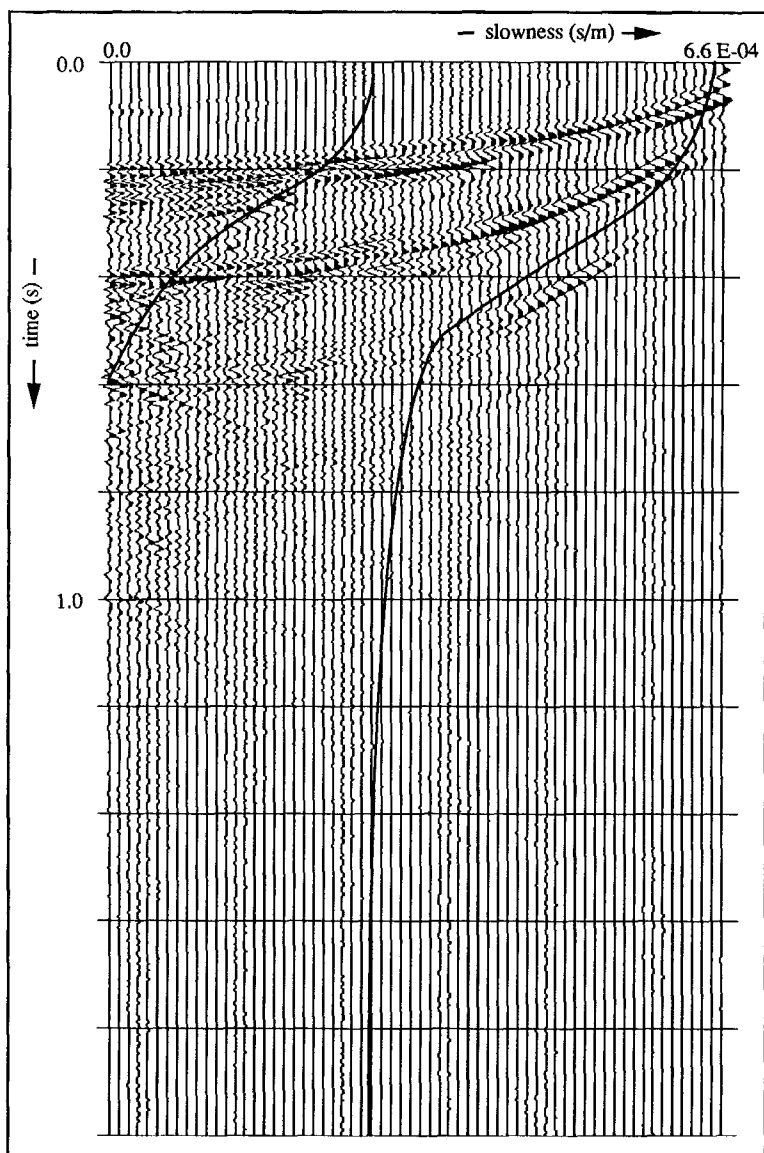


Fig.5.6.2c: The  $\tau$ - $p$  response of the raw North Sea data set;  $\Delta p = 5.2787 \text{ ms/km}$ .

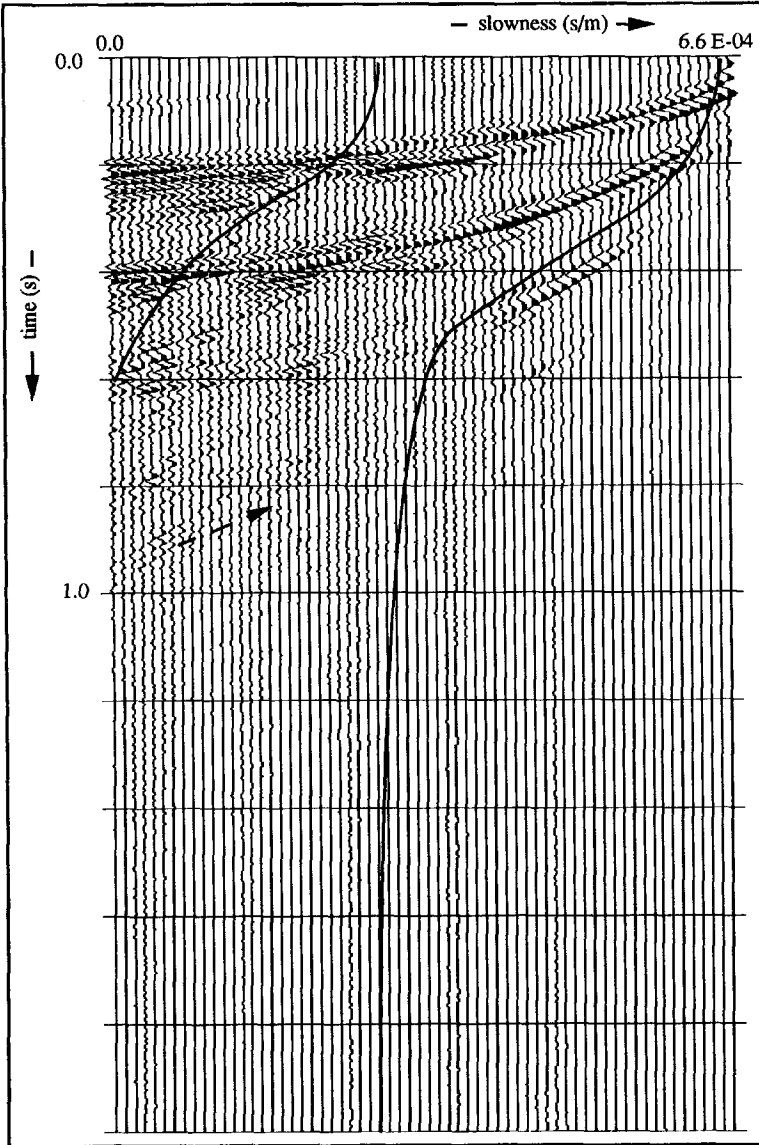


Fig.5.6.2d: The  $\tau$ - $p$  response of the  $f$ - $k$  filtered North Sea data set;  $\Delta p = 5.2787$  ms/km.

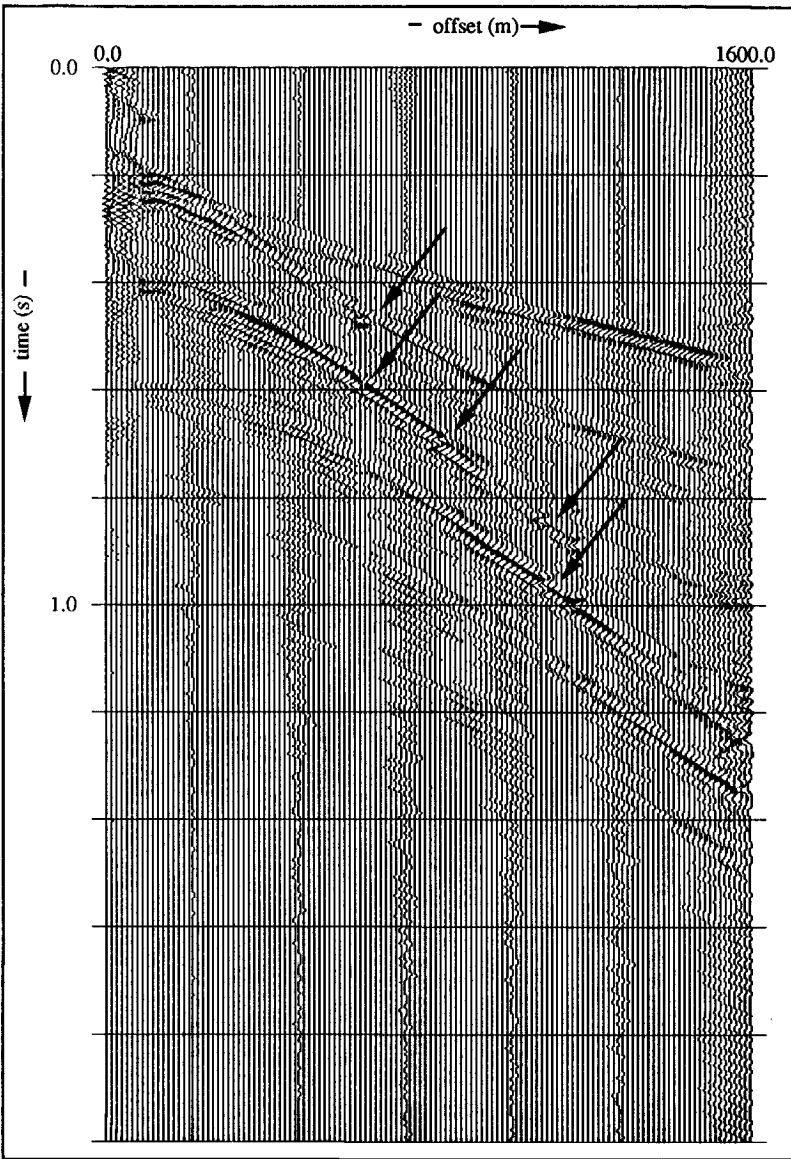


Fig.5.6.2e: The  $t$ - $x$  response of the raw North Sea data set after the forward and inverse Radon transform; first offset = 125 m and  $\Delta x = 12.5$  m.

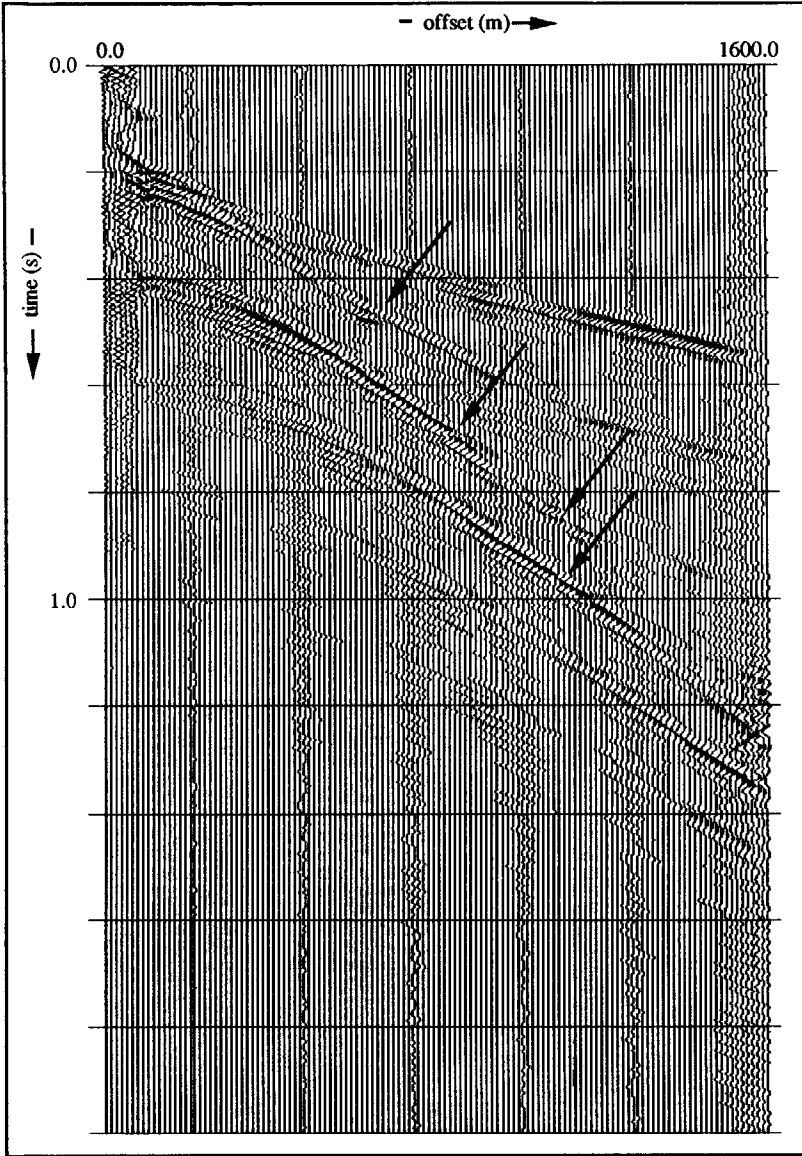


Fig.5.6.2f: The  $t$ - $x$  response of the  $f$ - $k$  filtered North Sea data set after the forward and inverse Radon transform; first offset = 125 m and  $\Delta x = 12.5$  m.

Finally, two seismograms are shown. The raw North Sea data set is transformed to  $\tau$ - $p$  according to

$$\hat{u}(p, f) = 2 \int_0^\infty \hat{u}(x, f) x dx \int_0^{\pi/2} e^{i2\pi f p x \cos \theta} d\theta \quad (5.6.1)$$

where the spatial integral runs from 0 till infinity. Then, only the down-dip events are present and the ellipses vanish (Fig.5.6.3a).

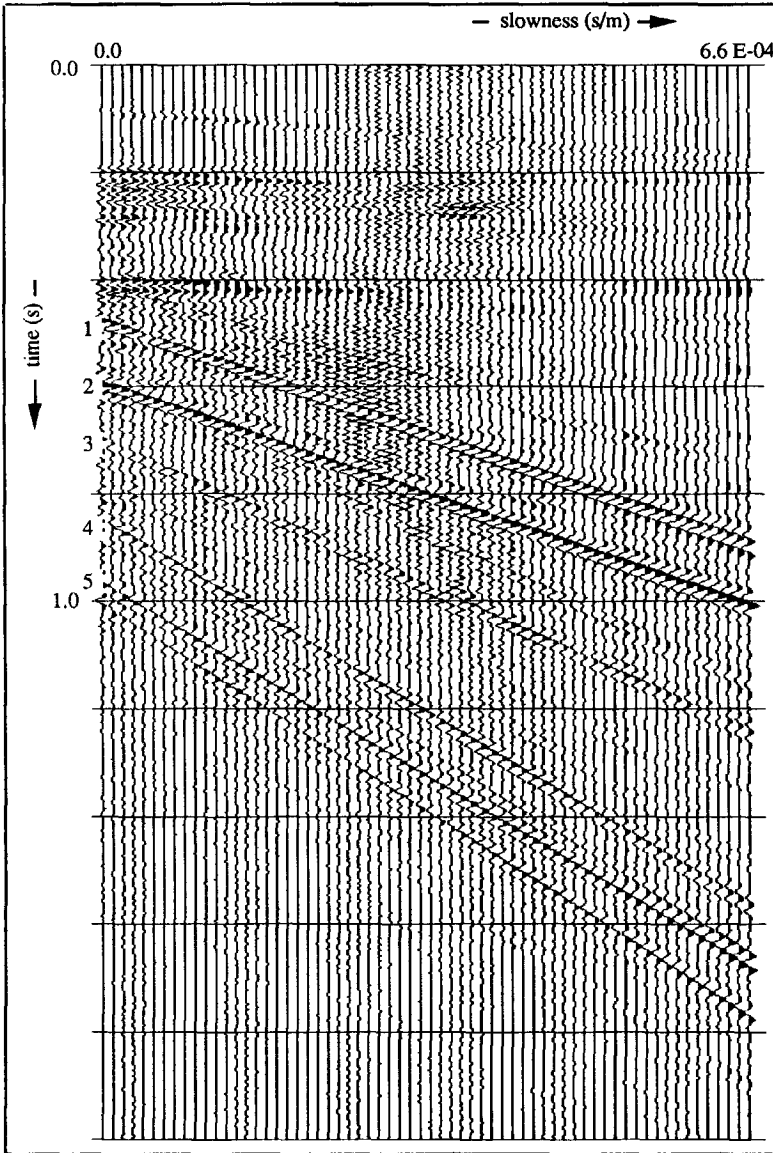


Fig.5.6.3a: The  $\tau$ - $p$  response of the raw North Sea data set;  $\Delta p = 5.2787$  ms/km.

Next, this seismogram (Fig.5.6.3a) is transformed back to  $t$ - $x$  (Fig.5.6.3b) with eq.(4.2.12) and then the starting positions of all the headwaves become visible. They are indicated by



arrows. The maximum value, plotted in Fig.5.6.3b is about 100 times less strong than in Fig.5.6.2e.

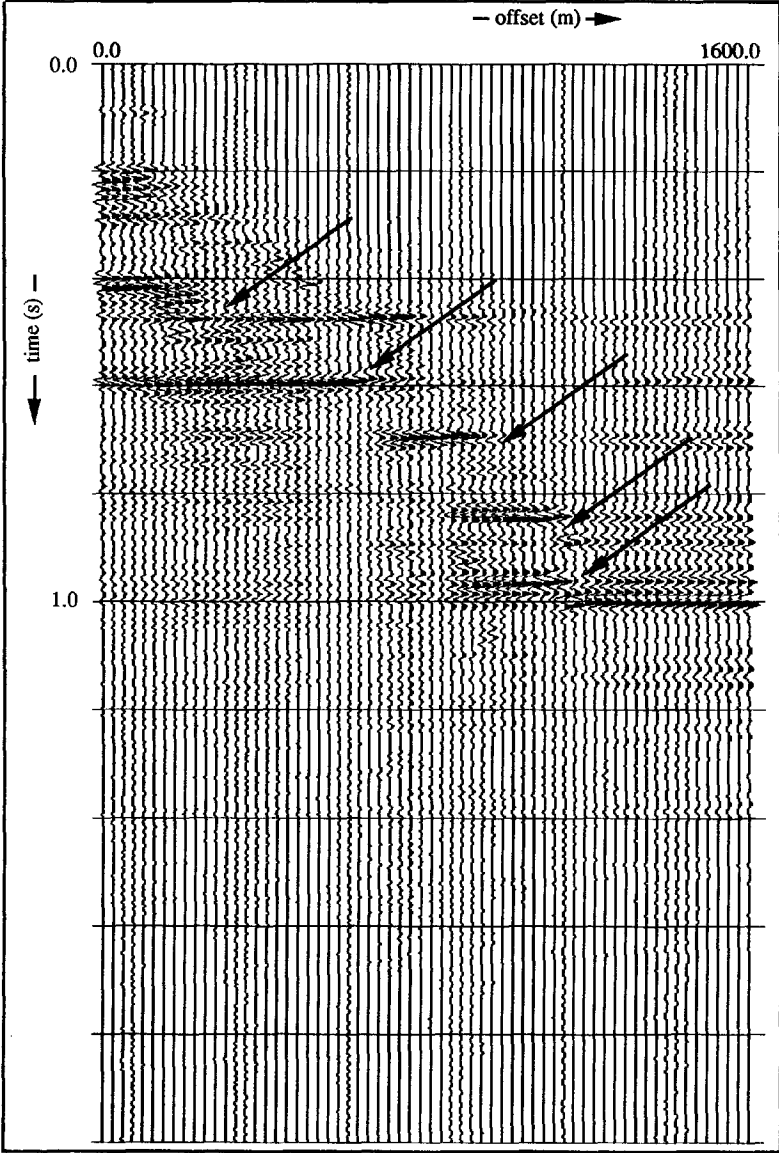


Fig.5.6.3b: The  $t$ - $x$  response of Fig.5.6.3a;  $\Delta x = 12.5$  m.

---

## THE FORWARD RADON TRANSFORM APPLIED TO T-X DATA: A SEISMIC LINE

---

### 6.1 Introduction

When a split-spread data set is taken as a whole (all shot gathers) and considered as a coherent set of information covering a certain subsurface, its spatial complexity shows a well-defined topological subdivision in the double Radon transformed domain. The main advantage of this method is the absence of the planar velocity constraint imposed on the data when compared with the algorithm given in Chapter 4.

In section 6.2 the theory is presented, where we start with the 3D formulation of the problem, and pass into a  $2\frac{1}{2}$ D formulation because we are dealing with point source and point receiver data, gathered in a 2D configuration. However, the whole algorithm can be completely formulated for a 3D configuration without facing any extra problems. The source is a point source of impulsive nature and we employ field coordinates implying that the point receiver is referenced with respect to the corresponding source position by true offset.

Then, we represent the total scattered field as a superposition of distinct primary contributions originating from a finite number of interfaces. By applying a forward Radon transform with respect to the horizontal source and offset coordinates, the horizontal phase is separated from the vertical phase in the data. The next step is to carry out a high-frequency analysis. The result of this is a Fourier integral representing a decomposition of the complexity of the data set.

In section 6.3, we formulate a pre-stack migration procedure as the main application of this method. Our migration procedure is an alternative approach for the NMO, DMO, CMP stacking and the post-stack migration scheme. The conventional scheme works well on areas with uniform dip. However when the stacking velocities are dip-dependent the final image will be less accurate. The alternative is then to perform a full pre-stack migration. Although the result will be accurate, this technique suffers from large computational efforts and the requirement of a detailed velocity model. DMO, also referred to as pre-stack partial migration in the older literature, is a

method which bridges these extremes (Hubral, 1980, Hale, 1983, Deregowski, 1986 and Jacubowicz, 1990).

Section 6.4 discusses the theoretical and practical limitations of the pre-stack migration procedure due to our method as well as due to the data (section 6.4). The dip slowness curves, showing the dips of the interfaces in the double Radon transformed domain are also discussed.

The computational procedure is outlined in section 6.5. Section 6.6 shows five synthetic data examples, simulating a split-spread seismic profile (2D), and one land seismic data set, gathered in the Northern part of Holland. The synthetic data sets show an increasing complexity of the subsurface and all examples are pre-stack migrated.

## 6.2 Formulation of the problem

In Chapters 3 and 4 a number of assumptions are made. In this chapter, the planar velocity distribution is abandoned and non-planar interfaces are allowed. The earth model consists of  $M$  different acoustic layers separated by non-planar interfaces.

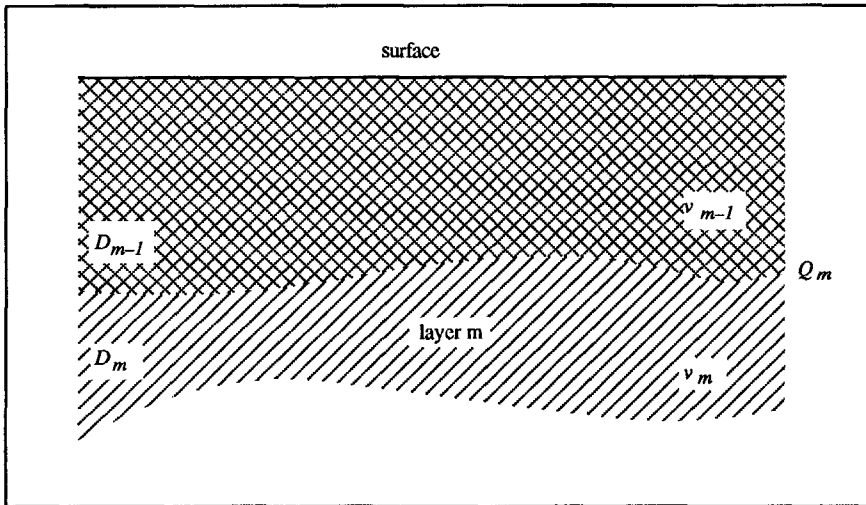


Fig.6.2.2: The total scattered field, decomposed.

Let  $\hat{p}^{sc}(\mathbf{x}^r, \mathbf{x}^s, t)$  denote the measured scattered field recorded at  $\mathbf{x}^r = \{x_1^r, x_2^r, x_3^r\}$  due to an impulsive point source which starts to act at  $t = 0$  and is located at  $\mathbf{x}^s = \{x_1^s, x_2^s, x_3^s\}$ . Then, we assume that the scattered response is considered as the superposition of  $M$  independent contributions such that

$$\hat{p}^{sc}(\mathbf{x}^r, \mathbf{x}^s, t) = \sum_{m=1}^M p_m(\mathbf{x}^r, \mathbf{x}^s, t), \quad (6.2.1)$$

where  $p_m$  represents the response of the  $m$ -th acoustic layer occupying the domain  $D_m$  bounded by the surface and the interface  $Q_m$ . Note that only the primary reflections are considered. The interface  $Q_m$  coincides with the true layer interface between the  $(m-1)$ -th and  $m$ -th layer, that is the intersection of the domains  $D_{m-1}$  and  $D_m$  denotes the  $m$ -th acoustic layer of the original model (Fig.6.2.1). Further, the domain  $D_m$  is acoustically characterized by the velocity  $v_m$  being the equivalent of the rms-velocity. When a data set is sorted into CMP gathers and only plane horizontal interfaces are considered, our model then corresponds to the conventional stacking model.

The next step is to transform the scattered field representation to the frequency domain

$$\hat{p}^{sc}(x^r, x^s, f) = \int_0^\infty e^{i2\pi ft} p^{sc}(x^r, x^s, t) dt, \quad (6.2.2)$$

where the inverse transform is, following eq.(2.2.9), given by

$$p^{sc}(x^r, x^s, t) = 2\text{Re} \left[ \int_0^\infty e^{-i2\pi ft} \hat{p}^{sc}(x^r, x^s, f) df \right]. \quad (6.2.3)$$

$\text{Re} [\dots]$  denotes the real part, and eq.(6.2.3) is evaluated for positive frequencies only.

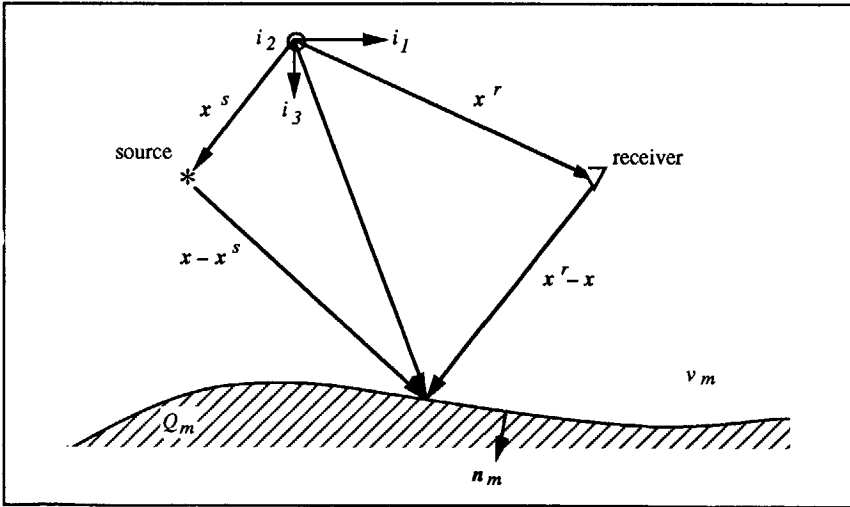


Fig.6.2.2: The scattering geometry.

Each interface,  $Q_m$  is described as

$$x_3 = h_m(x_1, x_2), \quad (6.2.4)$$

where  $h_m$  denotes an arbitrary function of the Cartesian coordinates  $x_1$  and  $x_2$ . We assume that both source and receiver are located above the interface  $Q_m$  such that  $x_3^r < x_3$  and  $x_3^s < x_3$  for all  $x_3$  on  $Q_m$  (Fig.6.2.2).

Then, the scattered field of the  $m$ -th interface is considered as the field generated by secondary surface sources at the interface  $Q_m$  and can be expressed in terms of these surface sources (Bleistein, 1984; Fokkema and vd Berg, submitted for publ. in 1991) as

$$\hat{p}_m(x^r, x^s, f) = \iint_{x \in Q_m} \left[ \hat{G}_m(x - x^r, f) n_m \cdot \nabla \hat{p}_m(x, x^s, f) - n_m \cdot \nabla \hat{G}_m(x - x^r, f) \hat{p}_m(x, x^s, f) \right] dA, \quad (6.2.5)$$

where  $n_m \cdot \nabla$  denotes the normal derivative in the direction pointing away from  $D_m$  and where  $\hat{G}_m$  presents the Green's function of the  $m$ -th interface. The Green's function,  $\hat{G}_m$  is defined as

$$\hat{G}_m(x, f) = \frac{1}{4\pi|x|} e^{\frac{i2\pi f|x|}{v_m}}, \quad (6.2.6)$$

with

$$|x| = \sqrt{x_1^2 + x_2^2 + x_3^2}. \quad (6.2.7)$$

Then, for large values of  $f$ , we employ a locally plane reflector approximation

$$\begin{aligned} \hat{p}_m(x, x^s, f) &= \eta_m \hat{p}_m^{inc}(x, x^s, f), \quad x \in Q_m \\ n_m \cdot \nabla \hat{p}_m(x, x^s, f) &= \zeta_m n_m \cdot \nabla \hat{p}_m^{inc}(x, x^s, f), \quad x \in Q_m, \end{aligned} \quad (6.2.8)$$

where  $\hat{p}_m^{inc}$  represents the incident field in the  $m$ -th background medium defined by the rms-velocity  $v_m$ . The quantities  $\eta_m(x, x - x^s)$  and  $\zeta_m(x, x - x^s)$  are real, frequency-independent functions of  $x$  and  $x - x^s$ , signifying the dependence on the absolute position on the reflector and the relative position with respect to the source, respectively. The incident field is defined as

$$\hat{p}_m^{inc}(x, x^s, f) = \hat{S}(f) \hat{G}_m(x - x^s, f), \quad (6.2.9)$$

where  $\hat{S}(f)$  denotes the source spectrum. Using the locally plane reflector approximation (eq.(6.2.8)) and substituting this in the integral representation of eq.(6.2.5), we obtain

$$\widehat{p}_m(x^r, x^s, f) = \widehat{S}(f) \iint_{x \in Q_m} \left[ \zeta_m \widehat{G}_m(x-x^r, f) \mathbf{n}_m \cdot \nabla \widehat{G}_m(x-x^s, f) - \eta_m \widehat{G}_m(x-x^s, f) \mathbf{n}_m \cdot \nabla \widehat{G}_m(x-x^r, f) \right] dA. \quad (6.2.10)$$

According to the reciprocity theorem, which states that source and receiver are interchangeable, the following equation is valid:

$$\widehat{p}_m(x^r, x^s, f) = \widehat{p}_m(x^s, x^r, f). \quad (6.2.11)$$

Then, the integral representation of eq.(6.2.10), extended to

$$\widehat{p}_m(x^r, x^s, f) = \widehat{S}(f) \iint_{x \in Q_m} \left[ \zeta_m(x, x-x^s) \widehat{G}_m(x-x^r, f) \mathbf{n}_m \cdot \nabla \widehat{G}_m(x-x^s, f) - \eta_m(x, x-x^s) \widehat{G}_m(x-x^s, f) \mathbf{n}_m \cdot \nabla \widehat{G}_m(x-x^r, f) \right] dA, \quad (6.2.12)$$

changes, using eq.(6.2.11) into

$$\widehat{p}_m(x^s, x^r, f) = \widehat{S}(f) \iint_{x \in Q_m} \left[ \zeta_m(x, x-x^r) \widehat{G}_m(x-x^s, f) \mathbf{n}_m \cdot \nabla \widehat{G}_m(x-x^r, f) - \eta_m(x, x-x^r) \widehat{G}_m(x-x^r, f) \mathbf{n}_m \cdot \nabla \widehat{G}_m(x-x^s, f) \right] dA. \quad (6.2.13)$$

This implies that

$$\begin{aligned} \zeta_m(x, x-x^s) &= -\eta_m(x, x-x^r) \\ \eta_m(x, x-x^s) &= -\zeta_m(x, x-x^r). \end{aligned} \quad (6.2.14)$$

Using the latter two equalities reformulates the integral representation of eq.(6.2.10) into

$$\widehat{p}_m(x^r, x^s, f) = -\widehat{S}(f) \iint_{x \in Q_m} \left[ \eta_m(x, x-x^r) \widehat{G}_m(x-x^r, f) \mathbf{n}_m \cdot \nabla \widehat{G}_m(x-x^s, f) + \eta_m(x, x-x^s) \widehat{G}_m(x-x^s, f) \mathbf{n}_m \cdot \nabla \widehat{G}_m(x-x^r, f) \right] dA. \quad (6.2.15)$$

which makes the scattered field representation independent of  $\zeta_m(x, x-x^s)$ .

The normal derivative operating on the Green's function is given by

$$\mathbf{n}_m \cdot \nabla \hat{G}_m(\mathbf{x}, f) = \frac{i2\pi f}{v_m} \hat{G}_m \left( 1 - \frac{v_m}{i2\pi f |\mathbf{x}|} \right) \mathbf{n}_m \cdot \nabla |\mathbf{x}|, \quad (6.2.16)$$

so that eq.(6.2.15) simplifies to

$$\hat{p}_m(\mathbf{x}^r, \mathbf{x}^s, f) = \frac{-i2\pi f}{v_m} \hat{S}(f) \iint_{\mathbf{x} \in Q_m} \hat{B}_m \hat{G}_m(\mathbf{x} - \mathbf{x}^r, f) \hat{G}_m(\mathbf{x} - \mathbf{x}^s, f) dA, \quad (6.2.17)$$

with the function  $\hat{B}_m = \hat{B}_m(\mathbf{x}, \mathbf{x}^r, \mathbf{x}^s, f)$  as

$$\begin{aligned} \hat{B}_m(\mathbf{x}, \mathbf{x}^r, \mathbf{x}^s, f) = & \eta_m(\mathbf{x}, \mathbf{x} - \mathbf{x}^r) \left( 1 - \frac{v_m}{i2\pi f |\mathbf{x} - \mathbf{x}^r|} \right) \mathbf{n}_m \cdot \nabla |\mathbf{x} - \mathbf{x}^r| + \\ & \eta_m(\mathbf{x}, \mathbf{x} - \mathbf{x}^s) \left( 1 - \frac{v_m}{i2\pi f |\mathbf{x} - \mathbf{x}^s|} \right) \mathbf{n}_m \cdot \nabla |\mathbf{x} - \mathbf{x}^s|, \end{aligned} \quad (6.2.18)$$

which becomes independent of  $f$  as  $f \rightarrow \infty$ .

In view of the practical situation, the data are obtained along a line in a cross-sectional plane of the interfaces, for example  $x_2 = 0$ . Moreover, in our seismic experiment we do not obtain shot and receiver coordinates but shot coordinates and offset coordinates with respect to the source positions. Therefore, we define the following set of transverse coordinates

$$\begin{aligned} \mathbf{x}_T &= \{x_1, 0, x_3\} \\ \mathbf{x}_T^o &= \{x_1^r - x_1^s, 0, x_3^r\} \\ \mathbf{x}_T^s &= \{x_1^s, 0, x_3^s\} \end{aligned} \quad (6.2.19)$$

Then, the representation of eq.(6.2.17) in case of transverse coordinates is written as

$$\hat{p}_m(\mathbf{x}_T^o, \mathbf{x}_T^s) = \frac{-i2\pi f}{v_m} \hat{S}(f) \iint_{\mathbf{x} \in Q_m} B_m \frac{e^{\frac{i2\pi f}{v_m} \left( \sqrt{(R^o)^2 + x_2^2} + \sqrt{(R^s)^2 + x_2^2} \right)}}{16\pi^2 \sqrt{(R^o)^2 + x_2^2} \sqrt{(R^s)^2 + x_2^2}} dA, \quad (6.2.20)$$

where  $B_m = B_m(\mathbf{x}, \mathbf{x}_T^o, \mathbf{x}_T^s)$  is given by

$$B_m(x, x_T^o, x_T^s) = \eta_m(x_I - x_I^o - x_I^s, x_2 x_3 - x_3^r) \mathbf{n}_m \cdot \nabla \sqrt{(R^o)^2 + x_2^2} + \\ \eta_m(x_I - x_I^s, x_2 x_3 - x_3^s) \mathbf{n}_m \cdot \nabla \sqrt{(R^s)^2 + x_2^2} \quad \text{for } f \rightarrow \infty, \quad (6.2.21)$$

and where

$$R^o = \sqrt{(x_I - x_I^o - x_I^s)^2 + (x_3 - x_3^r)^2} \\ R^s = \sqrt{(x_I - x_I^s)^2 + (x_3 - x_3^s)^2} \quad (6.2.22)$$

The next step is to apply the forward Radon transform with respect to the offset and source coordinates:

$$\hat{\hat{p}}_m(p^o, 0, x_3^r; p^s, 0, x_3^s, f) = \int_{-\infty}^{+\infty} e^{-i2\pi f p^s x_I^s} dx_I^s \\ \int_{-\infty}^{+\infty} \hat{p}_m(x_T^o, x_T^s, f) e^{-i2\pi f p^o x_I^o} dx_I^o. \quad (6.2.23)$$

From the geometry and eq.(6.2.23) it follows immediately that when the  $m$ -th interface is plane we only have a contribution from that interface in the plane  $p^s=0$ , because in that case the scattered field representation of the  $m$ -th interface is independent of  $x^s$ . This implies that the spatial complexity of a non-planar interface has to lead to a certain distribution in the  $p^s$ - $p^o$  domain. After interchanging the order of integrations this results in the following representation

$$\hat{\hat{p}}_m(p^o, 0, x_3^r; p^s, 0, x_3^s, f) = \frac{-i2\pi f}{v_m} \hat{S}(f) \int_{x_T \in \Lambda_m} \sqrt{(\partial_I h_m(x_I, 0))^2 + 1} dx_I \\ \int_{-\infty}^{+\infty} dx_I^s \int_{-\infty}^{+\infty} dx_I^o \int_{-\infty}^{+\infty} B_m e^{i2\pi f \Phi} dx_2. \quad (6.2.24)$$

where  $\partial_I h_m$  denotes the spatial derivative of  $h_m$  with respect to  $x_I$  and  $\Lambda_m$  represents the cross-section of the interface  $Q_m$ . In this cross-section, the problem is 2D but since we are dealing with point source data, the present problem is called  $2\frac{1}{2}$ D (Bleistein, 1986). The phase function  $\Phi = \Phi(x, x_I^o, x_I^s)$  is given by



$$\Phi = \frac{\sqrt{(R^o)^2 + x_2^2} + \sqrt{(R^s)^2 + x_2^2}}{v_m} - p^s x_1^s - p^o x_1^o. \quad (6.2.25)$$

In order to evaluate the contribution of the right-hand side of eq.(6.2.24) for large frequencies,  $f \rightarrow \infty$ , we employ the method of stationary phase to the triple integral with respect to  $x_2$ ,  $x_1^o$  and  $x_1^s$  (Appendix, A.2). The stationary points follow from

$$\frac{\partial \Phi}{\partial x_2} = \frac{x_2}{v_m} \left( \frac{1}{\sqrt{(R^o)^2 + x_2^2}} + \frac{1}{\sqrt{(R^s)^2 + x_2^2}} \right) = 0, \quad (6.2.26)$$

$$\frac{\partial \Phi}{\partial x_1^o} = \frac{x_1^o + x_1^s - x_1}{v_m \sqrt{(R^o)^2 + x_2^2}} - p^o = 0, \quad (6.2.27)$$

and

$$\frac{\partial \Phi}{\partial x_1^s} = \frac{x_1^o + x_1^s - x_1}{v_m \sqrt{(R^o)^2 + x_2^2}} + \frac{x_1^s - x_1}{v_m \sqrt{(R^s)^2 + x_2^2}} - p^s = 0, \quad (6.2.28)$$

which give respectively

$$x_2 = 0, \quad (6.2.29)$$

$$x_1^s = x_1 + \frac{(p^s - p^o)(x_3 - x_3^s)}{q_m^s}, \quad \text{with } q_m^s = \sqrt{\frac{I}{v_m^2} - (p^s - p^o)^2}, \quad (6.2.30)$$

and

$$x_1^o = \frac{(p^o - p^s)(x_3 - x_3^s)}{q_m^o} + \frac{p^o(x_3 - x_3^r)}{q_m^o}, \quad \text{with } q_m^o = \sqrt{\frac{I}{v_m^2} - (p^o)^2}. \quad (6.2.31)$$

To determine the amplitude after the asymptotic approximation, we need the values of the second derivatives in the stationary points. These are obtained as

$$\frac{\partial^2 \Phi}{(\partial x_2)^2} = \frac{1}{v_m} \left( \frac{1}{R^o} + \frac{1}{R^s} \right) = \frac{q_m^o}{x_3 - x_3^r} + \frac{q_m^s}{x_3 - x_3^s}, \quad (6.2.32)$$

$$\frac{\partial^2 \Phi}{\partial x_1^o \partial x_2} = \frac{\partial^2 \Phi}{\partial x_2 \partial x_1^o} = 0, \quad (6.2.33)$$

$$\frac{\partial^2 \Phi}{(\partial x_1^o)^2} = \frac{v_m^2 (q_m^o)^3}{x_3 - x_3^r}, \quad (6.2.34)$$

$$\frac{\partial^2 \Phi}{(\partial x_1^s)^2} = \frac{v_m^2 (q_m^o)^3}{x_3 - x_3^r} + \frac{v_m^2 (q_m^s)^3}{x_3 - x_3^s}, \quad (6.2.35)$$

and

$$\frac{\partial^2 \Phi}{\partial x_1^o \partial x_1^s} = \frac{v_m^2 (q_m^o)^3}{x_3 - x_3^r}. \quad (6.2.36)$$

Then the determinant, denoted by  $Z$  in eq.(A.2.16), yields

$$Z = \frac{v_m^4 (q_m^s)^3 (q_m^o)^3 \left( q_m^o (x_3 - x_3^s) + q_m^s (x_3 - x_3^r) \right)}{(x_3 - x_3^r)^2 (x_3 - x_3^s)^2}. \quad (6.2.37)$$

Next, when evaluating the integral on the right hand side of eq.(6.2.24) at the three stationary points (eqs.(6.2.22)-(6.2.24)) following eq.(A.2.16), the phase function is approximated by

$$\Phi(p^o, x_3^r; p^s, x_3^s; x_T) = q_m^o (x_3 - x_3^r) + q_m^s (x_3 - x_3^s) - p^s x_1. \quad (6.2.38)$$

$B_m$  in eq.(6.2.21) must still be evaluated. This results in

$$\begin{aligned}
 n_m \cdot \nabla R^o &= \frac{-(x_1 - x_1^o - x_1^s) \partial_1 h_m + (x_3 - x_3^r)}{R^o \sqrt{1 + (\partial_1 h_m)^2}} \\
 n_m \cdot \nabla R^s &= \frac{-(x_1 - x_1^s) \partial_1 h_m + (x_3 - x_3^s)}{R^s \sqrt{1 + (\partial_1 h_m)^2}} ,
 \end{aligned} \tag{6.2.39}$$

and, after substitution of the stationary points of eqs.((6.2.29)-(6.2.31)), in

$$\begin{aligned}
 n_m \cdot \nabla R^o &= \frac{[p^o \partial_1 h_m + q_m^o] v_m}{\sqrt{1 + (\partial_1 h_m)^2}} \\
 n_m \cdot \nabla R^s &= \frac{[(p^s - p^o) \partial_1 h_m + q_m^s] v_m}{\sqrt{1 + (\partial_1 h_m)^2}} .
 \end{aligned} \tag{6.2.40}$$

Finally, substituting eqs.(6.2.37), (6.2.38) and (6.2.40) into eq.(6.2.24) leads to

$$\begin{aligned}
 \widehat{\widehat{p_m(p^o, x_3^r; p^s, x_3^s, f)}} &= \frac{\widehat{S(f)}}{8\pi \sqrt{-i f q_m^s q_m^o v_m}} \\
 &\int_{x_T \in \Lambda_m} B'_m e^{i2\pi f (q_m^o(x_3 - x_3^r) + q_m^s(x_3 - x_3^s) - p^s x_1)} dx_1 , \tag{6.2.41}
 \end{aligned}$$

where the amplitude factor  $B'_m(p^o, x_3^r; p^s, x_3^s)$  is given by

$$\begin{aligned}
 B'_m &= \frac{v_m \eta_m \left( \frac{-p^o_1(x_3 - x_3^r)}{q_m^o}, 0, x_3 - x_3^r \right) [p^o \partial_1 h_m + q_m^o]}{\sqrt{v_m q_m^o(x_3 - x_3^s) + v_m q_m^s(x_3 - x_3^r)}} + \\
 &\frac{v_m \eta_m \left( \frac{-(p^s_1 - p^o_1)(x_3 - x_3^s)}{q_m^s}, 0, x_3 - x_3^s \right) [(p^s - p^o) \partial_1 h_m + q_m^s]}{\sqrt{v_m q_m^o(x_3 - x_3^s) + v_m q_m^s(x_3 - x_3^r)}} . \tag{6.2.42}
 \end{aligned}$$

### 6.3 Application: a pre-stack migration procedure

To carry out our migration procedure, we start from eq.(6.2.1) and consider one interface, for example the  $m$ -th interface. Eq.(6.2.1) ignores any interaction between interfaces. Thus, no internal multiples are considered which means that multiple reflections are treated as primary reflections. This is the conventional assumption for migration. The first step is to perform a source and receiver alignment once by multiplying eq.(6.2.41) by the factor  $8\pi \sqrt{-i} \exp(i2\pi f q_1^o(x_3^r - x_3^s))$  and by a scaled filter,  $\sqrt{q_m^s q_m^o} v_m$  for each interface. Note that the source and receiver alignment is carried out for the first interface only. Now, let us define

$$\widehat{\widehat{P}}_m(p^o, p^s, f) = \sqrt{q_m^s q_m^o} v_m \widehat{\widehat{P}}_m(p^o, x_3^r; p^s, x_3^s, f). \quad (6.3.1)$$

Then, eq.(6.2.41) is rewritten as

$$\widehat{\widehat{P}}_m(p^o, p^s, f) = \widehat{S}(f) \int_{x_T \in \Lambda_m} B_m' e^{i2\pi f (\Psi_m T_m - p^s x_1)} dx_1. \quad (6.3.2)$$

where the normalised slowness function  $\Psi_m = \Psi_m(p^o, p^s)$  is given by

$$\Psi_m(p^o, p^s) = \frac{v_m}{2} (q_m^o + q_m^s), \quad (6.3.3)$$

while the laterally variant two-way traveltime,  $T_m = T_m(x_1)$  with respect to the source level follows from

$$T_m(x_1) = \frac{2(h_m - x_3^s)}{v_m}. \quad (6.3.4)$$

The next step is to introduce the domain  $\mathcal{D}_m^p$ , characterized by the dip-slowness,  $p^d_m \in \mathcal{D}_m^d$  according to

$$\mathcal{D}_m^p(p^d_m) = \left\{ (p^o, p^s) \in \mathcal{R}^2 \mid p^s = p^d_m \Psi_m \right\}, \quad (6.3.5)$$

where  $(p^o, p^s)$  pairs are chosen such that  $\Psi_m \leq 1$ , which is the reliable area of the stationary phase analysis. The family of the  $(p^o, p^s)$  pairs belonging to a dip-slowness  $p^d_m$  are called dip slowness curves (eq.(6.3.5)) and they are explained in more detail in section 6.4.

When we evaluate eq.(6.3.2) in this domain,  $\mathcal{D}_m^p$ , we obtain

$$\begin{aligned} \widehat{\widehat{P}}_m(p^o, p^s, f) &= \widehat{S}(f) \int_{x_T \in \Lambda_m} B'_m e^{i2\pi f \Psi_m(T_m - p_m^d x_1)} dx_1, \\ &\text{for } (p^o, p^s) \in \mathcal{D}_m^p(p_m^d) \end{aligned} \quad (6.3.6)$$

Operating in this way we have achieved a separation of the typical interface part  $(T_m - p_m^d x_1)$  from the  $(p^o, p^s)$  dependent part  $\Psi_m$  in the phase function. Since  $(T_m - p_m^d x_1)$  does not vary for a chosen  $p_m^d$ , the domain  $\mathcal{D}_m^p(p_m^d)$  represents a particular part of the spatial complexity of the interface. When for example,  $p_m^d = 0$ , we are considering the plane  $p^s = 0$  and in that case,  $\Psi_m$  presents the well-known elliptical move-out.

In order to correct for the phase difference of the elliptical or semi-elliptical move-out, we take the mean value of the frequency-scaled version of the quantity of eq.(6.3.6) over the domain  $\mathcal{D}_m^p(p_m^d)$  as

$$\widehat{\widehat{P}}_m^d(p_m^d, f) = \frac{\iint_{(p^o, p^s) \in \mathcal{D}_m^p(p_m^d)} \widehat{\widehat{P}}_m(p^o, p^s, \frac{f}{\Psi_m}) d\phi^o d\phi^s}{\iint_{(p^o, p^s) \in \mathcal{D}_m^p(p_m^d)} d\phi^o d\phi^s}. \quad (6.3.7)$$

This results in

$$\widehat{\widehat{P}}_m^d(p_m^d, f) = \int_{x \in \Lambda_m} \widehat{W}_m(x_1, p_m^d, f) e^{i2\pi f (T_m(x_1) - p_m^d x_1)} dx_1, \quad (6.3.8)$$

where

$$\widehat{W}_m(x_1, p_m^d, f) = \frac{\iint_{(p^o, p^s) \in \mathcal{D}_m^p(p_m^d)} \widehat{S}(\frac{f}{\Psi_m}) B'_m d\phi^o d\phi^s}{\iint_{(p^o, p^s) \in \mathcal{D}_m^p(p_m^d)} d\phi^o d\phi^s}. \quad (6.3.9)$$

From eq.(6.3.9), it follows that since  $\Psi_m \leq 1$ ,  $\widehat{W}_m$  is the mean value of the frequency-compressed version of the wavelet weighted by the local plane amplitudes. Furthermore, we recognize here the well-known NMO-stretch of the data as a compression in the frequency domain corresponding with a stretch in the time domain.

The last step is to evaluate eq.(6.3.8). If the frequency  $f$  tends to infinity, the main contribution of the integral of the right hand side of eq.(6.3.8) comes from the stationary point,  $x_I = x_I^{stat}$ , that is

$$\frac{\partial T_m}{\partial x_I} - p_m^d = 0 \quad \text{or} \quad \frac{2}{v_m} \frac{\partial}{\partial x_I} h_m = p_m^d. \quad (6.3.10)$$

This shows immediately the relation of the dip-slowness  $p_m^d$  to the true gradient of the interface. Further, the stationary point is a function of  $p_m^d$ . Therefore, we replace the integration variable  $x_I$  in the expression of  $\widehat{W}_m$  by the stationary point  $x_I^{stat}$ . This does not change the result of the integral on the right hand side of eq.(6.3.8) when  $f$  tends to infinity.  $\widehat{W}_m$  becomes a function of  $p_m^d$  only. But in this case we can reuse the expression of  $p_m^d$  of eq.(6.3.9) and define a function  $\widehat{W}_m(x_I, f)$  as

$$\widehat{W}_m(x_I, f) = \widehat{W}_m \Big|_{p_m^d} = \frac{2}{v_m} \frac{\partial h_m}{\partial x_I}, \quad (6.3.11)$$

which replaces eq.(6.3.8) by

$$\widehat{\widehat{P}}_m^d(p_m^d, f) = \int_{x \in \Lambda_m} \widehat{W}_m(x_I, f) e^{i2\pi f(T_m - p_m^d x_I)} dx_I \quad \text{for } f \rightarrow \infty. \quad (6.3.12)$$

Note that for  $f$  tends to infinity,  $\widehat{\widehat{P}}_m^d$  is the result of a forward Radon transform. Hence, by applying an inverse Radon transform we obtain

$$\widehat{P}_m^d(x_I, f) = \widehat{W}_m(x_I, f) e^{i2\pi f T_m} \quad \text{for } f \rightarrow \infty, \quad (6.3.13)$$

where

$$\widehat{P}_m^d(x_I, f) = f \int_{p_m^d \in \mathcal{D}_m} \widehat{\widehat{P}}_m^d(p_m^d, f) e^{i2\pi f p_m^d x_I} dp_m^d. \quad (6.3.14)$$

When we subsequently transform eq.(6.3.13) using eq.(2.2.9) back to the time domain and observe that eq.(6.3.13) holds for  $f \rightarrow \infty$ , we obtain

$$\lim_{t \downarrow T_m(x_I)} P_m^d(x_I, t) = \overline{W}_m[x_I, t - T_m(x_I)]. \quad (6.3.15)$$

It is clear that the space-time function of eq.(6.3.15) starts to act at the instant ( $T_m(x_1) = 2(h_m - x_3^s)/v_m$ ), so that we get a space-time image of the  $m$ -th interface. When we repeat this procedure for all the interfaces, the complete pre-stack migrated section is obtained.

In order to calculate the  $p^d_m$  dip slowness curves, we need to know the rms-velocities. To obtain the set of rms-velocities, we perform a conventional velocity analysis in the  $p^s=0$  plane where, due to the plane layer assumption, we expect to have the best control on determining the velocities. If the plane layer assumption does not hold when we have steep dipping interfaces or salt-tectonics for example, we have to examine the data in the  $p^o$ - $p^s$  domain and select planes, which show high concentration of energy and follow the dip-slowness curves according to eq.(6.3.5). These selected planes will display quasi-elliptic events as well, and again velocity analysis can be performed.

#### 6.4 Problems and limitations due to the method and due to the data

The input data set for the double Radon transform for the 2D case is a seismic line and for the 3D case is a seismic survey. Because of the use of the FFT in the algorithm the spacing between the subsequent sources as well as the spacing between the receivers has to be constant. If this is not the case, the data have to be interpolated.

When the data set is transformed into the double Radon domain, there are two main restrictions for our migration algorithm. The first restriction is the limitation of the Radon transform itself, extensively discussed in Chapter 5 and the second restriction is the maximum retrievable dip, which is present in the data itself. To explain the latter, the dip slowness curves are discussed.

##### *Dip slowness curves*

The dip slowness curves are given by eq.(6.3.3) which is repeated for convenience,

$$p^s = \frac{v_m}{2} (q_m^o + q_m^s) p^d_m, \quad (6.4.1)$$

and are symmetric with respect to  $p^s=2p^o$ . This is easily seen in Fig.6.4.1. When we take for example the pair  $(p^o, p^s)$  and keep the  $p^s$ -value the same according to reciprocity (eq.(6.2.11)) its equivalent is given by the pair  $(p^s, p^o, p^s)$ . Substituting  $(p^s, p^o)$  for  $p^o$  in eq.(6.4.1) does not alter eq.(6.4.1) nor does it change the phase function of eq.(6.3.8) or the amplitude factor of eq.(6.2.42), as expected.

Then solving eq.(6.4.1) gives

$$p^s = \frac{\frac{(p^d m v_m)^2}{2} p^o + p^d m v_m \sqrt{\frac{1}{v_m^2} - (p^o)^2}}{1 + \frac{(p^d m v_m)^2}{4}} \quad (6.4.2)$$

However,  $p^s$  and  $p^o$  are valid only within the theoretical outer limits, that is  $p^s \leq p^o \pm 1/v_m$  and  $p^o \leq \pm 1/v_m$ , shown in Fig.6.4.1. These theoretical limits are simply based on the condition that  $q^s_m$  and  $q^o_m$  must be real (eqs.(6.2.30) and (6.2.31)).

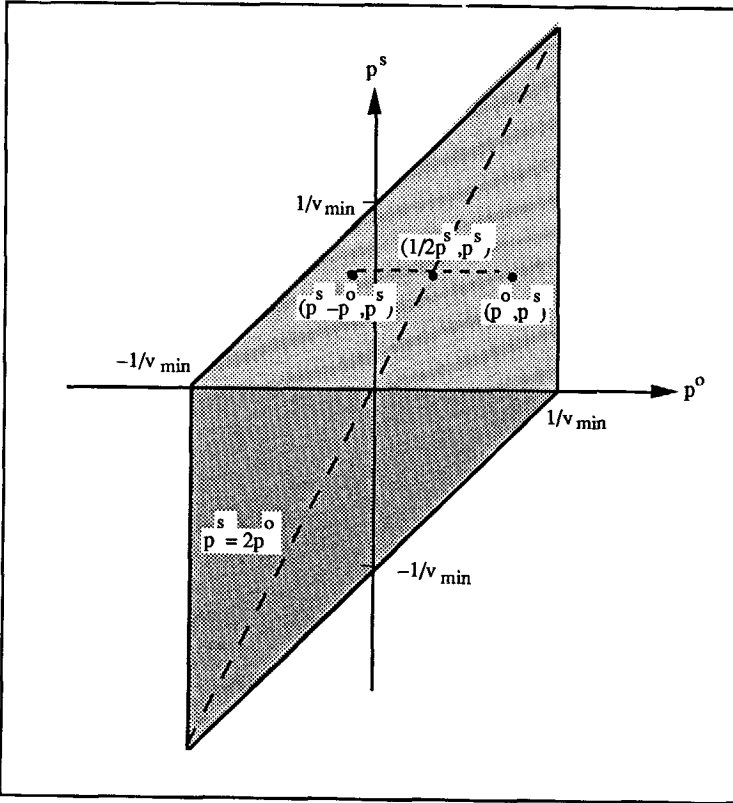


Fig.6.4.1: The top view of the  $p^s$ - $p^o$  plane with the axis of symmetry, the theoretical limits and reciprocity.

This means that, due to the theoretical limits,  $p^s \leq p^o \pm 1/v_m$ , the following constraint is imposed on  $p^s$



$$|p^s| \leq \frac{\frac{(p_m^d v_m)^2}{2}}{v_m \left( \frac{(p_m^d v_m)^2}{4} + 1 \right)} \quad (6.4.3)$$

The figure shown below shows one family of dip slowness curves,  $p_m^d$  belonging to a certain rms-velocity. The increment in the dip-slowness is chosen constant. Furthermore, the theoretical limits (eq(6.4.4)) are drawn in solid lines and the more realistic limits (eqs.(6.4.5) & (6.4.6)) in dashed lines, which are discussed below.

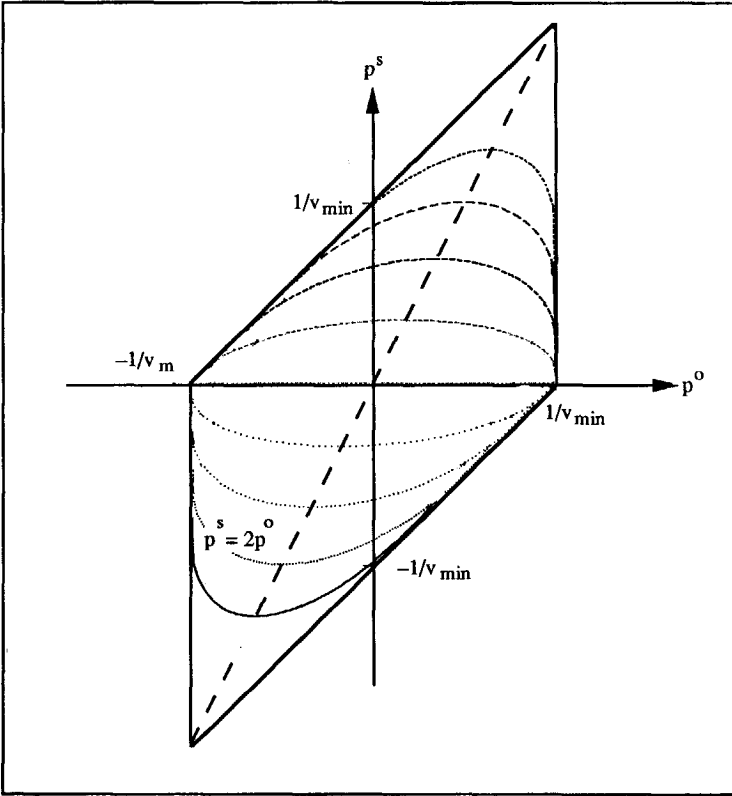


Fig.6.4.2: The top view of the  $p^s$ - $p^o$  plane with dip slowness curves, the theoretical and practical limits.

The inequality of eq.(6.4.3) is valid if the offset recorded for the data set is infinite. In reality, this is never obtained. Therefore, following the same argumentation as in Chapter 5, the two stationary points, given in eqs.(6.2.27) and (6.2.28) define the limits wherein the data are valid in the double Radon domain. Those limits are then given by

$$|p^o| \leq \frac{|x_1^o + x_1^s - x_1|}{v_m R^o}, \quad (6.4.5)$$

and

$$|p^s| \leq p^o + \frac{|x_1^s - x_1|}{v_m R^s}. \quad (6.4.6)$$

where  $|x_1^o + x_1^s - x_1|$  is the length of the seismic line.

As is clear from Fig.6.4.1 and eqs (6.4.5) and (6.4.6), the maximum possible observable dip in the data is determined by the offset, the depth of the interface and its rms-velocity. That is, the higher the velocity and the deeper the interface, the less the maximum retrievable dip for that particular interface. When the maximum retrievable dip is not enough, the offset should be increased. Thus, when the data set is transformed into the double Radon domain, the maximum chosen  $p$ -value for the offset as well as for the source has to be calculated in consideration of eqs.(6.4.5) and (6.4.6). Otherwise, we are looking at artifacts of the transform due to lack of data.

## 6.5 *The computational procedure and the presentation of the data*

### *Computational procedure*

Fig.6.5.1 shows the computational procedure for the double Radon transform. The first step is to apply a Radon transform to all the shot gathers. Then the data set is reordered into constant  $p^o$ -gathers. After that, the second Radon transform is applied resulting in the  $p^s$ - $p^o$  response of the complete seismic line.

The pre-stack migration scheme is outlined in the next figure. When the double Radon transform is applied to the data set, the first step is to perform a source and receiver alignment with the scaled filter according to eq.(6.3.1). Note that if the depth of source and receiver are equal, the correction for the alignment becomes zero. Then, after a conventional velocity analysis in the  $\tau$ - $p$  domain for the plane  $p^s=0$ , the first picked rms-velocity is used to calculate its family of  $p_m^d$  dip slowness curves. These curves gives us the scaling of the frequency for each  $(p^o, p^s)$  pair of the data set.

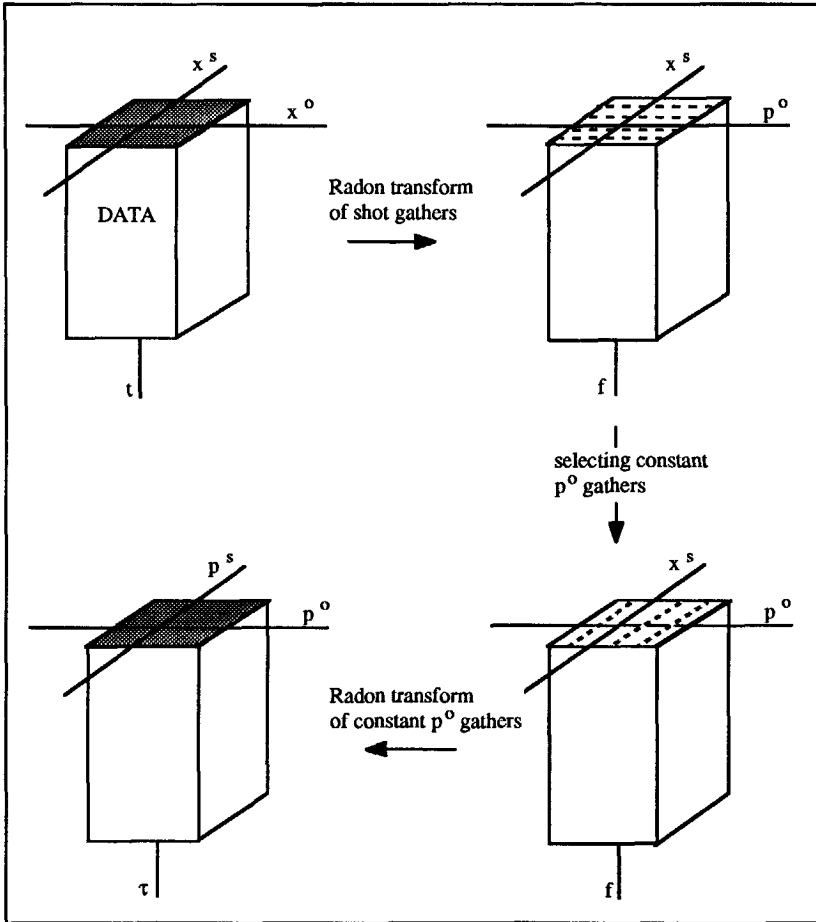


Fig.6.5.1: Overview of the numerical procedure of the double Radon transform.

Then, taking the mean value of the frequency-scaled data (eq.(6.3.7)) results in a  $\tau$ - $p$  section, ready to be inverse Radon transformed. When this procedure is repeated for every rms-velocity, that is for every interface, the pre-stack migration is completed. The only step left, is to select the correct time window from each generated section and store them into one final section to visualize the complete pre-stack migrated section of the whole seismic line.

### Presentation of the data

Of each data set, three different kind of pictures are shown in the  $p^s$ - $p^o$  domain. In order to show the complexity of the data set in the  $p^s$ - $p^o$  domain, stacking in the time direction is performed. The values of each  $(p^s, p^o)$  trace is squared and summed, giving one value (Fig.6.5.3). This summed value gives a measure for the amount of energy present in that particular  $(p^s, p^o)$  pair. In stead of applying this procedure over the whole length of the trace, also

a certain part of the trace can be used. In this way more detailed information is obtained for certain reflectors.

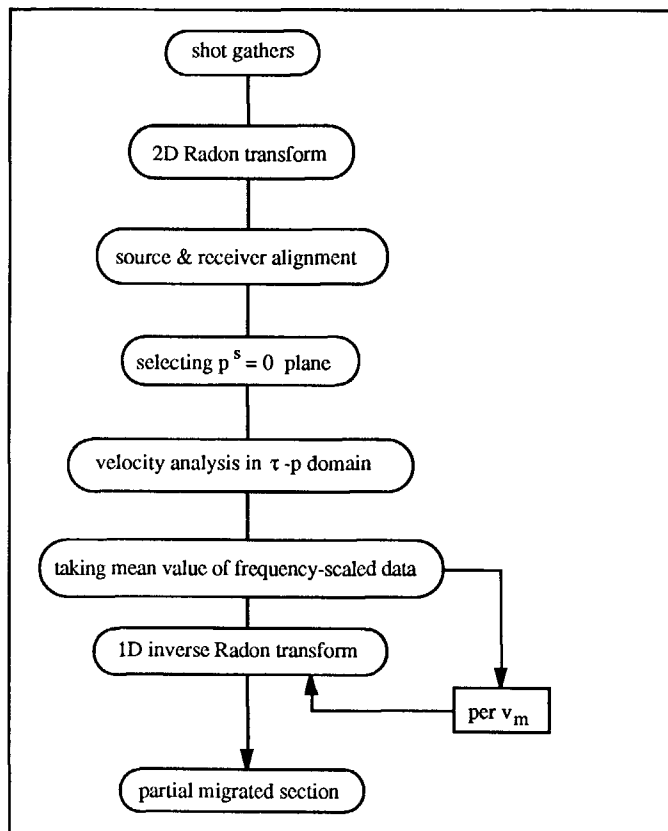


Fig.6.5.2: The processing steps of our pre-stack migration procedure in  $p^s$ - $p^o$  domain.

Further, the plane  $p^s=0$  which shows all the horizontal information present in the data, and the plane  $p^o=0$  are selected. The latter gives information about the number of main events present in the data and the character of these main events (dipping or horizontal and the consistency in dip). The third kind of picture displays the result of pre-stack migration, that is the mean-valued frequency-scaled data in the  $\tau$ - $p$  domain and the final result, its  $t$ - $x$  response. Of the first three synthetic examples, two more pictures are displayed. One plane, selected from the  $p^o$ - $p^s$  data set for a constant  $p^o_m$  before the frequency scaling and the same selected plane after the frequency scaling. Then, quasi-elliptic events becomes flattened.

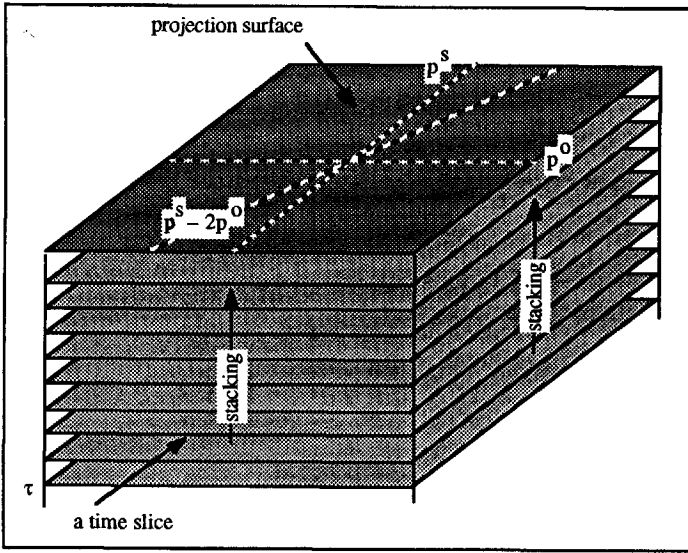


Fig.6.5.3: The stacking procedure with respect to time.

## 6.6 Data examples

Five synthetic data examples and one land data set are shown. The first four models are calculated acoustically with point scatterers (one interface consists of an infinite number of point scatterers) and the last model is generated with an acoustic finite difference scheme. All the synthetic data sets consist of 127 shot gathers and each gather is simulated with 127 receivers in a split spread configuration. When the shot moves along the line, the receivers do the same. The increment between two successive shots and the distance between two receivers is held the same as well as the depth of source and receiver. A section of each model is shown.

### *Four point scatterers, all at the same spatial position*

In the first example, we consider four point scatterers buried in a homogeneous background and they are placed beneath the centre midpoint. This example was used originally by Yilmaz (1987, p 337).

Fig.6.6.1 shows the depth of the four point scatterers, while the next figure displays the four subsequent stacked time slices. The spatial increment of two successive sources as well as the receiver spacing is 15 m and the velocity is chosen to be 3000 m/s. Further,  $\Delta p^s$  and  $\Delta p^o$  equal  $4.4 \times 10^{-6}$  s/m. Because diffractors are modelled, the energy is scattered over the whole  $p^o$ - $p^s$  space with no particular dip showing. Note the axis of symmetry,  $p^s = 2p^o$  in all four time windows and the similarity between the time slices. In Fig.6.6.3a and 6.6.3b, the two selected planes,  $p^o = 0$  and  $p^s = 0$  both show symmetric elliptical events. Fig.6.6.3c depicts how the frequency scaling performs on the plane,  $p^s = 0$ , Fig.6.6.3a. At both ends of the section after the frequency scaling,

some stretching of the wavelet is visible. The last picture of this example is the mean-valued data set in  $\tau$ - $p$  (Fig.6.6.4a) and the migrated result in  $t$ - $x$ . As we can see the four scatterers are collapsed into points.

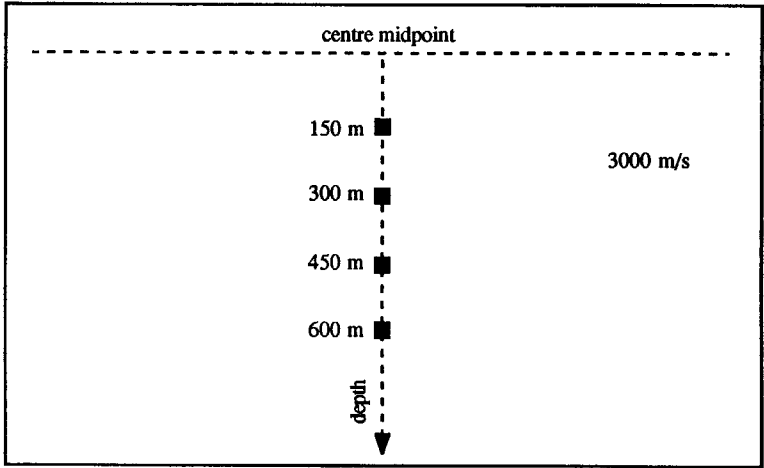


Fig.6.6.1: The  $x_3$ - $x_1$  configuration of the first model.

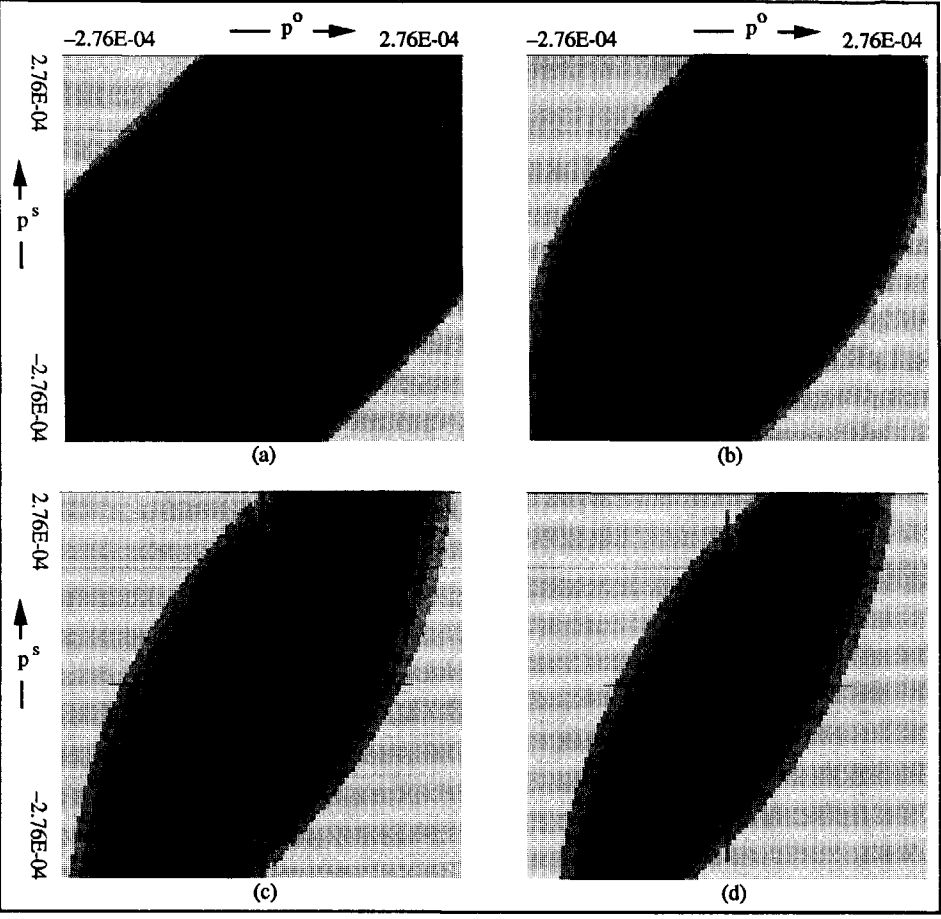


Fig.6.6.2: The "stacked" time slices: (a) 0.05 - 0.15 s, (b) 0.15 - 0.25 s, (c) 0.25 - 0.35 s and (d) 0.35 - 0.45 s.

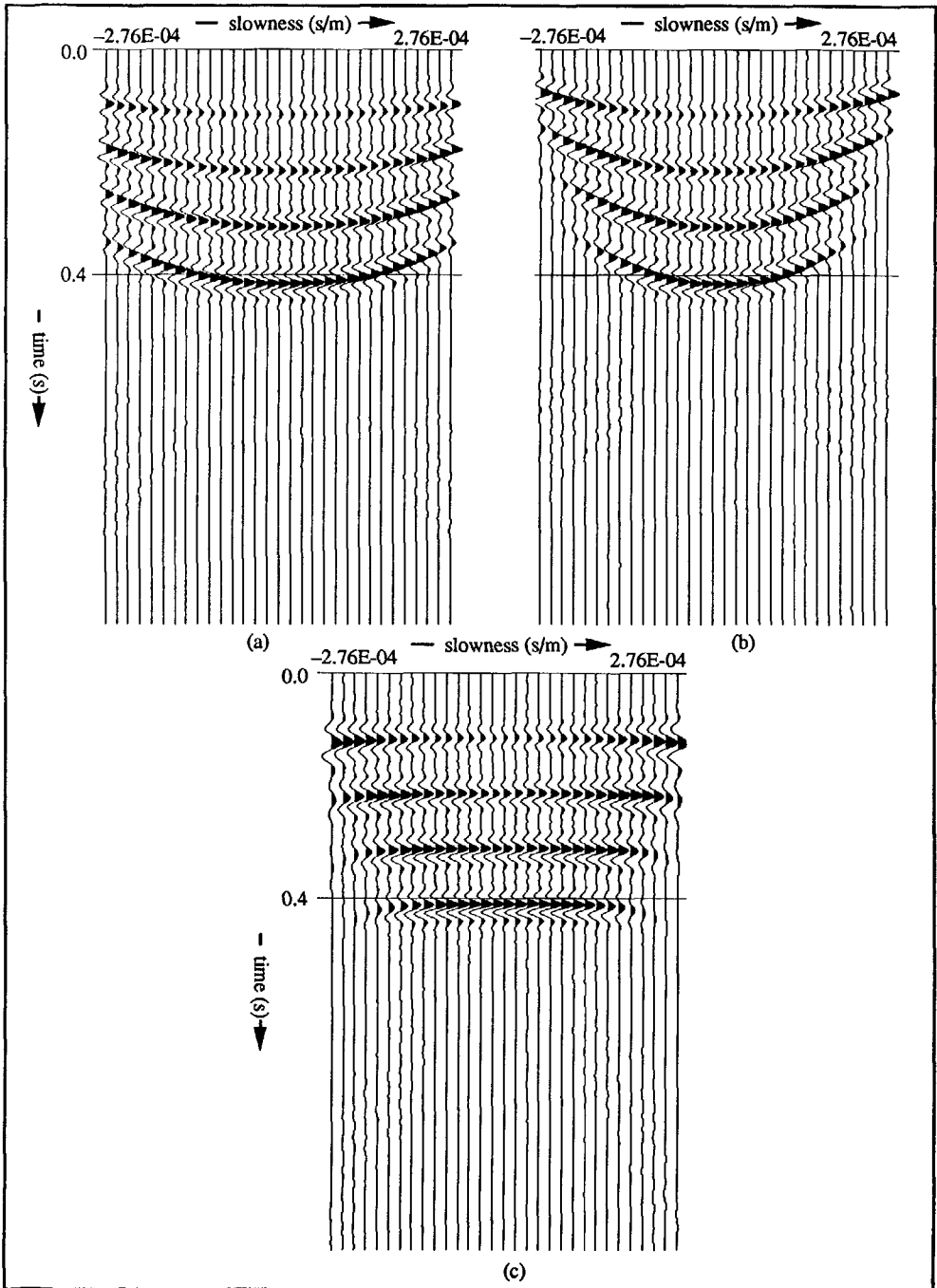


Fig.6.6.3: The selected planes: (a)  $p^o=0$  and (b)  $p^s=0$  and (c) after the frequency scaling of (a) following eq.(6.3.7).



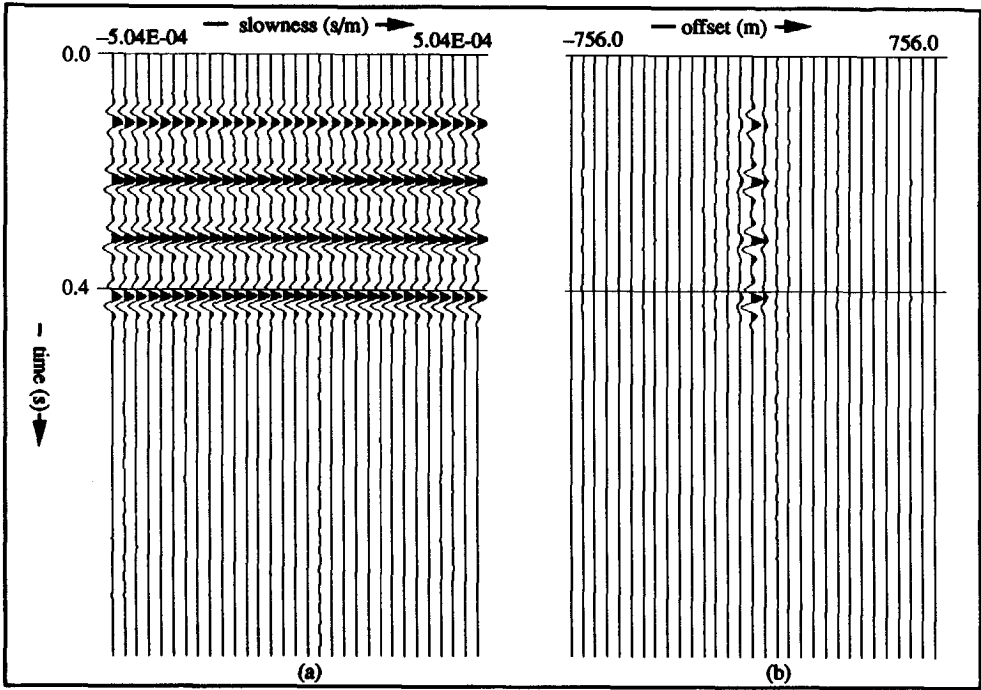


Fig.6.6.4: The pre-stack migrated result of the complete line in (a)  $\tau$ - $p$  and in (b)  $t$ - $x$ .

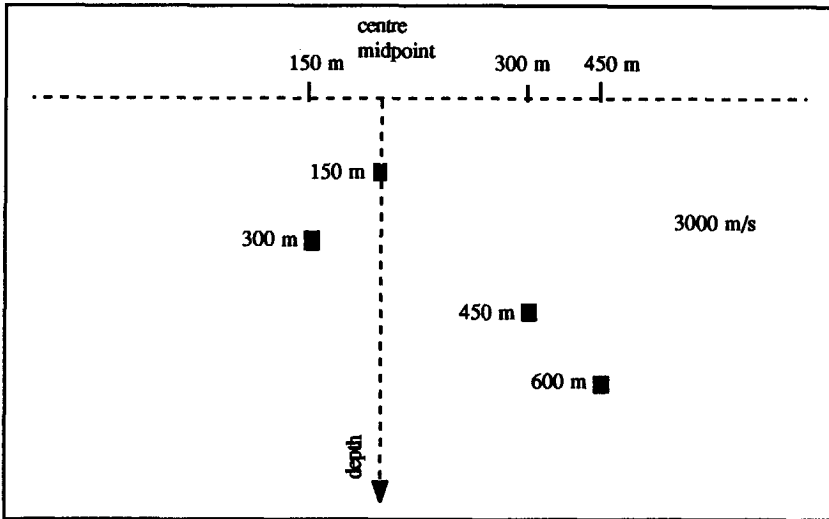


Fig.6.6.5: The  $x_3$ - $x_1$  configuration of the second model.

#### Four point scatterers, each at different spatial positions

The next example has a slightly different configuration (Fig.6.6.5). Now, the four scatterers are placed outside the centre midpoint, showing the lateral performance of our method. The input parameters of the data set are held the same as in the previous model. When we look at the "stacked" time slices (Fig.6.6.6) the axis of symmetry is still present but the energy distribution of the data set has changed and its maximum value is shifted either to the positive or to the negative  $p^s$ -value depending on the spatial position of the scatterer. If the scatterer is positioned at the right hand side of the centre midpoint, the maximum is moved to the positive  $p^s$ -value and vice-versa. Another difference with the previous example is the selected plane,  $p^o=0$  (Fig.6.6.7a) because three out of the four scatterers do not behave symmetrically any more with respect to the centre midpoint. As we see, the quality of the migrated result (Fig.6.6.8b) is not influenced by the spatial position of the scatterers. The four scatterers are migrated to exactly the same place where they were positioned in the first place.

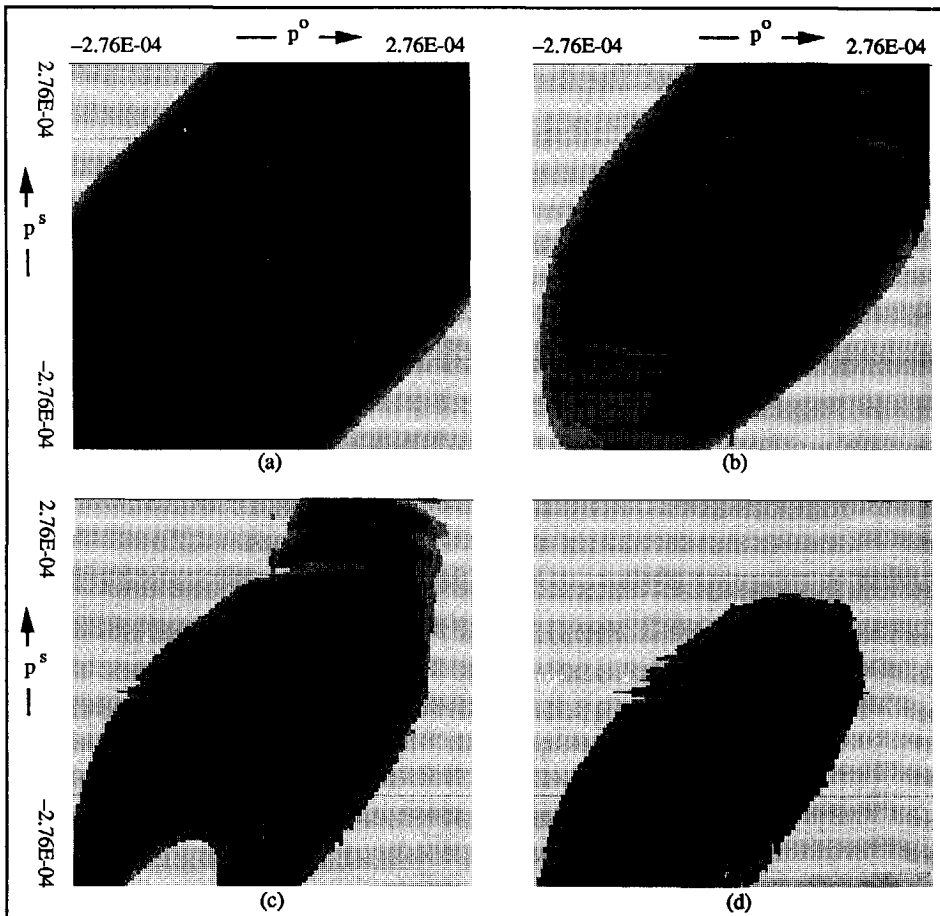


Fig.6.6.6: The "stacked" time slices: (a) 0.05 - 0.15 s, (b) 0.15 - 0.25 s, (c) 0.25 - 0.35 s and (d) 0.35 - 0.45 s.

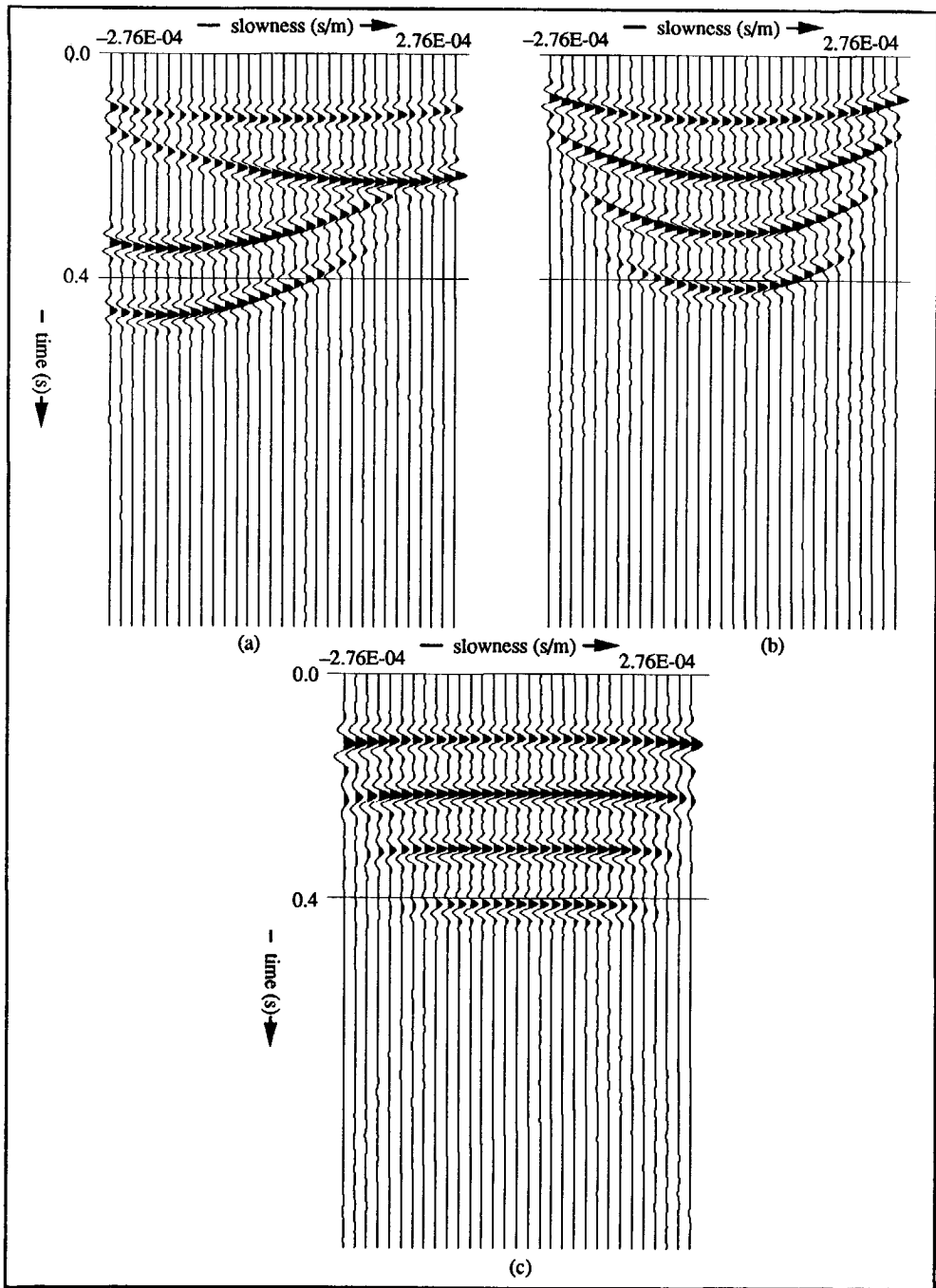


Fig.6.6.7: The selected planes: (a)  $p^0=0$  and (b)  $p^s=0$  and (c) after the frequency scaling of (a) following eq.(6.3.7).

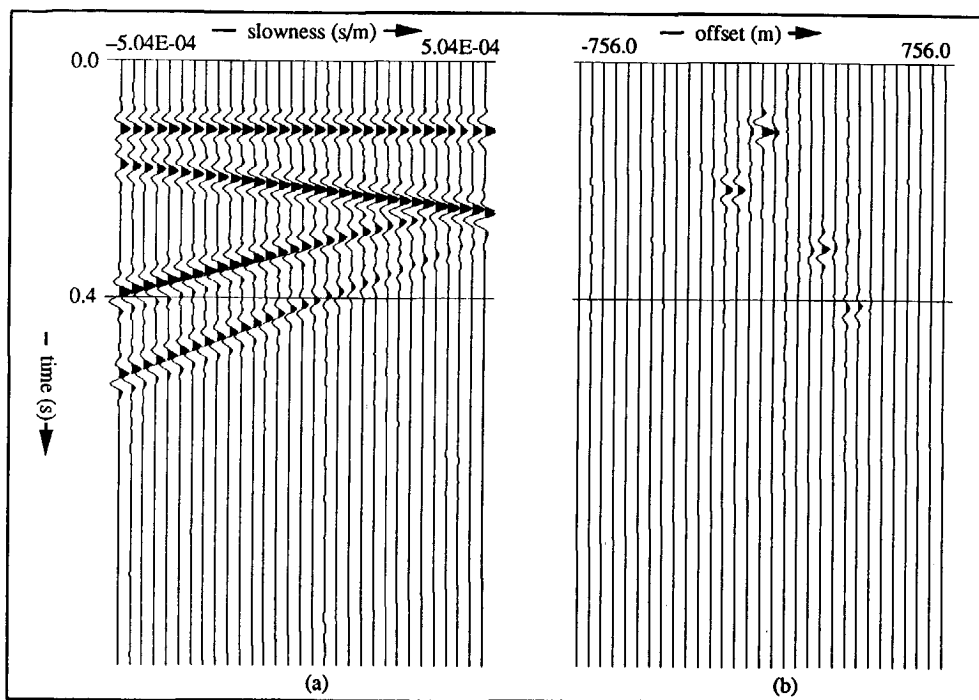


Fig.6.6.8: The pre-stack migrated result of the complete line in (a)  $\tau$ - $p$  and in (b)  $t$ - $x$ .

### A constantly dipping interface

The third model contains one dipping interface of finite length. The spatial increment of two successive sources and the receiver spacing is 12 m where the velocity is chosen to be 1500 m/s. Further,  $\Delta p^s$  and  $\Delta p^o$  equal  $8.0E-6$  s/m.

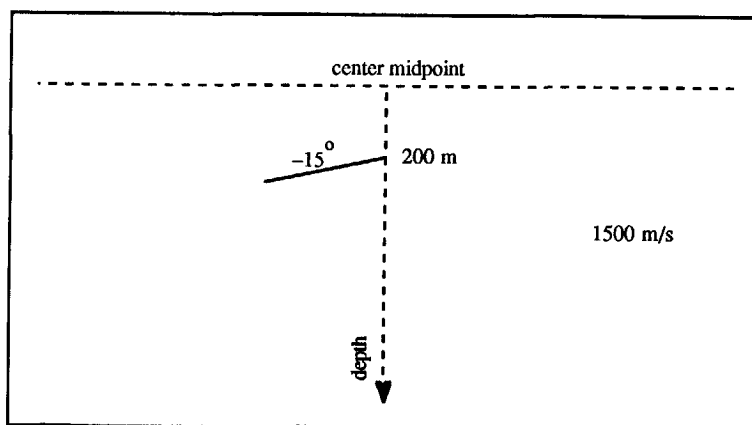


Fig.6.6.9: The  $x_3$ - $x_1$  configuration of the third model.

Because there is only one event in the data set, the time slice is "stacked" over the whole time window (Fig.6.6.10). Further, the event is mapped into a broad band of energy and not into a narrow zone because of the diffraction energy of both ends of the finite interface. The centre of the zone gives us the exact dip of the interface, which in this case is 15 degrees. Then, Fig.6.6.11 shows in (a) as well as in (b) two elliptic events originating from the ends of the interface as diffraction energy. If the interface has been of infinite length, only one elliptic event would show. Again, a plane is selected in the  $p^o$ - $p^s$  space and depicted before and after the frequency scaling is applied (Fig.6.6.11c and 6.6.11d). Because of the large move-out at the maximum  $p$ -value, stretching of the wavelet becomes visible. Fig.6.6.12 shows the final migrated result with the correct position and dip of the interface.

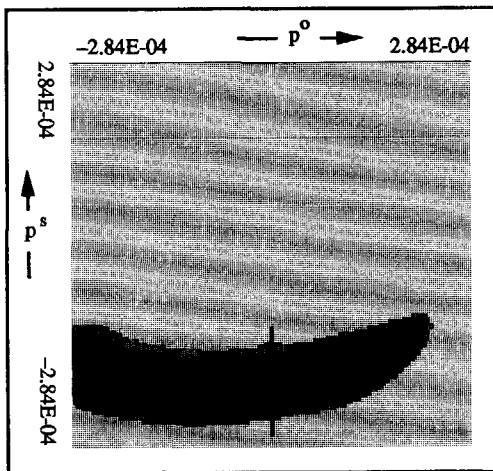


Fig.6.6.10: The "stacked" time slice (0.0 - 1.0 s).

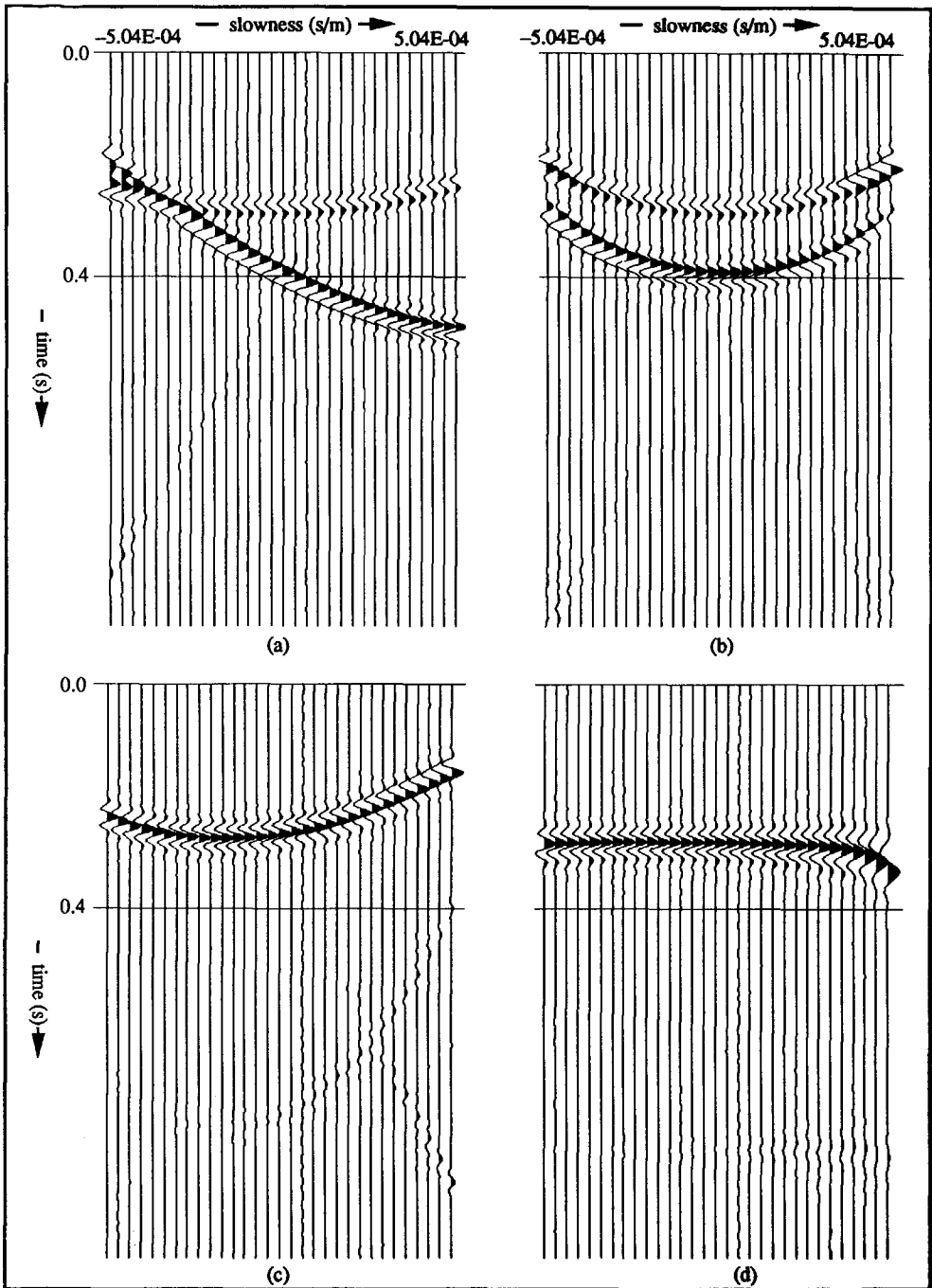


Fig.6.6.11: The selected planes: (a)  $p^o=0$  and (b)  $p^s=0$  and a selected  $p_m^d$  curve before (c) and after (d) the frequency scaling according to eq.(6.3.7).

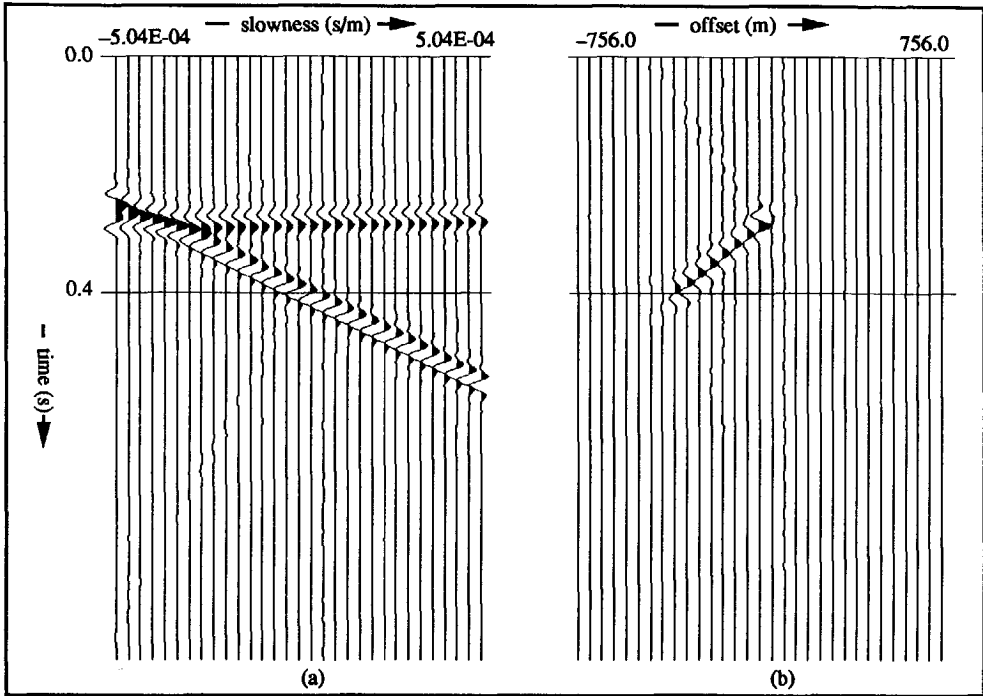


Fig.6.6.12: The pre-stack migrated result of the complete line in (a)  $\tau$ - $p$  and in (b)  $t$ - $x$ .

#### A pyramid-shape interface

The fourth model has a pyramid-shaped interface with a horizontal part at both ends. The  $\Delta x$  of source and receiver are again 12 m and the velocity is 1500 m/s. Further,  $\Delta p^s$  and  $\Delta p^o$  equal  $4.5E^{-6}$  s/m.

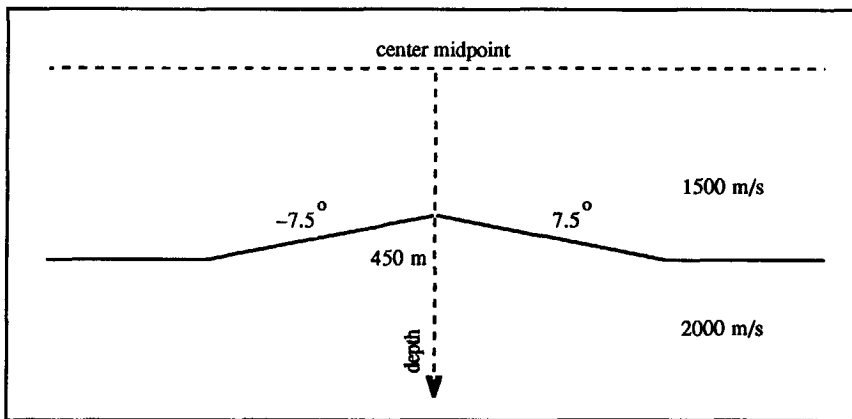


Fig.6.6.13: The  $x_3$ - $x_1$  configuration of the fourth model.

When we look at the time slice (Fig.6.6.14), three main contributions are visualized. One contribution of the two horizontal parts of the interface, one of the positive dipping part and one of the negative dipping part. Furthermore, all three contributions are connected with one another because of the diffraction energy, caused by the sudden change in dip of the interface. Then the effect of our migration procedure becomes again clear when we compare Fig.6.6.15b with Fig.6.6.16a. At both ends of the section, the events are flattened. The final migrated section (Fig.6.6.16b) shows the interface accurately. Note the collapse of the diffraction energy at the top of the interface.

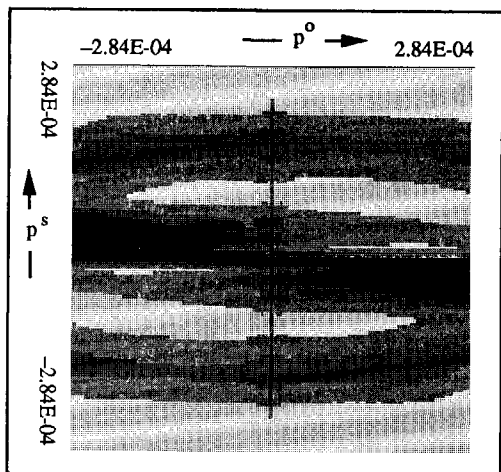


Fig.6.6.14: The "stacked" time slice (0.0 - 1.0 s).



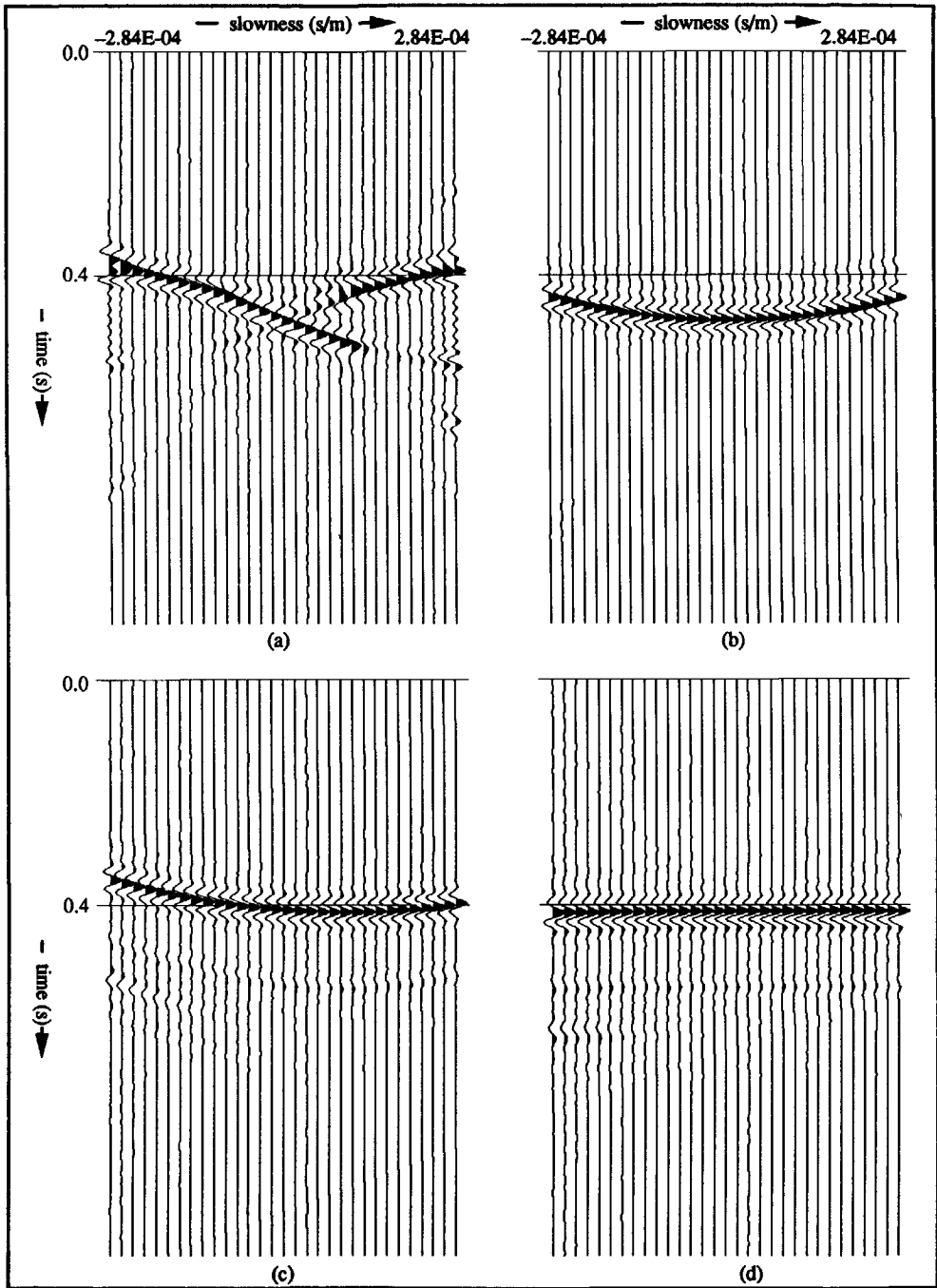


Fig.6.6.15: The selected planes: (a)  $p^o=0$  and (b)  $p^f=0$  and a selected  $p_m^d$  curve before (c) and after (d) the frequency scaling according to eq.(6.3.7).

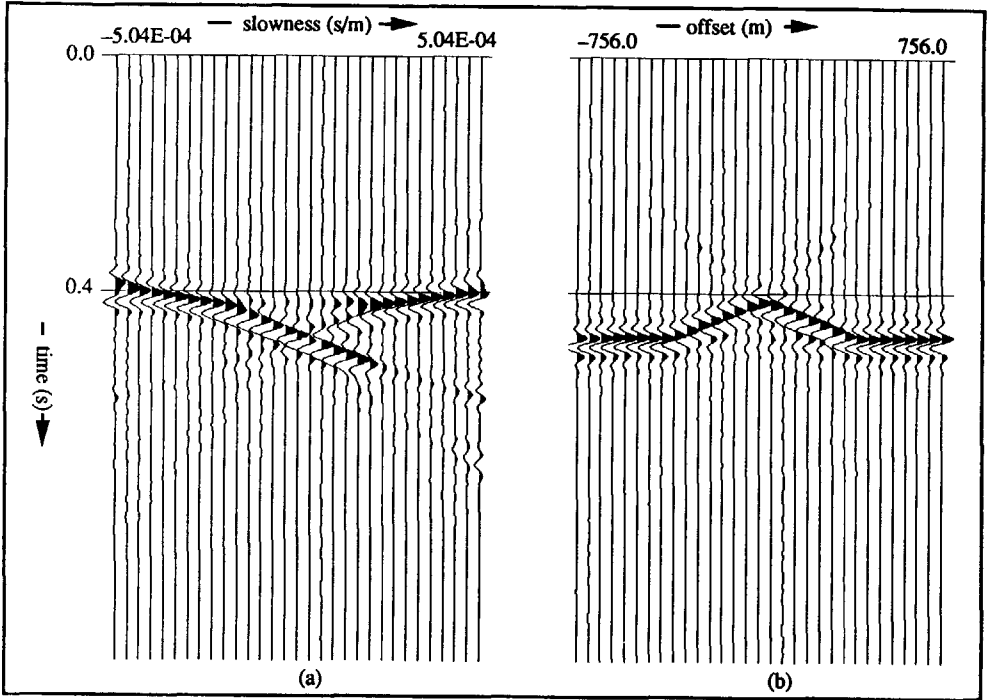


Fig.6.6.16: The pre-stack migrated result of the complete line in (a)  $\tau$ - $p$  and in (b)  $t$ - $x$ .

**A pyramid-shape interface sandwiched between two horizontal layers**

The last synthetic model is an extension of the previous model: one horizontal interface above

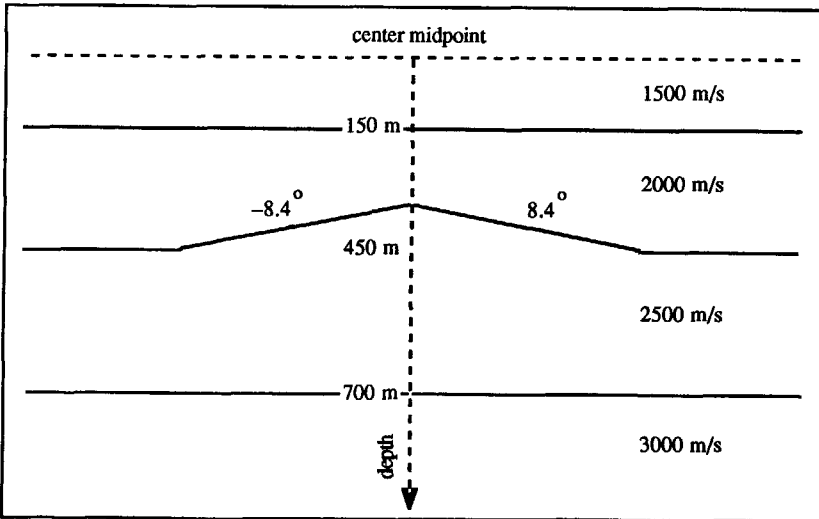


Fig.6.6.17: The  $x_3$ - $x_1$  configuration of the fifth model.

and one below the pyramid-shaped interface. The  $\Delta x$  of source and receiver are again 12 m and the velocities are respectively 1500 m/s, 2000 m/s and 2500 m/s. Further,  $\Delta p^s$  and  $\Delta p^o$  equal  $4.5E^{-6}$  s/m. Three "stacked" time slices are shown (Fig.6.6.18), where the lower horizontal interface shows the smallest aperture. Note also that it is influenced by the overburden. It no longer appears to be completely horizontal. In Fig.6.6.19b, the three events are displayed, each representing one interface. Then the last picture of this data set displays the migrated section (Fig.6.6.19d). Note that the multiple energy is still present in the section, the first multiple at about 0.4 s and the second multiple at 0.7 s.

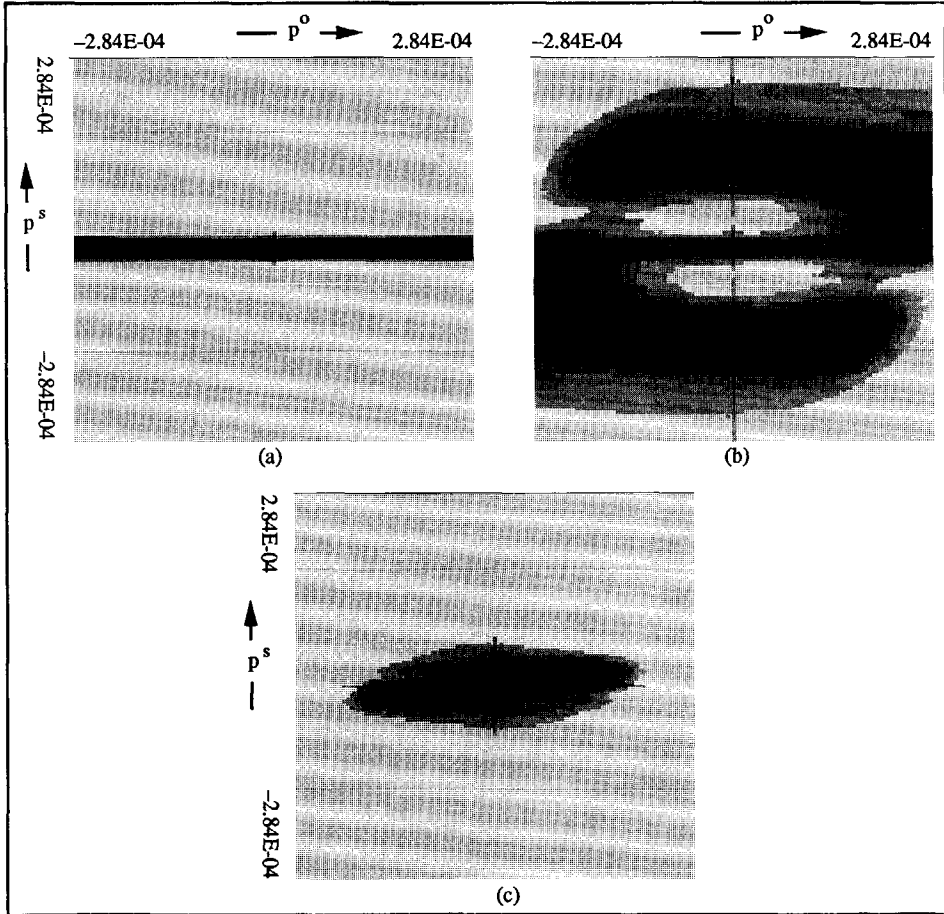


Fig.6.6.18: Three "stacked" time slices: (a) 0.0 - 0.32 s, (b) 0.32 - 0.64 s and (c) 0.64 - 0.96 s.

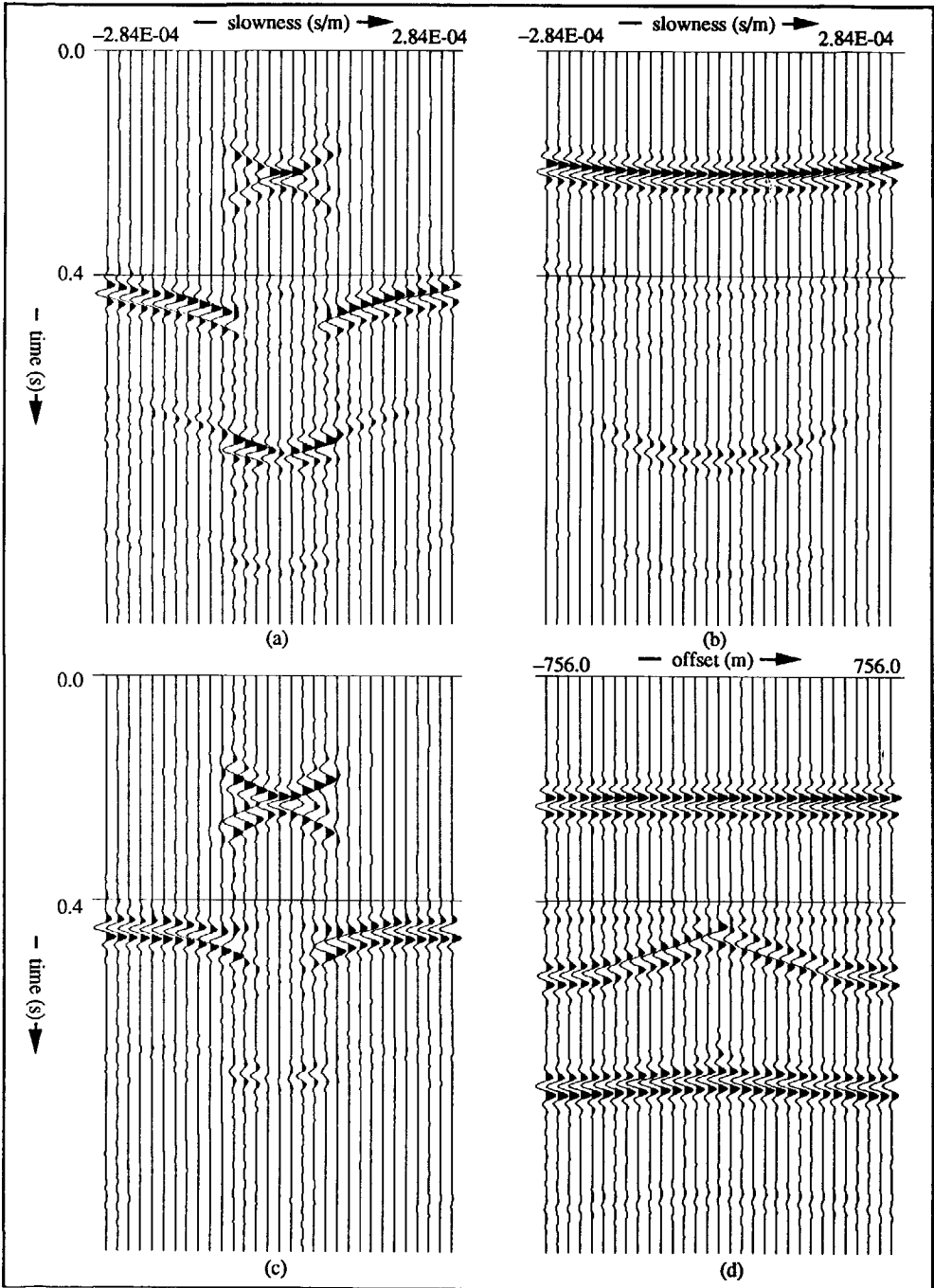


Fig.6.6.19: The selected planes: (a)  $p^o=0$  and (b)  $p^s=0$  and the pre-stack migrated result of the complete line (c) in  $\tau$ - $p$  and (d) in  $t$ - $x$ .

### A land data set

The last example is a land data set, shot in the Northern part of Holland. The line consists of 32 shots where each shot is recorded by 240 receivers with split spread geometry. Because of irregular spacing between the successive shots, the data was interpolated linearly at each 25 m, resulting in 59 shot gathers. To undo the elevation static corrections are applied. The spacing between the receivers is 10 m. Depth of the source is 8 m. Then, Fig.6.6.20 shows three shot

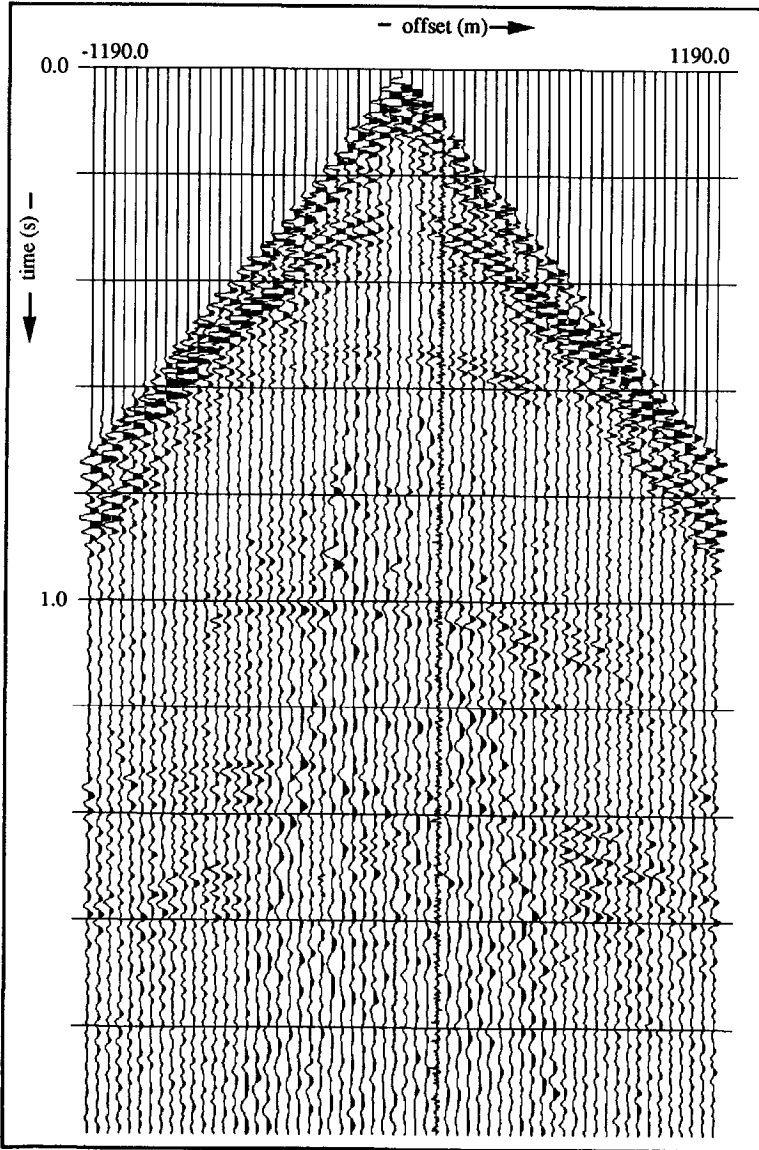


Fig.6.6.20a: The shot gather of the land data set in the beginning of the seismic line.

gathers, (a) at the beginning of the line, (b) in the middle and (c) at the end of the line. The time slices (Fig.6.6.21) are calculated over every 0.2 s, where the spreading of energy decreases with increasing two-way traveltime. Note the difference of the energy distribution between (d) and (e). The next figure (Fig.6.6.22) shows the two selected planes, displaying only five main events as was already clear from the slices. Finally, the migrated section (Fig.6.6.23b) is shown.

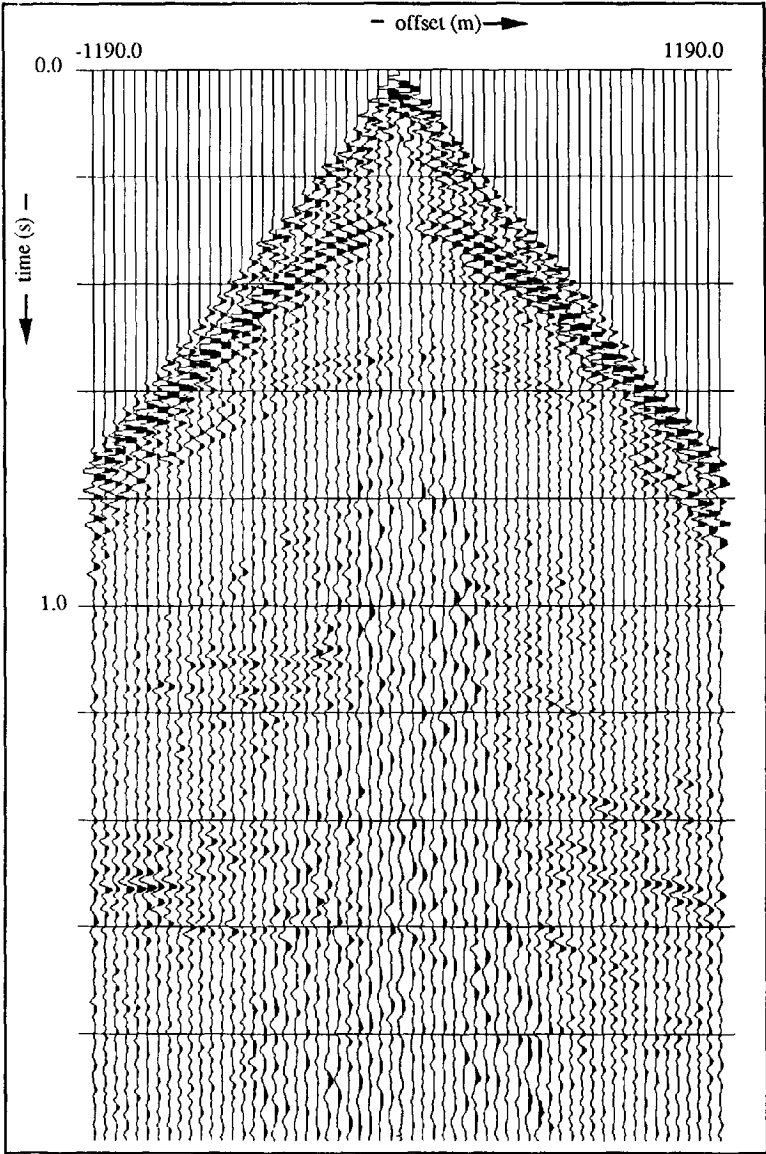


Fig.6.6.20b: The shot gather of the land data set in the middle of the seismic line.

In order to give an idea how our migration method performs, it is compared with the conventionally migrated section (Fig.6.6.23c), covering the same part of the seismic line. The same velocities are used for both migration methods. Comparing the two sections (Fig.6.6.23b and c), we notice that a dipping event, starting at 1.0 s is only present in the conventionally migrated section. Other differences are the two reflectors at 1.4 s and at 1.6 s. They are clearly in our migrated section but only vaguely present in the conventionally migrated section.

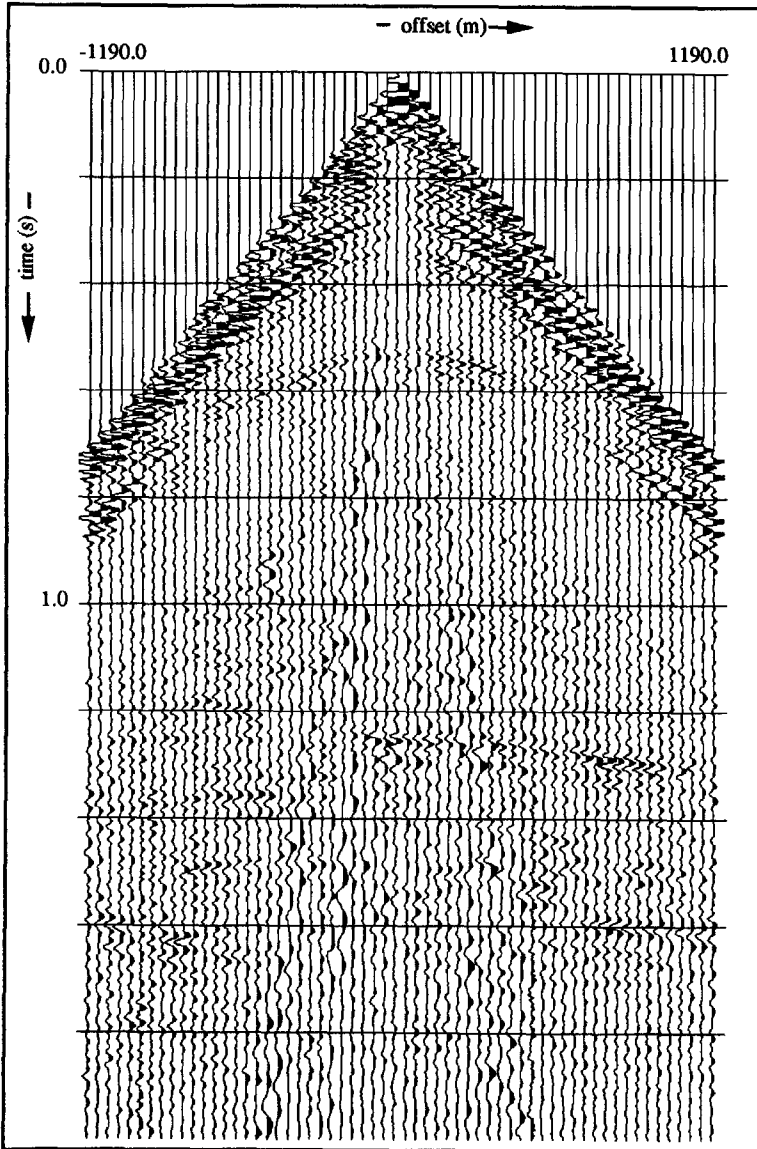


Fig.6.6.20c: The shot gather of the land data set at the end of the seismic line.

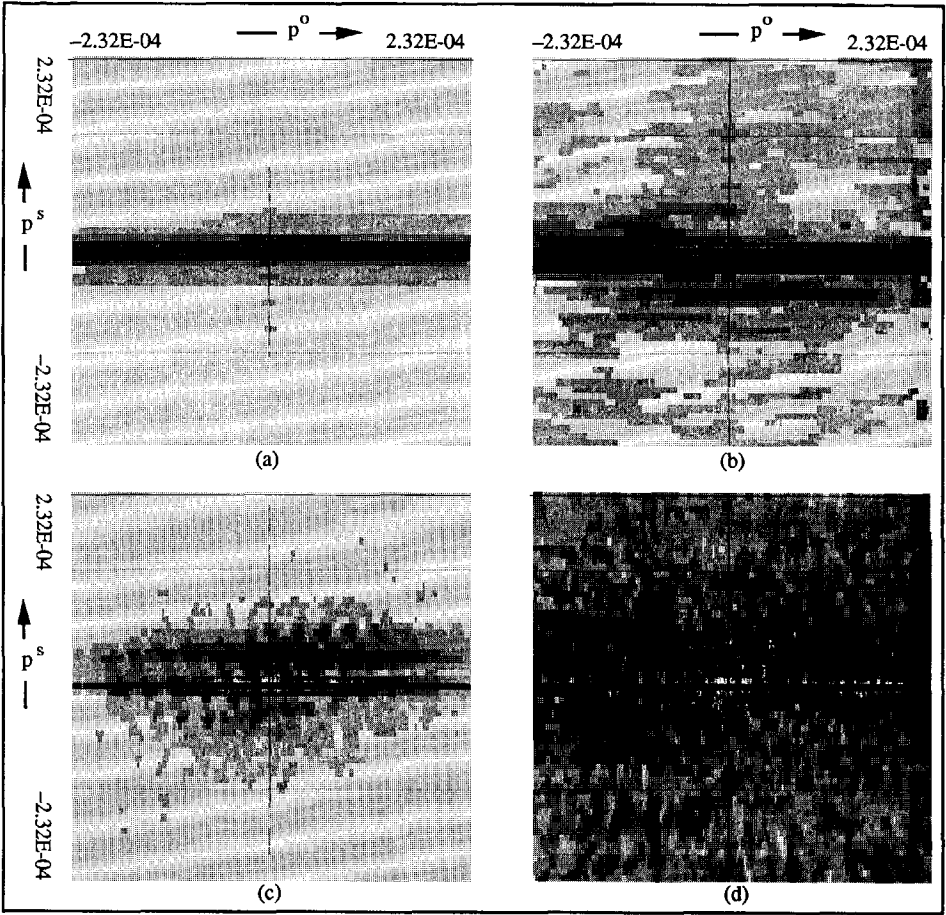


Fig.6.6.21a-d: The "stacked" time slices: (a) 0.0 - 0.2 s, (b) 0.2 - 0.4 s, (c) 0.4 - 0.6 s and (d) 0.6 - 0.8 s.



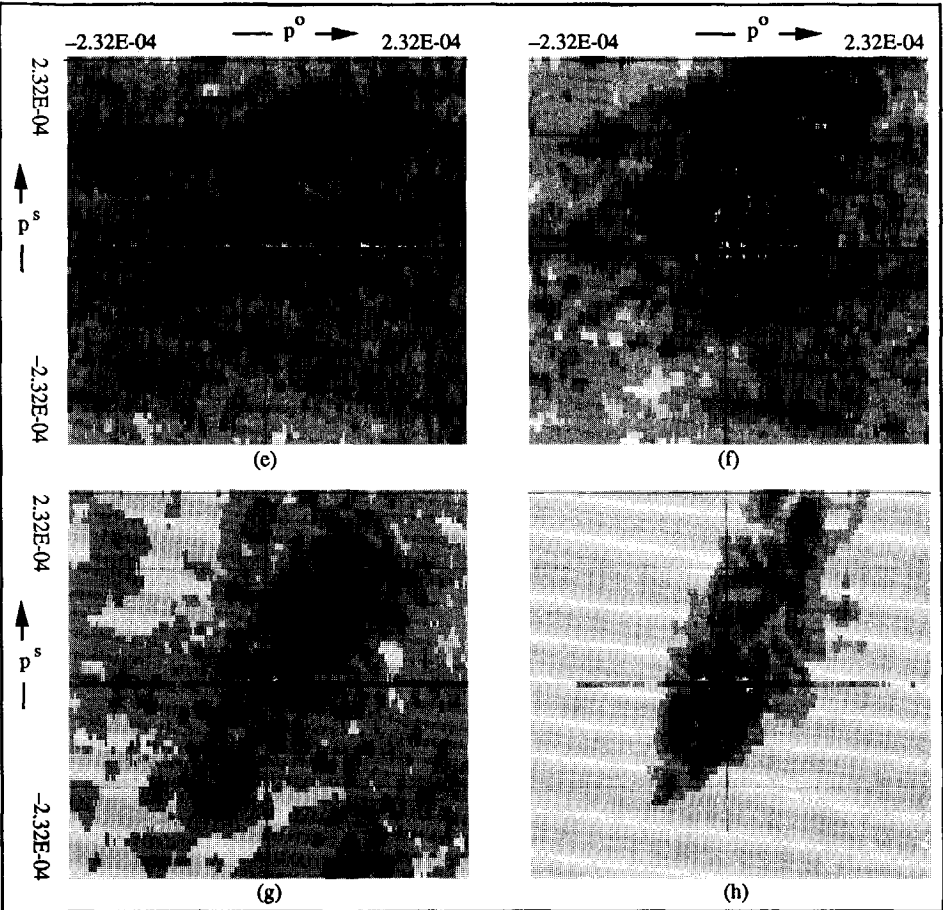


Fig.6.6.21e-h: The "stacked" time slices: (e) 0.8 - 1.0 s, (f) 1.0 - 1.2 s, (g) 1.2 - 1.4 s and (h) 1.4 - 1.6 s.

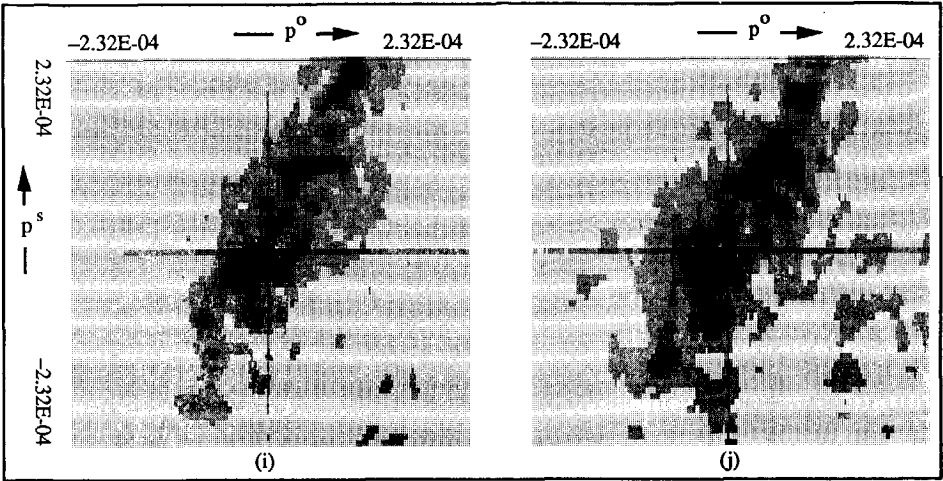


Fig.6.6.21i-j: The "stacked" time slices: (i) 1.6 - 1.8 s and (j) 1.8 - 2.0 s.

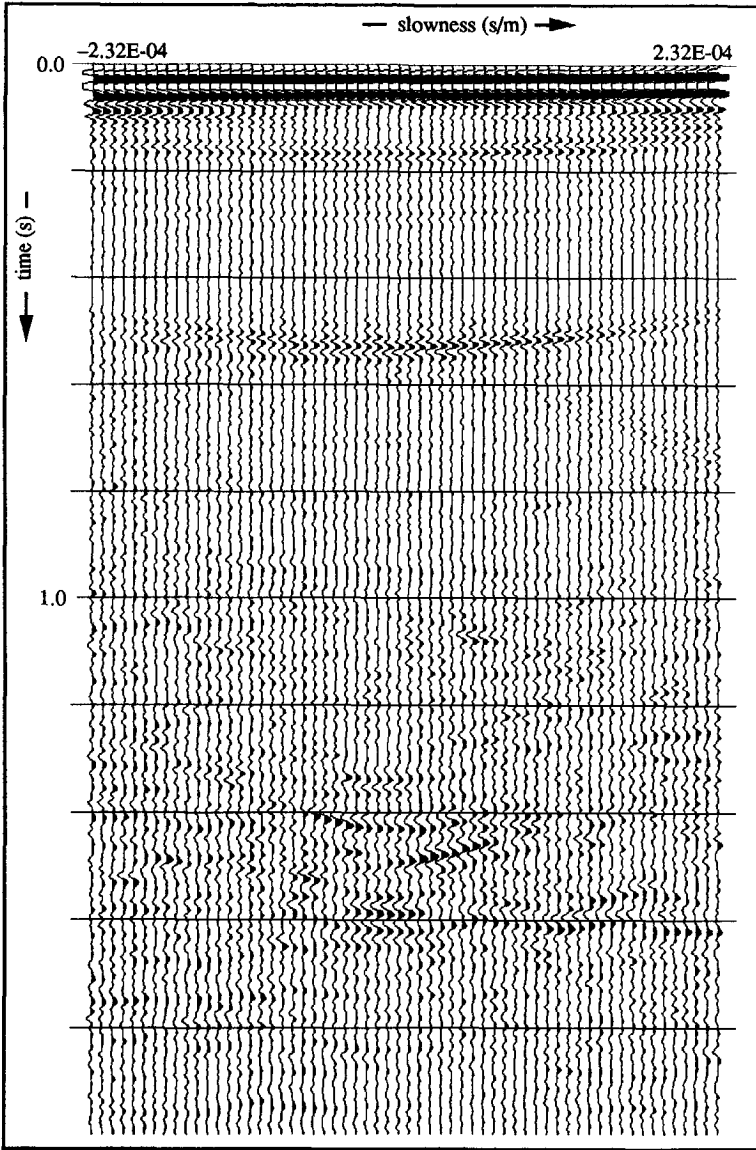
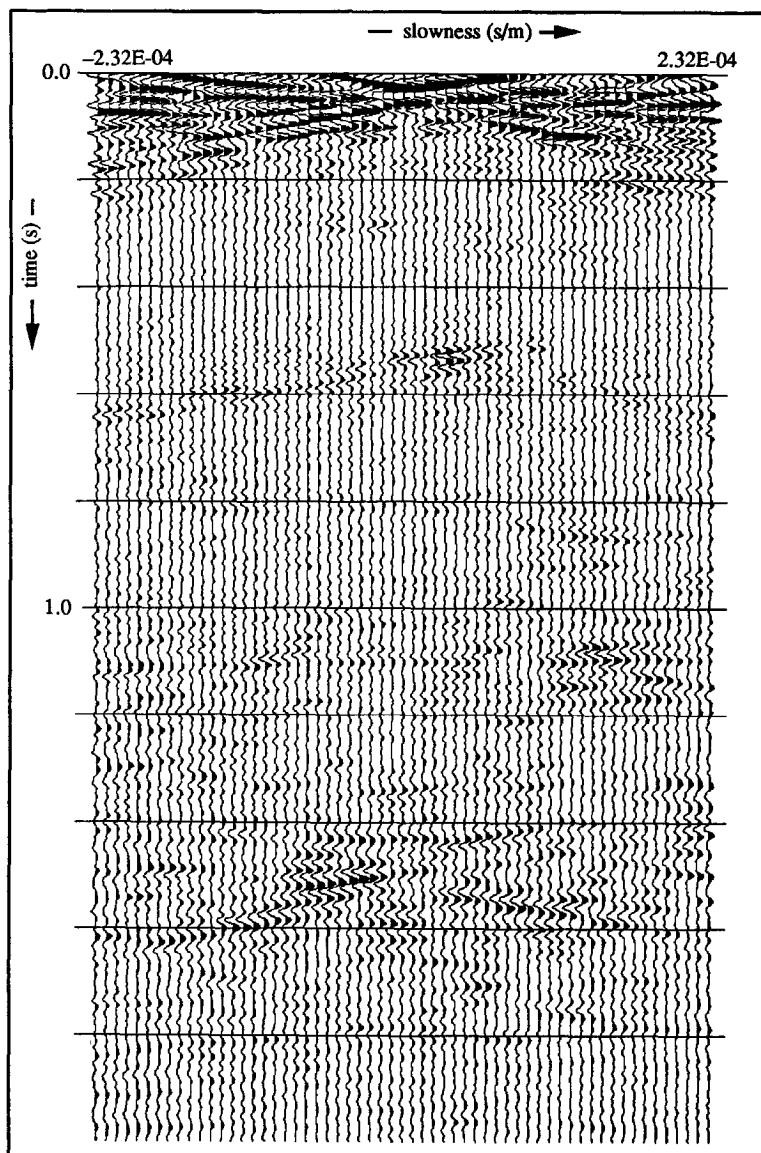


Fig.6.6.22a: The selected planes:  $p^s=0$ .

Fig.6.6.22b: The selected planes:  $p^0=0$ .

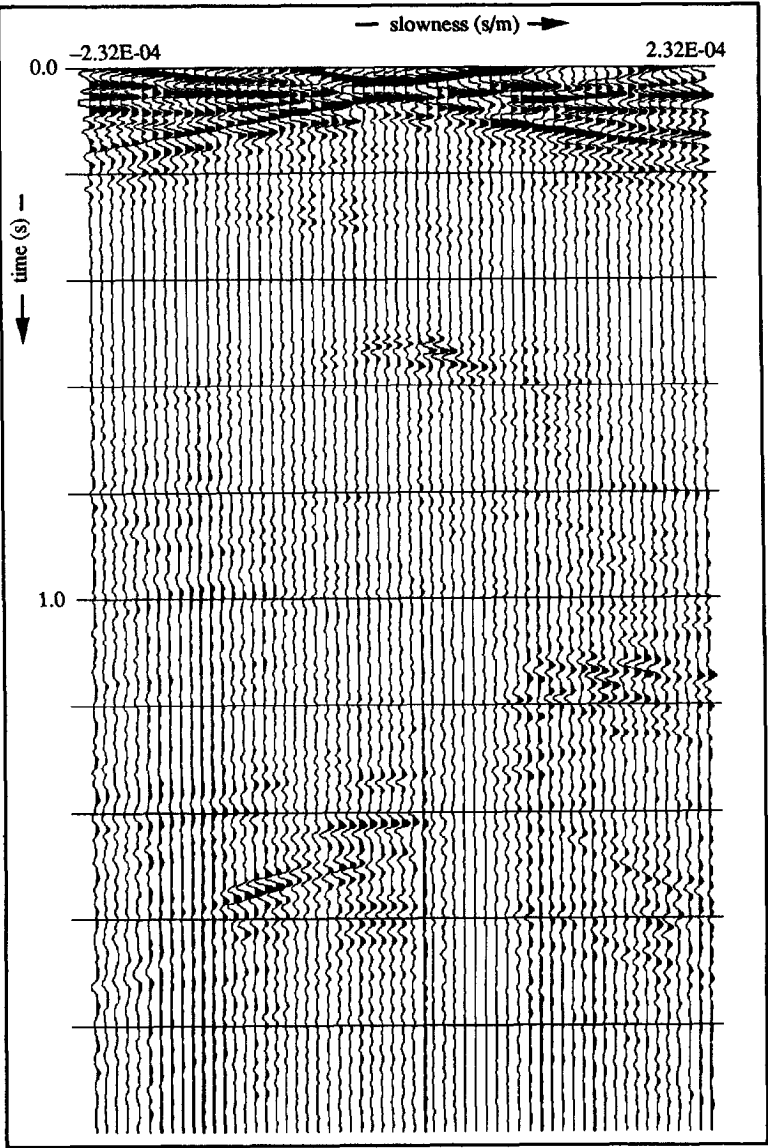


Fig.6.6.23a: The pre-stack migrated result of the complete line in  $\tau$ - $p$ .

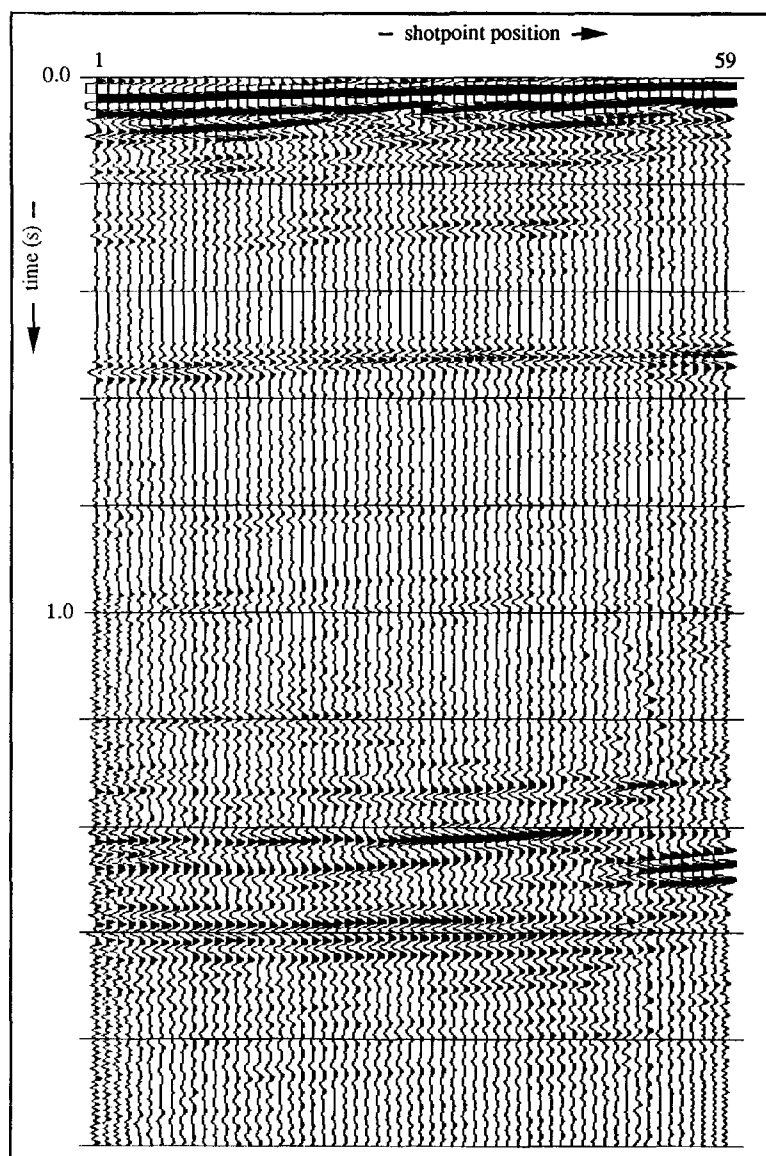


Fig.6.6.23b: The pre-stack migrated result of the complete line in  $t$ - $x$ .

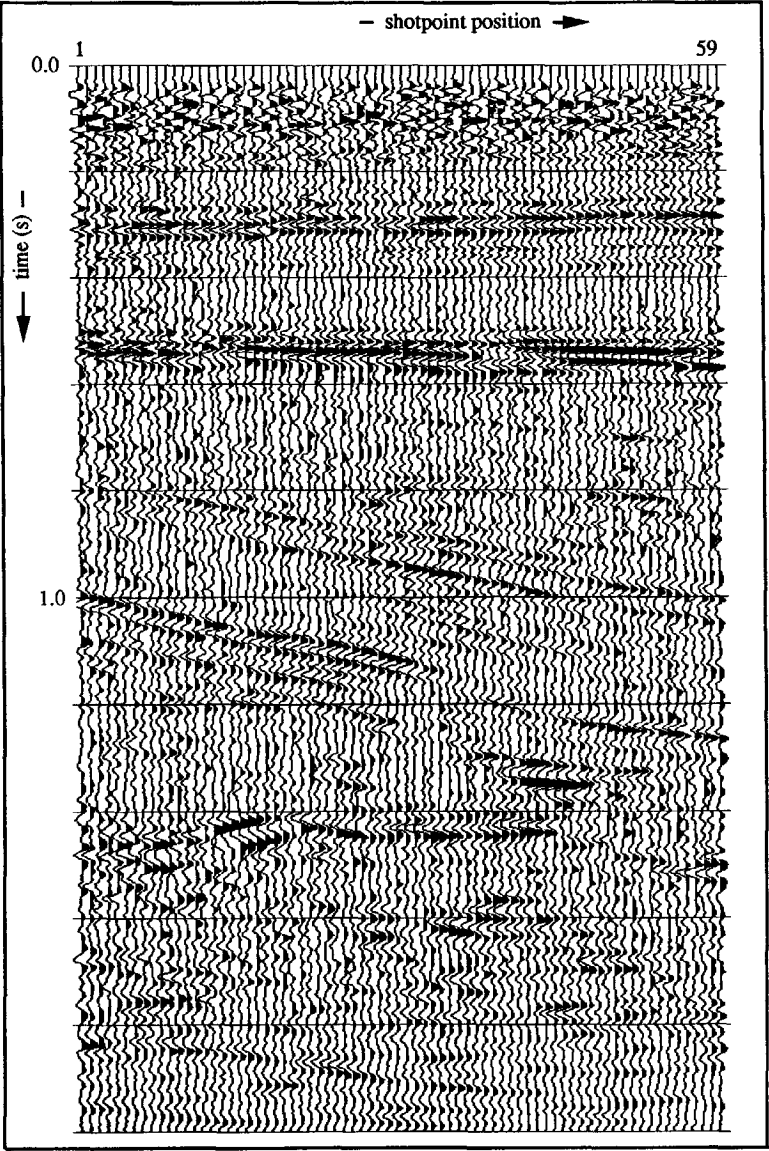


Fig.6.6.23c: The conventionally migrated section.

---

## CONCLUSIONS

The Radon transform has conventionally been applied to seismic data to decompose the data into plane-wave components. This decomposition allows waves which travel with different slownesses to be separated. In land seismic data for example, the Radon transform can be applied to separate compressional waves, shear waves and surface waves, and in VSP data, the Radon transform may be applied to separate the upgoing from the downgoing waves. In the calculation of synthetic seismograms from well-logs the theory of wave propagation in plane horizontal layers is very often handled in the  $f$ - $p$  domain using the reflectivity method. In order to compare the synthetic seismograms with field data in the  $t$ - $x$  domain, the synthetic data have to be transformed to the  $t$ - $x$  domain with the inverse Radon transform.

Thus the forward Radon transform is required for plane-wave decomposition and allows further data processing to proceed on each plane-wave component separately. The inverse Radon transform is required either to get the data back to the  $t$ - $x$  domain after processing in the plane-wave domain, or to transform synthetic data to the  $t$ - $x$  domain for comparison with field data. Owing to a number of difficulties in its numerical implementation, the Radon transform is not used very extensively. One difficulty is that the forward and inverse discrete Radon transforms are not exactly reversible. Something is always lost when the Radon transform is applied to a data set.

In this thesis, the theory of the Radon transform is examined, and an efficient and accurate numerical implementation is developed.

### *Data modelled in the frequency-slowness domain*

When a data set is modelled in the  $f$ - $p$  domain using the reflectivity method and transformed to the  $t$ - $x$  domain with the inverse Radon transform, three main numerical problems arise:

- 1) How to map the completely calculated elliptic events into hyperbolic events with finite offset: this is solved by introducing a frequency dependent  $p$ -increment, where the  $p$ -increment is chosen such that the unaliased part of the calculated earth's response in the  $f$ - $p$  domain is



sampled with a constant number of slowness values. Owing to this restriction put on the modelled data in the  $f$ - $p$  domain, the wrap-around noise in the  $t$ - $x$  domain is reduced as well. However, the choice of the sampling interval and the number of samples of the slowness as well as the frequency have to be accurate. They have to agree with the complexity of the chosen earth model, that is the larger the number of the layers and the thinner the layers, the smaller the sampling interval and the larger the number of samples (section 3.6).

2) How and when to interpolate and what order of interpolation: the inherent interpolation is carried out in the frequency domain instead of in the time domain, and it is performed after the spatial Fourier transform. To improve the interpolation procedure, the analytically known Fourier transform of the interpolator is calculated and the modelled earth's response is divided by it. Linear interpolation is preferred because it is cheaper, but cubic spline is more accurate. When a cubic spline is compared with a linear interpolation, the spline interpolator performs much better. But when both interpolators are implemented in the algorithm and when the modelled earth's response is first divided by the analytically known Fourier transform of the interpolator, the results are very similar. The reason for this is that when the calculated earth's response is sampled far beyond aliasing, a higher order interpolator becomes redundant (section 3.7).

3) How to evaluate the Bessel function of the first kind in the case of cylindrical symmetry: this is solved by rewriting the Bessel function as a spatial Fourier transform followed by a frequency dependent square-root filter. The Bessel function can also be replaced by its asymptotic expansion, but for small values of the argument of the Bessel function, the approximation fails. Further, a synthetic data set (primaries only) obtained with the inverse Radon transform is compared with a data set modelled with the exact Cagniard-de Hoop technique. The results are equally good within the chosen bandwidth but the Fourier-Bessel method takes less computational effort (section 3.8).

### ***Data in the time-space domain***

When we start with a synthetic or field data set in the  $t$ - $x$  domain and apply a forward Radon transform to it, the data must fulfil the following condition:

$$fp < \frac{1}{2\Delta x}, \quad (7.1)$$

because the data are aliased outside that range in the  $f$ - $p$  domain. If this condition is not fulfilled, the input data have to be muted according to the orthogonal hyperbola (eq.(7.1); section 4.4). The second problem of the numerical implementation translates to the finite aperture of the data set, which makes the range of integrations finite. It is well-known that the analytic solution of a Radon transformed hyperbolic event is an elliptical event and that the analytic solution of a linear event (for example, a headwave) is a point. However, due to the discrepancy between the analytic and discrete Radon transform, only part of the elliptical event is truly elliptical. Because of the finite aperture of the Radon transformed data set, the last part of the elliptical event is no longer elliptical, but becomes tangent to the ellipse at the focus point. And, if the first offset of

the data set is not equal to zero, the first part of the elliptical events also becomes the tangent and therefore unreliable (section 5.2). Secondly, a linear event in  $t$ - $x$  does not map into a point but maps into two linear events with a positive and a negative dip starting at the  $\tau$ -axis. The intercept time on the  $\tau$ -axis relates to the time value in the  $t$ - $x$  domain where the linear event starts, while the slope in  $\tau$ - $p$  represents the corresponding offset (section 5.3). A high frequency approximation, using the method of stationary phase confirms these results. Moreover, this approximation allows us to predict the reliable range of a Radon transformed data set, where the larger the  $\tau$ -value, the smaller the reliable  $p$ -range becomes according to the orthogonal hyperbola (section 5.2).

Then, the method of calculating the Radon transform is extended to two- and three-dimensional earth models, thereby allowing lateral velocity variations. By applying a double forward Radon transform, one with respect to the offset coordinates and one with respect to the source coordinates, the spatial complexity of the data set shows a well-defined topological subdivision in the double Radon transformed domain. As the main application, we developed a pre-stack migration algorithm, which is an alternative approach for the conventional normal-move-out, dip-move-out, common depth point stacking and a post-stack migration scheme. The algorithm ignores just as the conventional migration methods any interaction between the interface, that is multiple reflections (internal multiples and free surface effects) are treated as primary reflections. The advantages of our algorithm are lateral varying velocities, the restricted computational effort and the lack of required detail of the velocity model due to the robustness of our procedure. And, the computation time becomes a smaller fraction of the total time as more processes are performed in the double Radon transformed domain.

Because of the use of the FFT in the migration algorithm, the spacing between the subsequent sources as well as the spacing between the receivers has to be constant. If not, the data have to be interpolated. Further, there are two more restrictions, (1) the limitation due to the Radon transform, and (2) the maximum retrievable dip, present in the data itself (eq.(7.2); section 6.4). The maximum possible dip is, using the stationary points of the transform integral, determined by the offset, the depth of the interfaces and their rms-velocities:

$$|p^o| \leq \frac{|x_I^o + x_I^s - x_I|}{v_m R^o} \quad \text{and} \quad |p^s| \leq p^o + \frac{|x_I^s - x_I|}{v_m R^s} \quad (7.2)$$

Therefore, the maximum slowness with respect to the source and with respect to the offset have to be chosen in harmony with the data set. Otherwise, we are looking at artifacts of the transform due to lack of the data.

Comparing the pre-stack migration method with the conventional procedure, two conclusions can be drawn from the field data set: (1) the dipping event at 1.0 s in the conventionally migrated section is outside the range of the maximum retrievable dip following eq.(7.2) and therefore not present in the pre-stack migrated section, and (2) the event at 1.6 s is far better focussed with the pre-stack migration method than with the conventional migration procedure.

### A.1 Calculation of the Green's function for the acoustic case

The spherical waves emitted by a point source can be regarded as a sum of plane waves; these plane waves are reflected and transmitted at the interfaces. After the calculation of the response of each plane-wave component, the plane-wave responses are superposed to give the complete point source response. A plane-wave modelling scheme, based on the reflectivity method (Fuchs and Müller, 1971; Fokkema and Ziolkowski, 1987) is used, assuming that the earth is horizontally-layered.

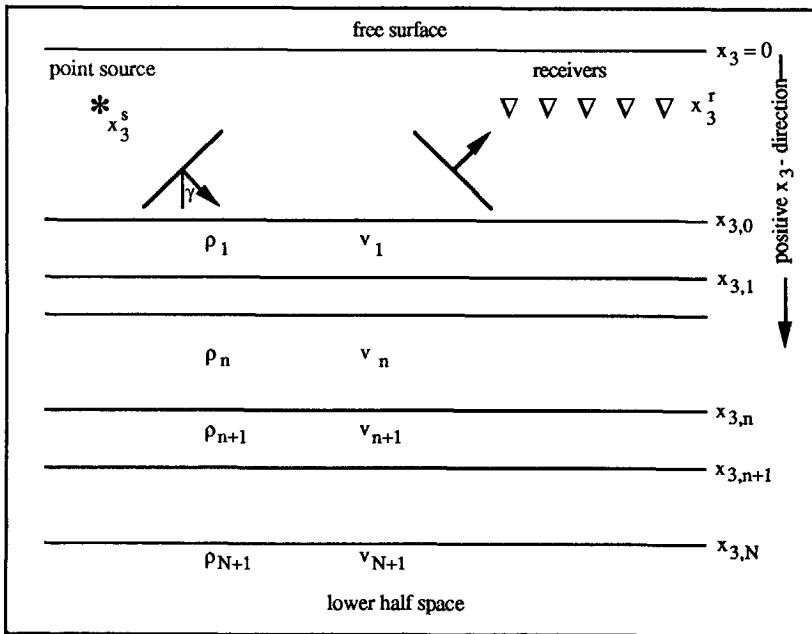


Fig.A.1.1: The point source configuration.

The model shown in Fig.A.1.1 consists of  $N+1$  fluid layers, bounded by a free surface on top and a homogeneous half space at the bottom. The source and the receivers are situated in the top fluid layer at depths  $x_3^s$  and depth  $x_3^r$ , respectively. The plane wave is defined by its horizontal slowness  $p$  and vertical slowness  $q$ , and are related in the following way:

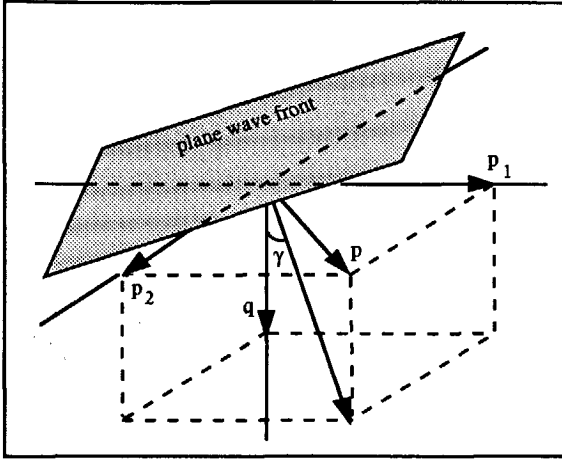


Fig.A.1.2: A plane wave in a homogeneous medium.

The  $q$  is found as that component of the direction of propagation that is normal to the  $p_1$ - $p_2$  plane and  $p$  is found by projecting the direction of propagation onto the  $p_1$ - $p_2$  plane (Fig.A.1.2). This is mathematically formulated as

$$p = \frac{\sin(\gamma)}{v} \quad \text{and} \quad q = \sqrt{\frac{1}{v^2} - p^2} \quad (\text{A.1.1})$$

and

$$p^2 = p_1^2 + p_2^2, \quad (\text{A.1.2})$$

where  $\gamma$  denotes the angle of incidence in Fig.A.1.2 and  $v$  the propagation velocity in the layer.

The pressure  $P_0$  in the top fluid layer consists of an incident field  $P^{inc}$  and a scattered field  $P^{sc}$ :

$$P_0(p_1, p_2, x_3, f) = P^{inc}(p_1, p_2, x_3, f) + P^{sc}(p_1, p_2, x_3, f). \quad (\text{A.1.3})$$

The incident field satisfies the inhomogeneous wave equation

$$\frac{\partial^2 P^{inc}}{\partial x_3^2} + (2\pi f)^2 q_0^2 P^{inc} = -S(f) \delta(x_3 - x_3^s), \quad (\text{A.1.4})$$

in which  $\hat{S}(f)$  is the source spectrum and  $q_0$  represents the vertical slowness in the upper layer and is defined as

$$q_0^2 = \frac{1}{v_0^2} - p_1^2 - p_2^2. \quad (\text{A.1.5})$$

The well-known solution of eq.(A.1.4) for the incident field is obtained as

$$\hat{P}^{inc}(p_1, p_2, x_3, f) = \frac{\hat{S}(f)}{i4\pi f q_0} e^{i2\pi f(p_1 x_1 + p_2 x_2 + q_0 |x_3 - x_{3,0}|)}, \quad (\text{A.1.6})$$

where the first factor represents the source spectrum with a scaling term. The exponential term  $[i2\pi f(p_1 x_1 + p_2 x_2)]$  of eq.(A.1.6) is common in both the incident and scattered field and will be omitted in the next equations for simplicity. Then, the scattered field consists of the upgoing and the downgoing wavefield and is given as

$$\hat{P}^{sc}(p_1, p_2, x_3, f) = \hat{A}_0^+(p, f) e^{i2\pi f q_0 x_3} + \hat{A}_0^-(p, f) e^{-i2\pi f q_0 (2x_{3,0} - x_3)}, \quad (\text{A.1.7})$$

in which  $\hat{A}_0^+$  is the spectrum of the pressure wave propagating in the positive  $x_3$ -direction and  $\hat{A}_0^-$  is the spectrum of the pressure wave propagating in the negative  $x_3$ -direction. We now find the global reflection coefficient  $\hat{R}_0$  at the boundary  $x_3 = x_{3,0}$ , which is the ratio of the upgoing to downgoing wave field, and the downgoing wave field consists of both the incident wave field and the scattered wave field:

$$\hat{A}_0^-(p, f) = \hat{R}_0(p, f) \left[ \frac{\hat{S}(f)}{i4\pi f q_0} e^{-i2\pi f q_0 x_{3,0}} + \hat{A}_0^+(p, f) \right]. \quad (\text{A.1.8})$$

At the free surface  $x_3 = 0$ , the boundary condition is that the pressure is zero. Therefore, from eqs.(A.1.3), (A.1.6) and (A.1.7) it follows that

$$\hat{A}_0^-(p, f) e^{-i2\pi f q_0 x_{3,0}} = -1 \left[ \frac{\hat{S}(f)}{i4\pi f q_0} e^{i2\pi f q_0 x_{3,0}} + \hat{A}_0^+(p, f) \right], \quad (\text{A.1.9})$$

in which the well-known reflection coefficient  $-1$  is clearly recognizable. Eqs.(A.1.8) and (A.1.9) can be solved for  $\hat{A}_0^-$  and  $\hat{A}_0^+$ , thus enabling the scattered field  $P^{sc}$  in eq.(A.1.7) to be determined. Combining this result with eq.(A.1.6) yields the complete expression of the total field at depth  $z$

$$\hat{P}(p_1, p_2, x_3, f) = \frac{\hat{S}(f)}{i4\pi f q_0} \left( \hat{P}^{inc}(p_1, p_2, x_3, f) + \hat{P}^{sc}(p_1, p_2, x_3, f) \right), \quad (\text{A.1.10})$$

where

$$\hat{P}^{inc}_{(p_1, p_2, x_3, f)} = e^{i2\pi f q_0 |x_3 - x_3^s|} - e^{i2\pi f q_0 (x_3 + x_3^s)}, \quad (\text{A.1.11})$$

in which the first term of eq.(A.1.11) represents the direct wave from the source, and the second term the reflection of this wave against the free surface (the source ghost). The scattered field, containing all the information of the layered earth, is then given as

$$\hat{P}^{sc}_{(p_1, p_2, x_3, f)} = \frac{\hat{R}_0(p, f) e^{i2\pi f q_0 (2x_{3,0} - x_3^s - x_3)}}{1 + \hat{R}_0(p, f) e^{i4\pi f q_0 x_{3,0}}} \left( 1 - e^{i4\pi f q_0 x_3^s} \right) \left( 1 - e^{i4\pi f q_0 x_3} \right), \quad (\text{A.1.12})$$

where five factors are present:  $\hat{R}_0$  is the global reflection coefficient at depth  $x_3 = x_{3,0}$  and  $q_0$  is the vertical slowness in the fluid layer. The denominator describes the multiple behaviour in the upper layer, the factor  $[1 - \exp[i4\pi f q_0 x_3^s]]$  represents the ghost operator at the source, the term  $[1 - \exp[i4\pi f q_0 x_3]]$  represents the ghost operator at the receiver and the factor  $[e^{i2\pi f q_0 (2x_{3,0} - x_3^s - x_3)}]$  accounts for the time delay from the source to the first interface and back to the receiver. The global reflection coefficient  $\hat{R}_0$  is obtained recursively from the bottom of the model upwards and is given at the  $n$ -th interface by

$$\hat{R}_n(p, f) = \frac{r_n + \hat{R}_{n+1}(p, f) e^{i4\pi f q_n x_{3,n+1}}}{1 + r_n \hat{R}_{n+1}(p, f) e^{i4\pi f q_n x_{3,n+1}}}, \quad (\text{A.1.13})$$

where the term  $\exp[i4\pi f q_n x_{3,n+1}]$  introduces the two-way traveltime in the  $n$ -th layer, the denominator describes the behaviour of the internal multiples in the layers and  $r_n$  denotes the local reflection coefficient at the  $n$ -th interface given by:

$$r_n = \frac{q_n \rho_{n+1} - q_{n+1} \rho_n}{q_n \rho_{n+1} + q_{n+1} \rho_n}. \quad (\text{A.1.14})$$

Since the model is bounded at the bottom by a half space, the recursion is started by assuming that there are no upward travelling waves in the lower half space, thus:

$$\hat{R}_{N+1}(p, f) = 0. \quad (\text{A.1.15})$$

The way the recursion is carried out, is shown below.

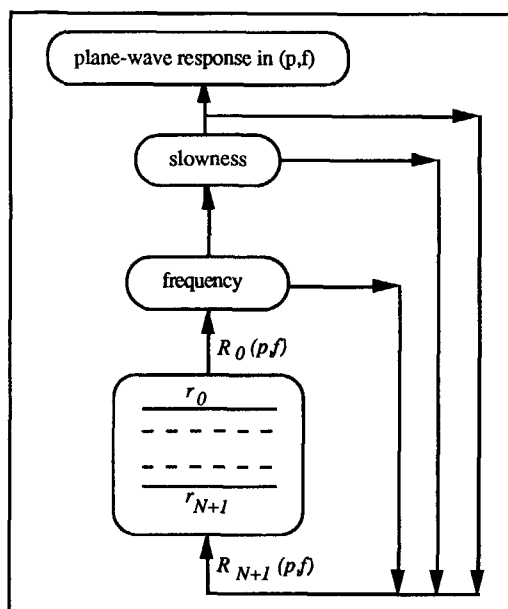


Fig.A.1.3: The flow diagram of the recursion: the inner loop presents the layers, the next loop the frequency and the outer loop denotes the  $p$ -values.

## A.2 The method of stationary phase

The method of stationary phase is well known and has existed for many years. The method is a high frequency approximation and it therefore emphasizes the onset of events. The following type of integral (Erdélyi, 1956) is evaluated

$$g(p) = \int_B^C A(x) e^{i2\pi fh(p,x)} dx, \quad \text{for large values of } f, \quad (\text{A.2.1})$$

where the exponential factor denotes a phase function

$$h(p,x) = G(x) \pm px \quad (\text{A.2.2})$$

that for the purposes of this thesis can represent either a hyperbolic move-out corresponding to primary and multiple reflections, or a linear move-out corresponding to headwaves. The hyperbolic or linear move-out is written as  $G(x)$  and its relation to  $h(p,x)$  is given in eq.(A.2.2). The  $p$  denotes the horizontal slowness,  $x$  the offset,  $f$  the frequency,  $A(x)$  gives some space dependent amplitude factor and  $B$  and  $C$  represent the end values of the integral. Then, evaluating the integral for large values of  $f$ , the major contribution to the integral arises from the immediate vicinity of the endpoints of the interval and from the vicinity of those points at which the phase function is stationary according to

$$\frac{\partial h(p,x)}{\partial x} = h'(p,x_s) = 0 \quad \text{and} \quad \frac{\partial^2 h(p,x)}{\partial x^2} = h''(p,x_s) \neq 0, \quad (\text{A.2.3})$$

where  $x_s$  denotes the stationary point of the phase function.

The exponent goes through a large number of periods, while the amplitude function,  $A(x)$  changes comparatively slowly. Thus the integrand approximates a constant function,  $A(x)$  multiplied by a rapidly varying exponent, which varies between  $+1$  and  $-1$ . Therefore, destructive interference between the various contributions to the integral will make it vanish, except for those values of  $x$  for which the phase function is stationary. In the first approximation the contribution of the stationary points, if there are any, is more important than the contribution of the endpoints.

Then expanding  $h(p,x)$  in a Taylor series around the stationary point  $x_s$  ( $\xi$  is small) yields

$$h(p,x) = h(p,x_s + \xi) = h(p,x_s) + \xi h'(p,x_s) + \frac{\xi^2}{2!} h''(p,x_s) \dots \quad (\text{A.2.4})$$



We ignore higher-order terms in eq.(A.2.4) and substitute for  $h(p, x)$  into eq.(A.2.1), in which the integration is now allowed to run from  $-\infty$  to  $+\infty$ . Since  $h(p, x_s)$  is zero, by definition of eq.(A.2.3), this yields

$$g(p) = A(x_s) e^{i2\pi fh(p, x_s)} \int_{-\infty}^{+\infty} e^{i\pi fh''(p, x_s) \xi^2} d\xi. \quad (\text{A.2.5})$$

Evaluating the integral in eq.(A.2.5), following Abramowitz & Stegun (1968) gives

$$\begin{aligned} \int_{-\infty}^{+\infty} e^{i\pi fh''(p, x_s) \xi^2} d\xi &= \int_{-\infty}^{+\infty} \cos(\pi fh''(p, x_s) \xi^2) + i \sin(\pi fh''(p, x_s) \xi^2) d\xi \\ &= (1 + i) \sqrt{\frac{\pi}{2\pi fh''(p, x_s)}} = \sqrt{\frac{1}{-ifh''(p, x_s)}} \end{aligned} \quad (\text{A.2.6})$$

and substituting it in eq.(A.2.5) finally results in

$$g(p) \approx \frac{1}{\sqrt{-ifh''(p, x_s)}} A(x_s) e^{i2\pi fh(p, x_s)}. \quad (\text{A.2.7})$$

The method of stationary phase is valid only when one integral has to be evaluated. In case of two integrals (Chapter 5), a similar approach is used. Following Felsen and Marcuvitz (1973), we start from

$$g(p) = \int_{B_1}^{C_1} \int_{B_2}^{C_2} A(x) e^{i2\pi fh(p, x, \theta)} dx d\theta, \quad (\text{A.2.8})$$

where the exponential factor denotes a phase function

$$h(p, x, \theta) = G(x) \pm px \cos \theta \quad (\text{A.2.9})$$

with  $G(x)$  being either a linear or a hyperbolic move-out.  $B_{1,2}$  and  $C_{1,2}$  present the end values of the integrals. Then, again, the main contribution to the integral arises from the immediate vicinity of the endpoints and from the vicinity of those points at which the phase function,  $h(p, x, \theta)$  is stationary according to

$$\frac{\partial h(p, x, \theta)}{\partial \theta} = h'(p, x_s, \theta_s) = 0 \quad \text{and} \quad \frac{\partial h(p, x, \theta)}{\partial x} = h'(p, x_s, \theta_s) = 0$$

and

$$\frac{\partial^2 h(p, x, \theta)}{\partial \theta^2} = h''(p, x_s, \theta_s) \neq 0 \quad \text{and} \quad \frac{\partial^2 h(p, x, \theta)}{\partial x^2} = h''(p, x_s, \theta_s) \neq 0, \quad (\text{A.2.10})$$

where  $x_s$  and  $\theta_s$  denote the two stationary points. Then, it is entitled to assume by Taylor's theorem for two independent variables that

$$\begin{aligned} h(p, x, \theta) = & h(p, x_s, \theta_s) + (x - x_s) \frac{\partial}{\partial x} h(p, x_s, \theta_s) + \frac{1}{2} (x - x_s)^2 \frac{\partial^2}{\partial x^2} h(p, x_s, \theta_s) + \\ & (\theta - \theta_s) \frac{\partial}{\partial \theta} h(p, x_s, \theta_s) + \frac{1}{2} (\theta - \theta_s)^2 \frac{\partial^2}{\partial \theta^2} h(p, x_s, \theta_s) + \\ & (x - x_s)(\theta - \theta_s) \frac{\partial}{\partial \theta} \frac{\partial}{\partial x} h(p, x_s, \theta_s). \end{aligned} \quad (\text{A.2.11})$$

Of the terms in the exponential factor, apart from the first term of eq.(A.2.11), only the quadratic group needs to be kept in the exponent. Then, to attain an accuracy equivalent to the terms retained in eq.(A.2.11), the slowly varying factor  $A(x)$  needs to be expanded by Taylor's theorem for the two variables only up to second derivatives. Integrating successively over  $x$  and  $\theta$ , a tedious calculation punctuated by extensive cancellation of laboriously computed terms ultimately leads to

$$g(p) \approx \frac{1}{if \sqrt{Z}} A(x_s) e^{i2\pi f h(p, x_s, \theta_s)}, \quad (\text{A.2.12})$$

where the denominator,  $Z$  is the determinant of the system which is given by

$$Z = \begin{pmatrix} \frac{\partial^2 h}{\partial x^2} & \frac{\partial^2 h}{\partial x \partial \theta} \\ \frac{\partial^2 h}{\partial \theta \partial x} & \frac{\partial^2 h}{\partial \theta^2} \end{pmatrix}, \quad (\text{A.2.13})$$

or writing out by

$$Z = \frac{\partial^2}{\partial x^2} h(p, x_s, \theta_s) \frac{\partial^2}{\partial \theta^2} h(p, x_s, \theta_s) - \left[ \frac{\partial}{\partial \theta} \frac{\partial}{\partial x} h(p, x_s, \theta_s) \right]^2. \quad (\text{A.2.14})$$

For the expansion of three integrals (Chapter 6), when we begin with

$$g(p) = \int_{B_1}^{C_1} \int_{B_2}^{C_2} \int_{B_3}^{C_3} A(x_1, x_2, x_3) e^{i2\pi f h(p, x_1, x_2, x_3)} dx_1 dx_2 dx_3, \quad (\text{A.2.15})$$

the asymptotic approximation is, following Felsen and Marcuvitz (1973) given by

$$g(p) \approx \frac{1}{\sqrt[3]{if}} \frac{e^{i(\pi/4)\sigma}}{\sqrt{Z}} A(x_{1,s}, x_{2,s}, x_{3,s}) e^{i2\pi f h(p, x_{1,s}, x_{2,s}, x_{3,s})}, \quad (\text{A.2.16})$$

where the denominator,  $Z$  is the determinant of the system, given by

$$Z = \begin{pmatrix} \frac{\partial^2 h}{\partial x_1^2} & \frac{\partial^2 h}{\partial x_1 \partial x_2} & \frac{\partial^2 h}{\partial x_1 \partial x_3} \\ \frac{\partial^2 h}{\partial x_2 \partial x_1} & \frac{\partial^2 h}{\partial x_2^2} & \frac{\partial^2 h}{\partial x_2 \partial x_3} \\ \frac{\partial^2 h}{\partial x_3 \partial x_1} & \frac{\partial^2 h}{\partial x_3 \partial x_2} & \frac{\partial^2 h}{\partial x_3^2} \end{pmatrix}, \quad (\text{A.2.17})$$

and where

$$\sigma = \sum_{i=1}^3 \text{sgn } d_i, \quad (\text{A.2.18})$$

and where  $d_i$  denote the eigenvalues of the matrix comprising the elements of the determinant  $Z$ .

### A.3 Complex frequency

When singularities are present along the path of integration, large numerical errors are made. This problem is commonly avoided by choosing a different path of integration, around the singularities. In this section, it is shown that singularities on the real frequency axis are avoided by introducing complex frequencies. When the temporal Fourier transform pair for complex frequencies is derived for causal time functions, its inverse transform must be defined for positive frequencies only because we need a unique relation between the wavenumber  $k$  and the horizontal slowness  $p$  for the Radon transform ( $k=2\pi fp$ ).

Following eqs.(1.2.1) and (1.2.2), the temporal Fourier transform pair for causal time functions is given by

$$\hat{u}(f) = \int_0^{+\infty} e^{i2\pi ft} u(t) dt, \quad (\text{A.3.1})$$

and

$$u(t) = \int_{-\infty}^{+\infty} e^{-i2\pi ft} \hat{u}(f) df. \quad (\text{A.3.2})$$

Next, consider the contour  $C^-$  in the complex  $f$ -plane in the upper half in Fig.A.3.1.

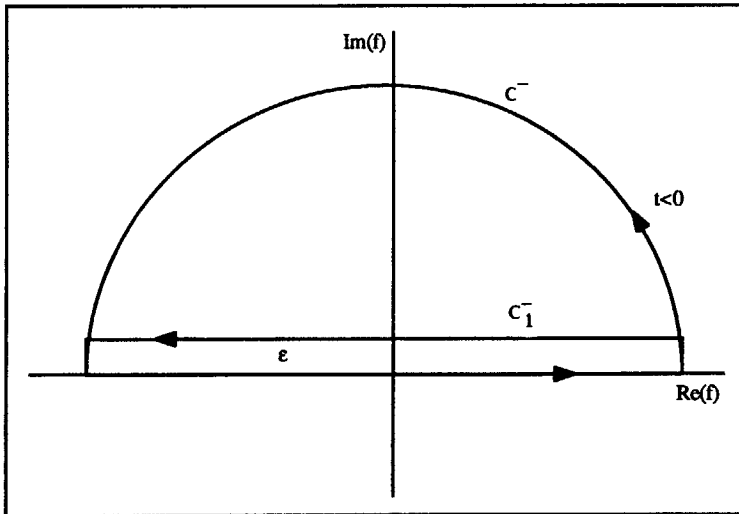


Fig.A.3.1: The path of integration in the complex  $f$ -plane.

According to Cauchy's theorem, the contour integral  $C^-$  along this path equals the sum of the residues in the upper half plane. When  $u(t)$  is causal,  $\hat{u}(f)$  contains no poles in the upper half

plane. Therefore it is allowed to choose any closed contour in the upper half plane. Then the equality

$$\oint_{C_I^-} \hat{u}(f) e^{-i2\pi ft} df = 0, \quad (\text{A.3.3})$$

is true for negative times. The contour  $C_I^-$  consists of four contributions, two parallel and two perpendicular to the real  $f$ -axis (Fig.A.3.1). Since  $\hat{u}(f)$  has no singularities for  $f \rightarrow \infty$ , the integration interval for the end contributions is finite and vanishes. Then eq.(A.3.3) can be written as

$$\int_{-\infty}^{+\infty} \hat{u}(f) e^{-i2\pi ft} df + \int_{i\varepsilon+\infty}^{i\varepsilon-\infty} \hat{u}(f) e^{-i2\pi ft} df = 0, \quad (\text{A.3.4})$$

and after substitution of eq.(A.3.2), as

$$u(t) = \int_{i\varepsilon-\infty}^{i\varepsilon+\infty} \hat{u}(f) e^{-i2\pi ft} df. \quad (\text{A.3.5})$$

Now, introducing a new variable of integration  $f' = f - i\varepsilon$ , eq.(A.3.5) is reformulated as

$$u(t) = \int_{-\infty}^{+\infty} \hat{u}(f' + i\varepsilon) e^{-i2\pi(f' + i\varepsilon)t} df'. \quad (\text{A.3.6})$$

or as

$$u(t) e^{-2\pi\varepsilon t} = \int_{-\infty}^{+\infty} \hat{u}(f' + i\varepsilon) e^{-i2\pi f' t} df'. \quad (\text{A.3.7})$$

The causal function  $u(t)$  is evaluated for complex frequencies by using a standard FFT-routine, followed by an inverse taper in the time domain. Next, the Heaviside step function according to eq.(1.2.5) is introduced in eq.(A.3.7)

$$u^B(t) = e^{+2\pi\varepsilon t} \int_{-\infty}^{+\infty} \hat{h}(f') \hat{u}(f' + i\varepsilon) e^{-i2\pi f' t} df' \quad (\text{A.3.8})$$

and, following eqs.(1.2.5)-(1.2.7), eq.(A.3.8) is rewritten as

$$u^B(t) = \frac{1}{2} \left[ e^{-2\pi\epsilon t} u(t) - i\mathcal{H} \left[ e^{-2\pi\epsilon t} u(t) \right] \right], \quad (\text{A.3.9})$$

where  $\mathcal{H}$  denotes the Hilbert transform. Because  $u(t) = 2\text{Re}[u^B(t)]$ , the temporal Fourier transform pair for causal time functions (eqs.(A.3.1) and (A.3.2)) is now defined as

$$\hat{u}(f+i\epsilon) = \int_0^\infty e^{i2\pi f't} u(t) dt, \quad (\text{A.3.10})$$

and

$$u(t) e^{-2\pi\epsilon t} = 2\text{Re} \left[ \int_0^\infty e^{-i2\pi f't} \hat{u}(f+i\epsilon) df' \right], \quad (\text{A.3.11})$$

where  $\text{Re} [\dots]$  denotes the real part, and is evaluated only for positive frequencies, as required.

#### A.4 Interpolation as part of the Radon transform

Interpolation is inherent to the Radon transform, but the order of the interpolation is open for discussion. We have chosen for linear interpolation which is the least time consuming but a higher-order interpolation might improve the results. In this section we compare the results of the linear interpolation with the results of the cardinal cubic spline interpolation. The cardinal cubic spline is a third order polynomial and is required to be periodic. By taking advantage of the continuity of the function and filling in the boundary conditions, the system of equations can be solved. Then, the spline is uniquely determined by its function-values at the points of support and by the sampling interval. According to this, the triangle function (eq.(3.4.10))

$$\phi(y) = \begin{cases} 1 - \frac{|y|}{\Delta y}, & |y| \leq \Delta y \\ 0, & |y| > \Delta y \end{cases} \quad \text{FFT} \quad \Leftrightarrow \quad \tilde{\phi}(p) = \frac{\sin^2(\frac{\pi p \Delta y}{2})}{(\pi p)^2 \Delta y} \quad (\text{A.4.1})$$

changes into

$$\phi(y) = \sum_{i=-M/2}^{M/2-1} \delta_i + p_i (y-y_i) + \frac{q_i}{2} (y-y_i)^2 + \frac{r_i}{6} (y-y_i)^3, \text{ for } y_i \leq y < y_{i+1}, \quad (\text{A.4.2})$$

where the interpolator  $\phi(y)$  is written as a Taylor expansion and in which  $p_i$ ,  $q_i$  and  $r_i$  denote respectively the first, second and third order derivative of the spline and  $\delta_i$  the Dirac pulse at the point of support  $i$ . Since the spline is an even function, its Fourier transform can be written as a cosine transform, resulting in

$$\tilde{\phi}(p) = 2 \sum_{i=0}^{M/2-1} \int_{y_i}^{y_{i+1}} \left( \delta_i + p_i (y-y_i) + \frac{q_i}{2} (y-y_i)^2 + \frac{r_i}{6} (y-y_i)^3 \right) \cos(yp) dy, \quad (\text{A.4.3})$$

where  $M$  denotes the number of points in the spline. So, eq.(A.4.3) is equivalent to the right hand side of eq.(A.4.1). The larger  $M$  is, the more accurate the result will be, but the more calculation time is required. After some testing (Fig.A.4.1) it was decided to continue with  $M = 4$ . Then filling in the 4-point spline, the complete point source response in  $f$ - $x$ , given below (eq.(3.4.14))

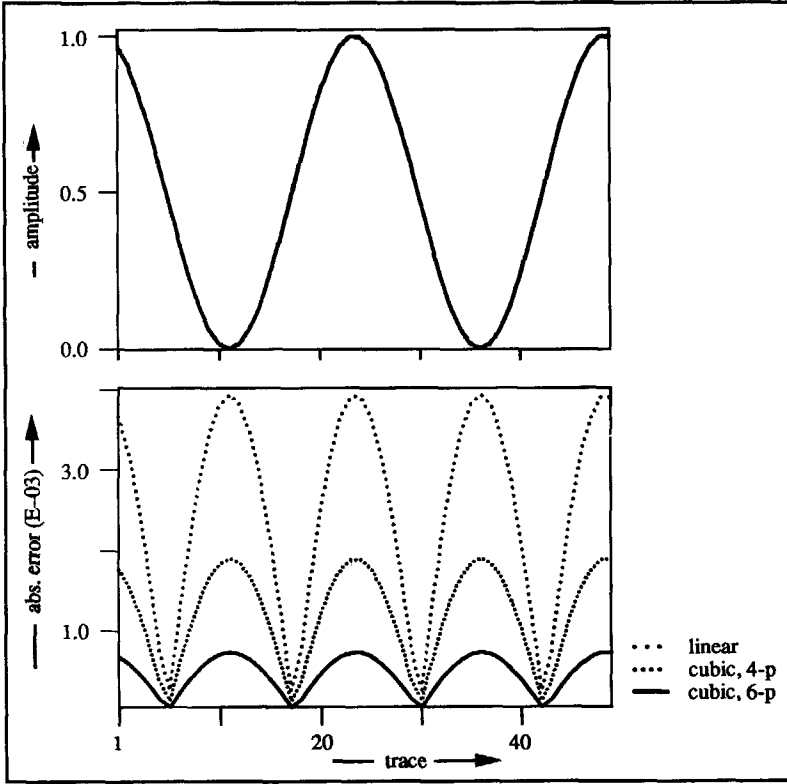


Fig.A.4.1: (a) The cosine function to interpolate and (b) the relative error of the linear interpolator compared with the spline interpolator with 4 and 6-points of support.

$$\begin{aligned} \hat{u}(x, x_3, f + i\epsilon) = & \sum_{n=1}^k \left[ (n A_{n-1} - (n-1) A_n) \arcsin \left( \frac{n \gamma_{n-1} - (n-1) \gamma_n}{(rn)^2} \right) + \right. \\ & \left. (A_{n-1} - A_n) (\gamma_{n-1} - \gamma_n) \right] + ((k+1) A_k - k A_{k+1}) \arcsin \left( \frac{\gamma_k}{rn} \right) + \\ & (A_{k+1} - A_k) \gamma_k, \quad \gamma_n = \sqrt{(rn)^2 - \left( \frac{y_n}{\Delta y} \right)^2} \text{ and } rn = \frac{w}{\Delta y}. \quad (\text{A.4.4}) \end{aligned}$$

changes into



$$\hat{u}(x, z, f + i\varepsilon) = \sum_{n=1}^k \left[ B_{n-1} \int_{y_{n-1}}^{y_n} \frac{dy}{\sqrt{\frac{w^2}{2} - y^2}} + C_{n-1} \int_{y_{n-1}}^{y_n} \frac{(y - y_n) dy}{\sqrt{\frac{w^2}{2} - y^2}} + \right. \\ \left. D_{n-1} \int_{y_{n-1}}^{y_n} \frac{(y - y_n)^2 dy}{\sqrt{\frac{w^2}{2} - y^2}} + E_{n-1} \int_{y_{n-1}}^{y_n} \frac{(y - y_n)^3 dy}{\sqrt{\frac{w^2}{2} - y^2}} \right] +, \quad (\text{A.4.5a})$$

$$B_k \int_{y_k}^w \frac{dy}{\sqrt{\frac{w^2}{2} - y^2}} + C_k \int_{y_k}^w \frac{(y - y_k) dy}{\sqrt{\frac{w^2}{2} - y^2}} + \\ D_k \int_{y_k}^w \frac{(y - y_k)^2 dy}{\sqrt{\frac{w^2}{2} - y^2}} + E_k \int_{y_k}^w \frac{(y - y_k)^3 dy}{\sqrt{\frac{w^2}{2} - y^2}}, \quad k = \text{int} \left( \frac{w}{\Delta y} \right), \quad (\text{A.4.5b})$$

where

$$B_n = \hat{A}_n(f + i\varepsilon) \quad C_n = \sum_{i=1}^2 \hat{A}_n(f + i\varepsilon) p_{i-1} \\ D_n = \frac{1}{2} \sum_{i=1}^2 \hat{A}_n(f + i\varepsilon) q_{i-1} \quad E_n = \frac{1}{6} \sum_{i=1}^2 \hat{A}_n(f + i\varepsilon) r_{i-1}. \quad (\text{A.4.6})$$

Solving the integrations analytically for the first part (eq.(A.4.5a)) leads to

$$\hat{u}(x, z, f + i\varepsilon) = \sum_{n=1}^k \left[ B_{n-1} F_n + C_{n-1} (\gamma_{n-1} - \gamma_n - y_{n-1} F_n) + \right. \\ \left. D_{n-1} \left( F_n \left( \frac{w^2}{2} + y_{n-1}^2 \right) - \frac{3\gamma_{n-1} y_{n-1}}{2} - \gamma_n \left( \frac{y_n}{2} + 2y_{n-1} \right) \right) + \right. \\ \left. E_{n-1} \left( -F_n \gamma_{n-1} \left( \frac{3w^2}{2} + y_{n-1}^2 \right) + \gamma_{n-1} \left( \frac{2w^2}{3} + \frac{11y_{n-1}^2}{6} \right) - \right. \right. \\ \left. \left. \gamma_n \left( \frac{2w^2}{3} + \frac{y_n^2}{3} - \frac{3y_n y_{n-1}}{2} + 3y_{n-1}^2 \right) \right) \right], \\ \text{where } F_n = \arcsin \left( \frac{y_n \gamma_{n-1} - y_{n-1} \gamma_n}{w^2} \right), \quad (\text{A.4.7a})$$

and for the second part (eq.(A.4.5b)) to

$$\begin{aligned}
 & B_k F_k + C_k (\gamma_k - y_k F_k) + D_k \left( F_k \left( \frac{w^2}{2} + y_k^2 \right) - \frac{3\gamma_k y_k}{2} \right) + \\
 & E_k \left( -F_k y_k \left( \frac{3w^2}{2} + y_k^2 \right) + \gamma_k \left( \frac{2w^2}{3} + \frac{11y_k^2}{6} \right) \right), \\
 & \text{where } F_k = \arcsin \left( \frac{\gamma_k}{w} \right) \text{ and } \gamma_k = \sqrt{w^2 - y_k^2}.
 \end{aligned} \tag{A.4.7b}$$

The coefficients  $B_n$ ,  $C_n$ ,  $D_n$  and  $E_n$  in eq.(A.4.6) can be calculated with eq.(3.4.9) and  $p$ ,  $q$  and  $r$  are given by

$$p = \frac{3}{4\Delta y} \begin{pmatrix} 0 \\ 1 \\ 0 \\ -1 \end{pmatrix}; \quad q = \frac{3}{4\Delta y^2} \begin{pmatrix} -1 \\ 2 \\ -3 \\ 2 \end{pmatrix}; \quad r = \frac{3}{4\Delta y^3} \begin{pmatrix} 3 \\ -5 \\ 5 \\ -3 \end{pmatrix}. \tag{A.4.8}$$

---

REFERENCES

- Abramowitz, M. and Stegun, I.A., 1965, Handbook of mathematical functions: Dover Publications Inc., New York.
- Ahlberg, J.H., Nilson, E.N. and Walsh, J.L., 1967, The theory of splines and their applications, Academic Press, New York, London.
- Anderson, W.L., 1982, Fast Hankel transforms using related and lagged convolutions: AMC Trans. on Math. Software, 8, no. 4, 344-368.
- Baeten, G.J.M., 1989, Theoretical and practical aspects of the Vibroseis method: Dissertation, Delft University of Technology.
- Bagnuolo, W.G., 1985, Image restoration by shift-and-add algorithm: Optics Letters, 10, no.5, 200-202.
- Bâth, M., 1968, Mathematical aspects of seismology, Elsevier Publishing Company, Amsterdam-London-New York, 43-49.
- Benoliel, S.D., Schneider, W.A. and Shurtleff, R.N., 1987, Frequency wavenumber approach of the  $\tau$ -p transform: some applications in seismic data processing: Geophys. Pros., 35, 517-538.
- Beylkin, G., 1983, Inversion of the generalized Radon transform: Proceedings SPIE, Inverse Optics, 413, 32-39.
- Beylkin, G., 1987, Discrete Radon transform: IEEE Trans. on acoustics, speech and signal processing, 35, 2, 162-172.
- Bleistein, N., 1984, Mathematical methods for wave phenomena, Academic Press Inc., Orlando, London.
- Bleistein, N., 1986, Two-and-one-half dimensional in plane-wave propagation: Geophys. Pros., 34, 686-703.
- Bracewell, R.N., 1956, Strip integration in radion astronomy, Austr. J. Phys., 9, 198-217.
- Bracewell, R.N., 1978, The Fourier transform and its applications, McGraw-Hill, New York.
- Brysk, H. and McCowan, D.W., 1986, A slant-stack procedure for point-source data: Geophysics, 51, 1370-1386.
- Brysk, H. and McCowan, D.W., 1986, Edge effects in cylindrical slant stacks: Geophys. J. R. Astr. Soc., 87, 801-813.
- Chapman, C.H., 1978, A new method for computing synthetic seismograms: Geophys. J. R. Astr. Soc., 54, 481-518.
- Chapman, C.H., 1979, On impulsive wave propagation in a spherically symmetric model: Geophys. J. R. Astr. Soc., 58, 229-234.

- Chapman, C.H., 1981, Generalized Radon transforms and slant stacks: *Geophys. J. R. Astr. Soc.*, 66, 445-453.
- Deans, S.R., 1983, The Radon transform and some of its applications, A Wiley-Interscience Publ., J. Wiley & Sons, New York.
- Deregowski, S.M., 1986, What is DMO?: *First Break*, vol 4, 7, 7-24.
- Dietrich, M., 1988, Modeling of marine seismic profiles in t-x and  $\tau$ -p domains: *Geophysics*, 53, 453-465.
- Dietrich, M., 1990, An algorithm for the plane-wave decomposition of point-source seismograms: *Geophysics*, 55, 1380-1385.
- Dobbs, S.L., Wilson, C.R. and Backus, M.M., 1990, Accounting for limited spatial aperture in the waveform inversion of p- $\tau$  seismograms: *Geophysics*, 55, 452-457.
- Drijkoningen, G.G. and Fokkema, J.T., 1987, The exact seismic response of an ocean and a n-layer configuration: *Geophys. Pros.*, 35, 33-61.
- Durrani, T.S. and Bisset, D.A., 1984, The Radon transform and its properties: *Geophysics*, 49, 1180-1187.
- Erdélyi, A., 1956, Asymptotic expansions, Dover Publications, New York.
- Felsen, L.B. and Marcuvitz, N., 1973, Radiation and scattering of waves, Prentice Hall, Englewood Cliffs, N.J.
- Fokkema, J.T. and Ziolkowski, A.M., 1987, The critical reflection theorem: *Geophysics*, 52, 965-972.
- Fokkema, J.T. and vd Berg, P.M., 1991, Reflector Imaging: submitted for publ *Geophys. Journal Int.*
- Fuchs, K., 1971, The method of stationary phase applied to the reflection of the spherical waves from the transition zones with arbitrary depth-dependent elastic moduli and density: *Zeitschrift für Geophysik*, 37, 89-117.
- Fuchs, K. and Müller, G., 1971, Computation of synthetic seismograms with the reflectivity method and comparison with observations: *Geophys. J. R. Astr. Soc.*, 23, 417-433.
- Ghosh, D.P., 1971, The application of linear filter theory to the direct interpretation of geoelectrical resistivity sounding measurements: *Geophys. Pros.*, 19, 192-217.
- Ghosh, D.P., 1971, Inverse filter coefficients for the computation of apparent resistivity standard curves for a horizontally stratified earth: *Geophys. Pros.*, 19, 769-775.
- Gradshteyn, I.S. and Ryzhik, I.M., 1980, Table of integrals, series and products: Academic Pres, Inc., London.
- Guptasarma, D., 1982, Optimization of short digital linear filters for increased accuracy: *Geophys. Pros.*, 30, 501-514.
- Hale, I.D., 1983, Dip-moveout by Fourier transform, Ph.D thesis, Stanford Univ., SEP.36.
- Hansen, E.W., 1985, Fast Hankel transform algorithm: *IEEE Trans. on acoustics, speech and signal processing*, 33, 3, 666-671.
- Harding, A.J., 1985, Inversion methods for  $\tau$ -p maps of near offset data – linear inversion: *Geophys. Pros.*, 33, 674-695.

- Harding, A.J., 1985, Slowness-time mapping of near offset seismic reflection data: *Geophys. J. R. Astr. Soc.*, 80, 463-492.
- Harrington, R.F., 1968, *Field computation by moment methods*, The Macmillan Company, New York.
- Henry, M., Orcutt, J.A. and Parker, R.L., 1980, A new method for slant stacking refraction data: *Geophys. Res. Letters*, 7, no. 12, 1073-1076.
- Hubral, P., 1980, Slant stack migration: *Festschrift Theodor Krey zum 70*, Hannover, 72-78.
- Jacobowicz, H., 1990, A simple efficient method of dip-moveout correction: *Geophys. Pros.*, 38, 221-245.
- Johansen, H.K. and Sørensen, K., 1979, Fast Hankel transforms: *Geophys. Pros.*, 27, 876-901.
- Kappus, M.E., Harding, A.J. and Orcutt, J.A., 1990, A comparison of tau-p transform methods: *Geophysics*, 55, 1202-1215.
- Kelamis, P.G. and Mitchell, A.R., 1989, Slant-stack processing: *First Break*, 7, 43-54.
- Kennett, B.L.N., 1983, *Seismic wave propagation in stratified media*; Cambridge University Press, Cambridge.
- Koster, J.K., 1991, A direct layer-stripping approach to the inversion of marine seismic data: Dissertation, Delft University of Technology.
- McMechan, G.A. and Ottolini, R., 1980, A direct observation of a p- $\tau$  curve in a slant stacked wavefield: *Bull. Seis. Soc. Am.*, 70, 775-789.
- Mersereau, R.M. and Oppenheim, A.V., 1974, Digital reconstruction of multidimensional signals from their projections, *Proc. IEEE*, 62, 1319-1338.
- Milkereit, B., 1987, Decomposition and inversion of seismic data – an instantaneous slowness approach: *Geophys. Pros.*, 35, 875-894.
- Mitchell, A.R. and Kelamis, P.G., 1990, Efficient tau-p hyperbolic velocity filtering: *Geophysics*, 55, 619-625.
- Mithal, R. and Vera, E.V., 1987, Comparison of plane-wave decomposition and slant stacking of point-source seismic data: *Geophysics*, 52, 1631-1638.
- Moon, W., Carswell, A., Tang, R. and Dilliston, C., 1986, Radon transform wave field separation for vertical seismic profiling data: *Geophysics*, 51, 940-947.
- Noponen, I. and Keeney, J., 1982, Attenuation of water-borne coherent noise by application of hyperbolic velocity filtering during the  $\tau$ -p transform: preprint 53nd SEG, 1-40.
- Oppenheim, A.V. and Schaffer, R.W., 1975, *Digital signals processing*, Prentice-Hall Inc., Englewood cliffs, New Jersey.
- Parkes, G., Ziolkowski, A.M., Hatton, L. and Haugland, T., 1984, The signature of an airgun array: computations from near-field measurements including interactions – practical considerations: *Geophysics*, 49, 105-111.
- Phinney, R.A., Chowdhury, K.R. and Frazer, L.N., 1981, Transformation and analysis of record sections: *J. Geophys. Res.*, 67, 359-377.

- Radon, J., 1917, Über die bestimmung von funktionen durch ihre integralwerte langs gewisser mannigfaltigkeiten: Ber. Verh. Sachs. Akad., Wiss., 69, 262-277.
- Robinson, E.A., Treitel, S., Wiggins, R.A. and Gutowski, P.R., 1983, Digital seismic inverse methods: IHRDC, Boston.
- Schultz, P.S. and Claerbout, J.F., 1978, Velocity estimation and downward continuation by wavefield synthesis: Geophysics, 43, 691-714.
- Siegman, A.E., 1977, Quasi fast Hankel transform, Optics Letters, 1, no. 1, 13-15.
- Singh, S.C., West, G.F. and Chapman, C.H., 1989, On plane-wave decomposition: alias removal: Geophysics, 54, 1339-1343.
- Sommerfeld, A., 1909, Über die Ausbreitung der Wellen in der drahtlosen Telegraphie: Ann. der Physik, 28, 665-736.
- Stoffa, P.L., Buhl, P., Diebold, J.B. and Wenzel, F., 1981, Direct mapping of seismic data to the domain of intercept time and ray parameter – A plane-wave decomposition: Geophysics, 46, 255-267.
- Stokes, G.G. and Kelvin, W.T., 1887, Phil. Mag., 23, 252-255.
- Tatham, R.H., Keeney, J.W. and Noponen, I., 1982, Application of the tau-p transform in processing seismic reflection data: preprint 52nd SEG, 1-52.
- Tijdens, E.H., 1990, The effect of source directivity on the bandwidth of seismic data after stack: Msc. thesis, Delft University of Technology, Section Applied Geophysics.
- Treitel, S., Gutowski, P.R. and Wagner, D.E., 1982, Plane-wave decomposition of seismograms: Geophysics, 47, 1375-1401.
- Turner, G., 1990, Aliasing in the tau-p transform and the removal of spatial aliased coherent noise: Geophysics, 55, 1496-1503.
- VerWest, B.J., Young, C.Y. and Lee, S.S., 1984, Effects of limited spatial coverage on point source tau-p amplitudes: abstract SEG, 636-638.
- Vissinga, M., Fokkema, J.T. and vd Berg, P.M., 1989, A fast Laplace-Hankel transform for forward modelling: abstract SEG, 1072-1075.
- Vissinga, M., Fokkema, J.T. and vd Berg, P.M., 1990, Classification of events in the  $\tau$ -p domain: abstract EAEG, 71.
- Wenzel, F., Stoffa, P.L. and Buhl, P., 1982, Seismic modeling in the domain of intercept time and ray parameter: IEEE Trans. on acoustics, speech and signal processing, 30, 3, 406-422.
- Weyl, H., 1919, Ausbreitung elektromagnetischer Wellen über einem ebenen Leiter: Ann. der Physik, 60, 481-500.
- Whittaker, E.T., 1902, On the partial differential equations of physics: Math. Ann., 57, 333-355.
- Widder, D.V., 1946, The Laplace transform: Princeton, Princeton University Press.
- Wilson, C.R., 1986, The Abel-Fourier method of Hankel transformation: applications to seismic data: Geophys. Pros., 34, 545-568.
- Yilmaz, O., 1987, Seismic data processing: Society of Exploration Geophysicists, Tulsa.

- Ziolkowski, A.M., Parkes, G., Hatton, L., Haugland, T., 1982, The signature of an airgun array: computations from near-field measurements including interactions: *Geophysics.*, 47, 1413-1421.
- Ziolkowski, A.M., 1987, The determination of the far-field signature of an interacting array of marine seismic sources from near-field measurements: *First Break*, 5, 10-15.

---

**SUMMARY**

The Radon transform has conventionally been applied to seismic data to decompose the data into plane wave components, that is, to separate the waves which travel with different slownesses. The calculation of synthetic seismograms from well logs employing the theory of wave propagation in plane horizontal layers, is very often handled in the frequency-slowness domain using the reflectivity method. In order to compare the synthetic seismograms with field data in the time-space domain, the synthetic data have to be transformed to the same domain with the inverse Radon transform. In conventional data processing, the Radon transformed is not used extensively due to a number of difficulties in the numerical implementation. The forward and inverse discrete Radon transforms are not exactly reversible is one of the difficulties.

In this thesis, the theory of the Radon transform is examined, and an efficient and accurate numerical implementation is developed for the one-dimensional earth (only plane horizontal layers). Attention is paid to the inherent interpolation of the discrete Radon transform, the spatially finite integration, and the evaluation of the Bessel function of the first kind in the case of cylindrical symmetry. Furthermore, a detailed analysis is performed of Radon transformed synthetic and field data sets, subdividing the noise present in the intercept time-slowness seismograms into three components: (1) incoherent noise, (2) coherent noise due to the finite integration, and (3) coherent noise due to the inherent interpolation step of the discrete Radon transform.

The theory is extended and worked out for two- and three-dimensional earth models, allowing lateral velocity variations. The theory starts with the representation of the total scattered field which is considered as a superposition of distinct primary contributions of an infinite number of interfaces. By applying a forward Radon transform with respect to the offset and source coordinates (as the data are collected in the field), the horizontal phase becomes separated from the vertical phase in the data. The next step is to carry out a high-frequency analysis using the method of stationary phase. The result of this analysis is a Fourier integral representing a decomposition of the spatial complexity of the data set. Our main application is a pre-stack migration algorithm, being an alternative approach for the conventional normal-move-out, dip-move-out, common depth point stacking and a post-stack migration scheme. Our algorithm ignores just as the conventional migration procedures any interaction between the interfaces, that is multiple reflections are treated as primary reflections. The advantage of our algorithm is the restricted computational effort and the lack of required detail of the velocity model due to the robustness of our procedure. Further, the computation time becomes a smaller fraction of the



total time as more processes, for example the removal of free surface effects, are performed in the double Radon transformed domain. To demonstrate the accuracy of the migration algorithm, both synthetic and field data examples are migrated.

---

SAMENVATTING

---

De Radon transformatie is van oudsher gebruikt om seismische gegevens te ontbinden in vlakke golf componenten, dat wil zeggen die golven te scheiden die zich met een andere traagheid (reciproke snelheid) voortplanten. Het berekenen van synthetische seismogrammen gebaseerd op de golftheorie voor een horizontaal gelaagd medium en aan de hand van putgegevens, wordt vaak uitgevoerd in het frequentie-traagheids domein waarbij men gebruik maakt van de reflectiviteit's methode. Om de synthetische seismogrammen te vergelijken met de gemeten veldgegevens moeten de gegenereerde gegevens naar het tijd-ruimte domein getransformeerd worden met behulp van de inverse Radon transformatie. Echter, door een aantal numerieke problemen wordt de Radon transformatie in conventionele gegevens verwerking beperkt gebruikt. Het feit dat de voortwaardse en inverse Radon transformatie niet exact reversibel zijn is een van de redenen.

In dit proefschrift is de theorie van de Radon transformatie bestudeerd en een efficient en accuraat numerieke implementatie is ontwikkeld voor de één-dimensionale aarde. Er is uitgebreid aandacht besteed aan de interpolatie stap, inherent aan de discrete Radon transformatie, aan de spatieel eindige integratie en aan de evaluatie van de Bessel functie van de eerste soort wanneer er sprake is van cilindrische symmetrie. Verder is een gedetailleerde analyse uitgevoerd op Radon getransformeerde synthetische gegevens en gemeten veldgegevens. Hierbij wordt de ruis die aanwezig is na transformatie, onderverdeeld in drie componenten: (1) incoherente ruis, (2) coherente ruis veroorzaakt door eindige integratie en (3) coherente ruis vanwege de onontkoombare interpolatie stap in de discrete Radon transformatie.

Vervolgens is de theorie uitgebreid en ontwikkeld voor een twee- en drie-dimensionale aarde met als gevolg dat laterale snelheidsveranderingen nu mogelijk zijn. De theorie begint met de representatie van het totale verstrooide golfveld dat wordt beschouwd als de superpositie van gescheiden contributies van een oneindig aantal lagen. Dan wordt een voortwaardse Radon transformatie uitgevoerd met betrekking tot de offset coördinaten én de bron coördinaten. Hierdoor wordt de horizontale fase van de verticale fase in de gegevens gescheiden. Een hoge frequentie benadering, gebruik makend van de stationaire fase methode resulteert vervolgens in een Fourier integral die een ontbinding van de spatiele complexiteit van de gegevens bewerkstelligd. De toepassing van deze theorie is een migratie algoritme dat een alternatief biedt voor de conventionele "normal-move-out", "dip-move-out", "common midpoint stacking" en een "post-stack" migratie schema. Het algoritme verwaarloost net zoals de conventionele migratie schema's enige interactie tussen de lagen onderling, dat wil zeggen dat veelvoudige

reflecties op dezelfde manier worden behandeld als de primaire reflecties. Voordelen van deze migratie techniek zijn de beperkte rekentijd die nodig is en de afwezigheid van een gedetailleerd snelheidsmodel door de robuustheid van het algoritme. Bovendien wordt de benodigde rekentijd nog minder wanneer meerder bewerkingen, zoals het verwijderen van "free surface effects" ook in hetzelfde domein worden uitgevoerd. Om de toepasbaarheid van het migratie algoritme te laten zien, worden zowel synthetische als veldgegevens gemigreerd.

---

## ACKNOWLEDGEMENTS

The research described in this thesis could only be carried out with the help and the support of others.

I am acknowledged to prof. A.M. Ziolkowski for his valuable criticism and suggestions during the writing of the manuscript, and I wish to express my gratitude to dr. ir. J.T. Fokkema for his continuous support and stimulating ideas throughout the four years. Also, I like to thank to Evert and Guy for critical reading of the manuscript.

Further, I greatly appreciate the use of the marine seismic data supplied by Norske Shell and by Norsk Hydro. The Tubbergen data, supported by the EEC-project under contract nr. TH/0112/88/NL and the synthetic data, generated with the acoustic finite difference program of the Acoustics group of the Physics department, are gratefully accepted.

C V

---

**CURRICULUM VITAE**

3 mei 1961	geboren te Rijswijk, Zuid-Holland
1980	diploma Gymnasium-B Stedelijk Gymnasium te Leiden
1980 - 1982	Universiteit van Leiden (Biologie)
1982 - 1986	Universiteit van Amsterdam (Geologie)
febr. 1985	kandidaats-diploma biologie
dec. 1986	doctoraal-diploma geologie
15 april 1987 - 30 april 1991	Assistent in opleiding (AIO) bij de vakgroep Petroleum- winning en Technische Geofysica van de faculteit Mijn- bouwkunde en Petroleumwinning aan de TU Delft
1 mei 1991 - heden	Seismische interpretator bij Mobil

## Stellingen

behorend bij het proefschrift

"The Radon transform and its application to the interpretation of seismic data"

- 1- Wanneer een functie ver beneden het Nyquist criterium wordt bemonsterd, is lineaire interpolatie voldoende nauwkeurig en bovendien kostenbesparend vergeleken met bijvoorbeeld een derde orde interpolatie zoals de kubische spline.

Hoofdstuk 3, dit proefschrift

- 2- De stationaire punten, die geassocieerd zijn met de stationaire-fase analyse van de Radon transformatie, schrijven voor welke waarden van inverse snelheid nog betrouwbaar zijn, gegeven een bepaalde offset en voortplantingssnelheid. Het hyperbolische snelheidsfilter, o.a. van Mitchell en Kelamis (1990), is hieraan nauw gerelateerd en beoogt hetzelfde effect.

Mitchell, A.R. and Kelamis, P.G., 1990, Efficient tau-p hyperbolic velocity filtering: Geophysics, 55, 619-625.

Hoofdstuk 5, dit proefschrift

- 3- In het dubbel Radon getransformeerde domein waarbij de bron- en offset-coördinaten gescheiden behandeld worden, leidt de spatiële complexiteit van de volledige data set tot een goed gedefinieerde topologische klassificatie. De stationaire punten uit de transformatie integraal kwantificeren de beperking van de data set, d.w.z. de grootste helling van een laag die nog betrouwbaar is in de gemigreerde sectie, wordt bepaald door de offset, de voortplantingssnelheid en de diepte van de laag.

Hoofdstuk 6, dit proefschrift

- 4- Het equivalente horizontale snelheidsmodel, behorend bij een seismische data set, wordt verkregen door in het dubbel Radon getransformeerde domein een conventionele snelheidsanalyse uit te voeren in het subdomein waar de inverse snelheidscomponent gerelateerd aan de bron, gelijk is aan nul.

Hoofdstuk 6, dit proefschrift

- 5- De dubbel Radon getransformeerde data set leent zich uitstekend voor een richtingsafhankelijke deconvolutie aangezien zowel bron- als offset-coördinaten gescheiden getransformeerd worden.

- 6- Voor een betrouwbare numerieke behandeling van de Radon transformatie is een symmetrische bedekking ten opzichte van de oorsprong noodzakelijk. Voor seismische data met een enkelzijdige bedekking, bijvoorbeeld een mariene data set, kan een gedeeltelijke reconstructie van de symmetrische bedekking gerealiseerd worden door gebruik te maken van het reciprociteitsbeginsel voor bron en ontvanger.
  
- 7- Het verrichten van metingen door een geoloog en door een geofysicus onderscheidt zich fundamenteel door de schaal van de metingen. Het daaruit voortvloeiend verschil in oplossend vermogen van de parameters kan bij het geforceerd correleren van die geofysische en geologische parameters leiden tot wetmatigheden die niet gestoeld zijn op fysische wetten.
  
- 8- De conventionele methode om een synthetisch seismogram uit te rekenen is gebaseerd op een niet-realistische configuratie van bron en geofoon. Wanneer men er vanuit gaat dat bolvormige golven, uitgezonden door een puntbron (bijv. dynamiet) beschouwd kunnen worden als de som van een oneindig aantal vlakke golven en dat deze vlakke golven gereflecteerd en gebroken worden op de grensvlakken, dan zal de superpositie van al deze golven de complete puntbron responsie geven. Daarom verdient het de aanbeveling het synthetisch seismogram te berekenen in het inverse snelheidsdomein.  

Vissinga, M., Ziolkowski, A.M. and Fokkema, J.T., 1989, A new method for matching stacked seismic data with well log information: abstract EAEG, p. 117
  
- 9- De gebruikersvriendelijkheid van sommige software pakketten doet vermoeden dat deze geschreven zijn door én voor niet-gebruikers.
  
- 10- Een goede samenwerking kenmerkt zich door de mate waarin beide partijen bereid zijn compromissen te sluiten.